FINITE ELEMENT ANALYSIS OF SHEAR BAND FAILURE WITH PARTICULAR APPLICATION TO CIRCULAR PLATE IMPACT

By

A.P. BELL, B.Sc.

Thesis submitted to City University in candidature for the degree of Doctor of Philosophy

Sponsoring establishment:

City University
Department of Civil Engineering
London

Collaborating establishment:

Finite Element Analysis Limited
London

August 1989

ACKNOWLEDGEMENTS

The research described in this thesis was performed within the Civil Engineering department, a division of the Faculty of Engineering at City University. During the course of the research, the author received encouragement and advice from many people. In particular the author would like to express gratitude to the following:

To the Science and Engineering Research Council for the funding of the majority of this project.

To Dr L.F. Boswell, the author's academic supervisor, for the initial instigation of the project and his subsequent constructive guidance.

To Dr L.P.R. Lyons, the author's industrial supervisor, for his practical help during the course and particularly for making the LUSAS finite element system freely available.

The Library staff of The City University have also been of invaluable assistance in obtaining many of the papers referenced herein.

To the author's colleagues at both City University and Finite Element Analysis Ltd. who have offered advice and encouragement on many occasions.

To Mr D.P. Barry, for his guidance and encouragement during the initial stages of this work.

To Mr T.M.N. Clifton, for his assistance in preparing certain of the figures used herein.

I also want to express much thanks to my family and friends who have been so supportive in my endeavours to finish this project.

Finally, to my closest friend, without whom none of this would have been possible.

SUMMARY

This thesis addresses the problem of the numerical simulation of the shear band or 'plugging' mode of failure in metallic solids. Particular reference is made to the normal impact between blunt projectiles and circular plates of thin to intermediate thickness.

The thesis presents a two dimensional axisymmetric and plane strain finite element computer program related to the Lagrangian reference frame. A four node element with one point quadrature and associated stabilisation is utilised, and is shown to be superior to standard isoparametric implementations when applied within an explicit time integration scheme. Finite deformation capabilities are included, together with material nonlinearity in the form of a von Mises elastic-plastic model. The algorithms used in this work are dictated to a large degree by the emphasis which is placed upon efficiency, although this is not at the expense of accuracy. Numerical stability in the presence of severe stress gradients is achieved through the use of an artificial viscosity scheme.

The impact conditions along the contacting interface are governed by the use of a penalty-based slideline technique which permits arbitrarily large relative deformations of the contact surfaces.

With the foregoing numerical basis, the penalty-based slideline technique has been extended in this work to facilitate the discrete modelling of the fracture process present during plugging.

The computational model has been embedded within the LUSAS finite element system which provides extensive pre and post processing facilities.

A detailed discussion of the problems involved in the solution of high velocity impact calculations is given, together

with an assessment of the effects of several material related parameters on the solution.

Several numerical comparisons with experimental evidence are also performed to indicate the effectiveness of the method.

Finally, relevant conclusions have been made and suggestions for further study are provided.

CONTENTS

NOTATION

$\underset{\sim}{\ }$	Vector
$\cap$	Union
$(\ )^T$	Transpose of a vector or matrix
$(\ )^{-1}$	Inverse of a vector or matrix
$(\ )^n$	Evaluated at timestep (t=n)
$d(\ )$	Differentiation of given variable
$(\dot{\ })$	Rate
$(^\circ)$	Referred to unrotated configuration
$(^j)$	Nodal point reference
$\Sigma(\ )$	Summation
$(\ )_{,i}$	Differentiation with respect to current variables
$(\ )_{,I}$	Differentiation with respect to original variables
a_i	Acceleration vector
a,b	Local element coordinate axes
A_e	Element area
A,h	Material rate parameters
b_1, b_2	Region occupied by two bodies in their deformed configuration
B_i	Bulk modulus for element i
B_{ij}	Strain displacement matrix
B_1, B_2	Region occupied by two bodies in their undeformed configuration
c	Current dilational material wave speed in elastic material
c_i	Diagonal damping matrix
$\underset{\sim}{c}$	Relative position vector between current and local node
C_{ijkl}	Elastic constitutive matrix
d_i	Nodal displacement vector in global axes
dS	Current length of a line segment
dS_e	Increment of surface area
dS_o	Original length of a line segment
dt	Time step increment

dtcr	Critical time step
dV_e	Increment of volume
D_a	Maximum distance between two adjacent contact nodes
D_{ij}	Velocity strain tensor
D^p_{eff}	Effective plastic strain
e_{ij}	Almansi strain tensor
E	Youngs modulus
E_p	Plastic hardening modulus
E_t	Tangent modulus
E_{ij}	Green-Lagrange strain tensor
f_i	Element load vector
f_{ni}	Normal interface force on contact node i
f_{ti}	Tangential interface force on contact node i
f_{ri}, f_{zi}	Hourglass resistance forces
F_i	Internal force vector
F_{ij}	Deformation gradient matrix
$\dot{F}_{ij}$	Deformation gradient rate matrix
g	Hourglass coefficient
g_{ij}	Any element function
g_o	Value of g_{ij} at element centroid
G	Shear modulus
G_i	Diagonal viscous force matrix
h_r, h_z	Hourglass velocity
H_i	Hourglass resistance vector
J_{ij}	Jacobian matrix
k_i	Interface stiffness coefficient for local segment i
K	Bulk modulus
K_{cr}	Time step growth restraint constant
K_i	Nodal interface stiffness of adjacent node i
K_r	Time step reduction factor
l	Length of local contact segment
L	Length of element in direction of wave propagation
L_c	Shortest signal path across an element
L_d	Length of longest element diagonal
M_{ii}	Diagonal mass matrix
M_{ij}	Consistent mass matrix

n_e	Number of elements in structure
n	Unit segment normal vector for current node
$\tilde{n}_{ij}$	Unit normal vector to segment ij
N_a	Number of adjacent nodes
N_{ij}	Rectangular interpolation matrix
N	Number of nodes on an element
$p_i( )$	A global function
p_o	Value of function $p_i( )$ at centroid of element
p	Hydrostatic pressure
P_i	External load vector
q	Artificial bulk viscosity pressure
Q	Constant to account for bulk viscosity effect in critical time step computation
Q_h	Hourglass constant
Q_1, Q_2	Dimensionless constants
r_o	Current radius of element centroid (axisymmetry only)
r_i, z_i	Element nodal coordinates
r_z	Contact zone radius
R_{ij}	Rotation matrix
s_{ij}	Deviatoric stress tensor
S_e	Element surface area
S_i	Segment definition code
t	Time
t_i	Thickness of local contact segment
T	Natural period of oscillation of a system
T_i	Surface traction vector
Tol	Contact segment extension parameter
u_i	Particular displacements
U_{ij}	Right stretch tensor
v_i	Velocity vector
v_o	Initial velocity of projectile
V_e	Volume of element
V_{ij}	Left stretch tensor
V_o	Original volume
w	Current density
w_o	Original density
x_i	Current particle coordinates (x_i, y_i)

$\underset{\sim}{x}_i$	Unit segment tangent vector for current node
$\underset{\sim}{x}_{ij}$	Unit tangent segment vector to segment ij
X_α	Material particle coordinates (X_i, Y_i)
X_i	Coordinates for contact node i
$\underset{\sim}{X}_c$	Contact location point coordinates
X_n	Normal penetration distance for current node
α_r	Radial overlap constant
$\alpha,^n$	Axisymmetric internal force terms
α_1, α_2	Dimensionless history contact location point parameters
$^n_1$, $^n_2$	Dimensionless current contact location point parameters
Γ_i	Hourglass deformation vector
Γ_{max}	Maximum eigenvalue
δ_{ij}	Kronecker delta
δb_1, δb_2	Boundaries of regions B_1 and B_2
δf_{ti}	Tangential interface force increment on contact node i
δX_{ti}	Tangential displacement increment for node i
ϵ_{ij}	Total strain tensor
μ	Coefficient of friction
σ_i	Cauchy stress vector
σ'_i	Augmented Cauchy stress vector
σ_{ij}	Cauchy stress tensor
σ_y	Yield stress
σ_Θ	Cauchy hoop stress term
τ_{rz}	Cauchy shear stress term
ϕ_i	Element shape functions
Ω	Region of Euclidean space
Φ	Interface stiffness scale factor
Θ	Angle between two adjacent segments

LIST OF FIGURES

LIST OF TABLES

CHAPTER 6

CHAPTER 1

GENERAL INTRODUCTION

1.1 OVERVIEW

The mechanics of penetration and perforation of solids has long been of interest in military applications. Now, however, as civilian technology grows more sophisticated, increasingly exacting demands are being made on the behaviour of materials under very short duration loading. It is thus becoming mandatory that a rigorous understanding of impact behaviour be attained for the safe and cost effective design of structures involving such conditions.

Any item capable of being launched can become a projectile and may produce serious damage if allowed to come into contact with a suitable target. Military projectiles are probably the most familiar, but they actually form only a very small subset of possible missiles. For example, during the demolition of buildings made of prestressed concrete, small fragments may be formed as a result of rapid unloading. In hard concrete or steel, these may acquire speeds in the region of 100 ms^{-1} and can be lethal. Telephone poles, cars, and assorted tornado debris, as well as aircraft, equally have the potential for exacting structural damage.

Typical examples of current interest in which this type of projectile plays a significant role in the impact process include;

(i) The integrity of nuclear reactor pressure vessels with respect to internally created projectiles.

(ii) Crashworthiness of vehicles and the protection of their occupants or cargo.

(iii) Transportation safety of hazardous materials.

(iv) Protection of spacecraft from meteoroid impact. Similarly, the multiple impact by ice, water and sand particles upon high speed aircraft and re-entry vehicles also constitutes a continual hazard.

(v) Explosive forming and welding of metals.

(vi) The vulnerability of military vehicles, aircraft and structures to impact and explosive loading.

(vii) The containment of components from failed industrial machinery such as turbine blades and pipes.

The response experienced during the impact between such targets and projectiles is influenced by variables such as material properties, impact velocity, target support position, projectile shape and the relative dimensions of both target and projectile. The impact velocity is, in many ways, the most fundamental because it overrides almost any other consideration, and is commonly used as a rudimentary method for classifying the impact process. This leads to the commonly held grouping of impact phenomena into three distinct impact regimes, and these are;

Low velocity impact (<250ms^{-1}), which is identified by the presence of local indentations or penetrations which are strongly coupled to the overall deformation of the structure. The gross response is dominated by the low frequency components of the modal spectrum to give loading and response times in the millisecond time domain. Pressures are generated within the impacting bodies of the order of the material elastic modulus. Elastic collisions are also included in this regime.

High velocity impact (0.25-12kms^{-1}), which is typically governed by the behaviour of the material within a small zone. The material response is characterised by a high frequency content and the loading and response times are now of the order

of microseconds. As the velocity increases within this range, pressures are generated which exceed the elastic moduli of the colliding materials by several orders of magnitude, particularly in the early stages of the impact process. During this initial transitory period the rate of energy deposition in the impact zone is sufficiently high that a change of state may occur. Furthermore, the deviatoric (shear) deformation typically becomes insignificant with respect to the volumetric behaviour and the material behaves essentially like a fluid. Material shear strength is still, however, of considerable influence at later times.

Hypervelocity impact (>12kms^{-1}). Within this regime hydrodynamic pressure dominates the behaviour of the solids throughout the impact process. The equations of motion, together with a high pressure equation of state, are the principal descriptors of material behaviour.

A summary of the material response to different impact velocities is given in Table 1.1, but it should be noted that the impact velocity ranges given are reference points only. The actual transitions are extraordinarily flexible in practice and are dependent on the numerous additional parameters mentioned previously.

The failure of a target is no less complicated and is due to the interaction of a variety of failure mechanisms. Low velocity impact tends to be the simplest and is characterised by unacceptable levels of plastic deformation, while the most frequent types in the high velocity domain consist of fracture resulting from the initial compression wave, fracture in the radial direction, spalling, scabbing, plugging, front or rear petaling, fragmentation in the case of brittle targets and ductile hole enlargement. These failure modes are depicted in Figure 1.1. Towards the limit of the high velocity regime hydrodynamic erosion of both target and projectile may also

occur. Increasing initial velocities beyond this point to the tremendous rates of energy transfer associated with hypervelocity impact typically produces explosive vaporisation in the contact zone.

It is well understood that the rate of loading has a significant effect on the response of many metals and is an additional complexity in the consideration of the impact process. The modulus of elasticity and Poissons ratio appear to be quite insensitive to changes in strain rate and are only moderately affected by temperature variations. The elastic range of many metals is, however, extended considerably with increase in strain rate over that corresponding to static loading. Also, the dynamic plastic stress-strain relation is generally in excess of the static curve. This feature is particularly pronounced in the case of materials with a definite yield point. Strain rate and temperature may also play an important role in determining the type of fracture in a given impact configuration.

A thorough understanding of the perforation process has, thus, been impeded by the involved manner in which these configurational and material parameters interact. It is not surprising, therefore, that the bulk of research in this area has been experimentally based and, at present, there is no unified theory available which covers the various types of phenomena which can occur under differing conditions. Thorough reviews of the fundamentals of solid collisions and typical associated phenomena have previously been prepared by Goldsmith (1960), (1963), Backman and Goldsmith (1978), Zukas (1982) and Kimsey (1983).

The limited nature of understanding in this whole subject area has led many experimentalists to study the impact problem using simple physical geometries, such as circular plates, cylinders with various shaped ends or slender bars. The intention being that the results from these tests would develop a fundamental understanding to enable the prediction of the structural behaviour of prototype designs. In recent years the

use of numerical methods to augment such experimental work has greatly increased and is partly due to the following statement from a specialist committee set up to assess the state of the art of material response to ultra-high loading rates, NMAB (1980);

> "... rough computations using simple material models with published or even estimated material properties, may be used in conjunction with exploratory test firings to scope an initial design. Comparisons of test data with the predictions may reveal discrepancies which suggest refinements in the computations of material models, and the need for some dynamic material property measurements. Once reasonable agreement has been achieved, another round of computations may then be performed to refine the design. Test firings of this design might use more detailed diagnostic instrumentation. This sequence is iterated, including successively more detail in material models, material property studies and ordnance test firings, until a satisfactory design is achieved. In this procedure, unnecessarily detailed computations, material property studies or test firings are minimised; only the details necessary to achieve a satisfactory design are included."

It has become clear that the continued application of numerical techniques to penetration mechanics problems in this suggested manner has greatly enhanced the understanding of the penetration and perforation process. Moreover, any erroneous numerical predictions may be detected within the confines of this dual environment and increasingly sophisticated numerical techniques are thus developed. In the course of this combined method of investigation, the inadequacies of the current numerical methods and particularly the finite element method, to model such behaviour is now apparent.

In view of the above it is the objective of this thesis to develop a computational model for the numerical simulation of

failure in metallic plates of thin to moderate thickness impacted by flat ended projectiles, with particular reference to the plugging mode of failure. It is intended that the research will overcome certain inadequacies of existing numerical techniques and to use the improved techniques to develop a method of solution which will enable the aforementioned NMAB proposal to be performed with a greater degree of accuracy, flexibility and reliability.

The opinion of the author is that fracture surfaces developed during an impact failure situation may be modelled by application of an existing numerical contact interface technique. The choice of the plugging mode of failure to investigate this supposition has been motivated by the qualities that this particular mechanism exhibits. The qualities are summarised as follows;

(i) This mechanism is one of the few essentially two dimensional failure modes.

(ii) The crack progression is regular and readily lends itself to the attention of contact interface methods.

(iii) A characteristic of the majority of perforation applications is that shear modes of failure such as occur in the plugging process are far more common than tensile modes.

The remainder of this chapter will provide an overview of the plugging failure mode. The intention is not to give complete coverage but rather establish the main characteristics to be of use in succeeding chapters. The proposed numerical model and a fuller description of the objectives of this work will also be presented. A statement of the thesis layout will complete the chapter.

1.2 DEFINITIONS

The following definitions will be adopted in this thesis, Backman and Goldsmith (1978);

Projectile
Any object that is considered to initiate an impact. No functional constraints will be imposed.

Target
The smallest functionally and/or structurally independent object whose performance is to be impaired by the projectile.

Impact
The entry of the projectile into any region of the target, which may be considered as three distinct structural environments.

(i) Contact
The projectile is deflected, being neither stopped by, nor perforating through, the target.

(ii) Penetration
The projectile remains embedded in the target after complete dissipation of system kinetic energy.

(iii) Perforation
The complete traversal of the target thickness by the projectile.

Ballistic limit
The average of two striking velocities; the highest velocity giving penetration and the lowest velocity giving perforation.

Target classification
It is convenient to classify targets by thickness;

(i) Thin plate
The stress and deformation gradients are uniform throughout the thickness.

(ii) Intermediate plate
The distal surface exerts a considerable influence on the deformation process during the projectile motion.

(iii) Thick plate
The distal boundary is only influenced by the impact process after substantial travel into the target.

Furthermore, problems governed by the equations of motion may be broadly categorised into either wave propagation or inertial domains, Belytschko (1983);

Wave Propagation response

Excitation of a large number of natural frequencies of the system is seen to be the dominating response mechanism in which the behaviour and accurate representation of the subsequent wavefront is of engineering importance.

Inertial Response

Inertial problems are dominated by low frequency response. and are often referred to as a structural dynamics problem. The rise time and duration of the load relative to the time required for a wave to traverse the structure may be used as a preliminary criterion for classifying the problem. If the rise time and duration of the load exceed several times the traversal time of the wave across the body of interest, the problem is usually of the inertial type.

1.3 SHEAR BAND PHENOMENA

Consider the interaction between a projectile and a target plate. Immediately after initial contact, strong compressive stress waves propagate into both bodies. A relief wave is

simultaneously created at the laterally free surface of the projectile and propagates inward, crossing at the centreline and producing a region of high tensile stress. The initiation of radial flow in the projectile is a result of this stress field.

The initial transient is very brief and soon followed by a stable, plastic flow field which steadily propagates throughout the target.

The balance between the initial transient and subsequent plastic flow magnitudes have a major influence on the particular failure process which subsequently occurs, Ravid and Bodner (1983). The plugging mode of failure, which is also known as shear banding, occurs when the transient magnitude is smaller than that required to initiate spall. If the impact velocity were sufficiently high, then for the same geometry, spall would be experienced in preference to the plugging mode, Mescall (1977).

Plugging is more generally observed during the impact process between a cylindrical flat ended projectile and a hard metallic target plate. Conditions may be met at almost any time during the impact process, but for projectiles whose diameter is of the order of the target thickness, these are satisfied very soon after impact, Sedgwick et al (1978). The bluntness of the projectile and the hardness of the target tend to minimise the radial flow so that the underlying target material is constrained to move ahead of the projectile producing a narrow band of very high shear strain, Awerbuch and Bodner (1974b), Woodward (1984). Experimental evidence clearly suggests that this band originates from the frontal face and propagates along a cylindrical surface whose diameter is roughly equal to that of the projectile. Failure occurs on this surface at some critical value of the shear strain and, at velocities over the ballistic limit, a cylindrical 'plug' is ejected, Mescall (1977). Final separation can also include ductile fracture at the distal surface.

The plugging phenomena has been modelled as a three phase process, Awerbuch and Bodner (1974a), Awerbuch and Bodner

(1974b), Woodward (1984). More recently, however, this model has been updated to include a more detailed five phase interpretation, Liss et al (1983), Goldsmith (1985). To elucidate the foregoing discussion the latter description will be summarised here.

Indentation

Initial acceleration of the plug material occurs during which axial compression and some limited radial flow are observed. The effect of shear strain in this phase is limited.

Plug formation

The plug material continues to be accelerated and shear band formation occurs due to the relative motion between the target plate and the plug material. The onset of the maximum resistive shear force along the shear band boundary indicates the termination of this stage.

Plug separation

Separation of the plug is followed by fracture along the shear band boundary. It is important to note here that fracture is an independent process from the formation of shear bands, although it is true to say that the two are closely associated since cracking is very often observed to form and grow preferentially near or within the shear band region. Observations tend to indicate that the distal surface of the plate rapidly acquires the terminal velocity of the projectile once it is set in motion. The implication is that within this phase the distance moved by the plug is very small and, moreover, complete plug disengagement occurs, Mescall (1977).

Plug slipping

The newly formed plug and projectile are then free to perforate the target if the impact velocity is sufficiently high. Large shear forces are observed between the plug and target during this phase.

Post perforation deformation.

This may be observed if the plug has been completely separated before acquiring projectile velocity. A plastic stress wave, originating at the projectile-plug interface and causing the plug to accelerate now traverses the thickness of the plug. Deformation occurs as a result of the now laterally free plug responding to this wave.

Frictional effects between the projectile and target are generally observed to be small as a result of an adiabatic heat generation process at their interface. This process generates a thin layer of fluid which acts as a lubricant to the ensuing motion. Although the influence of friction increases as the projectile velocity decreases, experimental evidence has shown that the energy lost in this manner amounts to a maximum of 3% of the initial projectile energy, Krafft (1955). More recent research has produced results in substantial agreement with this finding except in the region of the ballistic limit where it has been suggested that frictional losses are of considerable importance. The assumption has been supported empirically by observing the entrapment of projectiles subsequent to plug ejection at post ballistic limit velocities together with the deposits of target material on projectiles which have perforated the target, Woodward and Morton (1976).

Shear effects are significant, however, along the interface between the plug and the target material as interference occurs between these two regions subsequent to initial shear failure, Awerbuch and Bodner (1974b), Wingrove (1972). Test results indicate the presence of a continuous shear force between the plug and plate, which is characterised by an initial instantaneous peak subsequently decaying rapidly but at a decreasing rate. The maximum interface force becomes larger with increasing impact velocity. A small secondary increase of the shear force after the initial drop is also detected and is attributed to the need for rapid initial acceleration of the target around the crater vicinity. Figure 1.2 is representative

of typical experimental results, Liss and Goldsmith (1984). There is evidence to suggest that this force is viscous in nature, Awerbuch and Bodner (1974b).

The plug thickness is approximately equal to the plate thickness at the ballistic limit and tends to decrease with increasing impact speed. In general, the plug and plate diameters are not cylindrical. The distal diameter of the plug is less than the frontal diameter while the distal diameter of the plate is greater than the frontal diameter (see Figure 1.1d). Results have shown that frontal face plug diameters differ only slightly from those of the associated steel projectiles.

A typical radial strain history of an aluminium plate impacted by a blunt rigid projectile at less than the ballistic velocity is shown in Figure 1.3, Liss and Goldsmith (1984). The region directly beneath the projectile clearly experiences a high compressive strain. At radii greater than three times the projectile radius the presence of asymmetric bending strains may be seen. A transition zone exists between the two.

In conclusion, therefore, a typical plugging type response experiences large deformations at the point of impact with the inclusion of material failure as an added complication. The strong coupling between these localised effects and the smoother nature of the overall structural behaviour is indicative of a transitional stage between wave propagation and inertial responses. It is clear that the presence of material failure emphasises the wave propagation effects of the response on the final solution, since the underlying plate impact problem is essentially of a structural dynamics type.

The loading and response times are typically in the sub-millisecond regime and imply the presence of steep stress and velocity gradients in the structure. These are not of sufficient magnitude, however, to cause the creation of shock fronts. It is the combination of these highly localised effects, which yield the finite deformation and rotation fields commonly experienced

and which themselves propagate material failure due to an unacceptable level of plastic strain along planes of maximum shear stress. For the sake of clarity in future discussions the plugging failure mechanism and the associated environment to produce such impact behaviour will be termed a high velocity phenomenon.

1.4 THE NUMERICAL MODEL

The finite element computer codes currently available for impact studies use one of two methods to describe particle motion; Lagrangian or Eulerian. Each method has a certain advantages for various problem classes.

Lagrangian codes follow the motion of fixed elements of mass, the computational grid is fixed in the material and distorts with it. Their primary advantage is in their ability to accurately track material boundaries and interfaces, furthermore, they are ideally suited for constitutive models which use time history variables. Because the Lagrangian grid distorts with material flow, deformations may become severe during an impact process and require the mesh to be rezoned.

Eulerian codes have computational grids fixed in space, through which material passes. They are ideally suited for large distortions in the sense that the finite element grid is now independent from material flow. These calculations may be carried out either by including the convective derivatives implicitly in the discretisation scheme or by performing a two step operation, the first phase is a Lagrangian calculation whilst the second (or 'transport') phase amounts to a rezoning of this distorted Lagrangian grid back to the undistorted Eulerian grid. Of the two methods, this latter procedure, termed a Lagrangian-Eulerian link, is the most effective within the high velocity regime at present and is used when severe mesh distortions in a Lagrangian solution give rise to unacceptably large values of truncation

errors. Even the most sophisticated rezone routines, however, have been disappointing for the two dimensional case, while none exist for their three dimensional counterparts, Backman and Goldsmith (1978). Moreover, difficulties arise in the rezoning procedure during the averaging of internal state variables representing material memory, since a given new mesh may cover several old meshes, each of which having experienced a somewhat different history. The problems involved in the convective operation necessary with the Eulerian codes is actually a major limitation in high velocity impact analyses which require both an accurate determination of material history as well as a detailed description of nonlinear boundary conditions.

It is, therefore, generally desirable to formulate high velocity impact computer codes within the Lagrangian frame if they have the capability to adequately represent the various physical phenomena which occur. Furthermore, their efficiency is increased over the Eulerian method by virtue of the reduced mesh description required, Johnson and Stryk (1986).

The very large deformations present in impact situations has historically made the Eulerian grid the only choice because of limitations in Lagrangian methods for this class of problem. Current research to present a Lagrangian algorithm capable of simulating the severe distortion experienced during a typical plugging failure in a routine manner has, therefore, several motivations and these are;

(i) Elimination of the time consuming transport phase of the Eulerian method.

(ii) The diffusive factor inherent in the Eulerian method is a critical limitation in the accurate physical modelling of advanced failure.

(iii) The extension of the Lagrangian frame to this class of problem will enable the use of identical constitutive models and thus yield increased numerical consistency in computational results.

(iv) Several rezoning operations may be required before a successfully rezoned grid is obtained. Moreover, the final result is very dependent on the experience of the operator performing the rezoning.

It is only recently, however, that interest has been shown in the flexibility of contact interface methods and their ability to extend the functionality of the Lagrangian codes into severely distorted domains.

The commencement of this recent work appears to have been instigated by the development of an eroding interface algorithm. This approach allows elements which have developed a specified strain to erode off the interacting solids. The elements essentially disappear except for the retention of the nodal mass, while the contact interfaces are updated as necessary. The initial work was implemented in the EPIC-3 code, but had limited usefulness since the eroded area had to be determined a priori, Johnson (1982). More general algorithms were subsequently developed in two dimensions whereby both projectile and target elements were permitted to be eroded while the interfaces were updated in an automatic manner, Stecher and Johnson (1984). The three dimensional version of these general routines has now been developed using both hexahedral elements, Belytschko and Lin (1987) and tetrahedral elements, Johnson and Stryk (1986).

The application of contact interface methods to plugging situations is currently extremely limited and is presented in an investigatory manner by Ringers (1983), who developed a technique based on the velocity constraint method as implemented in the EPIC codes, Johnson (1977). Later research has shown its applicability to adiabatic shear situations, Ringers (1985). The former report by Ringers is the only published paper known to the author in relation to this subject, however, no quantitative comparisons with existing experimental data were given.

The velocity constraint method used to model the fracture

surface in the code above has inherent weaknesses which will be discussed further in Chapter Three. Furthermore, the formulation of the EPIC code with its sole use of the linear triangular element has also been shown to have a number of deficiencies, Hallquist et al (1977), and these are;

(i) The triangular elements behave very poorly under conditions of large deformation, plastic flow in two dimensions. These elements have been observed to be excessively stiff, almost to the point of locking.

(ii) The use of an equivalent strain measure which is path independent may create unrealistic plastic material response since it is free to either increase or decrease throughout the solution.

(iii) The explicit time integration scheme used possesses negative damping. This causes the solution error in small deformation elastic problems to grow regardless of the step size; consequently its application to nonlinear problems seems unwise.

1.5 THESIS OBJECTIVES

The objectives of this work are seen to cover three principal areas;

(i) The development of a modified slideline method to enable the computation of ductile shear failure and which overcomes certain current numerical inadequacies which will be outlined in subsequent chapters.

(ii) The extension of an explicit numerical solution scheme using the Lagrangian frame of reference to the large deformation domain without recourse to any time consuming convective phases.

(iii) Both the qualitative and quantitative correlation of numerical results with existing experimentally obtained data.

This new tool will hopefully facilitate the advance of a complete solution to this formidable problem and increase confidence in the ability of this type of analysis to predict the physical behaviour in the region of the highly strained fracture surfaces. The principal contribution of this work will arise from the emphasis placed upon the simulation of crack propagation using the concept of Fracture Slidelines. Only planar and axisymmetric problems will be considered.

1.6 THESIS ARRANGEMENT

Chapter 2 discusses the finite element considerations necessary to model the special requirements involved in impact situations.

Chapter 3 introduces the concept of the slideline technique and discusses the theoretical and practical limitations inherent within this formulation of the contact problem.

Chapter 4 presents several comparisons between theory and experiment to validate the applicability of the slideline technique to this particular class of transient problem.

Chapter 5 describes the proposed Fracture Slideline numerical model for the plugging process.

Chapter 6 presents selected examples to demonstrate the capabilities of the proposed model.

Chapter 7 presents conclusions and discusses the achievements and restrictions of the model. Further areas for study are suggested.

1.7 REFERENCES

Awerbuch, J. and Bodner, S.R. (1974a). 'Analysis of the Mechanics of Perforation of Projectiles in Metallic Plates', Int. J. Solids Structures, Volume 10, pp 671-684.

Awerbuch, J. and Bodner, S.R. (1974b). 'Experimental Investigation of Normal Perforation of Projectiles in Metallic Plates', Int. J. Solids Structures, Volume 10, pp 685-699.

Backman, M.E. and Goldsmith, W. (1978). 'The Mechanics of Penetration of Projectiles into Targets', Int. J. Engng. Sci., Volume 16, pp 1-99.

Belytschko, T. (1983). 'An Overview of Semidiscretisation and Time Integration Procedures', Computational Methods for Transient Analysis, Volume 1, Belytschko and Hughes (Editors), North-Holland Press.

Belytschko, T. and Lin, J.I. (1987). 'A Three-Dimensional Impact-Penetration Algorithm with Erosion', Comput. struct., Volume 25, Number 1, pp 95-104.

Goldsmith, W. (1960). Impact - The Theory and Physical Behaviour of Colliding Solids, Edward Arnold, London.

Goldsmith, W. (1963). 'Impact : The Collision of Solids', Appl. Mech. Rev., Volume 16, Number 11, pp 855-866.

Goldsmith, W. (1985). 'Initiation of Perforation in Thin Plates by Projectiles', Metal Forming and Impact Mechanics, Reid (Editor), Pergamon Press.

Hallquist, J.O. and Werne, R.W. and Wilkins, M.L. (1977). 'High Velocity Impact in Three Dimensions', Discussion in J. Appl. Mech., Trans. ASME, pp 793-795.

Johnson, G.R. (1977). 'High Velocity Impact Calculations in Three Dimensions', J. Appl. Mech., ASME, Volume 99, Number 1, pp 95-100.

Johnson, G.R. (1982). 'Status of the EPIC Codes, Material Characterisation and New Computing Concepts at Honeywell', Proceedings of Computational Aspects of Penetration Mechanics (Lecture Notes in Engineering;3), Maryland, USA, Chandra and Flaherty (Editors).

Johnson, G.R. and Stryk, R.A. (1986). 'Eroding Interface and Improved Tetrahedral Element Algorithms for High-Velocity Impact Computations in Three Dimensions', Proc. of the Hypervelocity Impact Symposium, Texas.

Kimsey, K. (1983). 'Calculation of Penetration', Proceedings of the Workshop on the Theoretical Foundation for Large Scale Computations of Nonlinear Material Behaviour', Evanston, pp 165-181, Nemat-Nasser (Editor), Martinus Nijhoff Publishers.

Krafft, J.M. (1955). 'Surface Friction in Ballistic Penetration', J. Appl. Phys., Volume 26, pp 1248-1253.

Liss, J. et al. (1983). 'A Phenomenological Penetration Model of Plates', Int. J. Impact Engng., Volume 1, Number 4, pp 321-341.

Liss, J. and Goldsmith, W. (1984). 'Plate Perforation Phenomena due to Normal Impact by Blunt Cylinders', Int. J. Impact Engng., Volume 2, Number 1, pp 37-64.

Mescall, J.F. (1977). 'Computer Simulation of Penetration', Proc. 14th Annual Meeting of the Society for Engineering Science, Bethlehem PA, pp 81-93.

NMAB. (1980). 'Materials Response to Ultra-High Loading Rates', Report of the Committee on Materials Response to Ultra-High Loading Rates, National Materials Advisory Board, Report Number NMAB-356.

Ravid, M. and Bodner, R. (1983). 'Dynamic Perforation of Viscoplastic Plates by Rigid Projectiles', Int. J. Engng. Sci., Volume 21, Number 6, pp 577-591.

Ringers, B.E. (1983). 'New Sliding Surface Techniques enable the Simulation of Target Plugging Failure', Ballistic Research Laboratory, Aberdeen Proving Ground, Maryland, Report ARBRL-TR-02541.

Ringers, B.E. (1985). 'Modeling Adiabatic Shear', Ballistic Research Laboratory, Aberdeen Proving Ground, Maryland, Report BRL-TR-2662.

Sedgwick, R.T. et al. (1978). 'Numerical Investigations in Penetration Mechanics', Int. J. Engng. Sci., Volume 16, pp 859-869.

Stecher, F.P. and Johnson, G.R. (1984). 'Lagrangian Computations for Projectile Penetration into Thick Plates', Computers in Engineering, Volume 2, ASME, pp 292-299.

Wingrove, A.L. (1972). 'The Forces for Projectile Penetration of Aluminium', J. Phys. D: Appl. Phys., Volume 5, pp 1294-1303.

Woodward, R.L. and Morton, M.E. (1976). 'Penetration of Targets by Flat-Ended Projectiles', Int. J. Mech. Sci., Volume 18, pp 119-127.

Woodward, R.L. (1984). 'The Interrelation of Failure Modes Observed in the Penetration of Metallic Targets', Int. J. Impact Engng., Volume 2, Number 2, pp 121-129.

Zukas, J.A. (1981). 'Three-Dimensional Impact Simulations: Resources and Results', Computer Analysis of Large Scale Structures, AMD-49, Washington D.C.

Zukas, J.A. (1982). Impact Dynamics, Wiley Interscience, New York.

Table 1.1

Impact Response Classification

Impact Velocity	Material Response
0-50 ms^{-1}	Primarily elastic with limited local plasticity
50-500 ms^{-1}	Primarily plastic
0.5-4 kms^{-1}	Viscous material strength is still significant
4-12 kms^{-1}	Pressure approaches or exceeds the elastic modulus and materials behave as fluids in which density is an increasingly important variable
>12 kms^{-1}	Explosive impact with vaporisation of the colliding solids

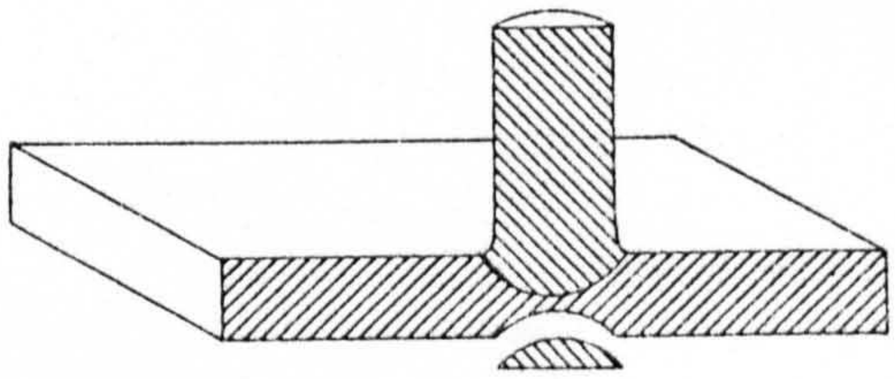

a) Fracture due to initial stress wave

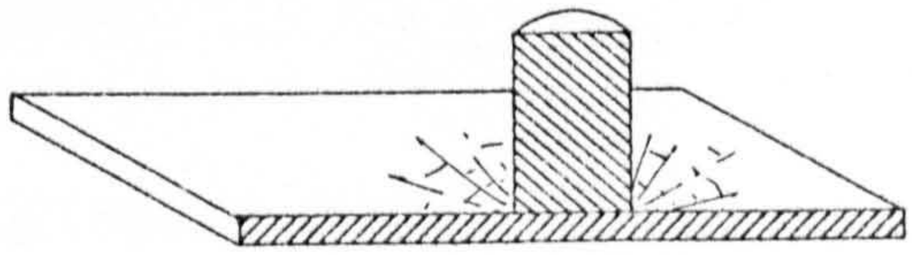

b) Radial fracture behind initial wave in a brittle target

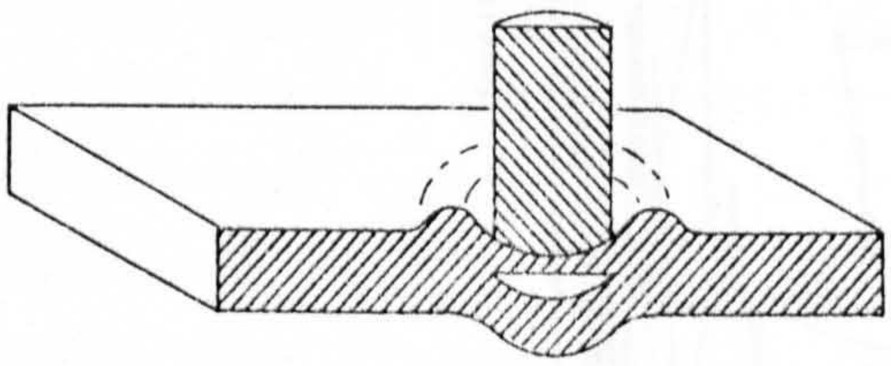

c) Spall failure (scabbing)

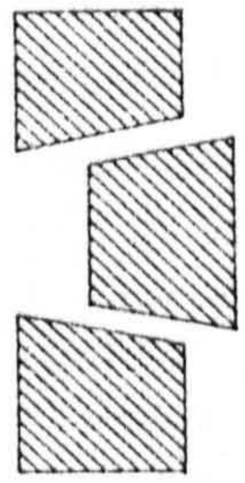

d) Plugging

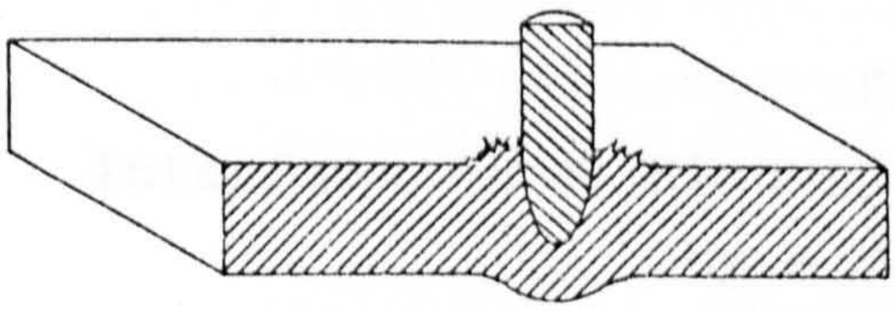

e) Petalling (frontal)

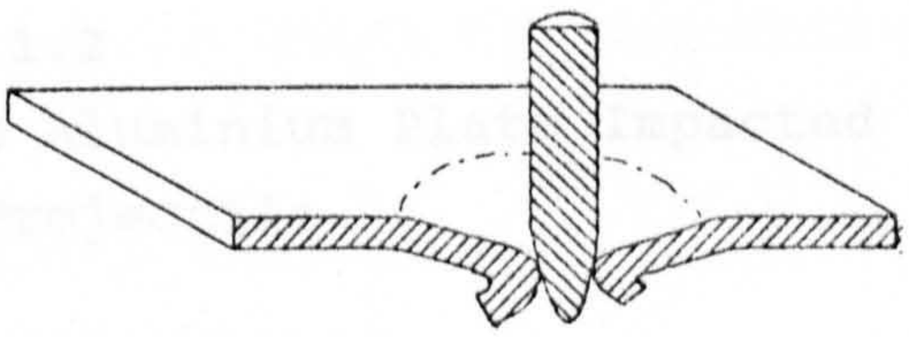

f) Petalling (rearward)

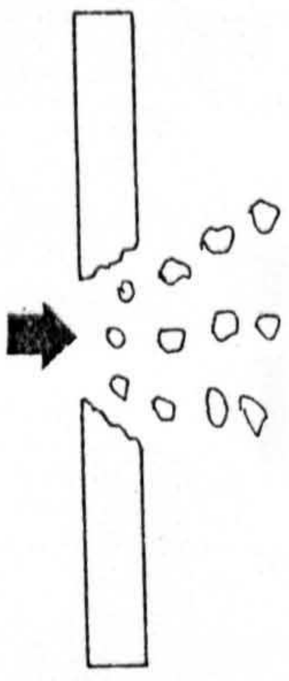

g) Fragmentation

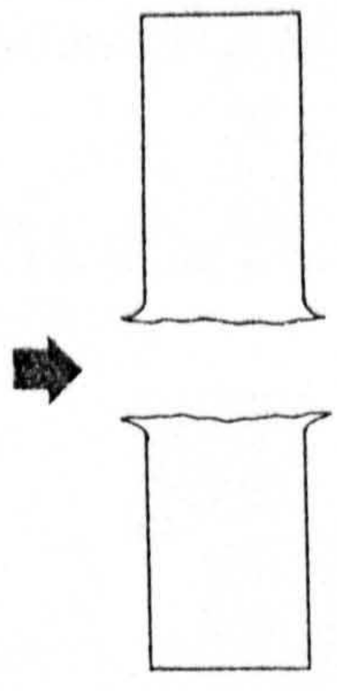

h) Ductile hole enlargement

Figure 1.1
Typical Failure Mechanisms

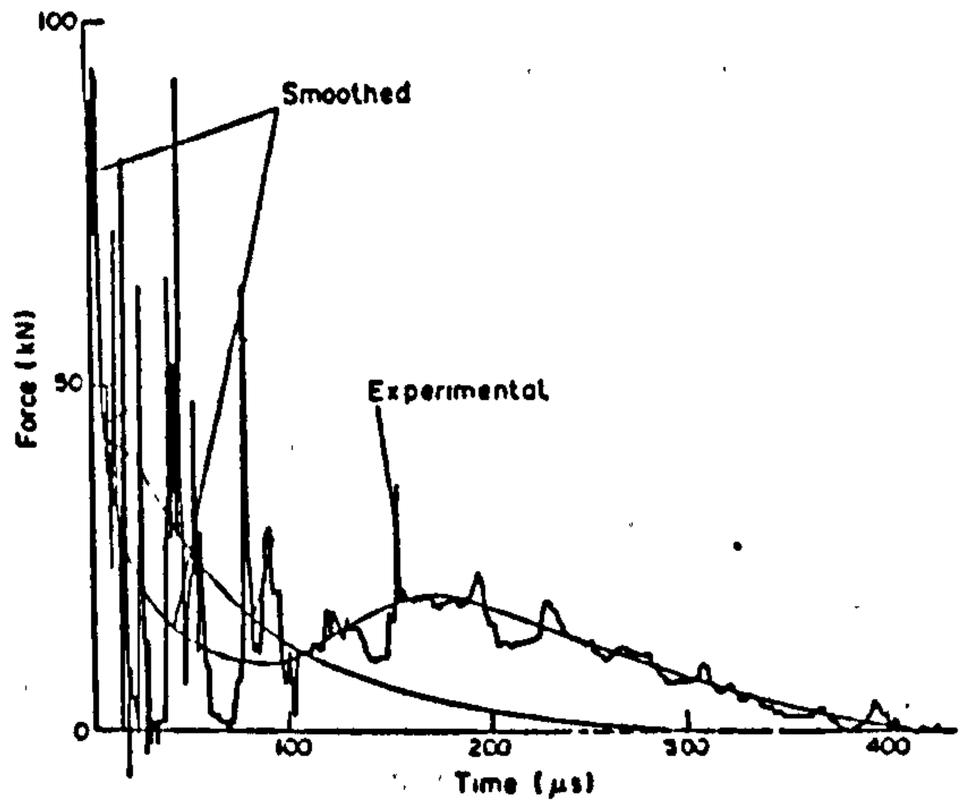

Figure 1.2
Interface Force History of an Aluminium Plate Impacted by a Blunt Projectile

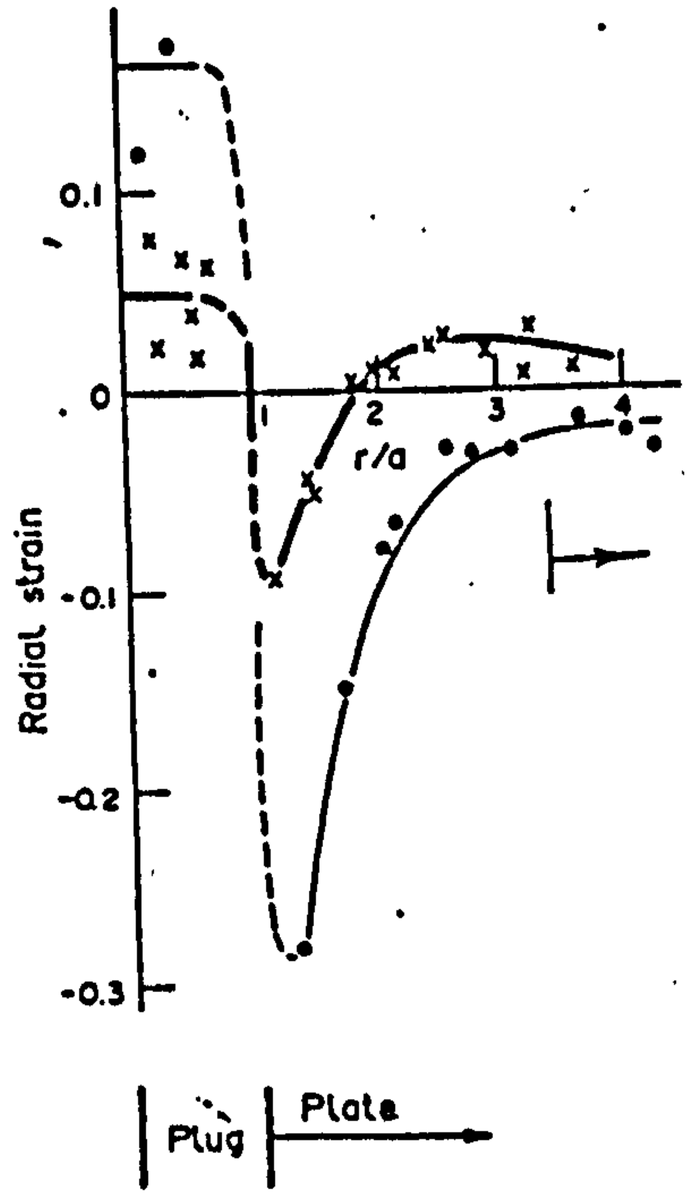

Figure 1.3
Radial Strain History of an Aluminium Plate Impacted by a Blunt Projectile

CHAPTER 2

THE FINITE ELEMENT SOLUTION PROCEDURE

2.1 INTRODUCTION

In this chapter, the finite element basis for the solution of high velocity impact problems will be reviewed. The intention is not to give a complete coverage of all the aspects of such a vast subject but rather to establish only those ideas which will be pertinent to the developments of later chapters. A full description of the broader aspects of the finite element method may be obtained from a number of sources such as Bathe (1982) and Cook (1974).

In the equations that follow the tensor indicial notation will be used unless otherwise stated, in which the repetition of an index will represent summation.

The equations of motion in finite element form are a suitable starting point in the development of such a computational procedure, and are given at time t=n as;

$$M^n_{ij}\ a^n_i = P^n_i - F^n_i + H^n_i \qquad (2.1)$$

in which a^n_i is the acceleration vector and M^n_{ij} is the mass matrix, defined over an element volume dV_e as;

$$M^n_{ij} = \int_{V_e} N^T_{ij}\ N_{ij}\ w\ dV_e \qquad (2.2)$$

and where w is the current density. P^n_i accounts for the element external force and may be defined as;

$$P^n_i = \int_{S_e} N^T_{ij}\ T_i\ dS_e \qquad (2.3)$$

in which T_i is the surface traction vector over the element surface S_e. Similarly, the element internal force over the

element volume dV_e is given as

$$F_i^n = \int_{V_e} B_{ij}^T \sigma_i \, dV_e \qquad (2.4)$$

where σ_i is the Cauchy stress vector referred to the current configuration. The computation of these terms, together with the rectangular interpolation matrix N_{ij}, the strain displacement matrix B_{ij} and H_i^n, the hourglass resistance force vector, will be discussed more fully under the six headings of; spatial discretisation, temporal discretisation, geometric nonlinearity, material nonlinearity, hourglass control and the control of numerical oscillations.

Although the choice in one area affects the possibilities in another, their separate consideration will nonetheless be beneficial.

2.2 TEMPORAL INTEGRATION

The central difference time integration operator will be used in this work. The following section will discuss some theoretical aspects of the method and proceed to review the factors relevant in the choice of such an algorithm.

2.2.1 The central difference method

In the following, assume that the displacement, velocity, and acceleration components for each nodal point at time t=n, denoted by d_i^n, v_i^n and a_i^n, respectively, are known. Let dt^n be the time increment between $t^n$and t^{n+1}. In addition, midstep values for velocities are defined at

$$t^{n+1/2} = 1/2 \; (\; t^n + t^{n+1}) \qquad (2.5)$$

by

$$v_i^{n+1/2} = v_i(t^{n+1/2}) \qquad (2.6)$$

Finite difference expressions are used to approximate the velocities and acceleration

$$v_i^{n+1/2} = (d_i^{n+1} - d_i^n)/dt^n \qquad (2.7)$$

and

$$a_i^n = (v_i^{n+1/2} - v_i^{n-1/2})/dt^{n-1/2} \qquad (2.8)$$

where

$$dt^{n-1/2} = 1/2 (dt^n + dt^{n-1}) \qquad (2.9)$$

by combining equations (2.7) and (2.8), and assuming the time step is constant, the acceleration may be written

$$a_i^n = (d_i^{n+1} - 2d_i^n + d_i^{n-1})/(dt^n)^2 \qquad (2.10)$$

The substitution of equation (2.10) into equation (2.1) with the right hand side forces of the latter being termed collectively as f_i^n gives

$$d_i^{n+1} = \frac{f_i^n}{M_{ij}^n} (dt^n)^2 + 2d_i^n - d_i^{n-1} \qquad (2.11)$$

Since the external and internal forces which determine f_i^n depend only on the loads and stresses at time step t^n, all of the terms on the right hand side are historical in that they are known at time step t^n. Therefore, new displacements can be determined directly without solving any equations provided that M_{ij}^n is diagonal. The term d_i^{n+1} is thus based on the equilibrium conditions at time t^n, and for this reason the integration scheme is described as an explicit procedure. The motion is advanced in

time by updating the acceleration using equation (2.1), which is rearranged to give

$$a_i^n = \frac{f_i^n}{M_{ii}^n} \qquad (2.12)$$

in which f_i^n is termed the effective load vector and M_{ii}^n is the effective diagonal stiffness matrix which will be discussed in section 2.3.3. Substituting the new acceleration in equation (2.8) gives the updated velocity at the midpoint as

$$v_i^{n+1/2} = v_i^{n-1/2} + a_i^n \, dt^{n-1/2} \qquad (2.13)$$

which is distinctly preferable in this type of problem where a rate constitutive relation requiring the midpoint velocity gradient governs the response. Finally, the total displacements are computed through equation (2.7)

$$d_i^{n+1} = d_i^n + v_i^{n+1/2} \, dt^n \qquad (2.14)$$

The error in the expansions of equations (2.7) and (2.8) is of order $(dt^n)^2$, Belytschko and Mullen (1977a). The central difference operator has been shown to overestimate the frequencies of the system, but this error will be seen later to have a beneficial effect on the nature of the total error in the integration scheme, Kreig and Key (1973).

A backwards difference form must be used for the velocity term to maintain the explicitness of the equations when a linear viscosity is desired in equation (2.7), while a diagonal damping matrix is essential to preserve the computational efficiency.

The viscous force, Belytschko (1977a), Key (1974) is given by

$$G_i^n = c_i(d_i^n - d_i^{n-1})/dt^{n-1} \qquad (2.15)$$

where the components of the diagonal damping matrix are given by C_i. For this form of viscous damping force, equation (2.11) becomes

$$d_i^{n+1} = (M_{ii}^n)^{-1} (dt^n)^2 \left[f_i^n - G_i^n \right] + 2d_i^n - d_i^{n-1} \qquad (2.16)$$

In the present work a much advocated alternative to this procedure will be used which is included directly in the constitutive relationship (Section 2.9). It should be noted here that the central difference operator with the explicit form of damping as described is non-dissipative.

2.2.2 Time step calculation

The central difference method, as with all such explicit techniques, is only conditionally stable, which limits the time step dt to an upper bound of dt_{cr}, called the critical time step. When dt is larger than the critical time step, high frequency modes in the numerical solution become exponential in time rather than harmonic solutions of the original equations.

The critical time step for the central difference method is given by Bathe (1982) as

$$dt_{cr} \leq \frac{2}{(\Gamma_{max})^{1/2}} \qquad (2.17)$$

where Γ_{max} is the maximum eigenvalue of the system. The estimate of the critical time step does not require the solution of the eigenvalue problem of the complete system in practice. The highest system eigenvalue must always be less than the highest eigenvalue of the individual elements Owen and Hinton (1980), so that the bound on the highest eigenvalue can be simply obtained by consideration of an individual element. The maximum eigenvalue for the linear displacement element with lumped mass is given by

$$\Gamma_{max} = \left[\frac{2\ c}{L} \right]^2 \qquad (2.18)$$

where L is a characteristic length of the element in the direction of wave propagation and the current dilational material sound speed in an elastic medium is given by

$$c = \{(K + 4G/3)/w\}^{1/2} \qquad (2.19)$$

where G is the shear modulus, K is the bulk modulus and w the current density. The critical time step then becomes

$$dt_{cr} \leq \frac{L}{c} \qquad (2.20)$$

this equation represents the Courant stability criterion and corresponds to the traversal time of the elastic wave across an element. In essence the critical time step of the central difference technique ensures that the period T corresponding to the highest frequency of the mesh will be integrated over π time steps since

$$T = \pi\ dt_{cr} \qquad (2.21)$$

The inclusion of material and geometric nonlinearity into the solution process, however, gives variations in the stiffness of the elements which may be significant as time progresses, Bathe (1982). The effect of geometric nonlinearity on the stability of the central difference method for a bar element sustaining an initial longtitudinal stress σ has been shown to yield an equation of the form

$$(dt_{cr})^2 \leq \frac{2}{\left(\Gamma_{max} + \dfrac{2\sigma}{w\ L^2}\right)} \qquad (2.22)$$

If the maximum eigenvalue is written as

$$\Gamma_{max} = \frac{4\ \sigma_{,\epsilon}}{w\ L^2} \qquad (2.23)$$

where ϵ represents a total strain measure, then the destabilizing effect of geometric nonlinearity may be seen not to be severe unless the stress σ is of the order of the instantaneous material modulus $\sigma_{,\epsilon}$. In the range of initial velocities considered in this work, the stresses occurring during solution are frequently two orders of magnitude smaller. The geometric nonlinearity is, therefore, not recognised as a source of instability in the computation of the critical time step, Belytschko et al (1975b).

Because of the destabilizing effects of round-off errors and other reasons that are poorly understood, such as the effects of rapidly varying material properties, the time step obtained by equation (2.20) for nonlinear problems must often be reduced if stability is to be maintained, although due regard to numerical efficiency should be made in this reduction, Belytschko and Mullen (1977a). For this reason the computation of dt_{cr} is a vital factor in the efficiency of the numerical algorithm. Furthermore, by operating as close to the stability limit as possible the accuracy of the central difference method has been shown to be maximised, Key (1978), although this is only significant for refined element meshes, Bathe (1982).

The time step evaluation equation used in this work is based on an extension of the linear result of equation (2.20), since there is considerable evidence that the extension of linear results to a nonlinear regime are valid provided the current highest frequency or wave speed is used in the equations, Belytschko (1976). Therefore at each time increment, a critical time step is computed for all elements, Hallquist (1983a) as

$$dt_{cr} = \frac{K_r \, L_c}{Q + (Q^2 + c^2)^{1/2}} \tag{2.24}$$

where

$$Q = Q_2 \, c + Q_1 \, L_c \, |D_{kk}| \tag{2.25}$$

and

$$L_c = \sqrt{2} \, \frac{A_e}{L_d} \tag{2.26}$$

in which A_e is the current element area, c is the dilational material sound speed, and Q_1 and Q_2 are dimensionless constants which default to 1.5 and 0.06 respectively. D_{kk} is the trace of the velocity strain tensor and will be discussed further in Section 2.6

L_c is defined as the shortest signal path across an element and represents the characteristic length for the element. L_d is the length of the largest element diagonal. The use of a characteristic length other than that of the shortest element dimension in the direction of wave propagation arises out of the requirement for maximum efficiency in the algorithm. This refinement has been used by Wilkins (1980) but the added expense both in terms of computer storage and cost is not deemed necessary for most problems, Hallquist (1983b). The measure used here provides a conservative estimate and also accounts for elements sustaining severe distortions or whose aspect ratios are large.

The effect of the factor, K_r, is used in this work to accomplish the time step reduction mentioned earlier and has a typical value of 2/3.

The term Q is included to account for the effects of the artificial bulk viscosity used to eliminate spurious numerical oscillations occurring during the solution (Section 2.9). The

addition of an artificial viscosity in the solution increases the hydrostatic pressure of elements in the region of the numerical oscillation, consequently the material sound speed is increased and the critical time step thereby reduced. Note that the equation reduces to the Courant condition in the absence of the Q term.

It has been suggested by Belytschko and Mullen, (1977a), that the use of a variable time step introduces artificial damping in the central difference operator. When the time step is decreasing the corresponding damping coefficient is positive, whereas, an increasing time step corresponds to a negative damping coefficient which leads to instability. The use of an explicit viscosity scheme to limit this type of numerical instability and by limiting the actual rate of increase of dt_{cr} has consistently yielded numerical solutions with no significant manifestation of the typical unbounded response, Goudreau et al (1983), Wilkins (1969). In order to limit the rate of increase of dt_{cr} the value actually used is given by Bertholf and Benzley, (1968) as

$$dt^n_{cr} = \min\ (dt^n_{cr},\ K_{cr}\ dt^{n-1}_{cr}\ ) \qquad (2.27)$$

where K_{cr} is a user specified constant and is taken to be 1.1. A further technique used is to average two successive time steps so that some semblance of centering is maintained, Hallquist et al (1977).

The computation of an explicit value for the critical time step in this way has been shown to provide a very good estimate. In particular, a nonlinear problem would certainly require more effort to recompute the exact eigenvalue at each time step than could possibly be saved by the corresponding slight increase in the critical time increment. Practical experience, however, has shown that a re-estimate of the critical time step at every point in this manner and the use of a time step kept slightly less than the critical value serves to keep the calculation stable, Belytschko (1983).

It should be noted that the time step limitation makes extreme mesh refinement in one particular area highly undesirable. Additionally, it is known that a significant proportion of the energy flux is reflected from the boundary between finite elements of different sizes in highly non-uniform meshes. This detracts further from the desirability of element size variation. However, the economic limitations imposed on the numerical analyst often enforces the use of such a mesh. A number of studies have now been performed and it is concluded that spurious reflection is only significant for wavelengths less than ten times the size of the largest elements and, furthermore, may be minimised by ensuring that adjacent element sizes differ by less than 10%, Bazant (1978).

2.2.3 Discussion of time integration scheme selection

The balance between the prevalent modal response of the physical system and the computational cost of the numerical algorithm is a major factor in the selection of an appropriate time integration scheme. In this section, the problem dependent nature and the implications of this balance are discussed and the principal reasons for the choice of integration scheme used in this work brought out.

The explicit nature of the chosen integration scheme implies that the effective stiffness matrix of the complete system need never be assembled and the solution essentially performed on an element level. This results in an algorithm which is computationally very compact, efficient and requires relatively little high speed storage, thus enabling systems of very large order to be solved efficiently.

The decrease in numerical operations that is associated with mass lumping is a benefit that is seldom overlooked in explicit schemes and which, moreover, may be further enhanced by its utilisation in conjunction with the central difference operator. This combination results in solutions for which the

respective spectral errors are compensatory, so that mass lumping is preferable both from the viewpoint of computational efficiency and accuracy, Belytschko (1978).

The conditional stability of explicit schemes can, however, impose catastrophic demands on computer time, although this is unavoidable if the excited frequencies of the system are to be integrated adequately. For this reason the explicit integration method is generally most applicable to wave propagation problems. Of the explicit schemes currently available, however, the central difference technique is seen to permit the largest critical time step, Kreig (1973).

For implicit schemes a solution to the nonlinear equilibrium equations is sought at t=n+1 which requires an iterative process involving expensive matrix manipulation. These manipulations render the implicit schemes considerably more expensive per time step than their explicit counterparts, Key (1978). Moreover, the algorithm resulting from the use of an implicit scheme requires a large amount of memory during the solution process which limits the size of the system equations that may be solved before disk input/output is required.

The algorithm resulting from the use of an implicit scheme is generally numerically stable with respect to the time step size and, consequently, the time step may be two or three orders of magnitude greater than that permitted explicitly. This advantage is degraded, however, when severe nonlinearities are present in a problem. For example, the introduction of step functions, which characterise phenomena such as impact, can cause a sawtooth type of response in implicit methods. Similar difficulties are found when analysing the early-time response of elastic-plastic structures subjected to severe loads. In these situations, an accurate simulation of the response generally requires a time step of the order of the stability limit, so little advantage is gained, Belytschko (1983). Furthermore, the local truncation error of most implicit schemes is of the same order as that of the explicit methods i.e. $(dt)^2$. While this is

insignificant for explicit schemes, it is a matter of concern for implicit methods, Zukas et al (1982).

In conclusion, therefore, the implicit methods available at present are seen to be expensive for this class of impact problem in which the accuracy demands imposed on the numerical algorithms require time steps in the region of the Courant limit. The central difference scheme is the simplest form of explicit time integration method available and has been chosen for use in this work.

2.3 SPATIAL DISCRETISATION

Various attempts have been made to utilise the obvious advantages of quadratic elements in the discretisation of high velocity impact problems. The codes produced are, however, intractable due either to their relative complexity or the assumptions necessary to bring the matrix evaluations to a competitive level, Hallquist (1983a). The implementation of such elements appears to be impractical for a number of reasons;

(i) The numerical noise resulting from the ad hoc way mass is lumped to generate a diagonal mass matrix.

(ii) The large number of elements required to adequately represent the severe displacement gradients often present in wave propagation problems would make their high cost limiting.

(iii) The use of shape functions of higher order than the linear form creates difficulties at the contact interface in the form of aliasing.

(iv) It has been shown that higher order continuum elements require a time step reduced from that of linear elements because of the greater mass associated with the interior nodes, Belytschko and Mullen (1977a).

Experience gained by current research workers has shown the

standard application of the linear isoparametric quadrilateral with one point integration to be far superior in the fast dynamics regime, Hallquist (1983), Bathe (1982), and will be used in this work. The linear triangular element has been used to good effect by Johnson (1976) in many applications and will also be included here. Its limitation for modelling regions in which large plastic flow occurs, however, has already been noted in Chapter One, consequently the later validation examples will predominantly use the quadrilateral element, particularly in the regions experiencing the greatest deformation.

The linear isoparametric element has a number of numerical advantages which have promoted its use and will be discussed in the following sections. Firstly, however, the spatial parameters defining the element will be given in terms of the Lagrangian reference frame.

2.3.1 The linear isoparametric element

Lagrangian finite element codes assign a mesh on a reference configuration and track particles through time. That is, the current configuration is expressed as a function of the reference configuration and time (a referential coordinate description). In terms of the two dimensional axis system x_i,

$$x_i = x(X(a,b), t) = \sum_{j=1}^{4} \phi_j(a,b)\, x_i^j(t) \qquad (2.28)$$

The element natural coordinates (a,b) are defined such that a and b vary from -1 to +1, and x_i^j are the nodal coordinates of the j^{th} node in the two global directions. The shape functions ϕ_j for the four node quadrilateral, map the curvilinear coordinates of a unit square into the cartesian coordinate system of the quadrilateral element and are defined as

$$\begin{aligned} \phi_1 &= 1/4(1-a)(1-b) \\ \phi_2 &= 1/4(1+a)(1-b) \\ \phi_3 &= 1/4(1+a)(1+b) \\ \phi_4 &= 1/4(1-a)(1+b) \end{aligned} \qquad (2.29)$$

The shape functions have characteristic values of unity at the particular node to which it is related and zero at all other nodes. Their summation at any point within an element is also unity. The displacements u_j at any point within an element are defined similarly

$$u_i = \sum_{j=1}^{4} \phi_j(a,b)\ d_i^j(t) \qquad (2.30)$$

where the d_i^j are the displacements at the jth element nodal point in the two global directions. The rectangular interpolation matrix, N_{ij}, is defined for the four node quadrilateral in the normal manner as;

$$N_{ij} = \left[\begin{array}{cc|cc|cc|cc} \phi_1 & 0 & \phi_2 & 0 & \phi_3 & 0 & \phi_4 & 0 \\ 0 & \phi_1 & 0 & \phi_2 & 0 & \phi_3 & 0 & \phi_4 \end{array}\right] \qquad (2.31)$$

giving the strain displacement matrix B_{ij} for the plane strain formulation as

$$B_{ij} = \left[\begin{array}{cc|cc|cc|cc} \phi_{1,x} & 0 & \phi_{2,x} & 0 & \phi_{3,x} & 0 & \phi_{4,x} & 0 \\ 0 & \phi_{1,y} & 0 & \phi_{2,y} & 0 & \phi_{3,y} & 0 & \phi_{4,y} \\ \phi_{1,y} & \phi_{1,x} & \phi_{2,y} & \phi_{2,x} & \phi_{3,y} & \phi_{3,x} & \phi_{4,y} & \phi_{4,x} \end{array}\right] \qquad (2.32)$$

where the comma denotes differentiation with respect to the given variable.

2.3.2 The spatial integration scheme

One point integration is used to evaluate the element matrices in equations (2.2) to (2.4). For example, if g_{ij} is some function defined over an element volume, then, for the quadrilateral element

$$\int_{V_e} g_{ij}\, dV_e = 4 g_o \det(J_{ij}) \qquad (2.33)$$

where the element volume V_e is approximated by

$$V_e = 4\det(J_{ij}) \qquad (2.34)$$

in which J_{ij} is the usual jacobian matrix and is computed at the local centroid of the element (a=b=0). The value of the function g_{ij} evaluated at (0,0) is g_o. This evaluation of the element volume is only adequate for small displacements and is entirely unsuitable for the very large deformations encountered in high velocity impact. The element volume may be evaluated exactly by considering the quadrilateral as a combination of two triangles. The area A_e of each triangle in terms of the nodal coordinates (x_i, y_i) is computed from Zienkiewicz (1977) as

$$A_e = 1/2 \begin{vmatrix} 1 & x_i & y_i \\ 1 & x_j & y_j \\ 1 & x_k & y_k \end{vmatrix} \qquad (2.35)$$

the corresponding volumes in the axisymmetric case may be obtained exactly by the product of the individual triangular element areas and the radius of the corresponding element centroid. Thus for the two dimensional axisymmetric element

$$V_e = 2\pi\, r_o\, A_e \qquad (2.36)$$

and for plane strain

$$V_e = A_e \qquad (2.37)$$

where r_o is the current radius of the element centroid. The total volume of the quadrilateral element is then the sum of the two individual components. Therefore,

$$\int_{V_e} g_{ij}\, dV_e = g_o\, V_e \qquad (2.38)$$

which is numerically exact and independent of the degree of displacement experienced by the element.

Spatial integration with one point quadrature has a number of consequences which are of particular value to explicit analyses. One such benefit is in the use of finite difference expressions to compute the partial differential terms of the element matrices.

It has been shown that, for the two dimensional linear element with one point quadrature, finite difference approximations to the first partial derivatives yield exactly the same result as the traditional finite element method. The former, however, have the added advantage of significantly increased numerical efficiency, Goudreau and Hallquist (1982). The usual method of generating finite difference expressions for spatial gradients uses a Taylor series expansion to give the derivatives as

$$\phi_{i,x} = 1/2\, \left[[\phi_i(1)-\phi_i(3)]Y_{24} - [\phi_i(2)-\phi_i(4)]Y_{13}\right]/A_e \qquad (2.39)$$

and

$$\phi_{i,y} = 1/2\, \left[[\phi_i(2)-\phi_i(4)]x_{13} - [\phi_i(1)-\phi_i(3)]x_{24}\right]/A_e \qquad (2.40)$$

where $\phi_i(j)$ is the function ϕ_i evaluated at node j. It is clear that the computation of the first partial derivatives in this manner eliminates the requirement to evaluate the Jacobian matrix or perform any shape function manipulation, and thus represents a significant saving in processing time.

2.3.3 The mass matrix

The consistent mass matrix defined by equation (2.2) is non-

diagonal, symmetric and in most regular meshes is usually banded. Its inversion, however, usually presents a formidable task and although its inverse maintains the same banded characteristics, it is no longer sparse. For these reasons the inertial properties of the mesh are often approximated by a diagonal matrix, known as a lumped mass matrix.

Consistent mass matrices tend to yield more accurate frequencies than their diagonal counterparts, although this advantage is reduced whenever the wavelength of the highest mode of interest spans five or more elements, White et al (1979). Their frequency error, moreover, usually represents an overestimate of the component frequencies in a given loading function, while the nature of the diagonal form is typically an underestimate, Belytschko (1976).

Most lumped masses for higher order isoparametric elements or structural elements are obtained by heuristic means since no consistent ways for lumping mass matrices are currently apparent, Belytschko (1978). Several alternative procedures have been proposed to perform this diagonalisation, Donea and Laval (1979). The most successful of these procedures when applied to the lower order elements, however, is the simple row summation technique, Zienkiewicz (1977), Belytschko (1983)

$$M^n_{ii} = \sum_{j=1}^{N} M^n_{ij} \qquad (2.41)$$

where N is the number of nodes of the element. This results in

$$M^n_{ii} = \sum_{j=1}^{N} (N^T_{ij} N_{ij}) \, w \, dV_e \qquad (2.42)$$

which leads to the following simple formulae for one point integration

$$M^n_{ii} = \frac{w}{N} V_e \qquad (2.43)$$

Two requirements must be satisfied by the resultant mass

matrix in order to produce stable accurate solutions, Donea and Laval (1979);

(i) The mass lumping should preserve the total mass of the element and

(ii) The nodal masses must be consistent with the nodal loads so that, for example, a plane wave injected into a slab remains plane during propagation.

It is readily seen that, for the case of the four noded isoparametric element using a one point integration rule, these two conditions are satisfied. Moreover experience gained has only served to substantiate this method, Key (1974), Goudreau and Hallquist (1982), Wilkins (1969).

2.3.4 Evaluation of element internal forces

Using the finite difference expressions of section 2.3.2, the strain displacement matrix of (2.32) is given as

$$B_{ij} = 1/2\ A_e \left[\begin{array}{cc|cc|cc|cc} y_{24} & 0 & y_{31} & 0 & y_{42} & 0 & y_{13} & 0 \\ 0 & x_{42} & 0 & x_{13} & 0 & x_{24} & 0 & x_{31} \\ x_{42} & y_{24} & x_{13} & y_{31} & x_{24} & y_{42} & x_{31} & y_{13} \end{array}\right] \qquad (2.44)$$

where

$$x_{ij} = x_i - x_j$$

$$y_{ij} = y_i - y_j \qquad (2.45)$$

Thus, the B matrix is computed directly from the current coordinates without recourse to a generalised shape function manipulation. Furthermore, the existence of a symmetric property in this matrix when evaluated at the element local axes (a=b=0) should be noted, in which

$$B_{11} = -B_{15} \qquad B_{22} = -B_{26}$$
$$B_{13} = -B_{17} \qquad B_{24} = -B_{28} \tag{2.46}$$

and leads to a further non-trivial reduction in the number of terms to be computed within each time step. The element force vector, evaluated over the current element area is given as

$$\begin{aligned} F_x^1 &= -F_x^3 = 1/2\ [\sigma'_x\ y_{24} + \tau_{xy}\ x_{42}] + n \\ F_x^2 &= -F_x^4 = 1/2\ [\sigma'_x\ y_{31} + \tau_{xy}\ x_{13}] + n \\ F_y^1 &= -F_y^3 = 1/2\ [\sigma'_y\ y_{42} + \tau_{xy}\ x_{24}] + \alpha \\ F_y^2 &= -F_y^4 = 1/2\ [\sigma'_y\ y_{13} + \tau_{xy}\ x_{31}] + \alpha \end{aligned} \tag{2.47}$$

where F_j^i is the element internal force on node i in global direction j, and τ_{xy} is the element shear stress. The direct total stress terms are augmented by the bulk viscosity term q to reduce numerical oscillations in the mesh (Section 2.9) thus

$$\sigma'_x = \sigma_x + q \tag{2.48}$$

and

$$\sigma'_y = \sigma_y + q \tag{2.49}$$

and an explicit treatment of the axisymmetry terms gives

$$n = 1/4\ (\sigma_r - \sigma_\Theta)\ V_e \tag{2.50}$$

and

$$\alpha = 1/4\ (\tau_{xy})\ V_e \tag{2.51}$$

Where σ_r and σ_Θ are the radial and hoop stress terms respectively. The elimination of the need to compile a global stiffness matrix in this manner is important in explicit analyses

where fine spatial discretisation is the norm. The computations for these problem types must be performed in memory to eliminate costly input/output to disk, so that the smaller memory requirement for a given problem enables a greater resolution in the solution, Belytschko et al (1976).

The subsequent reduction in the total number of time steps required to complete the solution permits the use of the more costly yet more accurate higher order elements. Significant reductions in the cycle time are expected, however, when a suitable method for controlling the hourglass modes in this domain is developed, since the benefits of one point integration may then be accrued.

The principal disadvantages to the one point integration of this element are the zero-energy deformation modes generated. This particular type of deformation (otherwise called hourglassing) arises when a pattern of the nodal degrees of freedom produces a strain field that is zero at the integration point. For instance, bending about either axis produces no strain at the integration point (a=b=0) while constant strain states are resisted adequately, Cook (1974).

Numerical problems exist in the control of these modes, not due to any inability to perform this control, but in formulating a method that is compatible with the extremely efficient code essential for high velocity problems.

2.4 GEOMETRIC NONLINEARITY

Problems in which finite rigid body rotation and displacement occur are called large deformation problems, for which a geometrical nonlinear capability is required in the solution scheme. The application of a linear strain measure to such problem types yields erroneous results because of its failure to disregard rigid body rotations. This means that a nonzero strain will be predicted when a solid is rotated as a

rigid body, with the result that the material behaviour will depend upon the choice of spatial coordinate system, a behaviour which is evidently unrealistic. Stated otherwise, linear strain is not seen to satisfy the constitutive equation requirement of frame invariance (or material objectivity).

It should be noted that by changing the orientation of a strained solid through rigid body rotation, the description of the state of strain in the solid is modified but remains equivalent. A solid described by a strain measure which is not invariant will, therefore, have upon finite rigid body rotation, a modified strain but no equivalency relative to the unrotated configuration.

The three most frequently used strain measures in the nonlinear regime are the Green-Lagrange strain tensor,

$$E_{ij} = 1/2 \left[x_{i,J} + x_{j,I} + x_{k,I}\, x_{k,J}\right] \tag{2.52}$$

the Almansi strain tensor,

$$e_{ij} = 1/2 \left[x_{i,j} + x_{j,i} - x_{k,i}\, x_{k,j}\right] \tag{2.53}$$

and the velocity strain (perhaps more usually termed the rate of deformation),

$$D_{ij} = 1/2 \left[\dot{x}_{i,j} + \dot{x}_{j,i}\right] \tag{2.54}$$

which is the symmetric part of the decomposed velocity gradient referred to the current configuration. Lower case suffices refer to the current configuration, whilst upper case suffices refer to a previous strain state which remains constant for the entire solution or for a particular increment of loading. The tensors, E_{ij} and e_{ij} measure the deformation by change in the lengths of line segments. This can be seen by considering their definitions

$$2\,E_{ij} = \frac{(dS)^2-(dS_o)^2}{(dS_o)^2} \tag{2.55}$$

and

$$2\,e_{ij} = \frac{(dS)^2-(dS_o)^2}{(dS)^2} \tag{2.56}$$

where dS and dS_o are the current and original lengths of a line segment. The velocity strain measures the rate of change of the current length (squared) of a line segment, thus

$$2\,D_{ij} = \frac{1}{(dS)^2}\,\frac{d}{dt}[(dS)^2] \tag{2.57}$$

Both E_{ij} and e_{ij} contain information about the original shape. The former is strictly frame invariant and while this is true for the latter, care is required in defining the reference configuration.

D_{ij}, however, only contains information about the rate of deformation in the current configuration and does not exhibit frame invariance, Malvern (1969). For this reason it is necessary to distinguish between the displacements due to stretching and those due to rigid body rotation to eliminate the effects of rigid body rotation and thus enable the use of D_{ij} in finite strain solutions. An exact technique valid for finite rotations is available without unreasonable cost and will be discussed in section 2.4.2.

Each of these strain measures may thus be used to model finite strain situations with arbitrarily large rotations.

The appropriate choice of deformation measure depends largely on the relative numerical convenience of implementation, although the class of material to be treated and, to a lesser extent, the type of time integration scheme also needs to be considered.

Consideration of these factors in the context of the class of impact problem discussed in this work has led to the measure of velocity strain being implemented for several reasons,

(i) For materials where the stress is a function of the original shape, such as rubber, the Green-Lagrange or Almansi strains are preferred. If the original state of the material can be characterised by a few state variables and the response depends principally on the current state of stress, a Cauchy stress/velocity strain formulation seems most suitable, Belytschko (1983). Such a condition is met in elastic-plastic materials with isotropic hardening in which the stress rate depends on the current stress, the current strain rate and the scalar yield stress. This is particularly true in the high velocity regime in which plasticity dominates the overall response, Belytschko (1975).

(ii) The eventual algorithm must not be computationally expensive, having a minimal number of logical steps. The velocity strain measure is based on the current deformed configuration and its relationship with the displacement rates is linear in contrast to the Green-Lagrange or the Almansi measures where the nonlinear relationship adds to the complexity of the numerical algorithm, Belytschko (1978).

(iii) The hypoelastic material behaviour considered in this work utilises velocity strain as the fundamental deformation measure. The use of this kinematic descriptor would, therefore, be both consistent and eliminate unnecessary strain rate transformation.

(iv) The measure is valid for arbitrarily large deformations and rotations as required by the physical modelling constraints.

There are, however, potential disadvantages in the use of this particular strain measure. With the total strain defined thus

$$\epsilon_{ij} = \int_{t_o}^{t} D_{ij} \; dt \qquad (2.58)$$

the integration in time for a material point does not generally yield a well defined path-independent tensor, so that information about phenomena such as total stretching may not be available in an algorithm which employs velocity strain only. A transformation of the velocity strain rate to either the Green-Lagrange or Almansi rates at each solution step is one technique, albeit expensive, to overcome this problem and would enable subsequent integration to yield a correct measure of the total deformation. A more common method in high velocity impact codes is to obtain the total strains at the required times during subsequent post processing from purely geometrical considerations.

The procedure to be used in the present work, however, exploits the small time increments present in explicit type analyses (typically less than 10^{-7} seconds), for which the assumption of a constant strain rate per cycle is not unreasonable. Equation (2.58) may now be used to evaluate the incremental strain experienced over each time step and in this way a total strain measure may be accumulated in a straightforward manner.

2.4.1 Deformation gradient

Once the velocities have been updated to (n+1/2) and the new deformed configuration at (n+1) is found, the strains and stresses may be advanced similarly to (n+1/2) and (n+1) respectively. The deformation gradient is calculated anew at each time step for use in the computation of the stress rotation matrix. This matrix is defined, subsequent to the spatial coordinate update as

$$F_{ij}^{n+1} = x_{i,j}^{n+1} \tag{2.59}$$

the midpoint deformation gradient rate is calculated in a similar manner as

$$\dot{F}_{ij}^{n+1/2} = \dot{x}_{i,j}^{n+1/2} \tag{2.60}$$

In the presence of finite displacement gradients, the symmetric and skew parts of the displacement gradient matrix ($x_{i,J}$) no longer provide an additive decomposition of the displacement gradient into the sum of a pure strain and a pure rotation. A multiplicative decomposition of the deformation gradient into the product of two tensors, one of which represents a rigid body rotation, while the other is a symmetric, positive definite tensor is, however, always possible. If R_{ij} denotes the orthogonal rotation tensor, then there exists two tensors U_{ij} and V_{ij} which satisfy

$$F_{ij} = R_{ij}\, U_{ij} = V_{ij}\, R_{ij} \tag{2.61}$$

where U_{ij} is the right stretch tensor and V_{ij} is the left stretch tensor. The decomposition of F_{ij} in this manner is frequently called polar decomposition. The evaluation of element stresses requires the use of a rotation matrix at times (n),(n+1/2), and (n+1), consequently the deformation gradient is also required at these times. Integration of the deformation gradient rate is performed thus

$$F_{ij}^{n+1/2} = F_{ij}^{n+1} - 1/2\, [\dot{F}_{ij}^{n+1/2}\, dt^n] \tag{2.62}$$

and

$$F_{ij}^{n} = F_{ij}^{n+1} - \dot{F}_{ij}^{n+1/2}\, dt^n \tag{2.63}$$

The application of the polar decomposition theorem using the deformation gradient matrices at these three states will obtain the respective rotation matrices.

The use of an integrated deformation gradient, as opposed to a direct recalculation at each integration point, makes it a part of the time integration scheme. The form used is compatible with the explicit time stepping method.

2.4.2 Stress evaluation

A stress measure is termed conjugate to the strain measure if their scalar product produces work. The corresponding conjugate stress to the velocity strain is the Cauchy stress measure and is used in this work.

Stresses for materials which exhibit elastic-plastic behaviour are more usually modelled by a hypoelastic constitutive relationship which is integrated incrementally in time thus

$$\sigma_{ij}^{n+1} = \sigma_{ij}^{n} + \dot{\sigma}_{ij}^{n}\, dt^{n} \qquad (2.64)$$

where $\dot{\sigma}_{ij}$ is the material time derivative of the Cauchy stress. Unfortunately this material rate is not vanishing under rigid body motion and as such does not satisfy the constitutive equation requirement of frame invariance. A method to overcome this problem which is currently gaining wide acceptance uses the stress rate attributed to Green and Naghdi, Johnson and Bammann (1982), and is based on a rotated Cauchy stress, whereby the constitutive variables are related to the unrotated position.

The essence of this stress rate formulation may be stated as follows. The rotated Cauchy stress, $\dot{\sigma}_{ij}^{n}$, evaluated at time (n) is

$$\dot{\sigma}_{ij}^{n} = (R_{ij}^{n})^{T}\, \sigma_{ij}^{n}\, (R_{ij}^{n}) \qquad (2.65)$$

and represents a transformation of the unrotated configuration

of the true Cauchy stress obtained during the previous time step. Before evaluation of the constitutive relations the rotated velocity strain is calculated similarly at (n+1/2) as

$$\dot{D}_{ij}^{n+1/2} = (R_{ij}^{n+1/2})^T \, D_{ij}^{n+1/2} \, R_{ij}^{n+1/2} \qquad (2.66)$$

where R_{ij} is the orthogonal rotation matrix from the last section. The rotated Cauchy stress at (n+1) is then evaluated from the elastic constitutive relationship as

$$\dot{\sigma}_{ij}^{n+1} = \dot{\sigma}_{ij}^{n} + C_{ijkl} \, \dot{D}_{kl}^{n+1/2} \, dt^{n+1/2} \qquad (2.67)$$

where C_{ijkl} is the elastic constitutive matrix. If plasticity is present the stress increment $\dot{\sigma}_{ij}$ will be constrained to the yield surface by the radial return technique (Section 2.8). The final true Cauchy stress is obtained by returning to the rotated configuration thus

$$\sigma_{ij}^{n+1} = R_{ij}^{n+1} \, \dot{\sigma}_{ij}^{n+1} (R_{ij}^{n+1})^T \qquad (2.68)$$

Implementation of the constitutive relations in the way described here can obtain nearly exact solutions in the presence of arbitrarily large rotations, Halleux and Casadei (1984).

2.5 MATERIAL NONLINEARITY

The details of the finite strain plasticity implementation will be presented. The underlying theory is time independent, non-thermal, with isotropic hardening and a von Mises yield surface together with an associated flow rule. The procedure is commonly termed radial return and has been found to produce both accurate and efficient solutions, Kreig and Key (1976). This is particularly true when the elastic stress increments exceed the yield stress by significant amounts, Nagtegaal (1982).

The algorithm uses the updated Cauchy stress σ_{ij} with rigid

body rotations removed as previously described. In this procedure the stress increment is calculated elastically in deviatoric stress space to give the elastically predicted total stress in the current time step as

$$\sigma^{e}_{ij} = \sigma^{n}_{ij} + d(s^{e}_{ij}) + p^{n+1}\ \delta_{ij} \qquad (2.69)$$

where $d(s^{e}_{ij})$ are the deviatoric elastic predictor stresses, p^{n+1} is the current hydrostatic pressure and δ_{ij} is the usual Kronecker delta. The deviatoric stresses in the current configuration are then calculated and if the yield function is satisfied then no further effort is required. If, however, the yield function is violated, an increment in plastic strain is calculated and the elastic predictive stress is subsequently decreased proportionally to satisfy the yield criterion, whilst simultaneously updating both the stress and yield surface size. The associated flow rule for the case of plasticity is given as

$$d(\epsilon^{p}_{ij}) = 2\Phi\ s^{n+1}_{ij} \qquad (2.70)$$

where $d(\epsilon^{p}_{ij})$ are the plastic strain increments, Φ is the plastic multiplier, and s^{n+1}_{ij} are the deviatoric stresses calculated at time n+1. The yield function is defined as

$$\pi = s_{ij}\ s_{ij} - 2/3\ (\sigma^{n+1}_{y})^{2} = 0 \qquad (2.71)$$

where the current radius of the yield surface σ^{n+1}_{y} is given by

$$\sigma^{n+1}_{y} = \sigma^{n}_{y} + E_{p}\ d(\epsilon^{p}_{eff}) \qquad (2.72)$$

in which σ^{n}_{y} is the initial uniaxial yield stress and $d(\epsilon^{p}_{eff})$ is the von Mises effective plastic strain, defined as

$$d(\epsilon^{p}_{eff}) = [2/3\ d(\epsilon^{p}_{ij})\ d(\epsilon^{p}_{ij})]^{1/2} \qquad (2.73)$$

The constant E_p is the plastic hardening modulus where

$$E_p = \frac{E_t\ E}{E - E_t} \qquad (2.74)$$

and E_t is the tangent modulus. Equation (2.72) relates the effective stress to the effective plastic strain, under the assumption of the existence of a universal plastic stress-strain curve, Malvern (1969). The deviatoric stress at time n+1 may be calculated from

$$s_{ij}^{n+1} = s_{ij}^{e} - 2G\ d(\epsilon_{ij}^{p}) \qquad (2.75)$$

where the superscript e denotes values at the end of the elastic prediction and G is the material shear modulus. By substitution of the flow rule into (2.75) we obtain

$$s_{ij}^{n+1} = \frac{1}{(1+4G\Phi)}\ s_{ij}^{e} \qquad (2.76)$$

which gives

$$\sigma_y = \frac{1}{(1+4G\Phi)}\ (2/3\ s_{ij}^{e}\ s_{ij}^{e})^{1/2} \qquad (2.77)$$

From the flow rule we have

$$d(\epsilon_{eff}^{p}) = 2\Phi\ (2/3\ s_{ij}^{n+1}\ s_{ij}^{n+1})^{1/2} \qquad (2.78)$$

and hence, using the yield function, obtain the plastic multiplier as

$$\Phi = \frac{3\ d\ (\epsilon_{eff}^{p})}{4\sigma_y^{n+1}} \qquad (2.79)$$

Substituting from (2.77) and (2.79) into (2.72), the effective plastic strain may now be evaluated as

$$d(\epsilon^p_{eff}) = \frac{(3/2\ s^e_{ij}\ s^e_{ij})^{1/2} - \sigma_y^{n+1}}{(3G + E_p)} \qquad (2.80)$$

and by substitution of (2.80) into (2.75) and using (2.77) and (2.78), the stress deviators are scaled back in the form

$$s^{n+1}_{ij} = s^e_{ij} - \frac{[3G\ d(\epsilon^p_{eff})]}{(3/2\ s^e_{ij}\ s^e_{ij})^{1/2}}\ s^e_{ij} \qquad (2.81)$$

The stress component ratios are assumed constant here due to the associated flow rule i.e. radial loading and unloading of the stresses.

2.6 HOURGLASS CONTROL

The principal disadvantage to the one point integration of the linear quadrilateral isoparametric element is the generation of zero-energy deformation modes and has been discussed in section 2.3.4.

In an attempt to avoid treating the spurious hourglass deformation modes associated with this particular element, developers have tried several alternative methods including the use of triangular elements, Johnson (1976), integrating the linear elements with full quadrature, Key et al (1978), and more recently by the use of higher order elements, again with full quadrature, Hallquist (1983a). The disadvantages associated with these techniques have been the subject of previous discussions, from which their suitability for use in this work was seen to be questionable. These alternatives are thus eliminated as potential solutions.

It is believed that unstable hourglass modes tend to form over a time duration that is typically much shorter than the time duration of the structural response and are frequently associated

with an oscillatory type behaviour. Hourglass modes that are a stable kinematic component of the global deformation modes, however, occur over a much longer time frame and obviously must be admissible. Hence, the true hourglass modes are resisted with a viscosity capable of preventing the formation of anomalous modes but having a negligible effect on these stable global modes. Furthermore, the kinematic discretisation of high frequency phenomena requires fairly fine mesh refinement and, hence, the non-rectangular component of the element shape is rather small. Together, these assumptions reduce the incentive to pay a high price to integrate exactly, Goudreau and Hallquist (1982).

The computational savings achieved using one point integration are maintained with the hourglass control procedure adopted here.

2.6.1 Definition of hourglass modes

Strain rate calculations in two dimensional planar geometry can be written as

$$D_{xx} = \sum_{i=1}^{4} \phi_{i,x}\, \dot{x}_i \tag{2.82}$$

$$D_{yy} = \sum_{i=1}^{4} \phi_{i,y}\, \dot{y}_i \tag{2.83}$$

$$D_{xy} = 1/2 \sum_{i=1}^{4} (\phi_{i,y}\, \dot{x}_i + \phi_{i,x}\, \dot{y}_i) \tag{2.84}$$

where $\dot{x}_i$ and $\dot{y}_i$ are the nodal velocities. The nodal displacement pattern or hourglass vector Γ_i for the linear quadrilateral is a result of recognising that the hourglass modes must not contribute to the rigid body modes to give

$$\sum_{i=1}^{4} \Gamma_i = 0 \tag{2.85}$$

and that the symmetry conditions in the strain-displacement matrix (equation 2.46) yield the necessary zero strain rates when multiplied by this vector

$$\phi_{i,x}\,\Gamma_i = 0 \qquad (2.86)$$

and is, therefore given by

$$\Gamma_i = \{\ 1 \quad -1 \quad 1 \quad -1\ \}^T \qquad (2.87)$$

Note that there are actually four identical hourglass modes for this element, but may all be obtained through the one hourglass vector applied in the two coordinate directions.

2.6.2 Diagonal drifting

Detection of the hourglass mode for the linear quadrilateral is performed using a concept usually termed diagonal drifting. For instance, if the two diagonals of an element are treated as vectors, then hourglassing will be occurring whenever these two vectors drift relative to one another and yet retain the same direction and magnitude. Note that the area of a quadrilateral computed from half the vector cross product of the diagonals, will remain unchanged for an hourglassing configuration. It is also interesting that the time step is not diminished by simple diagonal drifting, since neither the area nor the longest diagonal length change and so the shortest signal path across an element remains unchanged.

The rate of diagonal drifting may be defined by the velocity at which the midpoints of the element are separating or

$$\frac{v_1 + v_3}{2} - \frac{v_2 + v_4}{2} \qquad (2.88)$$

where v_i denotes the velocity of node i. This velocity does not contribute to the strains in the element, hence the deformation

pattern associated with this velocity field will be the object of minimisation. At the element level, therefore, any velocity field for which the quantities

$$\dot{x}_i \Gamma_i \quad \text{and} \quad \dot{y}_i \Gamma_i \tag{2.89}$$

are nonzero leads to the assumption that the element is hourglassing.

2.6.3 Hourglass damping

The controlling technique is based upon the the hourglass velocity, Hancock (1973) and is defined in terms of the diagonal drifting velocity in the two coordinate directions as

$$h_x = 1/4\ \dot{x}_i \Gamma_i \quad \text{and} \quad h_y = 1/4\ \dot{y}_i \Gamma_i \tag{2.90}$$

it should be noted that the hourglass modes are independent of the shape of the element. The corresponding viscous hourglass resisting forces are computed from;

$$f_{xi} = -g\ h_x \Gamma_i \quad \text{and} \quad f_{yi} = -g\ h_y \Gamma_i \tag{2.91}$$

in which

$$g = Q_h\ w\ c\ \sqrt{A_e} \tag{2.92}$$

Q_h is a constant which is usually set to a value between 0.05 and 0.15, Hallquist (1983b). Several remarks may be useful in conclusion.

(i) Alternative techniques are currently available, their application resulting in varying degrees of effectiveness depending upon the problem type. In all such methods, however, the accuracy is obtained by sacrificing the numerical operation count, whilst the formulation as given is seen to be over four times

faster than the most efficient of these, Goudreau and Hallquist (1982).

(ii) Energy losses due to this formulation are inevitable but it appears that the effects are minimal, Hallquist (1983b).

(iii) The procedure preserves the momentum of the velocity field at all points.

(iv) Simple bending of a column of elements is not resisted by this procedure. Although the hourglass velocity in each element would not be zero, the hourglass velocity at the centre of bending is zero. This is an important feature in plate impact situations where a large amount of bending is present.

2.7 CONTROL OF NUMERICAL OSCILLATIONS

Spurious numerical oscillations are often the result of applying explicit temporal integration to the spatially discretised momentum equations, particularly within the high velocity impact domain. This "noise" has the capacity to dominate the true solution in such a way as to virtually destroy it. Accurate results are obtained only if the superimposed oscillations are of considerably higher frequency than the principal features of the wave response sought. Their presence is a result of several possible factors, the discussion of these phenomena, however, is necessarily brief for this aspect of the problem is not well understood in the nonlinear domain, Belytschko (1975). The aim is to present a summary of current practice and to point out some pitfalls. Some of the pertinent aspects have already been mentioned but will be reviewed again for completeness.

Shock wave phenomena

A characteristic of high velocity impact situations is the

presence of shock waves (weak or otherwise), and arise as a consequence of the material sound speed increasing with pressure. A pressure wave can gradually steepen until it propagates as a discontinuity in the solution, thus leading to jumps in pressure, density, particle velocity and energy across the shock front. Difficulties are encountered in numerical solutions when these shocks fronts are present not only because of the discontinuity but also as a result of the associated trailing numerical oscillations, Hallquist (1983b).

Dispersion

All discrete parameter dynamic models exhibit dispersion, that is a phase velocity-frequency dependence, which may not be present in the physical structure. Alternatively, the wave frequencies excited by a transient loading situation such as impact, do not propagate with equal velocities. Both the temporal and spatial discretisation involved in the finite element method introduce a pattern of dispersion.

For the linear element proposed with diagonal mass approximation, the dispersion associated with the spatial discretisation has the tendency to reduce the phase velocity of the high frequency disturbances (negative dispersion), while lower frequency modes remain largely unaffected at the continuum wave speed. The effect of the central difference time integration scheme, however, is seen to increase the phase velocity of the high frequency modes (positive dispersion). This dispersive nature changes the shape of the propagating wave forms; negative dispersion results in a predominance of high frequency oscillations in the trailing portion of the disturbance, whilst negative dispersion yields leading edge perturbations, Shreyer (1983). These oscillations are at frequencies nearly equal to the cutoff frequency of the mesh, Shipley et al (1967). The variance in the computed waveform may thus have significant effect upon the accuracy of the computed response.

The additive effects of these two opposing dispersion patterns is seen to be beneficial, since the judicial combination

of the central difference operator and the lumped mass produces a total dispersive property that is much reduced from their individual contributions. As a result, this form of numerical instability is usually small, Key (1978).

Aliasing

Whilst mesh refinement in regions of interest has few drawbacks in static problems involving only elastic behaviour, the situation is not as simple in transient dynamic problems. The finite elements behave like low pass filters having definite passing bands and cutoff frequencies. The different cutoff frequencies depend on the type of propagating waves and the direction of propagation with respect to the mesh. Outside the passing band waves cannot propagate and the amplitudes of the waves are quickly attenuated spatially, Belytschko and Mullen (1977b).

For example, the numerical solution to a step type loading pulse will approximate the discontinuity with a finite slope as a consequence of the reduced number of frequency components, Kuhlemeyer and Lysmer (1973). Subsequent oscillations occur with a decreasing amplitude as the frequency attenuation occurs.

Variations in the time step

The use of a varying time step is mandatory in high velocity impact problems so as to maintain the highest numerical efficiency. That this introduces an artificial damping into the central difference operator, has been mentioned previously (Section 2.2.2), particularly the numerical instability associated with an increasing time step. Since the instability arises from the appearance of negative damping, an obvious remedy would be to apply an artificial term of sufficient magnitude to balance this effect.

2.7.1 The bulk viscosity method

Spurious oscillations may be reduced and even eliminated by

the bulk viscosity method, Belytschko and Mullen (1977a). Originally designed for use in shock wave applications, the shock discontinuity and the subsequent numerical oscillations are eliminated by spreading the shock front over a small number of elements.

In applying this method, the pressure in compressing elements is augmented by an artificial viscous term q before the evaluation of the element internal force. The q term is negligible at all places except those immediately in the shock locale ensuring that the solution remains relatively unperturbed.

It is generally believed that this type of formulation satisfies all shock conditions based on the countless numerical experiments performed over the years, in which excellent agreement has been obtained with either exact solution or experiment, Noh (1976). Examples of such codes include DYNA2D - Hallquist (1984), EPIC-2 - Johnson (1976), HONDO II - Key et al (1978), TOODY II - Bertholf and Benzley (1968), and work performed by Belytschko and Mullen (1977).

The exact form of artificial viscosity is somewhat arbitrary but all current code developments are based in some way on the viscosity originally proposed by von Neumann and Richtmyer (1950). In this work the q term is defined by

$$q = w\, L_c\, |D_{kk}|\, \left[Q_1\, L_c\, |D_{kk}| + Q_2\, c \right] \qquad (2.93)$$

where Q_1 and Q_2 are dimensionless constants which default to 1.5 and 0.06 respectively.

The quadratic term in strain rate is chosen to be very small except in regions of very large gradients and is consequently of little effect in the range of velocities considered in this report. The linear term, however, is included to control the small spurious oscillations following both the shock waves in which the gradients are insufficient to make the quadratic term effective and those resulting from the phenomena described

previously. Care should be taken with the linear term since there is a danger of distorting the solution, Bertholf and Benzley (1968).

In converging element geometries the centred strain rate term $|D_{kk}|$ is negative and the q term is then nonzero. This occurs even though no shocks are generated and results in a non physical generation of q. In view of the abundance of good correlation with this method, however, it is generally agreed that the effect is negligible.

2.8 DISCUSSION

A finite element program has been assembled to solve high velocity impact problems, specifically to provide a fundamental basis for investigation of the shear plug phenomenon. In the development of this program, a number of points worthy of discussion have been established.

The nature of the explicit time integration scheme involves literally millions of constitutive calculations. It is this requirement which has provided the motivation to ensure that the routines incorporated are as efficient as possible. The accuracy requirements have not been sacrificed in this work, merely a recognition that a general purpose finite element system is no match for those programs designed with computational speed as a high priority and with a limited range of objectives. Indeed, the solution of fast dynamics problems using programs with an element cycle time greater than 0.2 seconds (processing) becomes unobtainable even for comparatively coarse meshes.

Consider a mesh of 100 elements which is used to model a physical solid undergoing both geometric and material nonlinearity. A timing table, Table 2.1, has been obtained for both the traditional finite element approach and the present work, as implemented on a Vax 11/750 (without a floating point accelerator). This table enables some general statements to be

made regarding speed requirements and the optimum distribution of processing time.

Only the solution process is considered and has been divided into into four discrete sections. Ignoring all data input and output, a definition of each section is as follows;

(i) The **disk transfers** consist of all manipulations to read and write element records to disk during the post solution processing.

(ii) The **element loop** timings account for all other element based operations except those due to the database. This is a measure of the time to compute the internal force vector and all such component terms for each element.

(iii) The **slideline operations** are included for completeness only and will be discussed further in Chapter Three.

(iv) Under **miscellaneous** comprises the various initialisation and termination operations required outside the element loop, including overheads in descending to the element level from the top level subroutines and any further database manipulations involved with respect to general problem data. Also included here is the time spent in the top level system logic.

The timings from Table 2.1(a) represent a six-fold increase in execution time over those given in 2.1(b), the element cycle times are 0.67 and 0.11 sec/cycle respectively. The latter timing has enabled most truly transient problems to be solved.

Table 2.1(b) shows the predominance of the processing effort concentrated in the element loop, in which the central cost item is the construction and use of the strain displacement matrix for the internal force computation. It is the recognition of the symmetry within this matrix which accounts for much of the decrease in processing time in this loop.

Further reductions of the operation count in the element loop are available by virtue of the focus upon only one element type; Firstly, there is a significant decrease in the amount of code, facilitated by the use of specific finite difference formulae and, secondly, the subsequent elimination of many subroutine call overheads.

With respect to the database timings, the tremendous savings possible over the more traditional finite element numerical architecture may be dually stated in the following;

(i) The use of any form of database other than those which eliminate the time spent in expensive disk transfers and manipulate data in core, represent a significant limitation of the traditional architecture. This consideration alone can eliminate all but the specialist codes in many problems. Moreover, the advent of increasingly faster machines is only recently allowing even the specialist codes to solve the larger 3-D problems.

(ii) The adoption of one element type and the restriction to fast dynamics problems, enables the number of variables associated with each element to be considerably reduced. Since the time spent in extracting element data from a database varies with the number of variables, a significant saving in time is also accomplished here.

The implementation of both an in-core database manager and a reduced element variables set promotes a saving in the database timings by a factor of five. Additional savings are also experienced with the latter in the main entry and exit to the element constitutive routines by virtue of the reduced subroutine call overhead. The reduction in time is significant and is equivalent to an element cycle time (including database operations) in the modified code.

The final mesh cycle times are clearly independent from the miscellaneous timings shown. However, the unmodified miscellaneous timing represents 10% of the total time for the modified code and is a useful saving. Savings are accomplished here in the reduction of the amount of problem data extracted each time step from the database and in the subsequent reduced subroutine overheads. The restriction to a particular problem class eliminates any top level control logic and the whole process may be essentially performed within a small suite of routines.

The ideal situation is to have a distribution in which practically all the effort occurs within the element routines. All time spent in disk transfer is an expensive waste. The timings currently obtained do not fulfil this and are not optimum in this respect. They do, however, represent a mesh cycle time which is adequate for the work herein. Further savings may be expected with the implementation of a more effective database structure which will result in a mesh cycle time of 0.06 or better for this particular machine.

It is clear that the architecture of a finite element program based upon an explicit integration scheme differs markedly from those employing both static and implicit dynamic schemes. Although many analysts have used the traditional finite element approach, computing the nodal forces by multiplication of the tangential stiffness matrix with the incremental displacements, that approach is computationally inefficient, Belytschko et al (1975). Furthermore, the nature of the explicit scheme permits the segregation of different sections of the program to ease later modification. The constitutive equations are such an example. Since the stress rotation is performed independently from these equations, additional models may be added, or modifications made, to existing routines relatively simply. This is of vital importance at this current stage in the development of high velocity impact codes, where no definitive

material models have yet been forthcoming, Herrmann (1975).

2.9 CONCLUSION

This chapter has presented a finite element basis to the solution of high velocity impact problems. The discussion was presented under the main headings of; temporal discretisation, spatial discretisation, material nonlinearity, geometric nonlinearity, hourglass control and the control of numerical oscillations.

The formulation has been developed with due regard to the achievement of a numerically efficient code, although accuracy considerations have not been compromised. The result is a program which will model the large deformation, inelastic, dynamic response of materials subjected to impact loading and, moreover, facilitates solutions with a minimised number of operations.

The algorithms developed within each of the six sections for use in this work will be restated here as follows;

(i) Central difference time stepping scheme with automatic time step computation

(ii) Linear isoparametric elements integrated with one point quadrature

(iii) Radial return isotropic plasticity model using von Mises yield criteria

(iv) Finite strain calculations using the velocity strain measure

(v) Element stabilisation based on a diagonal drifting concept

(vi) Numerical stability achieved through the Von Neumann artificial viscosity scheme

Finally, a flowchart of the explicit impact solution scheme

is given in Table 2.2. The contact interface force computation is included for completeness and will be discussed in Chapter Three.

2.10 REFERENCES

Bathe, K. (1982). Finite Element Procedures in Engineering Analysis, Prentice-Hall.

Bazant, Z.P. (1978). 'Spurious Reflections of Elastic Waves in Nonuniform Finite Element Grids', Comp. Meth. Appl. Mech. Engg., Volume 16, pp 91-100.

Belytschko, T. (1975). 'Nonlinear Analysis Description and Numerical Stability', Shock and Vibration Computer Programs: Reviews and Summaries, University of Virginia, Volume SVM-10, W and B Pilkey (Editors).

Belytschko, T. and Holmes, N. and Mullen, R. (1975). 'Explicit Integration - Stability, Solution Properties, Cost', Finite Element Analysis of Transient Structural Behaviour, ASME, AMD-Volume 14, pp 1-21, Belytschko et al (Editors).

Belytschko, T. (1976). 'A Survey of Numerical Methods and Computer Programs for Dynamic Structural Analysis', Nuclear Engineering and Design, Volume 37, pp 23-34.

Belytschko, T. and Chiapetta, R.L. and Bartel, H.D. (1976). 'Efficient Large Scale Non-Linear Transient Analyses by Finite Elements', Int. J. Num. Meth. Engg., Volume 10, pp 579-596.

Belytschko, T. and Mullen, R. (1977a). 'Explicit Integration of Structural Problems', Int. Conf. in Nonlinear Solid and Structural Mechanics, Volume 2, Norway, Bergan (Editor).

Belytschko, T. and Mullen, R. (1977b). 'On Dispersive Properties of Finite Element Solutions', IUTAM Symp. on Modern Problems in Elastic Wave Propogation, Northwestern University, Evanston, Miklowitz and Achenbach (Editors), Wiley, New York.

Belytschko, T. (1978). 'Explicit Time Integration of Structure-Mechanical Systems', Advanced Structural Dynamics, pp 97-122, Applied Science Publishers Ltd, London.

Belytschko, T. (1983). 'An Overview of Semidiscretization and Time Integration Procedures', Computational Methods for Transient Analysis, Volume 1, pp 1-65, Belytschko (Editor).

Bertholf, L.D. and Benzley, S.E. (1968). 'TOODY II. A Computer Program for Two Dimensional Wave Propogation', Sandia National Laboratories, Albuquerque, NM, Report SC-RR-68-41.

Cook, R.D. (1974). 'Concepts and Applications of Finite Element Analysis', John Wiley and Sons, NY.

Donea, J. and Laval, H. (1979). 'An Improved Formulation of the Parabolic Isoparametric Element for Explicit Transient Analysis', Earthquake Engineering and Structural Dynamics, Volume 7, pp 23-29.

Goudreau, G.L. and Hallquist, J.O. (1982). 'Recent Developments in Large Scale Finite Element Lagrangian Hydrocode Technology', Comp. Meth. Appl. Mech. Engg, Volume 33, pp 725-757.

Goudreau, G.L. et al. (1983). 'Efficient Large-Scale Finite Element Computations In a Cray Enviroment', University of California, Lawrence Livermore National Laboratory, Report UCRL-89385.

Halleux, J.P. and Casadei, F. (1984). 'Transient Large Strain Analysis of Plane and Axisymmetric Structures by means of Biquadratic Finite Elements', Eng. Comput., Volume 1, pp 351-358.

Hallquist, J.O. and Werne, R.W. and Wilkins, M.L. (1977). Discussion on 'High Velocity Impact Calculations in Three Dimensions', J. Appl. Mech., Trans. of the ASME, Dec.

Hallquist, J.O. (1983a). 'Theoretical Manual for DYNA3D', University of California, Lawrence Livermore National Laboratory, Report UCID-19401.

Hallquist, J.O. (1983b). 'Lecture Notes for Bulk and Hourglass Viscosities in Wave Propogation Codes', University of California, Lawrence Livermore National Laboratory, Report UCRL-89156.

Hallquist, J.O. (1984). 'User's Manual for DYNA2D - An Explicit Two-Dimensional Hydrodynamic Finite Element Code with Interactive Rezoning', University of California, Lawrence Livermore National Laboratory, Report UCID 18756.

Hancock, S.L. (1973). 'An Hourglass Subtraction Procedure', TCAM Tech. Memo. 73-6, Physics International Co., San Leandro, California.

Herrmann, W. (1975). 'Nonlinear Transient Response of Solids', Shock and Vibration Computer Programs; Reviews and Summaries, University of Virginia, Volume svm-10, W and B Pilkey (Editors).

Johnson, G.R. (1976). 'Analysis of Elastic-Plastic Impact Involving Severe Distortions', J. Appl. Mech., Volume 43, pp 439-444.

Johnson, G.C. and Bammann, D.J. (1982). 'A Discussion of Stress Rates in Finite Deformation Problems', Sandia National Laboratory, Livermore, Report Sand 82-8821.

Key, S. (1974). 'A Finite Element Procedure for The Large Deformation Dynamic Response of Axisymmetric Solids', Comp. Meth. Appl. Mech. Engg., Volume 4, pp 195-218.

Key, S. (1978). 'Transient Response by Time Integration: Review of Implicit and Explicit Operators', Advanced Structural Dynamics, pp 71-95, Applied Science Publishers Ltd, London.

Key, S.W. and Beisinger, Z.E. and Kreig, R.D. (1978). 'HONDO II. A Finite Element Computer Program for the Large Deformation Dynamic Response of Axisymmetric Solids', Sandia National Laboratories, Albuquerque, NM, Report 78-0422.

Kreig, R.D. (1973). 'Unconditional stability in Numerical Time Integration Methods', J. Appl. Mech., Volume 40, pp 417-421.

Kreig, R.D. and Key, S.W. (1973). 'Transient Shell Response by Time Integration', Int. J. Num. Meth. Mech. Eng., Volume 7, pp 273-286.

Kreig, R.D. and Key, S.W. (1976). 'Implementation of a Time Independent Plasticity Theory into Structural Computer Programs', Volume 20 of Constitutive Equations in Viscoplasticity: Computational and Engineering Aspects, ASME, NY, pp 125-137.

Kuhlemeyer, R.L. and Lysmer, J. (1973). 'Finite Element Method Accuracy for Wave Propogation Problems', J. Soil. Mech. Found. Eng. Div., ASCE, Volume 99(SM5), pp 421-427.

Malvern, L.E. (1969). 'Introduction to the Mechanics of a Continuous Medium', Prentice-Hall, NJ.

Nagtegaal, J.C. (1982). 'On The Implementation of Inelastic Constitutive Equations with Special Reference to Large Deformation Problems', Comp. Meth. Appl. Mech. Engg., Volume 33, pp 469-484.

Noh, W.F. (1976). 'Numerical Methods in Hydrodynamic Calculations', University of California, Lawrence Livermore National Laboratory, Report UCRL-52112.

Owen, D.R.J. and Hinton, E. (1980). 'Finite Elements in Plasticity : Theory and Practice', Pineridge Press Ltd., Swansea.

Shipley, S.A. and Leistner, H.G. and Jones, R.E. (1967). 'Elastic Wave Propogation - A Comparison between Finite Element Predictions and Exact Solutions', Proc. Int. Symp. on Wave Propogation and Dynamic Properties of Earth Materials, Albuquerque, N.M, pp 509-519.

Shreyer, H.L. (1983). 'Dispersion of Semidiscretized and Fully Discretized Systems', Computational Methods for Transient Analysis, Volume 1, pp 268-299, Belytschko and Hughes (Editors).

Von Neumann, J. and Richtmyer, R.D. (1950). 'A Method for the Numerical Calculation of Hydrodynamical Shocks', J. Appl. Phys., Volume 21, p 232.

White, W. and Valliappan, S. and Lee, I.K. (1979). 'Finite Element Mesh Constraints for Wave Propogation Problems', Proc. Third Int. Conf. on Finite Element Methods, University of New South Wales, Australia, pp 531-539.

Wilkins, M.L. (1969). 'Calculation of Elastic-Plastic Flow', University of California, Lawrence Livermore National Laboratory, Report UCRL-7322.

Wilkins, M.L. (1980). 'Use of Artificial Viscosity in Multi-dimensional Fluid Dynamic Calculations', J. Comp. Phys., Volume 36, pp 281-303.

Zienkiewicz, O.C. (1977). 'The Finite Element Method', 3rd Edition, McGraw-Hill, NY.

Zukas, J.A. et al. (1982). 'Impact Dynamics', John Wiley and Sons.

TABLE 2.1

(a) TIMING CHART FOR FAST DYNAMICS PROGRAM

Program Block	Time for 100 Elements (1/100S)	% of Total Time
1	900	48
2	800	42
3	160	9
4	15	1
Total	1875	100

(b) TIMING CHART FOR TRADITIONAL DYNAMICS PROGRAM

Program Block	Time for 100 Elements (1/100S)	% of Total Time
1	4500	35
2	7200	55
3	1170	9
4	175	1
Total	13045	100

Key to Program Blocks

1 - Disk Transfers.
2 - Element Loop.
3 - Slideline Operations.
4 - Miscellaneous.

TABLE 2.2

Solution Strategy for High Velocity Impact

Initialisation

- Data Input
- Compute mass and initial load vectors
- Compute initial critical time step, $t = dt_{cr}$

Element Loop

1 · Loop e = 1 to number of elements, n_e
- Update element coordinates
- Compute midpoint velocity strains
- Compute hourglass resistance forces, f_h^{n+1}
- Update stress, σ^{n+1}
- Update time step increment for next step, dt_{cr}
- Compute artificial bulk viscosity pressure, q^{n+1}
- Augment σ^{n+1} to account for numerical oscillations
- Compute internal force, f_i^{n+1}
- Compute external force, f_e^{n+1}
- Compute reaction forces
- Assemble global residual, $f_r^{n+1} = f_e^{n+1} - f_i^{n+1} + f_h^{n+1}$
- If last element, go to 2

Solution Procedure

2 · Update $t = t + dt_{cr}$
- Compute contact interface force, f_c^{n+1}
- Update residual vector, $f_r^{n+1} = f_r^{n+1} + f_c^{n+1}$
- Compute global acceleration, $a^{n+1} = f_r^{n+1} M^{-1}$
- Compute velocity, $v^{n+1/2} = v^{n-1/2} + a^{n+1}\, dt_{cr}^{n+1/2}$
- Compute displacement increments, $d^{n+1} = d^n + v^{n+1/2}\, dt_{cr}$
- Go to 1 if $t \leq$ total solution time
- Otherwise, stop

CHAPTER 3

THE SLIDELINE TECHNIQUE

3.1 INTRODUCTION

The numerical method by which the contact process is modelled will be presented in this chapter. A brief review of the contact methods currently available is followed by a detailed description of the technique chosen for use in this work. The limitations of the chosen technique and a guide to its correct usage are also included.

Vector notation conveniently describes the geometric nature of this algorithm and will be used throughout this chapter.

3.2 SLIDELINE TERMINOLOGY

Consider the time dependent motion of two bodies occupying regions B_1 and B_2 in their undeformed configuration, Figure 3.1. In this state, assume that the intersection

$$B_1 \cap B_2 = 0 \qquad (3.1)$$

is satisfied. This is the impenetrability condition for contact. Define δB_1 and δB_2 as the boundaries of B_1 and B_2, respectively, and at some time later let these bodies occupy regions b_1 and b_2 bounded by δb_1 and δb_2. Since the deformed configurations are not permitted to penetrate,

$$(b_1 - \delta b_1) \cap b_2 = 0 \qquad (3.2)$$

must also be satisfied. Whenever the intersection $(\delta b_1 \cap \delta b_2)$ is nonzero, contact conditions are indicated and constraints imposed to prevent penetration.

In this work the surfaces δb_1 and δb_2 of the discretised bodies b_1 and b_2 become the master and slave surfaces respectively. This is an arbitrary choice when a symmetric treatment is employed, although the correct relative orientation is important in unsymmetric treatments.

Nodal points that define δb_1 are called master nodes and nodes that define δb_2 are called slave nodes. Likewise, a master/slave segment is any line joining two adjacent master/slave nodes, Figure 3.2. It is clear that contact segments thus correspond to external faces of the underlying element.

By way of explanation and in anticipation of the future discussion of slideline methods, the difference between an unsymmetric and a symmetric treatment should be noted. The former takes each potential contact node on the slave surface and imposes constraints on all those found to satisfy the penetration criterion. The symmetric treatment, however, consists of a further operation in which each potential contact node on the master surface is examined and the necessary constraints applied similarly.

3.3 EVOLUTION OF CURRENT SLIDELINE TECHNIQUES

Exact solutions to the static contact problem have been available for many years after the work performed by Hertz, Lubkin (1962). Due to the complexity of the problem, however, only relatively simple applications were attempted. In later years, the finite element method has proven to be a powerful tool for the numerical analysis of this class of problem.

The techniques employed to obtain solutions to the static contact problem include the use of a relative displacement vector to correspond to the clearance between the two bodies, Wilson and Parsons (1970). The two bodies are treated as one, but require the prior knowledge of the prescribed interference fit. Asano (1981) developed this further to solve for the final relative

displacement using an iterative method and thus eliminated any a priori knowledge.

Specially adapted constitutive laws were also developed to incorporate the contact discontinuities, Fredriksson (1976), Voyiadjis and Buckner (1983). This facilitated the simulation of elasto-plastic material models with hardening and friction, but iterative techniques were again required to solve for the nonlinear surface effects.

The use of various different iterative techniques applied to the finite element procedure has met with a good deal of success. Solutions are obtained by successive iteration subsequent to an assumed continuity condition at the contact interface, Mahmoud et al (1982), Rahman and Rowlands (1984), Osmont (1985), Ohte (1973), Tsuta and Yamaji (1973), Chan and Tuba (1971), Frankavilla and Zienkiewicz (1975), Sachdeva and Ramakrishnan (1981), Gaertner (1975).

The use of a contact element has been investigated in which various element formulations were applied to model the contact phenomena, Okamoto and Nakazawa (1979), Stadter and Wiss (1978), Yagawa and Hirayama (1984), Schafer (1975), Mazurkiewicz and Ostachowicz (1983), while the boundary displacement constraints have also been imposed via the Lagrange multiplier technique to good effect, Petersson (1977), Bathe and Chaudhary (1985).

These finite element contact formulations are not applicable to the high velocity impact problem because they lack one or more of the following capabilities;

(i) The facility to control the spurious mesh instabilities excited along the interface which are typically experienced in such dynamic processes.

(ii) Numerical efficiency within an explicit time integration environment.

(iii) Arbitrarily large relative deformations between adjacent sliding surfaces.

(iv) Collisions involving two or more deformable solids.

(v) Initial contact boundaries defined in terms of element regions rather than actual nodal contact locations.

(vi) Applicability to problems involving finite deformations and rotations.

Most of the significant developments in the treatment of high velocity contact by numerical methods have appeared in connection with the study of impact, explosive forming, and the general area of hydrodynamics. The concept of slidelines, that is material surfaces that can slide relative to one another, has its origin in these sources.

The usage of slidelines in more conventional structural analysis has been much more limited, principally because reliable algorithms have not been implemented in widely used finite element programs. Five algorithms have been used in the literature:

(i) Nodal constraint
(ii) Velocity constraint
(iii) Penalty-based
(iv) Distributed parameter
(v) Lagrange multiplier

The sliding interface procedures described above are of two types, that is kinematic or force;

Kinematic procedures alter nodal point velocities using impact relations when contact has occurred, and effectively introduce impulses of zero time duration to reflect contact behaviour. The smooth and accurate solution to impact problems is strongly dependent upon the description of these impact and

release conditions and, in some cases, can be unattainable.

Force procedures utilise nodal point restoring forces, and introduce an impulse of short but finite duration (tens of time steps) when the interaction occurs. This treatment requires the initial intervention by the analyst to provide a reasonable spring constant that will minimise unacceptable penetrations yet will not be so large as to prevent convergence, Guerra and Browning (1983).

3.3.1 Nodal constraint technique

The nodal constraint method, which uses the impact and release conditions of Hughes et al (1976), has been implemented in DYNA2D, Hallquist (1976), and DYNA3D, Hallquist (1977).

Constraints are imposed kinematically into the global equations by a transformation of the nodal displacement components of the slave nodes along the contact interface. This transformation has the effect of eliminating the normal degree of freedom of the slave nodes, and distributing its normal force component to adjacent master nodes. To preserve the efficiency of the explicit scheme, the mass is lumped to the extent that only the global degrees of freedom of each master node are coupled. This has the effect of creating a non-diagonal mass matrix with the associated numerical inefficiency. The impact and release conditions are imposed to ensure momentum conservation.

Problems arise with this method when master surface discretisation is finer than that for the slave surface as a result of the unsymmetrical treatment used in this procedure. Here, certain master nodes can penetrate through the slave surface without resistance and create a kink, Figure 3.3. Such kinks are relatively common with this formulation, especially when interface pressures are high, and serve to excite the hourglass mode of deformation, Hallquist (1983b). The nodal constraint method is most helpful in permitting sudden transitions in mesh refinement rather than the more usual gradual

transition zone.

The use of a semi-diagonal mass matrix and the requirement of a time step scaleback renders the implementation to be quite involved. The scaleback is necessary to ensure that a maximum of one potential contact node achieves contact conditions in each time step.

3.3.2 Velocity constraint technique

The momentum conservation process at the contact interface is again performed kinematically via the nodal velocities, and has been used with some degree of success by Johnson (1977) in the EPIC-2 and EPIC-3 codes. The momentum change caused by placing the penetrating slave node on the master surface is calculated and subsequently transferred to the adjacent master nodes.

The technique suffers from the mesh kinking described previously due to the unsymmetrical treatment of the slideline, although this is not as deleterious in Johnson's formulation since hourglass modes of deformation are not excited by the linear triangular element used in his work. It would appear, however, that unpublished work has now included this facility into the computations, Ringers (1983). Translational momentum is conserved exactly. The omission of a time step scaleback introduces errors into the centre of gravity positions when the slave node is moved to the master surface, since there is now no corresponding movement of the master nodes, which receive only an instantaneous velocity change. This centroidal error initiates further small errors in the rotational momentum.

The method is based upon the Newmark-Beta time integration scheme and the usual automatic time step computations are performed. It has been noticed that the technique becomes unstable if the time step is increased much beyond 30% of the Courant condition. Of itself, this presents no serious difficulty, however the additional computational cost may be quite considerable.

The technique works well for very simple contact laws such as frictionless in shear and normally rigid. A more complex approach is required, however, if more realistic laws are to be contemplated, Principia Mechanica (1984).

3.3.3 Penalty-based technique

The penalty-based method is used in the explicit finite element programs, Hondo II, Key et al (1978), DYNA2D, Hallquist (1984), DYNA3D, Hallquist (1983a) and the finite difference programs PR2D/PR3D, Principia Mechanica (1984). The method has also been used to good effect in the implicit codes; NIKE2D, Hallquist (1979), NIKE3D, Hallquist (1981), and in work carried out by Brockman (1982).

The method consists of placing normal interface springs between all penetrating nodes and the contact surface. The implicit and explicit treatments are similar with the exception of the assembly of the spring stiffness components into the global stiffness matrix for implicit solutions. HONDO II requires the user to choose a restoring force modulus for each side of the interface, whereas, the NIKE and DYNA codes compute a unique modulus for each slave and master segment, based on the thickness and bulk modulus of the element in which it resides. Pre-empting user control over this critical parameter greatly increases the success of the method, Hallquist (1983b).

The penalty-based method approach has been found to excite little, if any, mesh instability in contrast to the nodal and velocity constraint methods. This lack of noise is a result of the symmetrical treatment employed. An additional benefit of the technique is that the time step is not affected. Momentum is exactly conserved without the necessity of impact and release conditions and, furthermore, no special treatment of intersecting interfaces is required; thus greatly simplifying the implementation.

The interface stiffness is chosen to be less than the

stiffness of the interface elements normal to the interface. When interface pressures become large, as in explosive-structure interaction, unacceptable penetration has been found to occur. However, this situation is encountered within a different problem regime and is seldom attained in the class of high velocity impact considered here.

The technique is sufficiently flexible to permit the relatively straightforward implementation into implicit codes to obtain the additional benefits mentioned previously. Furthermore, computer hardware is reaching a level whereby the implicit codes are becoming increasingly competitive with respect to their explicit counterparts. The future of the penalty-based method is therefore assured.

3.3.4 Distributed parameter technique

This method is optional in DYNA2D, Hallquist (1984), and a specialisation of it may be found in DYNA3D, Hallquist (1983a). The technique is seldom utilised in structural calculations, since its usefulness is in the treatment of interfaces where the gaseous products of a high explosive act on a solid material.

The general procedure is as follows. One-half of the slave element mass of each element in contact is distributed to the covered master area. Also, the internal stress in each element determines a pressure distribution for the master surface area that received the mass. After completing this distribution of mass and pressure, the acceleration of the master surface is updated. Kinematic constraints are then imposed on slave node accelerations and velocities to ensure their movement along the master surface. The treatment is thus symmetric in nature although only one pass is actually performed.

3.3.5 Lagrange multiplier technique

This method has been implemented by Hughes et al (1976) and more recently by Chaudhary and Bathe (1986). The Lagrangian

multiplier method permits relationships between nodal degrees of freedom in addition to the basic stiffness equations. This method is numerically the most exact since these additional equations are inserted to ensure that the slave nodes are constrained to remain on the master surface exactly. The addition of extra variables in this way, however, requires the use of a more complicated equation solver.

The method is not symmetric since a slave node cannot contact two master surfaces at the same time. Because of this lack of symmetry the Lagrangian multiplier method does not necessarily preserve a smooth force distribution across the interface. The lack of a smooth force field excites the hourglass modes in many of the high velocity impact problems that have been solved, Hallquist et al (1984).

A further restriction is the applicability to implicit time integration schemes only. The problems inherent with implicit methods when referred to the high velocity regime have already been discussed in Section 2.2.3.

3.3.6 Selection of slideline technique

The lack of flexibility of the Lagrange multiplier method to be cast in an explicit form, the ineffectiveness of the distributed parameter method in structural problems and the lack of symmetry of the nodal constraint method have limited the majority of high velocity impact calculations to the use of either the penalty-based or the velocity constraint algorithms. The penalty-based procedure has been chosen to simulate the impact process in this work for several reasons;

(i) An objective of this work is to extend the penalty-based method to include fracture slideline capabilities. For reasons to be given in Chapter Five, the penalty-based method represents a more efficient and flexible alternative than that of the velocity constraint method.

(ii) The velocity constraint method appears to limit the critical time step to 30% of the Courant value to maintain stability at the interface, Hallquist (1987). The associated increase in solution time may therefore be a limiting factor.

(iii) The velocity constraint method is kinematic in nature and, in a similar way to the nodal constraint method, is expected to excite considerable mesh hourglassing when used in conjunction with a single point integration rule and the isoparametric four node quadrilateral.

(iv) The omission of any impact and release logic in the penalty-based method represents a simpler implementation than that of the velocity constraint method.

(v) The greater flexibility of the penalty-based method in dealing with tangential interface motion is important, especially in the treatment of the plugging process.

To avoid ambiguity in the following discussion of the symmetric treatment, the following terms will be defined (see Figure 3.4)

Current node : The potential contact node currently undergoing examination to determine its contact condition. It is clear that the current node will have been defined as a slave node in unsymmetrical treatments but may be a slave or a master node in symmetrical treatments.

Adjacent node : Any potential contact node which occurs on the opposite surface to the current node. For example, the slave surface nodes are the adjacent nodes with respect to the master surface.

Node pair : The two nodes, one on each contact surface, which are closest to one another. For each current node, then, there will be one associated node termed the local node. Note that for symmetric treatments the node pair association is not necessarily reversible and, therefore, must be computed for each contact surface.

Local segment : This is the contact segment associated with the local node and upon which the current node has, or is likely to, come into contact.

3.4 THE PENALTY-BASED SLIDELINE TECHNIQUE

The essential elements of the penalty-based method presented here are as follows. First, surface regions which represent potential areas of contact are defined. At each time step, each possible combination of surface nodes are screened using a simple conservative test to eliminate those pairs which are obviously not in contact. For remaining pairs, a more precise determination of the relative positions is then made. Finally, when a contact condition is detected, constraints are imposed in the equations of motion for the two bodies to restrict interpenetration of the contact surfaces and to determine the relative tangential motion according to the prescribed shear law. Each of these steps will be discussed in more detail below.

It has already been stated that the symmetric treatment involves a two pass process and eliminates the distinction between the slave and master surface terminology. Only those points necessary to define one complete pass will be discussed here, with the understanding that a second, identical, pass is also necessary.

All slideline calculations are performed within one suite of routines so that the simplicity of the overall computational strategy is maintained. These routines are called immediately prior to the central difference equations, thereby affecting the computation of the accelerations and the subsequent displacement

increments for the next time step. The position of this suite in the solution scheme may be seen in Table 2.1.

3.4.1 Definition of contact surfaces

The first step in the contact analysis is the designation of those surfaces between which contact might occur during the solution process. Their orderly definition is performed by the analyst using element node numbers in the region of the possible contact zone. Although the symmetric treatment is oblivious to the distinction between master and slave surfaces, the node arrangement is important in determining local contact segment axes.

Figure 3.7 defines the unit normal and tangential vectors ($\underset{\sim}{n}$, $\underset{\sim}{x}$) representing a typical local axis system. User input is governed to ensure the occurrence of this system by dictating that the numbering of the nodes on the defined surfaces be sequenced such that a traversal of each surface in the direction of the node numbering retains the adjacent surface to the left.

It should be noted that this sequence definition incorporates a slave node reversal. For example, consider the contact node sequence of Figure 3.2, where it is clear that the upper surface sequence is in opposition to that of the lower surface. This is simply to permit the use of the same algorithms in symmetric treatments rather than including a further suite of subroutines to deal with the reversed surface definition. The task is performed automatically at the data input stages. Chapter Five will discuss this further with respect to the fracture slideline technique.

3.4.2 Slave search

The use of slidelines for situations in which very large relative deformations of the sliding surfaces are present requires the continuous tracking of each current node in space relative to the associated local node and segment. The slave

search commences this process by extracting the nearest local node for each current node.

A benefit of the explicit time integration scheme is the small displacements which occur within a time increment. This practically ensures that the rate at which the local node changes is small. Current methods of implementing this slave search require that all adjacent nodes are searched for each current node, even if no change has occurred. This may consume a significant proportion of the time spent in the contact routines.

In recognition of this fact, the local nodes computed during the previous time step are used as a basis for a trial value in the current increment. A simple comparative procedure, Table 3.1, is used to detect any local node shifting in which both the local node and the minimum distance are updated as necessary. The use of this iterative scheme significantly reduces the time spent in the slave search algorithm, the new local node typically being located by consideration of three master nodes only.

3.4.3 Zonal contact detection

The cost of processing each surface node of a sliding interface is equivalent to half an element cycle. Typically, 20% of the total number of nodes of impact problems may be used in defining the slidelines, which is equivalent to a 10% increase in solution time. In most high velocity applications, the computer time is measured in terms of hours to tens of hours and this increase then becomes a serious consideration.

The examination of all the current nodes for contact at each time step is unnecessary, however, since only a small proportion will be active at any one time. For this reason an approximate screening procedure is used to eliminate those current nodes which clearly need no detailed consideration. When this procedure fails, a more accurate determination of the position of the current node is undertaken. In this way the efficiency of the overall algorithm is maintained.

A radial 'contact zone' is defined around each local node which is described in Figure 3.6. Contact is only possible if the current node is located within this zone. The contact zone radius r_z is a measure of the maximum distance D_a between any two neighbouring adjacent nodes and is continuously updated throughout the solution. Thus

$$r_z = \alpha_r D_a \tag{3.3}$$

where the constant α_r controls the degree of radial overlap between neighbouring contact zones and ensures that no current node may avoid detection by passing through their mutual tangent. Generally

$$\alpha_r \geq 0.5 \tag{3.4}$$

and a value of $\alpha_r = 9/5$ has given good performance.

3.4.4 Segment definition

For all current nodes passing the zonal contact detection test, tracking is continued by defining the local segment. This process obtains the segment direction cosines used in the refined contact detection test.

Consider a current node (i), on body b_2, and assume that a slave search on b_1, has located the local node (k). Figure 3.7 depicts a portion of the two bodies, including adjacent nodes (j) and (l). The unit tangent vector and unit normal vector are $\underset{\sim}{x}_{jk}$ and $\underset{\sim}{n}_{jk}$ respectively for local segment jk, and similarly for segment kl. The relative position vector between the current and local node is $\underset{\sim}{C}$. If the inequality

$$(\underset{\sim}{C} \quad \underset{\sim}{x}_{kl}) > 0 \tag{3.5a}$$

is satisfied, the accompanying unit normal vector would be

$$\underset{\sim}{n} = \underset{\sim}{n}_{kl} \tag{3.5b}$$

and the local segment defined as (Figure 3.8),

$$S = S_1 \tag{3.5c}$$

while the unit tangent vector is

$$\underset{\sim}{x} = \underset{\sim}{x}_{kl} \tag{3.5d}$$

the vectors $\underset{\sim}{x}$ and $\underset{\sim}{n}$ represent the local coordinate system for the segment. Similarly, if the inequality

$$(\underset{\sim}{C} \ \underset{\sim}{x}_{jk}) < 0 \tag{3.6a}$$

is satisfied, the accompanying unit normal vector would be

$$\underset{\sim}{n} = \underset{\sim}{n}_{jk} \tag{3.6b}$$

and the local segment defined as

$$S = S_2 \tag{3.6c}$$

with

$$\underset{\sim}{x} = \underset{\sim}{x}_{jk} \tag{3.6d}$$

The inequalities of equations (3.5a) and (3.6a) may be inconclusive as the mesh deforms, for example a current node may lie in the region between segments S_1 and S_2. This zone will be termed S_3, Figure 3.8. If Θ is the angle between the two segments then an extended segment is used such that

$$Tol = r_z \sin\Theta/_2 \tag{3.7}$$

where Tol is the extension to each contact segment, Figure 3.9.

In practice this has been found to be a rather liberal test and the actual value used is

$$Tol = 1/3\ r_z \sin\Theta/_2 \tag{3.8}$$

An important feature of this particular segment test is its ability to function for angles of 90° and greater, an arrangement which typically occurs in high velocity impact and especially with the addition of fracture. The inequalities to detect this region become

$$(\underset{\sim}{C}\ \ \underset{\sim}{x}_{jk}) > (-Tol) \tag{3.9a}$$

and

$$(\underset{\sim}{C}\ \ \underset{\sim}{x}_{kl}) < Tol \tag{3.9b}$$

The unit normal vector in this case will be

$$\underset{\sim}{n} = 1/2\ (\underset{\sim}{n}_{jk} + \underset{\sim}{n}_{kl}) \tag{3.9c}$$

and the segment

$$S = S_3 \tag{3.9d}$$

with

$$\underset{\sim}{x} = 0 \tag{3.9e}$$

3.4.5 Normal penetration evaluation

The normal penetration distance X_n of the current node through the local segment S is evaluated in local coordinates by

$$X_n = (\underset{\sim}{C}\ \ \underset{\sim}{n}) \tag{3.10}$$

if ($X_n < 0$), then penetration is assumed.

3.4.6 Contact location point

The identification of a contact location point $\underset{\sim}{X}_c$, defined as the point on the local segment which is nearest to the current node, is necessary for the evaluation of relative tangential sliding.

Consider a current configuration for which the local node k and the segment definition node 1, have node coordinates, $\underset{\sim}{X}_k$ and $\underset{\sim}{X}_1$, respectively, Figure 3.10. A parametric representation of the local segment S, for which the axis set ($\underset{\sim}{x}$, $\underset{\sim}{n}$) has been already computed, is given using the variables η_1 and η_2 such that the contact location point is evaluated as

$$\underset{\sim}{X}_c = \eta_1 \underset{\sim}{X}_k + \eta_2 \underset{\sim}{X}_1 \tag{3.11}$$

where

$$\eta_1 + \eta_2 = 1 \tag{3.12}$$

and

$$\eta_1 = \frac{(\underset{\sim}{C} \quad \underset{\sim}{x})}{| \underset{\sim}{X}_k - \underset{\sim}{X}_1 |} \tag{3.13}$$

$\underset{\sim}{X}_c$ is only computed for interface laws involving shear forces, for frictionless conditions it is ignored. The dimensionless parameters (η_1, η_2) are stored upon evaluation as history variables (α_1, α_2) for use in the following time step.

3.4.7 Tangential penetration evaluation

The tangential penetration distance is evaluated in the local segment axis system using an incremental process based upon the current configuration. For each current node, the new contact location point is defined to be $\underset{\sim}{X}^n_c$. The tangential displacement

increment $\delta \underset{\bullet}{X}_{ti}$ evaluated at time (n) is given by

$$\delta X^{n}_{ti} = | \underset{\sim}{X}^{n}_{c} - \underset{\sim}{X}^{n-1}_{c}| \qquad (3.14)$$

where $\underset{\sim}{X}^{n-1}_{c}$ is the contact location point from the last time step. It is evaluated in the current configuration using the history variables (α_1, α_2) so as to minimise the storage requirements for each current node and to eliminate any rigid body motion. The computation of this value will be not be unduly affected by any segment extensions because of the very small displacement increments.

3.4.8 Computation of interface stiffness

The efficiency of the penalty-based method rests in the elimination of the usual expensive tangent stiffness evaluation. A contact length-weighted bulk modulus has been found robust and considerable success has been achieved with its use, particularly where significant plastic deformation of the surfaces occurs, Guerra and Browning (1983).

The stiffness coefficient k_i for the segment S containing element i is given in terms of the bulk modulus B_i the length of the contact segment l and the thickness of the element t_i as

$$k_i = \Phi \frac{B_i \, l}{t_i} \qquad (3.15)$$

where Φ is a scale factor for the interface stiffness, generally

$$0.05 \leq \Phi \leqslant 1.0 \qquad (3.16)$$

Computation of the stiffness coefficient is performed once only at the commencement of the solution to eliminate any hysteretic energy losses on subsequent unloading. A simple averaging of adjacent segment values then provides a smooth nodal

interface stiffness. The effects of the smoothing are significant only for non-uniform mesh configurations or where variations in material properties occur in the vicinity of the contact region. The nodal stiffness values K_i of each adjacent contact node i are thus

$$K_i = 1/2 \; (\; k_i + k_{i+1} \;) \qquad (\; i = 1, \; Na) \tag{3.17}$$

where Na are the number of adjacent nodes.

3.4.9 Application of constraints

When the current node has penetrated the local segment, interaction forces are imposed upon both the current node and the two adjacent nodes defining the local segment. These forces must satisfy the following conditions to ensure conservation of translational and rotational momenta

$$f_{ni} = f_{nk} + f_{nl} \tag{3.18}$$

and

$$n_1 \; f_{nl} + n_2 \; f_{nk} = 0 \tag{3.19}$$

The forces are computed in the local axes of the segment and are shown in Figure 3.11. The force on the current node i due to normal penetration is computed as

$$f^n_{ni} = K^n_i \; X^n_{ni} \tag{3.20}$$

The assumption of a frictionless interface condition is often unrealistic. Any number of laws may be devised to define the frictional forces as functions of the interface pressure or the relative sliding velocity of the surfaces. In this work a velocity independent formulation based on the Coulomb friction coefficient μ is used. The tangential force increment δf_{ti} acting on the current node is defined as

$$\delta f_{ti}^{n} = K_i \ \delta X_{ti}^{n} \tag{3.21}$$

The sign is chosen such that the frictional force resists relative motion between the current node and the local segment. The total tangential force is

$$f_{ti}^{n} = f_{ti}^{n-1} + \delta f_{ti}^{n} \tag{3.22}$$

while application of Coulombs law ensures that

$$f_{ti}^{n} \leq \mu \ f_{ni}^{n} \tag{3.23}$$

During solution, a current node may experience several impact and release cycles, and it is necessary, therefore, to initialise the total tangential force for each current node on ocurrence of release.

Finally, the total interface forces corresponding to each current node are transformed into the global coordinate system and represent added force-deflection relations to the discrete system. The effects of these will be mentioned later.

3.5 NUMERICAL IMPLEMENTATION

A flowchart indicating the principal features of the penalty-based slideline technique is given in Table 3.2.

The efficiency and flexibility of any slideline algorithm is dependent upon the database methodology and its ability to track the location of each current node with respect to the local node and segment. The database has been designed with the application of the fracture slideline method in mind and will be discussed further in this context in Chapter Five.

Ideally, the data structure should support both master-slave

and symmetric algorithms, permit large relative tangential motion between the contacting bodies and also intermittent contact situations. A single surface collapsing on itself should also be allowed, together with a facility for any number of additional slidelines to be included easily throughout the solution. The method used is based upon a surface interaction table.

Consider the axisymmetric plate impact situation of Figure 3.12. Surfaces 1 and 2 are defined in terms of an orderly arrangement of the contact nodes, Section 3.4.1, and constitute slideline 1. The surface interaction table is defined for this configuration in Table 3.3.

The use of such a table enables the interaction of any two surfaces. It includes the capability to support a mixture of symmetric and unsymmetric sliding surfaces simultaneously, although this is beyond the scope of the present work. The only limit imposed on the number of slidelines permitted is the computer storage available.

The surface interaction table acts primarily as a pointer to three other contact tables; the integer and real contact data, ICONTD and ECONTD respectively, and the updated contact node coordinates, XYZCNT. In computional terms these tables represent three dimensional arrays (i,j,k) in which each history variable i associated with node j on surface k are stored. Data for each surface may be stored in any position k since all information concerning the location of each local surface is stored in the surface interaction table.

Table 3.4 gives the history variables required for the three contact arrays

Distinction should be made between the four pointers defined in Table 3.4(b). The current node pointer (location 3) defines the position of the local node in the contact data arrays. The three remaining pointers are simply to minimise the searches through the element and global system arrays in both the contact node coordinate update and the application of interface

constraints.

The slideline method developed herein incorporates a three level procedure. The top level selects the next appropriate slideline to be manipulated. At this point, the type of processing required may be determined for each slideline from additional handler data stored in the interaction table. For instance, this data may determine whether a symmetric treatment is neccessary or provide facility for differing frictional or scaling coefficients. The second level extracts from the interaction table the location of the two surfaces comprising the current slideline, while the main processing loop proceeds to examine the contact nodes on each surface in turn.

3.6 ASPECTS OF SLIDELINE USAGE

Several general guidelines should be adhered to in the use of slidelines to avoid numerical problems and these are;

(i) As far as possible, the mesh in the region of contact should be uniform so as to ensure both a meaningful zonal contact detection search and also that there be minimal discontinuities in the nodal stiffness values.

(ii) To eliminate slideline end effects in the segment definition stage (i.e. current nodes 'creeping' around the end of the local surface and escaping detection), a liberal definition of the adjacent nodes on each slideline surface should be used. The zonal contact detection routine will automatically ensure that only those current nodes required are activated, and efficiency will be maintained.

(iii) Assume that the contact region determines the critical time step value dt_{cr} then an estimate of the total initial displacement increment δ_x for an initial velocity v_o is

$$\delta_x = \frac{v_o \, r_z}{\alpha_r c} \qquad (3.24)$$

where c is the sound velocity in the medium. To ensure the correct treatment of each current node, the displacement increment should be maintained as

$$\delta'_x \leq r_z \tag{3.25}$$

or

$$\frac{v_o}{\alpha_r c} \leq 1 \tag{3.26}$$

therefore, any initial velocities which do not satisfy the above inequality require a suitable modification in α. Note that the upper limit remains unaltered as

$$\alpha_r \leq 0.5\dot{5} \tag{3.27}$$

(iv) The success of this method depends upon the choice of the scale factor Φ. If the interface force generated is not sufficiently large, the current node may penetrate into the element to such a depth that the program can no longer resolve the geometric relationships correctly. Conversely, too large a value will cause 'chattering' in the interface region. Furthermore, since the increased stiffness associated with the additional slideline forces is not accounted for in the stability calculations, the solution process may experience instability with exceptionally large values of scale factor. A solution to this problem is to scale back the time step size in the stability calculations.

(v) The nodal stiffness value K_i is a linear function of the element aspect ratio. The initial estimate of the scale factor may be affected by this relationship if the elements in the contact zone have aspect ratios significantly different from unity. A reduction in this factor will be required to account for

the increased element stiffness values associated with large aspects. An increase would also be in order for the reduced stiffness values accompanying the smaller aspects.

(vi) To some extent the iterative process necessary to obtain the proper scale factor does minimise the advantages gained by the fast execution speed. For most problems, however, the maximum interface force is attained early in the solution and by implementing careful checks the calculations may be halted on detection of an incorrect value. The effects of variations in the scale factor will be considered in the following chapter.

3.8 CONCLUSIONS

This chapter has presented the theoretical aspects of the slideline technique as applied within a finite element context. The methods currently available were discussed, from which the penalty-based formulation was established as having the most suitable qualities with respect to this current work. In particular, the flexibility of this formulation in dealing with the tangential sliding motion, together with its robust nature was found most desirable.

The lack of efficiency and robustness of slideline techniques in the past has been a major reason for their limited implementation within the more widely used finite element programs. The zonal contact detection scheme and the automatic determination of slideline surface extensions as described in sections 3.4.3 and 3.4.4 respectively represent a new method to overcome these particular limitations. Furthermore, the slave search (section 3.4.2) exploits the small displacement increments experienced in explicit time integration schemes and has also made reductions in the time spent extracting active contact nodes for processing within each time step.

The database structure for handling slideline information was also considered in some detail. An efficient implementation was described, which permits a continuous increase in the number

of slidelines throughout a solution, together with the capability of supporting several differing slideline schemes simultaneously.

3.9 REFERENCES

Asano, N. (1981). 'Principle of Virtual Work for Two Elasto-Impact Bodies in Separate State and its Application to the Finite Element Method', Bull. JSME, Volume 24, Number 193, pp 1123-1129.

Bathe, K.J. and Chaudhary, A.B. (1985). 'A Solution Method for Planar and Axisymmetric Contact Problems', Int. J. Num. Meth. Engng., Volume 21, pp 65-88.

Brockman, R.A. (1982). 'Numerical Solution of Large Deformation Problems Involving Surface Contact and Impact', Penalty Finite Element Methods in Mechanics, ASME, AMD-51, Arizona.

Chan, S. and Tuba, I. (1971). 'A Finite Element Method for Contact Problems of Solid Bodies-I. Theory and Validation', Int J. Mech. Sci., Volume 13, pp 615-625.

Chaudhary, A.B. and Bathe, K.J. (1986). 'A Solution Method for Static and Dynamic Analysis of Three-Dimensional Contact Problems with Friction', Comp. Struct., Volume 24, Number 6, pp 855-873.

Frankavilla, A. and Zienkiewicz, O. C. (1975). 'Note on the Numerical Computations of Elastic Contact Problems', Int. J. Num. Meth. Engg., Volume 9, pp 913-924.

Fredriksson, B. (1976). 'Finite Element Solution of Surface Non-Linearities in Structural Mechanics with Special Emphasis to Contact and Fracture Mechanics Problems', Comput. Struct., Volume 6, pp 281-290.

Gaertner, R. (1975). 'Investigation of Plane Elastic Contact Allowing for Friction', Comp. Struct., Volume 7, pp 59-63.

Guerra, F.M. and Browning, R.V. (1983). 'Comparison of Two Slideline Methods Using ADINA', Comp. Struct., Volume 17, Number 5-6, pp 819-834.

Hallquist, J.O. (1976). 'A Procedure for the Solution of Finite Deformation Contact-Impact Problems by the Finite Element Method', University of California, Lawrence Livermore National Laboratory, Report UCRL-52066.

Hallquist, J.O. (1977). 'A Numerical Procedure for Three-Dimensional Impact Problems', American Society of Civil Engineers, Preprint 2956.

Hallquist, J.O. (1979). 'NIKE2D : An Implicit, Finite-Deformation Finite-Element Code for Analysing the Static and Dynamic Response of Two-Dimensional Solids', University of California, Lawrence Livermore National Laboratory, Report UCRL-52678.

Hallquist, J.O. (1981). 'NIKE3D : An Implicit, Finite-Deformation, Finite-Element Code for Analysing the Static and Dynamic Response of Three-Dimensional Solids', University of California, Lawrence Livermore National Laboratory, Report UCID-18822.

Hallquist, J.O. (1983a). 'Theoretical Manual for DYNA3D', University of California, Lawrence Livermore National Laboratory, Report UCID-19401.

Hallquist, J.O. (1983b). 'Lecture Notes for Contact-Impact Algorithms for Large Deformation Finite Element Analysis', University of California, Lawrence Livermore National Laboratory, Report UCRL-89157.

Hallquist, J.O. (1984). 'User's Manual for DYNA2D - An Explicit Two-Dimensional Hydrodynamic Finite Element Code with Interactive Rezoning', University of California, Lawrence Livermore National Laboratory, Report UCID-18756.

Hallquist, J.O. and Goudreau, G.L. and Benson, D.J. (1984). 'Sliding Interfaces with Contact-Impact in Large Scale Lagrangian Computations', University of California, Lawrence Livermore National Laboratory, Report UCRL-91129.

Hallquist, J.O. (1987). Private communication

Hughes, T. and Taylor, R.L. and Kanoknukulchai, W. (1976). 'A Finite Element Method for a Class of Contact-Impact Problems', Comp. Meth. Appl. Mech. Eng., Volume 8, pp 249-276.

Johnson, G.R. (1977). 'EPIC-3. A Computer Program for Elastic-Plastic Impact Calculations in 3 Dimensions', U.S.A. Ballistic Research Laboratory, Maryland, Report AD-A043281.

Key, S.W. and Beisinger Z.E. and Kreig, R.D. (1978). 'HONDO II - A Finite Element Computer Program for the Large Deformation Dynamic Response of Axisymmetric Solids', Sandia National Laboratories, Albuquerque, NM, Report 78-0422.

Lubkin, J.L. (1962). 'Contact Problems', Handbook of Engineering Mechanics, Flugge (Editor), McGraw-Hill.

Mahmoud, F. and Salamon, N.J. and Marks, W.R. (1982). 'A Direct Automated Procedure for Frictionless Contact Problems', Int. J. Num. Meth. Engg., Volume 18, pp 245-257.

Mazurkiewicz, M. and Ostachowicz, W. (1983). 'Theory of Finite Element Method for Elastic Contact Problems of Solid Bodies', Comp. Struct., Volume 17, Number 1, pp 51-59.

Ohte, S. (1973). 'Finite Element Analysis of Elastic Contact Problems', Bull. JSME, Volume 16, Number 95, pp 797.

Okamoto, N. and Nakazawa, M. (1979). 'Finite Element Incremental Contact Analysis with Various Frictional Conditions', Int. J. Num. Meth. Engg., Volume 14, pp 337-357.

Osmont, D. (1985). 'A Finite Element Code for the Computation of the Dynamic Response of Structures Involving Contact Effects', Comp. Struct., Volume 20, Number 1-3, pp 555-561.

Petersson, H. (1977). 'Application of the Finite Element Method in the Analysis of Contact Problems', Proc. Int. Conf. on Finite Elements in Nonlinear Solid and Structural Mechanics, Volume 2, Norway.

Principia Mechanica. (1984). 'PR2D/PR3D - Theoretical Basis', Technical Note Number PR-TN-6.

Ringers, B.E. (1983). 'New Sliding Surface Techniques enable the Simulation of Target Plugging Failure', Ballistic Research Laboratory, Aberdeen Proving Ground, Maryland, Report ARBRL-TR-02541.

Rahman, M. and Rowlands, R. (1984). 'An Iterative Procedure for Finite Element Stress Analysis of Frictional Contact Problems', Comp. Struct., Volume 18, Number 6, pp 947-954.

Sachdeva, T. and Ramakrishnan, C. (1981). 'A Finite Element Solution for the Two Dimensional Elastic Contact Problem with Friction', Int. J. Num. Meth. Engg., Volume 17, pp 1257-1271.

Schafer, H. (1975). 'A Contribution to the Solution of Contact Problems with the Aid of Bond Elements', Comp. Meth. Appl. Mech. Engg., Volume 6, pp 335-354.

Stadter, J. and Weiss, R. (1978). 'Analysis of Contact through Finite Element Gaps', Comp. Struct., Volume 10, pp 867-873.

Tsuta, T. and Yamaji, S. (1973). 'Finite Element Analysis of Contact Problems', Theory and Practice in Finite Element Structural Analysis, University of Tokyo Press, Japan.

Voyiadjis,B. and Buckner, N. (1983). 'Indentation of a Half Space with a Rigid Indenter', Int. J. Num. Meth. Engg., Volume 19, pp 1555-1578.

Wilson, E. and Parsons, B. (1970). 'Finite Element Analysis of Contact Problems using Differential Displacements', Int. J. Solids and Structures, Volume 2, pp 387-395.

Yagawa, G. and Hirayama, H. (1984). 'A Finite Element Method for Contact Problems Related to Fracture Mechanics', Int. J. Num. Meth. Engg., Volume 20, pp 2175-2195.

Table 3.1

Modified slave search procedure

Initialisation phase

(a) All adjacent nodes are searched for each current node to obtain the local node.

General Procedure

(a) Extract local node, n_1, from previous time step.

(b) Set trial value, $n_t = n_1$

(c) Calculate distance between current node and node n_{t-1} (= D_1).

(d) calculate distance between current node and node n_t (= D_2).

(e) calculate distance between current node and node n_{t+1} (= D_3).

(f) Compare D_1, D_2 and D_3.

If $D_1 < (D_2, D_3)$ update $n_1 = n_{t-1}$

If $D_2 < (D_1, D_3)$ update $n_1 = n_t$

If $D_3 < (D_1, D_2)$ update $n_1 = n_{t+1}$

Figure 3.5 depicts the distances D_1,D_2 and D_3

TABLE 3.2

Penalty-based Slideline Flowchart

---

1 Initialisation

(a) Recover contact variables and arrays

(b) Update contact node coordinates

(c) Compute nodal interface stiffness values

(d) Compute initial value of contact zone radius

2 Contact detection phase

(a) Extract current and local surfaces

(b) Extract current node on surface

(c) Slave search

(d) Zonal contact detection *

(e) Segment definition *

(f) Normal penetration detection *

(g) Tangential penetration detection

3 Force application phase

(a) Application of constraints

(b) Assembly of interface force into global force vector

(c) Repeat steps 2(b)-3(b) for each current node on surface

(d) Repeat steps 2(a)-3(b) for each current surface

Note : * denotes points at which a current node may fail contact detection tests. At such points the current node is automatically rejected

Table 3.3

Surface interaction table for typical plate impact configuration

Slideline	Master Surface	Slave Surface
1	1	2

Table 3.4

Contact Data Arrays for Slideline technique

(a) Real Data : ECONTD

Location	Data description
1	Nodal stiffness value
2	Total tangential force
3-4	Contact location point Coordinates
5-6	Current interface force (for output only)

(b) Integer Data : ICONTD

Location	Data description
1	Current node number
2	Local node pointer
3	Current node pointer in element arrays
4-5	Current node pointer to global arrays
6	Previous local node pointer

(c) Coordinate Data : XYZCNT

Location	Data description
1-2	Updated contact node coordinates

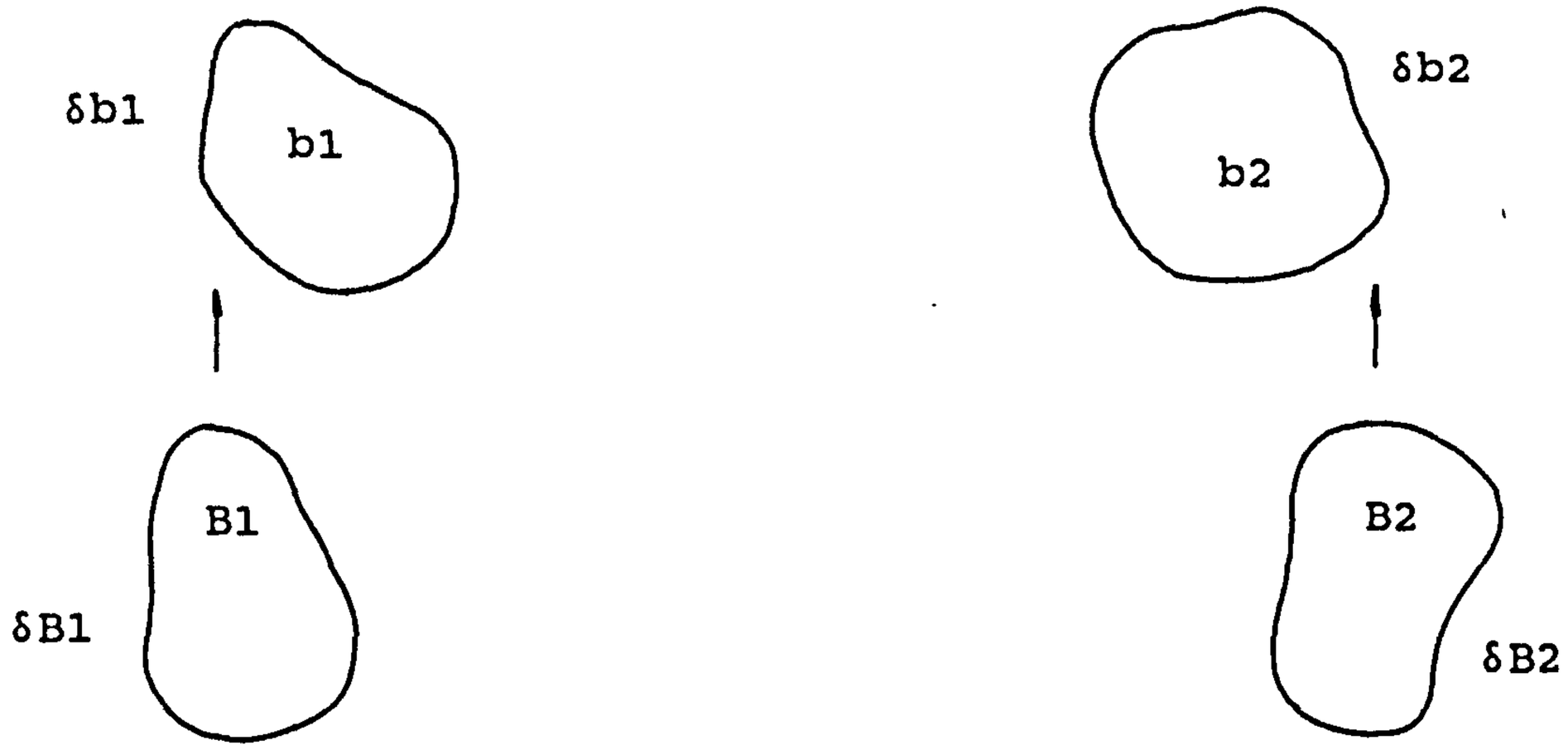

Figure 3.1
Reference and deformed configuration of two solids

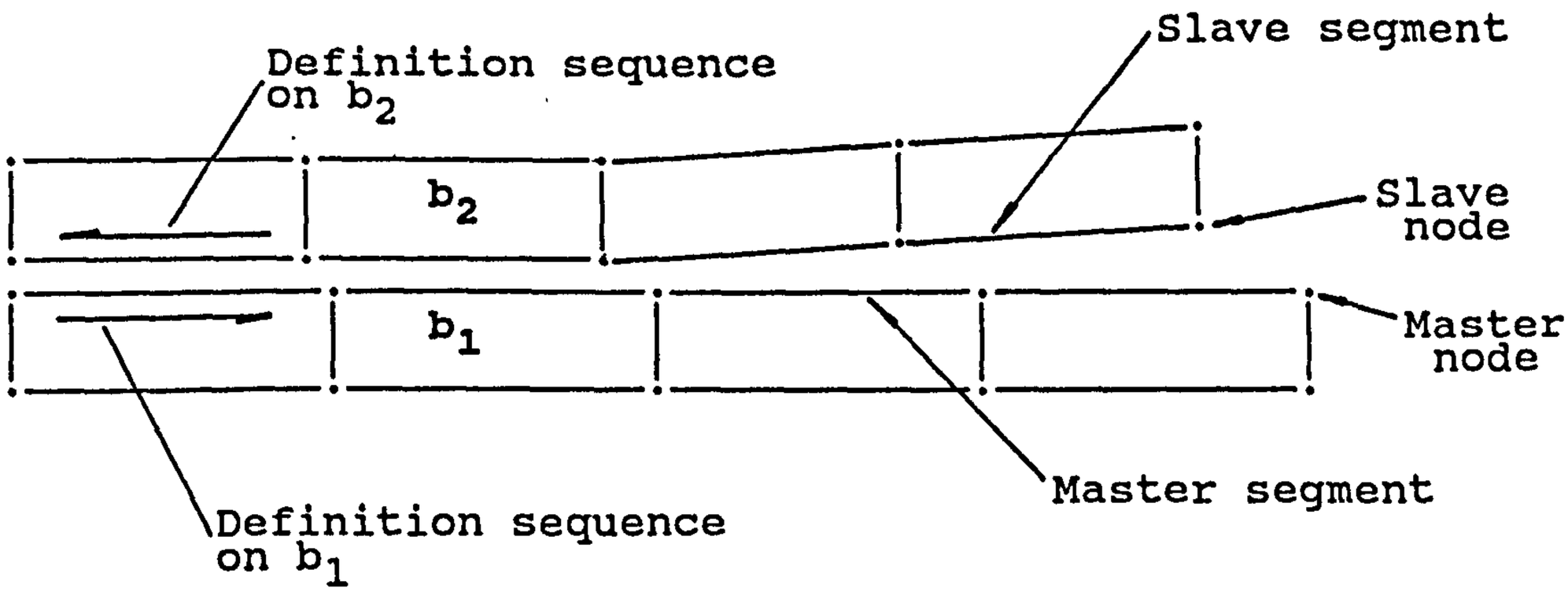

Figure 3.2
Contact parameter definition

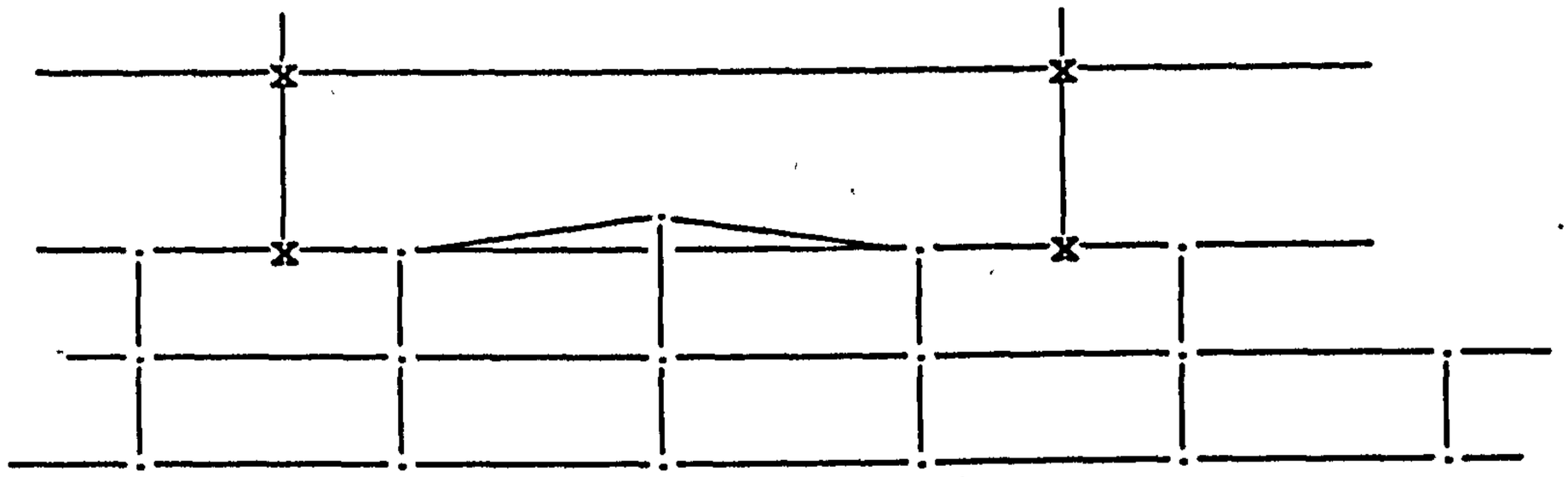

Figure 3.3
Mesh kinking with unsymmetrical slideline methods

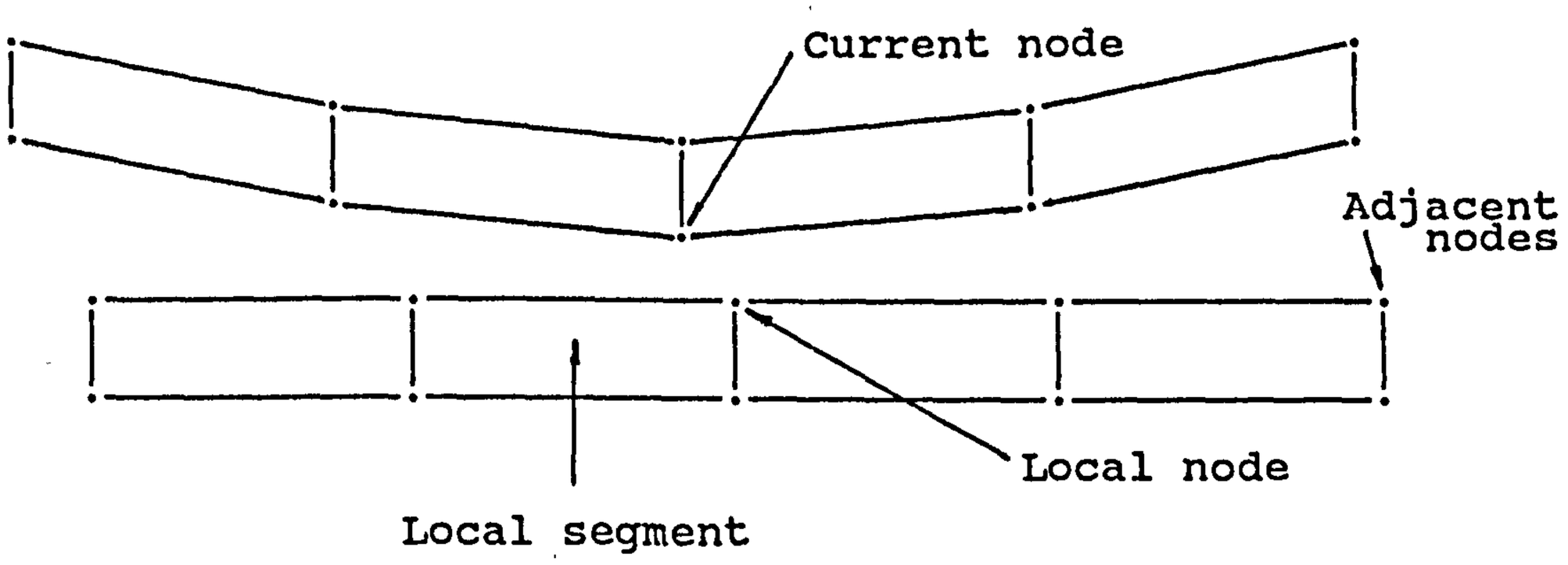

Figure 3.4
Contact zone parameter definition

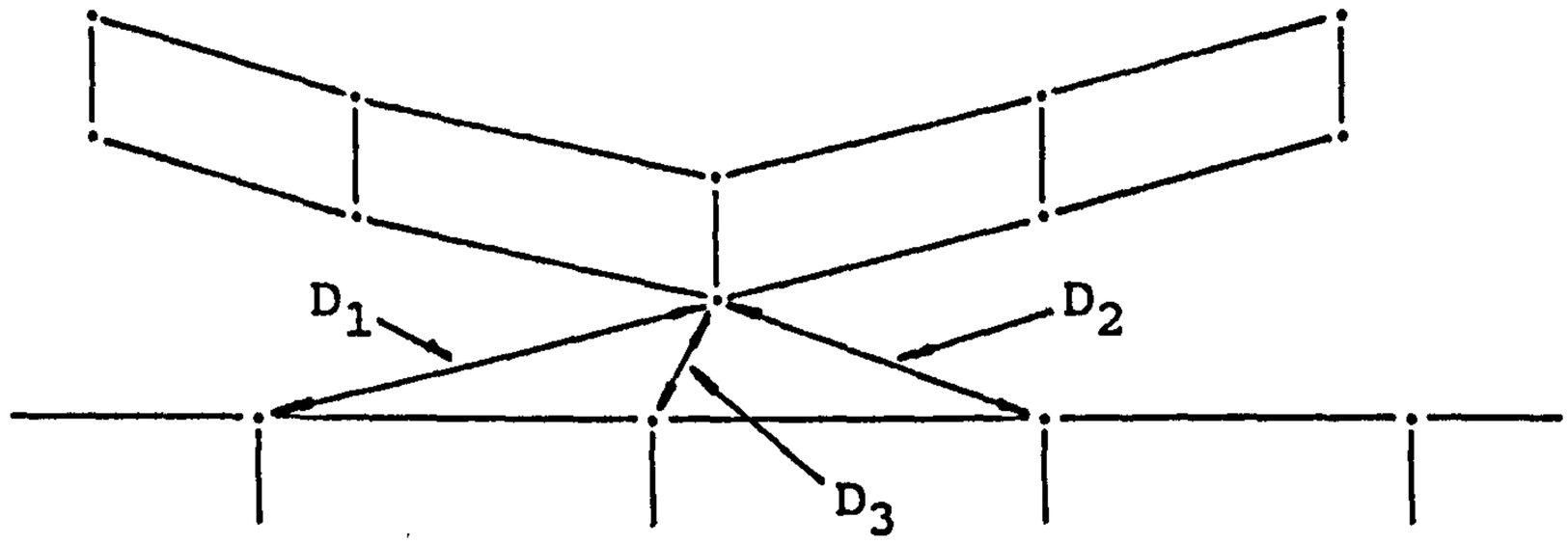

Figure 3.5
Slave search distance relationship

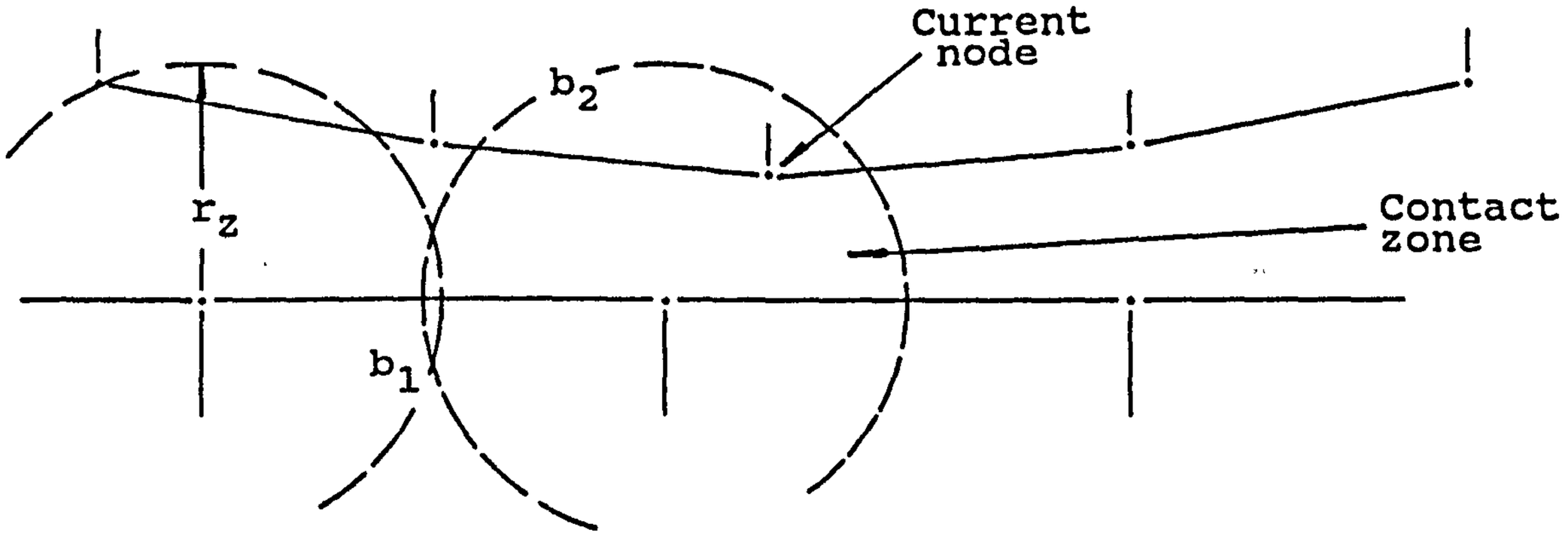

Figure 3.6
Zonal contact detection test configuration

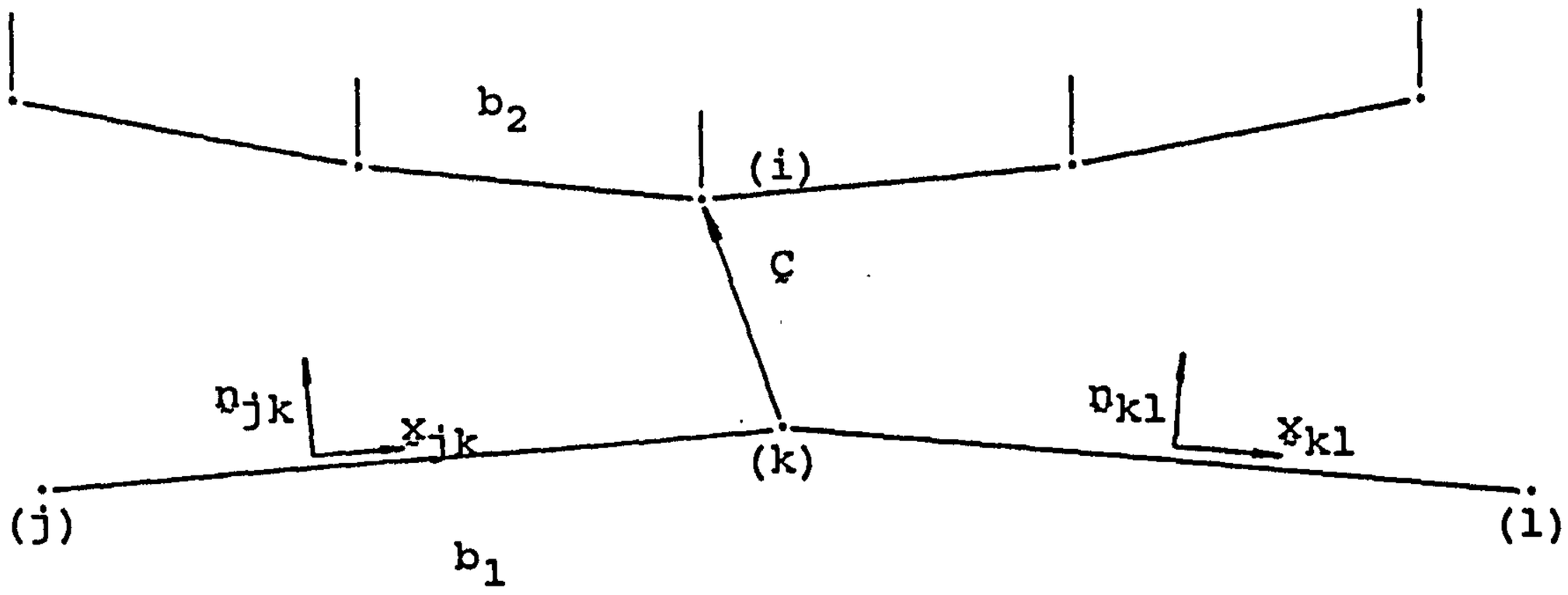

Figure 3.7
Refined contact detection test

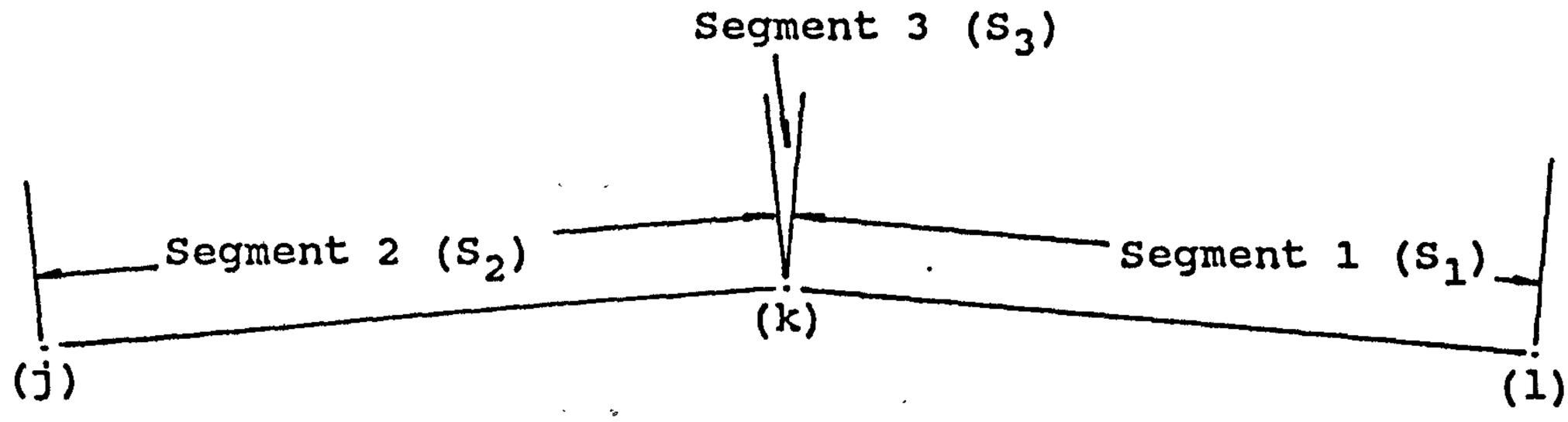

Figure 3.8
Contact segment definition

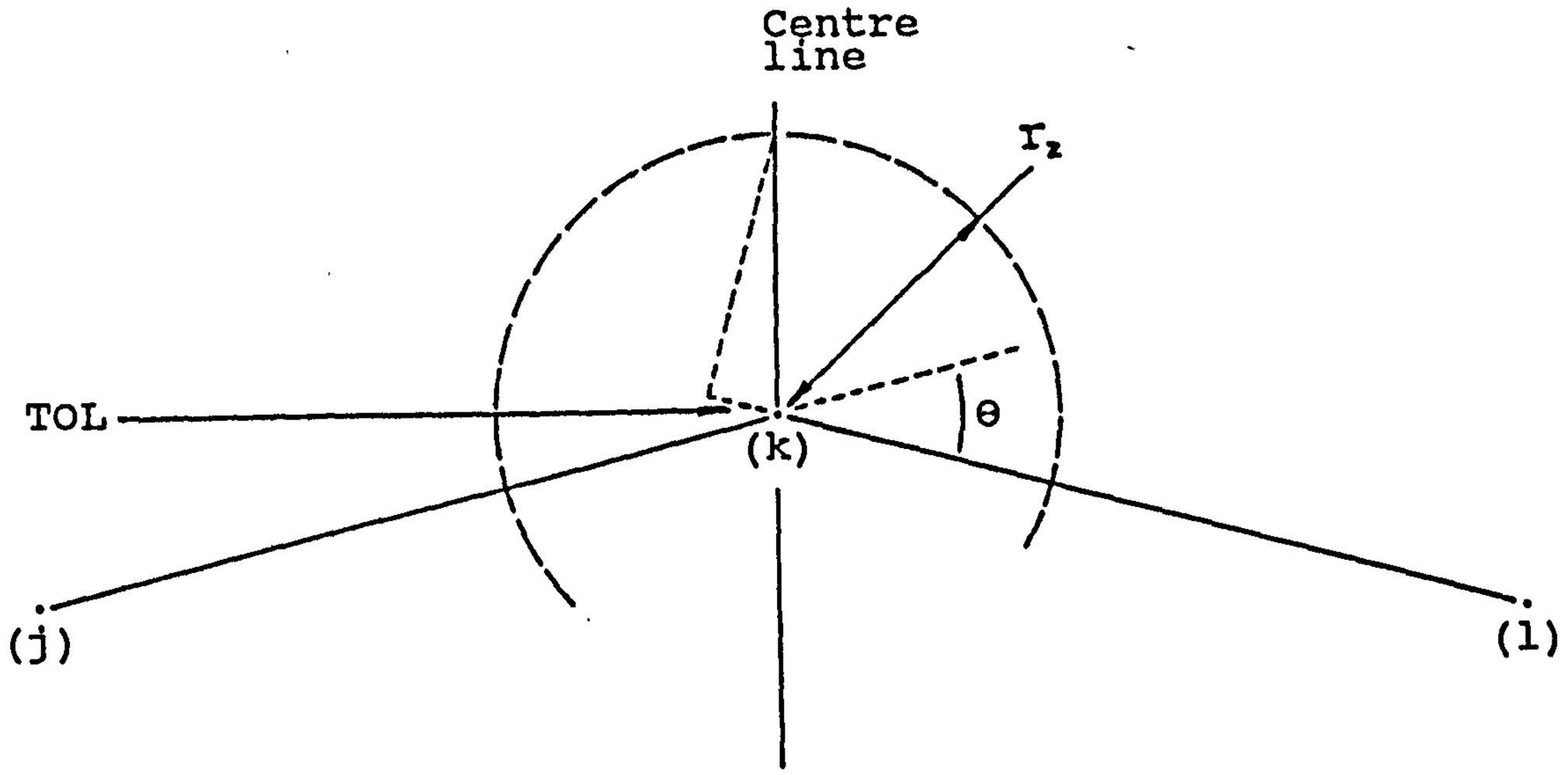

Figure 3.9
Contact segment extension

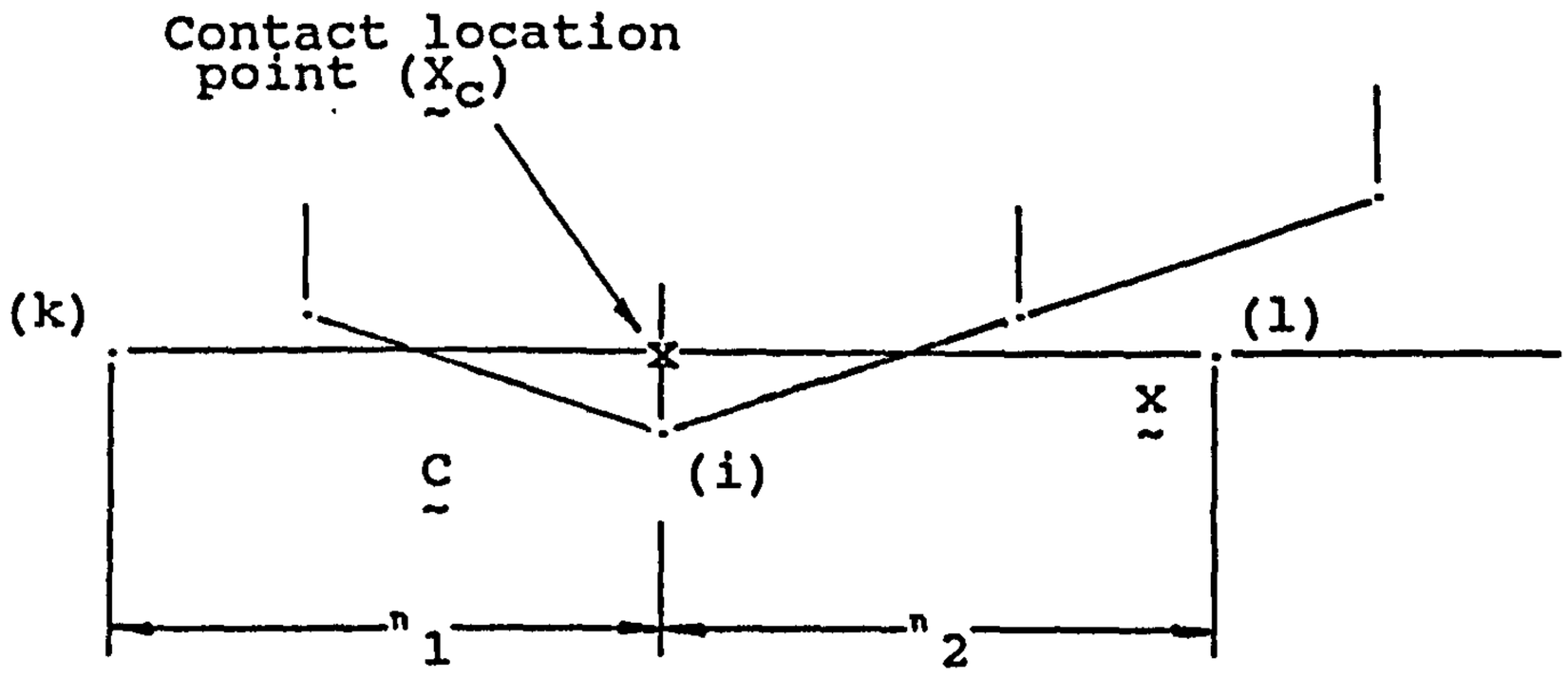

Figure 3.10
Contact location point

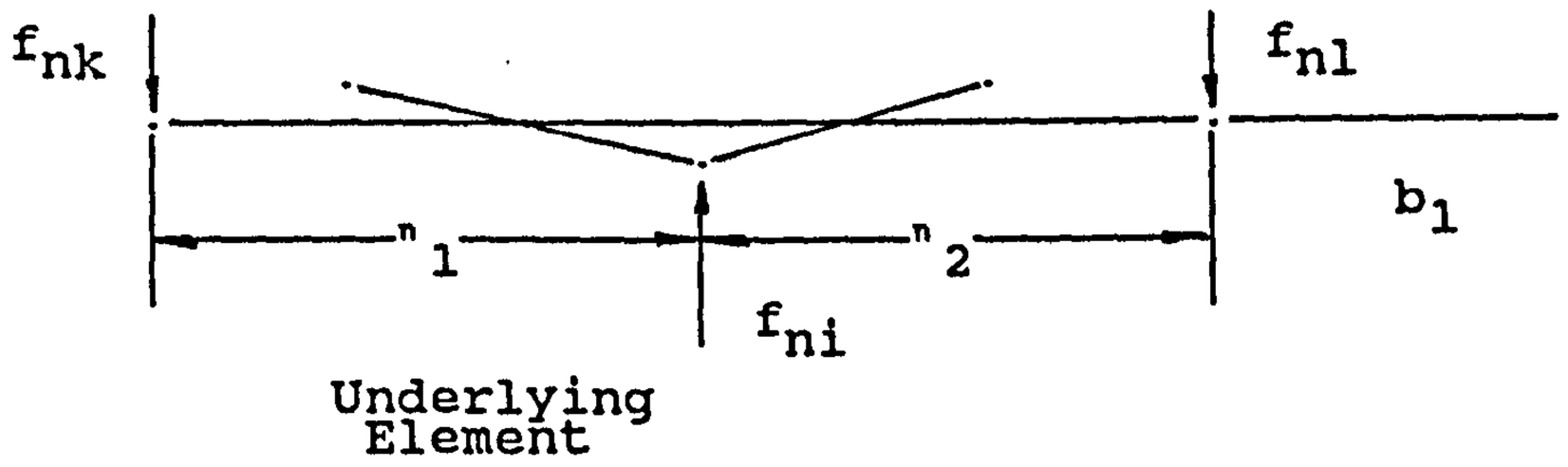

Figure 3.11

Distribution of normal interface force

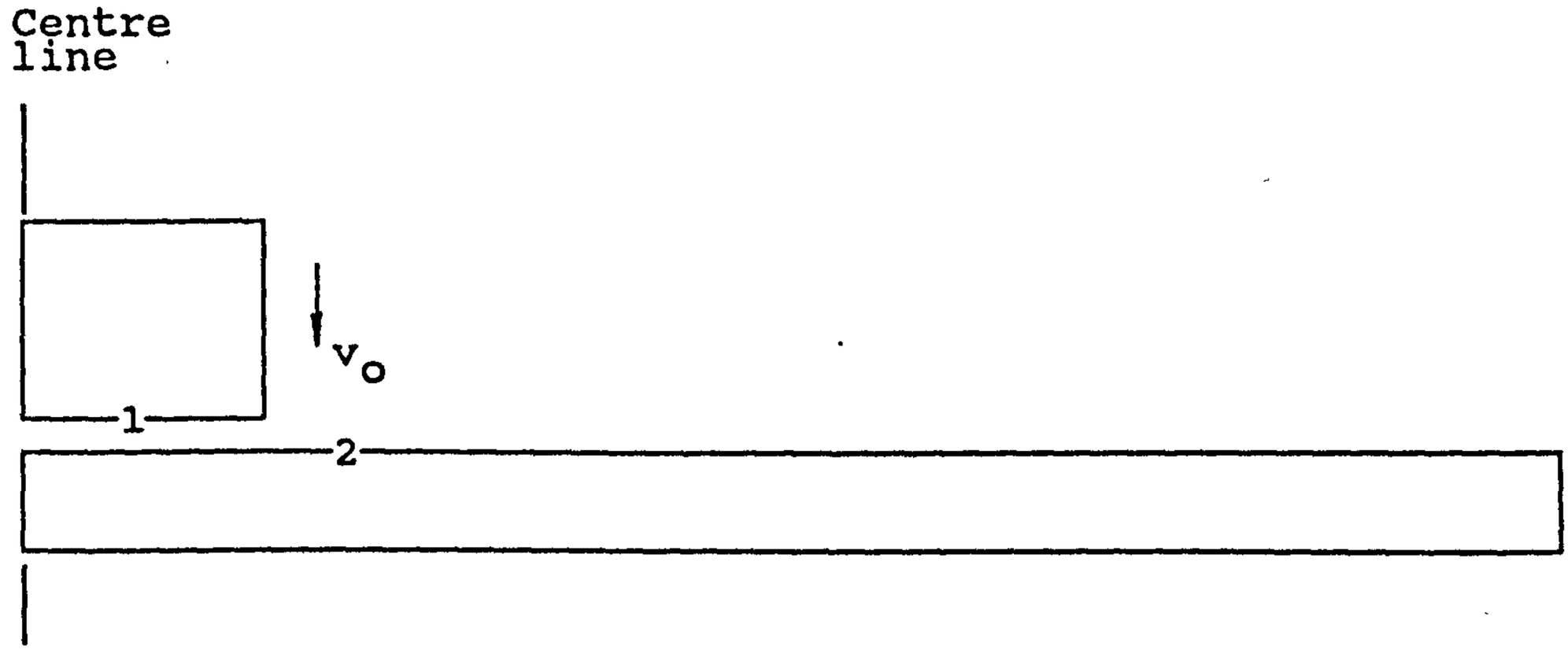

Figure 3.12

Typical slideline configuration for plate impact without perforation

CHAPTER 4

VALIDATION OF THE SLIDELINE TECHNIQUE

4.1 INTRODUCTION

The application of a fast dynamics program as described requires experience to produce a stable solution without an excessive amount of computer time. The current literature has concentrated on the more complex commercial problems and very little information is available concerning the effects of the various user defined parameters on the final solution. In view of this, a number of objectives will be pursued in the following chapter and these are;

(i) The effect of the interface scale factor upon the final solution will be qualitatively evaluated.

(ii) The magnitude of the coefficients to control the hourglassing and spurious oscillatory modes are dependent upon the individual response of each problem and are briefly examined to give some indication of their respective effects.

(iii) The quantitative comparison of the proposed impact solution scheme with experimental or theoretical results for increasingly complex problems will verify its validity.

Seven examples will be considered to demonstrate the effectiveness and generality of the method. The complexity of the impact problem leads to the use of experimental results as a basis of comparison with regard to the three elastic-plastic examples, whilst the remaining four elastic problems use well known analytical solutions.

4.2 ELASTIC BAR IMPACT AGAINST A RIGID WALL

The impact of a linear elastic bar travelling at constant velocity and impinging longtitudinally upon a rigid wall will be considered. This problem is a source of considerable insight into the effectiveness of the slideline computations to resolve the impact and release phenomena by virtue of the constant contact area maintained throughout the solution. The simplicity of both the analytical and numerical solutions readily permits the effects of the bulk viscosity and scale factor to be assessed.

4.2.1 Finite element idealisation

The plane strain finite element discretisation of a bar of length L and depth t, travelling at a constant velocity v_o, is shown in Figure 4.1, together with the relevant dimensions. The bar is modelled with boundary restraints in the lateral direction only. The impact velocity and material properties used are as follows;

$$E = 100.0$$
$$w = 0.01$$
$$\mu = 0.30$$
$$v_o = 10.0$$

The default value, 0.1, for the hourglass coefficient was used.

4.2.2 Theoretical considerations

The longtitudinal impact of a bar in this way has been analysed by means of the one-dimensional wave equation, which postulates a uniform stress distribution across the rod and is achieved here with a ratio of L/t > 50. The contact point is instantaneously brought to rest by the impact from which a step wave of stress σ is produced and propagates through the bar with a velocity c. The magnitude of this wave is given by Goldsmith

(1960) as

$$\sigma = w\, c\, v_o = -11.60$$

where the negative sign indicates a compressive stress. The dilational wave speed c in an elastic material is given by

$$c = \left[\frac{(1-\mu)\ E}{(1+\mu)(1-2\mu)w} \right]^{1/2} = 116.02$$

The wave will be reflected at the free end with an equal amplitude but with opposite phase. The effect of this reflected wave will eventually reduce the stress at the contact point to zero at time t_c, where

$$t_c = \frac{2\ L}{c} = 0.172$$

at which time separation will occur. Figure 4.2 graphically illustrates the progression of a typical wave through a bar.

4.2.3 Results and discussion

Figures 4.3 to 4.5 show the variation of total kinetic energy loss, maximum developed interface force and contact duration time with scale factor Ŧ, respectively. These results have been obtained using both null and default values of the bulk viscosity coefficients, Q_1 and Q_2.

Considering the latter results, it is clear that for all Ŧ, the contact duration and maximum interface force are both overestimated. The contact duration time approaches the theoretical value with increasing Ŧ, having an error of 1% at Ŧ=3.0, whilst the interface force remains essentially constant at 2% above the theoretical value. The interface force behaviour is

largely unaffected because of the elimination of the geometrically nonlinear effects within the contact region.

The tests performed using null values for the bulk viscosity coefficients have been included with the above curves, which clearly show the expected destabilising effects. The particularly pronounced instability in the maximum nodal interface force curve of Figure 4.4 is due to its direct dependence upon the element internal force and, consequently, the artificial pressure. The element derived interface force is observed to behave in a similar oscillatory manner in response to this nodal behaviour. In contrast, the contact duration time is not significantly affected, by virtue of the prior passage of the oscillatory internal force through the integration process associated with the time stepping scheme.

The kinetic energy loss for the default curve, Figure 4.3, indicates a steady rise to a maximum loss of around 5%, whilst the null value curve shows the expected reduction. A stable solution is only possible now, however, within a greatly reduced range of scale factor, Φ = 0.4 to 0.5.

Figures 4.6 to 4.13 depict the same variables but with respect to time. The reduction in time step and the increase in kinetic energy loss with increasing Φ are evident from Figure 4.6, while the further decrease associated with zero values of artificial viscosity is clear from Figure 4.7.

The velocity-time and interface force-time curves of Figures 4.8, 4.10 and 4.12, respectively, indicate a steepening response curve together with an associated magnification of numerical oscillations as the scale factor is increased. The velocity-time curve demonstrates the effect of a wave reflection from the free end at rebound time, for which there is a slight perturbation of the curve, more noticeably for Φ=0.5, occurring as a secondary tensile reflected wave reduces the velocity of the nodes in the impact region immediately after rebound. The significant reduction in the magnitude of this reflection for increasing Φ is

noticeable, and would suggest that the release conditions are more exactly met for higher values of scale factor.

The effect of the elimination of artificial viscosity is shown in Figure 4.9 where the characteristic instability is present in the form of oscillations about the original values.

The interface force may be computed from integration of both the element stresses over their tributary areas or extracted from the slideline routines themselves. Their results are in good agreement but those computed from the interface algorithms appear to give a more rapid response to time varying situations. Again, the destabilising effects of a reduced artificial viscosity are indicated in Figures 4.11 and 4.13.

In all of the time varying graphs a comparison with the theoretical values shows the dispersive effects and the low pass characteristics of the mesh upon the solution. Increasing the scale factor is seen to decrease this effect, albeit at the expense of a certain amount of numerical overshoot, indeed, as would mesh refinement.

It is clear that a stable solution with an adequate degree of accuracy is obtained for all values of scale factor between 0.5 and 3.0. By using large values, the solution approaches that of the given theoretical results, however, this is at a sacrifice to the numerical stability of the results as well as the conservation of energy. The achievement of this balance is at the root of all such analyses performed using this particular technique. The dominating effect of the strain rate in this respect will be noted further in the final discussion.

The 50 element numerical model required 200 time steps to reach 0.225 seconds.

4.3 LONGTITUDINAL IMPACT OF TWO ELASTIC BARS

The impact of two linear elastic bars travelling at equal and opposite, constant initial velocities and impinging upon each

other longtitudinally will be considered. The presentation takes advantage of the simple treatment of the contact region of the previous example but will be extended to include the geometrically nonlinear effects of impact between two independent and flexible bodies.

4.3.1 Finite element idealisation

The 100 element plane strain finite element discretization of the two bars, travelling with velocity v_o, is shown in Figure 4.14, together with the relevant geometry. Each bar is modelled with lateral boundary restraints. The impact velocity and material properties for both bars are as follows;

$$E = 100.0$$
$$w = 0.01$$
$$\mu = 0.30$$
$$v_o = \pm 10.0$$

Both the geometry and the material properties of each bar are identical to those used in the previous section, to enable further comparison. The theoretical considerations are as given in Section 4.2.2. Once again, default values for the hourglass viscosity coefficient were used.

In the following discussion reference will be made to only one of the impacting bars unless otherwise stated, namely that of the initially positively proceeding bar, since their results are identical.

4.3.2 Results and discussion

Figures 4.15, 4.16 and 4.17 show the effect of variations in the scale factor on the total kinetic energy loss, maximum interface force and contact duration. It may be observed that a similar trend to that of the previous example is indicated. A further aspect, however, may be seen in the instability of the solution for values greater than 2.0. This is due to the

occurrence of chatter at the contact interface, and is portrayed most clearly in Figure 4.16 which depicts the variation of the maximum interface forces. The subsequent, violent, changes in nodal velocities within the contact region account for the unstable effects in both kinetic energy and the contact duration time.

The chattering occurs at the interface where the contacting surfaces are repeatedly coming into contact, receiving too great a restraining force and subsequently rebounding from each other, only to be driven back to one another by the accumulated residual force at these times. The effects of chattering may be seen further in Figures 4.19, 4.20 and 4.21.

The reduced range of scale factors permissible with this problem in comparison to the previous example is attributed to the two differing types of boundary condition. Because of the force formulation implemented here it is not possible to bring the contact nodes immediately to rest without recourse to an unreasonably reduced time step throughout the solution. With the rigid wall example the initial contact force will be proportional to the initial depth of penetration (v_o dt), while the current example has an initial depth of penetration of ($2v_o$ dt), yielding twice the initial contact force of the previous example. This large initial force accounts for the fast rise time of the force and velocity for Φ=0.5. However, as Φ increases, the rise time reaches a point at which such a severe change occurs in the velocity and contact force that an oscillatory response ensues from which recovery is never attained. As mentioned before, the situation may be remedied by manually determining a reduced time step, but is not a significant problem since the instability may be detected shortly after the occurrence of impact and the solution restarted with a decreased value of scale factor. Alternatively the artificial coefficients Q_1 and Q_2 may be augmented to handle the oscillations directly. Furthermore, the greater magnitude of the kinetic energy loss for each Φ is also attributed to the differing boundary conditions.

The dispersion of the finite element solution may be seen once again in Figures 4.20 and 4.21 in the form of a finite interface force rise time or similarly in Figure 4.19 in terms of the velocity at the interface element.

Accurate solutions to this problem may thus be obtained with Φ ranging between 0.4 and 1.5, with an optimum value being approximately 1.25.

Again, the model required 200 time steps for a complete solution.

4.4 PLASTIC BAR IMPACT AGAINST A RIGID WALL

When a cylindrical projectile strikes perpendicular to a rigid boundary, a high stress occurs at the projectile impact end. If the stress exceeds the elastic limit of the material, a plastic front moves back into the projectile, while the still elastic portion of the projectile flows into the plastic front, fails by plastic flow, and shortens as material flows radially out. This elastic portion can support stresses no greater than the elastic limit. These stresses, which move between the plastic front and the free end, decelerate the projectile. Thus the rate of retardation is due to the material strength. The greater the strength, the faster the deceleration for a given impact velocity.

A series of experiments were performed to confirm these and other theoretical observations, Wilkins (1973). Only the experimental final lengths of the bars were reported.

4.4.1 Finite element idealisation

The 115 element axisymmetric finite element discretisation of a steel bar of initial length 23.47 mm and diameter 7.62 mm, travelling at a constant velocity of 175 ms^{-1}, is shown in Figure 4.22. Frictionless boundary conditions are used along the contact interface. The material properties refer to 1090 steel in the annealed condition and are given as follows;

$$E = 211 \text{ Gpa}$$
$$w = 7840 \text{ Kg M}^{-3}$$
$$\mu = 0.30$$
$$\sigma_o = 1.2 \text{ Gpa}$$
$$E_t = 1 \text{ Mpa}$$

The default value, 0.1, for the hourglass coefficient was used.

4.4.2 Results and discussion

It is stated in the cited paper that the final cylinder length is very sensitive to the yield strength, and would suggest that the test is a good indicator of the elastoplastic capability as well as demonstrating the effectiveness of the slideline algorithms at higher impact velocities. This problem may be seen as a further extension to the complexity of the bar impact example of Section 4.2, through the inclusion of a velocity dependent contact area. The problem requirements here are particularly stringent, demanding both material and geometric nonlinear capabilities together with those nonlinearities pertaining to the contact region.

The response was again solved with a range of scale factors, but the variation in the computed final lengths, Figure 4.23, was found to be negligible. The final length for the configuration considered herein being 21.55 mm. The computational error in this result amounts to an overestimate of the final length by 0.7% and represents a very reasonable result in the light of the rather coarse mesh used in this analysis. In this example, the dominant deformation response is that of plastic flow which permits a lower spatial resolution since the propagation of such waves is generally an order of magnitude slower than the corresponding elastic wave front.

Figure 4.24 depicts the more discernible variations in the contact duration time. Although no experimental results are

available for this parameter, it would appear that a similar response to that of the previous examples is experienced, in spite of the highly nonlinear behaviour now included in the solution within the contact region.

A further result was obtained using identical bar geometry and material properties but for an initial velocity of 252 ms^{-1}, and in conjunction with a scale factor of 0.1. A numerical final length of 19.89 mm was obtained in comparison with the experimental final length of 19.76 mm, and represents a similar computational overestimate of 0.7%. The two results obtained here are compared with the series of experimental results in Figure 4.25 and show a good agreement in the limited range covered.

The effects of the decrease in element dimensions in the impact region is an important factor in the selection of a proper time integration scheme, since the automatic time step computations are essentially based upon the smallest of these dimensions. Figures 4.26 and 4.27 depict the final deformation patterns for the initial velocities of 175 and 252 ms^{-1} respectively and demonstrate admirably the considerable deformation experienced by the elements during the solution. A graph of the accumulated time step for each solution is shown in Figure 4.28 which clearly depicts the tremendous increase in computational effort experienced, particularly note that the reduction in time step occurs at a very early time. The ratio of the initial time steps to those at the moment of rebound are given in Table 4.1.

The impact response means that the number of time steps required to solve a problem of this type are significantly increased, for the latter example a threefold increase in computational steps is necessary (from 400 to the actual value of 1100). The use of an implicit scheme independent of the effects of changes in element dimension would be a tempting alternative in this problem, particularly for the higher initial impact velocities. A similar problem has been encountered by Stronge (1981) in his investigation of the deformation of soft

projectiles against steel plates.

The high degree of material plasticity is indicated in the effective plastic strain contours given in Figure 4.29 for the highest initial velocity solution.

4.5 ELASTIC SPHERE IMPACT AGAINST A RIGID WALL

Hertz incorporated a theory of local indentations in a solution scheme which is able to yield analytical solutions for the case of a elastic spheres impacting both, other spheres or plane rigid walls, Lubkin (1962). This scheme has met with a considerable degree of success when used within the inherent assumptions. Moreover, even outside of these limits, the solution scheme has given accurate predictions for most of the experimentally available parameters.

This problem is of interest here because it is one of the few three dimensional impact problems for which there exist analytical information. Despite the fact that the body is governed by both linear elasticity theory and small deformation/rotation considerations, this is a bona fide nonlinear problem in which the contact area is a function of the current velocity.

4.5.1 Finite element idealisation

Figure 4.30 shows the sphere of radius 5, having an initial velocity of 3.0 together with the rigid wall in the initial configuration. The impact velocity and material properties of the sphere are as follows;

$E = 1000.0$

$w = 0.01$

$\mu = 0.30$

$v_o = 3.0$

The hourglass viscosity was set to the default value of 0.1.

4.5.2 Theoretical considerations

Consider a sphere of radius R and mass M, having an initial velocity of v_o, colliding with a rigid wall. We have, Goldsmith (1960);

$$P = n\ \alpha^{3/2}$$

where P is the interface compression force, n is a constant and α is the compression of the sphere. If

$$k = \frac{1 - \mu^2}{\pi E} = 0.00029$$

and

$$n = \frac{4\ R^{1/2}}{3\pi k} = 3276.29$$

then α_m, the maximum compression experienced by the sphere is

$$\alpha_m = \left[\frac{15\pi\ M\ k\ v_o^2}{16\ \sqrt{R}} \right]^{2/5} = 0.200$$

which gives the maximum compressive force as

$$P_m = n\ \alpha_m^{3/2} = 293.93$$

Finally, the contact duration time is given as

$$t_c = 4.530 \left[\frac{k\ M}{\sqrt{(R\ v_o)}} \right]^{2/5} = 0.1964$$

4.5.3 Results and discussion

The solutions were carried out for variations in Φ from 0.1 to 3.0 to evaluate the effects within a two dimensional axisymmetric problem. The contact duration time variation of Figure 4.31 demonstrates a similar response to that of examples 4.2 and 4.3 in that convergence to a stiffer type of behaviour is quickly achieved. In contrast to the rigid wall solution of example 4.2, however, the exact response is achieved for Φ=0.85.

The magnitude of the two derived contact forces, shown in Figure 4.32, initially demonstrates a rapid increase which gradually reduces to a constant value. This is in contrast to the wholly constant response obtained in the elastic bar impact, principally due to the inclusion of nonlinearity into the solution process through a time varying contact area.

The error for both the maximum contact force and the contact duration time is of the order of 5% at Φ=3.0 and represents a good response evaluation.

The kinetic energy loss variation given in Figure 4.33 demonstrates losses an order of magnitude less than that for the elastic bar examples. The variation has a similar trend to that of the previous elastic bar examples in which the loss increases with scale factor. The perturbations are due to the vibratory effects of the sphere subsequent to rebound, making an accurate determination of the final kinetic energy difficult.

The variation of kinetic energy with time shown in Figure 4.34 indicates a smooth response together with the expected small final loss. The minimum value of total kinetic energy is reached at half the contact duration time and is therefore attained sooner with increasing Φ. Note that the values given in Figures

4.33 and 4.34 are with respect to a radian segment.

As before, the element derived contact forces lag behind those developed from the contact algorithms in their response, Figures 4.35 and 4.36.

The small deformation effects in this problem do not affect the time step computation markedly. A total of 1700 time steps were required to solve the 84 element model.

4.6 LONGTITUDINAL IMPACT OF TWO ELASTIC SPHERES

The problem of the impact of two elastic spheres travelling at constant, equal and opposite velocities will be considered next. As in the elastic bar impact examples, the capability of the slideline routines to handle impact between two independent bodies and the comparison with the rigid wall solution is of interest here. Similarly, this is a truly nonlinear problem in which the contact area is a function of the current velocity.

4.6.1 Finite element idealisation

Figure 4.37 shows the spheres of radius 5, having initial velocities of ±3.0 in the initial configuration, while Figure 4.38 depicts a portion of the 144 element discretisation in the contact region. The material properties of the spheres are as follows;

$$E = 1000.0$$
$$w = 0.01$$
$$\mu = 0.30$$

The hourglass viscosity was set to the default value of 0.1.

4.6.2 Theoretical considerations

Consider two spheres of radius R and of mass M colliding, both having initial velocities of v_o. We have

$$P = n\ \alpha^{3/2}$$

where P is the interface compression force, n is a constant and α is the relative compression of the two spheres. If

$$k = \frac{1 - \mu^2}{\pi E} = 0.00029$$

then

$$n = \left[\frac{2\ R}{9\pi^2 k^2} \right]^{1/2} = 1156.993$$

and α_m, the maximum relative compression of the two spheres is

$$\alpha_m = \left[\frac{5}{4n\ n_1} (2v_o)^2 \right]^{2/5} = 0.4010$$

where

$$n_1 = \frac{2}{m} = 0.3820$$

which gives the maximum compressive force as

$$P_m = n\ \alpha_m^{3/2} = 293.93$$

Finally, the contact duration time is given as

$$t_c = \frac{1.47\ \alpha_m}{v_o} = 0.1964$$

4.6.3 Results and discussion

The variation of kinetic loss with Φ is shown in Figure 4.39 and indicates the typical response expected, that is, increasing energy loss with scale factor. The loss appears to reach a limit of approximately 0.9% at Φ=3.0. There is no increase in loss over the rigid wall calculations, as seen in the elastic bar examples.

The contact duration and maximum interface force variations, Figures 4.40 and 4.41, again indicate the typical convergent response as Φ is increased together with the stiffer response associated with the contact of two flexible solids. The optimum value here is Φ=0.5 to yield accurate contact duration times and maximum interface force values. Note the absence of chattering in this problem and the large range of values of Φ for which adequate solutions may be obtained. Notice also the negligible difference in the two numerical interface force curves.

The minimum value of Φ to achieve a solution without the bodies passing through one another was of the order of 0.1, whilst example 4.2 gave a value of 0.5. This threshold magnitude of scale factor is important in the determination of Φ for a given problem. For example, both the initial velocity and critical time step of the former example were smaller than that of the latter and as a consequence, the displacement increments were initially significantly greater, requiring the use of a augmented Φ.

Figure 4.42 shows the typical kinetic energy response in the time domain with the associated shift towards the origin as Φ is increased. Due to the limited variation in maximum interface force the curves of Figures 4.43 and 4.44 are practically identical.

Finally, an equal number of time steps were required to that of the previous problem (1700).

4.7 IMPULSIVE LOADING OF AN ELASTIC-PLASTIC BEAM

This example involves the prediction of the response of a doubly built-in beam subject to an initial explosive load at its midspan. This is an experiment which is commonly performed to study structural response at high strain rates. The problem exhibits considerable geometric nonlinearity, because the doubly built-in configuration causes the initial bending response to become dominated by membrane effects as soon as displacements of the order of the beam thickness occur. In the actual experiment the motion is initiated by a constant impulse per unit length of the beam caused by detonating a uniform sheet of explosive, so that a constant initial velocity is imparted to that part of the beam to which the explosive is bonded. Thus a certain kinetic energy is provided initially, and this must be matched in the discrete finite element model. This example essentially represents a test of the explicit formulation without the inclusion of contact interface conditions. The problem has experimental results available for the midspan transient displacement and also incorporates material nonlinearity, Wu and Witmer (1971).

4.7.1 Finite element idealisation

Figure 4.45 shows the beam of length 254 mm and depth 3.175 mm, impulsively loaded with a velocity of 127 ms^{-1} over a centre segment of 50.8 mm. The width of the beam is 30.48 mm and so the analysis is essentially one of plane strain. The beam is fully fixed at both its extremities. The material properties of the beam refer to 6061-T6 aluminium and are as follows;

$E = 71.7E9\ Nm^{-2}$

$w = 2770\ Kgm^{-3}$ (assumed)

$\mu = 0.3$

$\sigma_o = 295E6\ Nm^{-2}$

$E_t = 543E6\ Nm^{-2}$

4.7.2 Results and discussion

The transient displacement results obtained from the current finite element model are given in Figure 4.46, together with the experimental values. The predictions follow the general trend of the experimental results, in the sense that the peak displacement value and the time at which it occurs are reasonably well matched, but the analysis does not predict the detailed response particularly closely. This is not uncommon in cases like this, and many explanations may be offered, ranging from poor modelling of boundary conditions (the fully restrained end condition is difficult to achieve experimentally, but is critical to the membrane stiffening that plays a primary role in determining the response) to the simplicity of the material and geometry models assumed for the analysis, Neilson (1983). In spite of the lack of detailed agreement, the results clearly provide information that is useful in a design environment.

A series of deformed plots are given in Figure 4.47 for completeness, where the transient wave effects may clearly be seen traversing the bar.

4.8 CYLINDRICAL PROJECTILE IMPACT ON A THIN PLATE

Following the initial survey calculations, the impact of a cylindrical steel, blunt faced, projectile against a square steel plate will be considered, in anticipation of the calculations contained in the subsequent chapters. Once again, the problem will tax the capabilities of the current code capabilities in modelling the high degree of nonlinearity present. The results used have been taken from a series of recent experiments carried out at City University, Hallett (1988).

4.8.1 Finite element idealisation

Figure 4.48 shows the undeformed mesh, the 48 elements of which are modelling a 5.111 mm thick plate, 600 mm square, together with the 40 mm diameter projectile of mass 40.5 Kg

travelling at an initial velocity of 6.97 ms^{-1}. Frictionless interface conditions are assumed. The material properties for both target and projectile are given as

$$E = 211E9\ Nm^{-2}$$
$$w = 7765\ Kgm^{-3}$$
$$\mu = 0.3$$
$$\sigma_o = 280E6\ Nm^{-2}$$
$$E_t = 690E6\ Nm^{-2}$$

Together with the default values for the artificial viscosity and hourglass coefficients.

The limited availability of computer time restricted the projectile modelling to a rather simplified form, in which the length dimension was decreased to permit the use of fewer elements yet maintaining the total mass by a corresponding increase of the material density. The assumption is valid in such cases where the projectile deformation is negligible and any wave propagation effects are insignificant. That this is reasonable has been discussed previously by Goldsmith et al (1965).

4.8.2 Theoretical considerations

The effect of modelling non-circular plates axisymmetrically has been discussed by Neilson (1980) and for very low velocity impact problems ($v_o < 14\ ms^{-1}$) it is concluded that these effects are not significant if a corrected plate diameter is utilised, based on a simple equivalent elastic stiffness calculation. Furthermore, the plate impact experiments conducted by Hallett (1987) only serve to substantiate this observation.

For elastic plates under central point loadings, the maximum deflection δ_{max} is given by an equation of the form

$$\delta_{max} = \alpha\ a^2\ \frac{P}{D}$$

where P is the load, a is the plate dimension and D is the flexural rigidity given as

$$D = \frac{Eh^3}{12(1-\mu^2)}$$

h being the plate thickness. For clamped circular plates of diameter a, α=0.00497, and for square plates side a, α=0.0056. For equality of plate stiffness therefore;

$$\alpha_s a_s^2 D_s = \alpha_c a_c^2 D_c$$

where subscripts s and c represent parameters with respect to the square plate and the circular plate respectively. The equivalent diameter to represent a square plate if both plates have the same material properties and are equally thick is

$$a_c = (\alpha_s / \alpha_c)^{1/2} a_s$$

The actual dimensions of the plate are 600 mm x 600 mm, hence, from the above, the diameter of the equivalent circular plate will be 636.90 mm.

4.8.3 Results and discussion

A comparison between the numerical and experimental central displacements of the plate and the deflection of the blunt surface of the projectile are given with respect to time in Figure 4.49. The correlation in both cases is good. Note the void which almost immediately appears between the projectile and plate along the axis of symmetry, a feature commonly found in thin plate impact experiments (see for example Neilson (1983)). The maximum displacement of the target at the centreline was computed as 26.87 mm at 5.83 s in comparison with the experimental values of 27.6 mm at 5.47 s and represents errors of 3% and 7% respectively. A series of deformation plots are given in Figure

4.50.

The effects of transient material response is thus treated adequately, albeit within a low velocity regime. The solution required 36000 time steps to attain 11 ms and is generally more efficiently treated within an implicit solution scheme, and demonstrates the limiting nature of the Courant stability limit in explicit methods for problem types consisting of thin plates.

The dominant membrane response of the plate in this example permitted the use of few elements through the thickness, but even so, the magnitude of the time step was still approximately 0.33 μs. Therefore, responses for which the transient behaviour is required at times greater than 5 ms generally represent prohibitively expensive solutions. For instance, the time for each increment in this particular problem is 5.28 s and gives a solution time of 26 hours to 5 mS on the Vax 11-750 used in these tests, an unrealistic computer usage for the majority of impact code users.

The default value of the hourglass viscosity coefficient restrained any excitation to insignificant levels even within the immediate contact region, It is clear that the hourglass method of control is capable of simulating a membrane dominated response with few elements if only the global displacements are required. Obviously, the number of elements through the thickness would increase the accuracy of any stress results required.

4.9 CONCLUSIONS

The penalty-based slideline method has been applied to a number of impact problems and comparisons made with existing theoretical or analytical solutions. The problems have been selectively chosen to incorporate an increasing amount of nonlinearity and permit, to some degree, a segregation of the numerous facets of this form of solution scheme. The results have been in good agreement.

Extensive work is currently taking place in several British institutions such as; British Nuclear Fuels, Monks (1987); The United Kingdom Energy Authority Establishment, Andress (1987) and The National Nuclear Corporation, Salih (1987), to validate the effectiveness of the explicit impact codes available. The lack of available transient data is being a serious handicap to this process and is driving these centres to generate the required results internally. As a result similar problems are being tackled with little helpful communication of results and the subsequent slow progress of this subject area. These results, although of a rudimentary nature, have not been made available before and will hopefully enable a greater understanding, particularly in the choice of both material and slideline parameters.

The use of such codes to solve the impact problem is neither straightforward nor inexpensive. It is clear that a good understanding of the code as well as experience in the choice of the various coefficients is of paramount importance. In no way can these type of codes be treated as 'black boxes'. In conclusion, therefore, a number of points can be made;

(i) The effects of $\dot{\varepsilon}$ on the contact duration time may be explained in terms of the strain rate magnitude, for it is clear that greater scale factors lead to higher initial compressive strain rates in the elements at the point of contact.

The critical time step is modified to account for the increase in pressure due to the artificial bulk viscosity technique, Equation 2.24. Since the value of this pressure is dependent upon the strain rate, an increase in scale factor will give a subsequent decrease in the critical time step. The energy loss associated with the use of artificial viscosity may also be seen to increase with the scale factor, but the overall effect on the accuracy of the solution is small.

(ii) The interface force developed is similarly affected by changes in scale factor, particularly for $\Phi<1.0$, since the problem actually converges upon a slightly different solution in which there is a certain amount of surface overlap. The shape of the curve is due to the nonlinear dependency of the penetration distance upon the scale factor.

(iii) The typical variation of contact duration time with scale factor is independent of impact velocity for the range of Φ considered here.

(iv) For rigid wall impact, a scale factor of greater magnitude is required than that for the flexible body contact, to take account of the reduced penetration distance. The essential effect of this type of boundary condition is, therefore, to artificially increase the interface stiffness.

(v) Rigid wall impact by the elastic or elastic-plastic materials considered here appears to require scale factors of the order of unity for convergence to the correct solution. This requirement, however, is not so important when dealing with problems in which there is limited contact nonlinearity. i.e. the contact area is not a function of velocity.

(vi) Flexible body impact has been shown to provide a greater initial interface force than rigid wall impact and as such requires a slightly reduced scale factor for convergence, typically of the order of 0.5. It is noted that the permissible range of the scale factor is reduced and that chattering of the interface occurs more readily.

(vii) The disadvantage of a solution depending upon both the correct selection of an appropriate scale factor and the iterative procedure often necessary to achieve this is understood. Nevertheless, an acceptable accuracy of ±5% is attainable for most problems using scale factors between 0.1 and 2.0. The fundamental problems considered here have indicated that the most likely form of problem for flexible body impact is the generation of an insufficiently large interface force such that colliding bodies pass through one another. In this event, the detection may be very simply achieved and the solution halted to prevent any further waste of computer resources, in this way the turnaround time may be reduced to a matter of minutes.

(viii) The penetration of the contact nodes within adjacent bodies is seen to be very limited from the maximum deformation plots given.

(ix) The inclusion of automatic void opening and closing has been shown to have considerable advantages, particularly when large relative deformations at the interface are present. The solution scheme is able to make the required adjustment without recourse to any predetermined contact positions and will represent the physical behaviour well, according to the degree of mesh refinement and the accuracy of the material characterisation.

(x) There is sufficient indication in these examples to show that the plastic behaviour of the material requires much attention by the analyst, particularly in any late time responses required. The addition of failure response in the study of plugging failure will be seen to have a significant effect on the numerical results, particularly in dealing with thin plates.

(xi) The energy losses which are expected from the presence of artificial viscosity have been shown to be small, and for the solutions described above, the loss amounted to no more than 5%. In fact a typical value for a truly nonlinear contact problem is an order of magnitude smaller than this.

(xii) The choice of artificial viscosity coefficients appears to effect the range of scale factors which yield a reasonable solution. A lowering of the magnitude of these parameters is shown to produce numerical oscillations in the solution, which is manifest in interfacial chattering. With the appropriate value of scale factor, the default magnitudes of these parameters has been found an adequate controlling influence.

4.10 REFERENCES

Andress, J.C. (1987). 'An Example of Validation of DYNA3D for Nuclear Plant Accident Assessment', DYNA3D User Group Conference, London.

Goldsmith, W. (1960). 'Impact - The Theory and Physical Behaviour of Colliding Solids', Edward Arnold, London.

Hallett, N. (1987). 'Large Deflection Impulsive Loading of Plates', PhD Thesis Dissertation, City University, London.

Lubkin, J.L. (1962). 'Handbook of Engineering Mechanics',McGraw-Hill Book Company, Flugge, W. (Editor).

Monks, G.W. (1987). 'Collapse of Lateral and Toroidal Tubes', DYNA3D User Group Conference, London.

Neilson, A.J. (1980). 'Missile Impact on Metal Structures', Nucl. Energy, Volume 19, Number 3, pp 191-198.

Neilson, A.J. (1983). 'A DYNA3D Calculation for Impact on a Pipe Target', Safety and Engineering division, AEE Winfrith, Report Number AEEW-M2058.

Salih, M.S.H. (1987). 'Use and Testing of DYNA3D at NNC', DYNA3D User Group Conference, London.

Stronge, W.J. and Schulz, J.C. (1981). 'Projectile Impact Damage Analysis', Comput. Struct., Volume 13, pp 287-294.

Wilkins, M. (1973). 'Impact of Cylinders on a Rigid Boundary', J. Appl. Phys., Volume 44, Number 3 pp 1200-1206.

Wu, R.W.H and Witmer, E.A. (1971). 'Finite Element Analysis of Large Elastic-Plastic Transient Deformations of Simple Structures', AIAA J., Volume 9, Number 9, pp 1719-1724.

TABLE 4.1

Comparison of time step magnitudes for the impact of an elastic-plastic bar against a rigid wall

Impact velocity m/s	Initial time step (t_1) s	time step at max. deformation (t_2) s	Ratio of t_2 to t_1
175	0.7949E-7	0.5E-7	0.629
252	0.7949E-7	0.2E-7	0.252

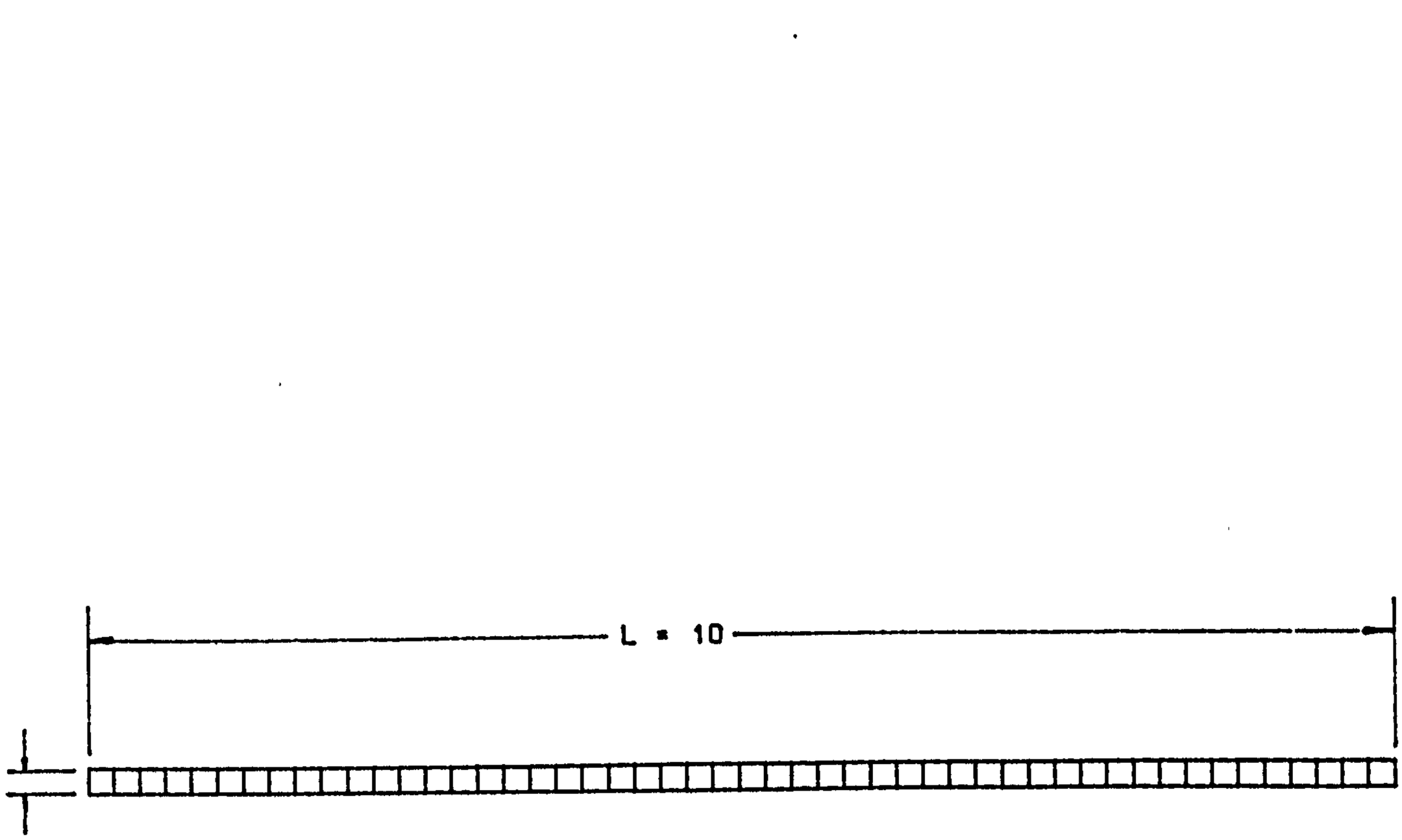

Figure 4.1
Finite element discretisation for the impact of an elastic bar against a rigid wall

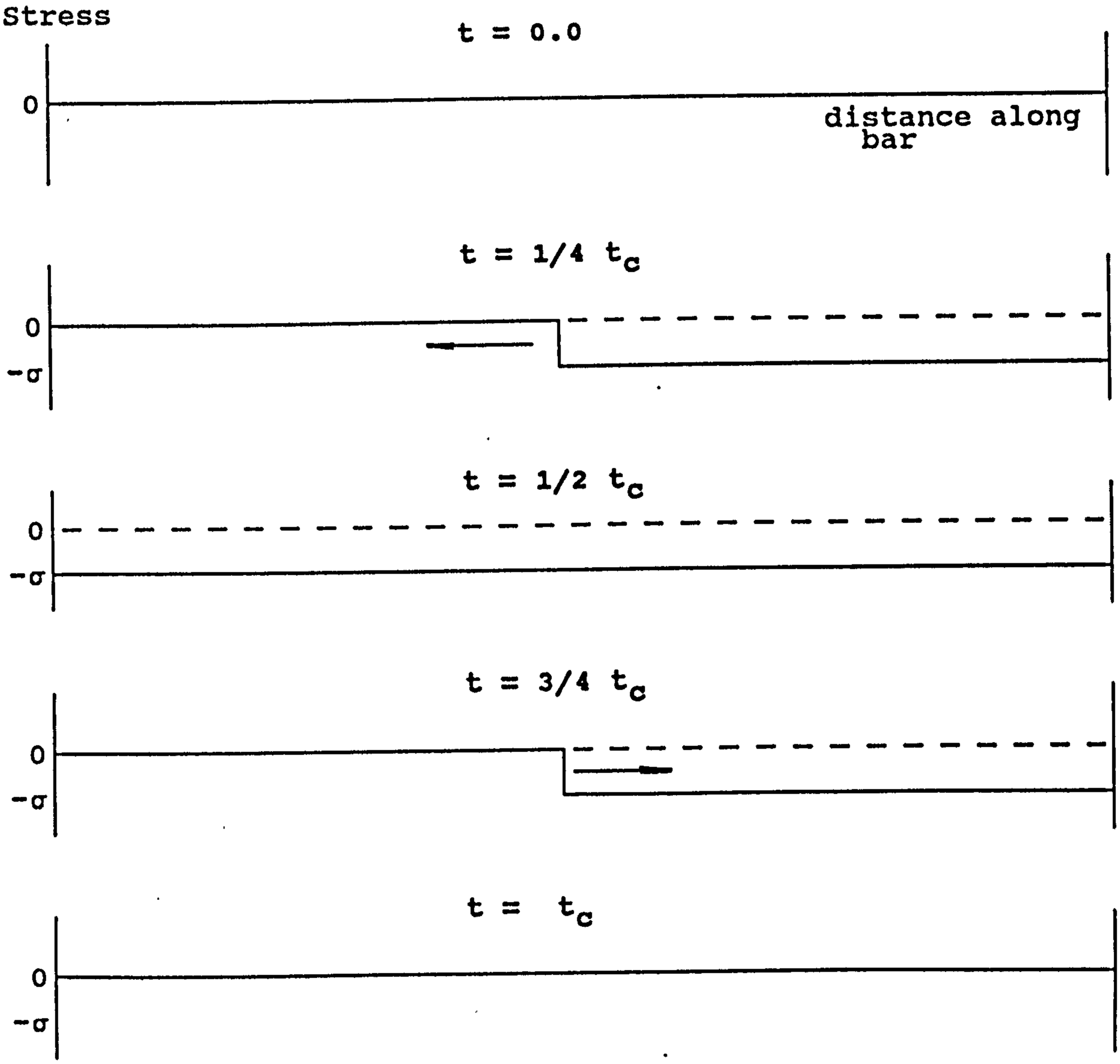

Figure 4.2
Progression of a longtitudinal stress wave in an elastic bar

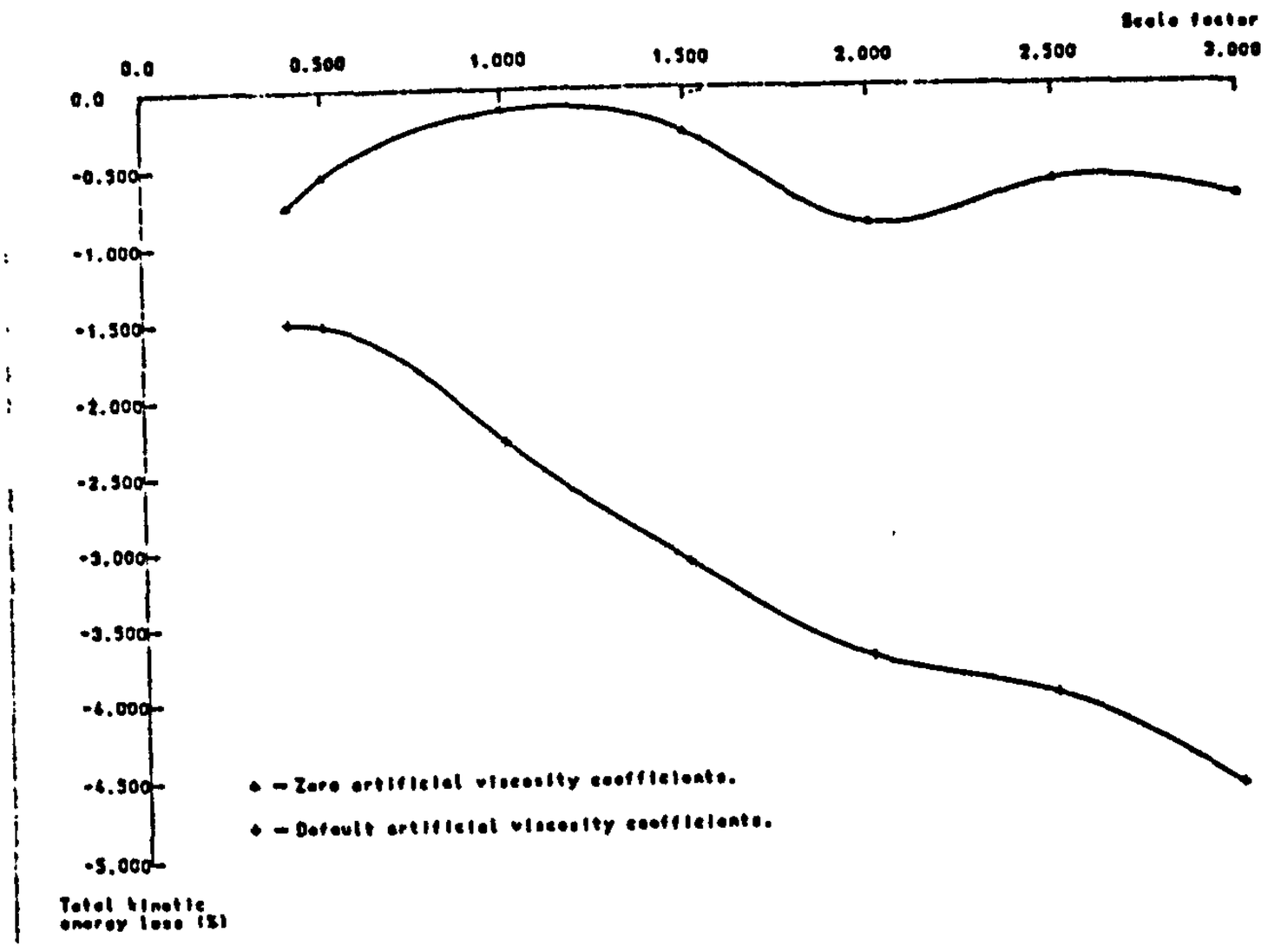

Figure 4.3

Total kinetic energy loss versus scale factor for the impact of an elastic bar against a rigid wall

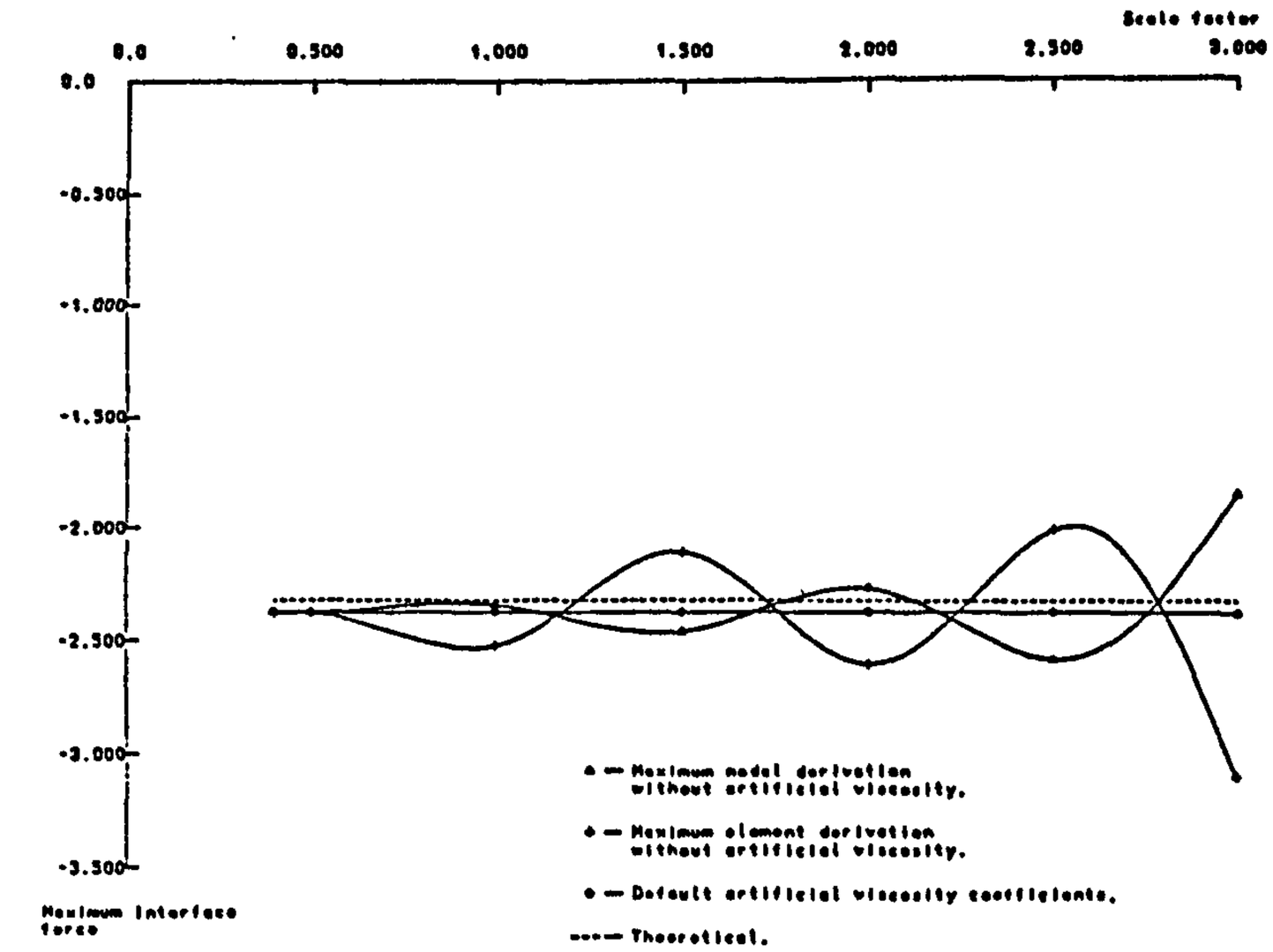

Figure 4.4

Maximum developed interface force versus scale factor for the impact of an elastic bar against a rigid wall

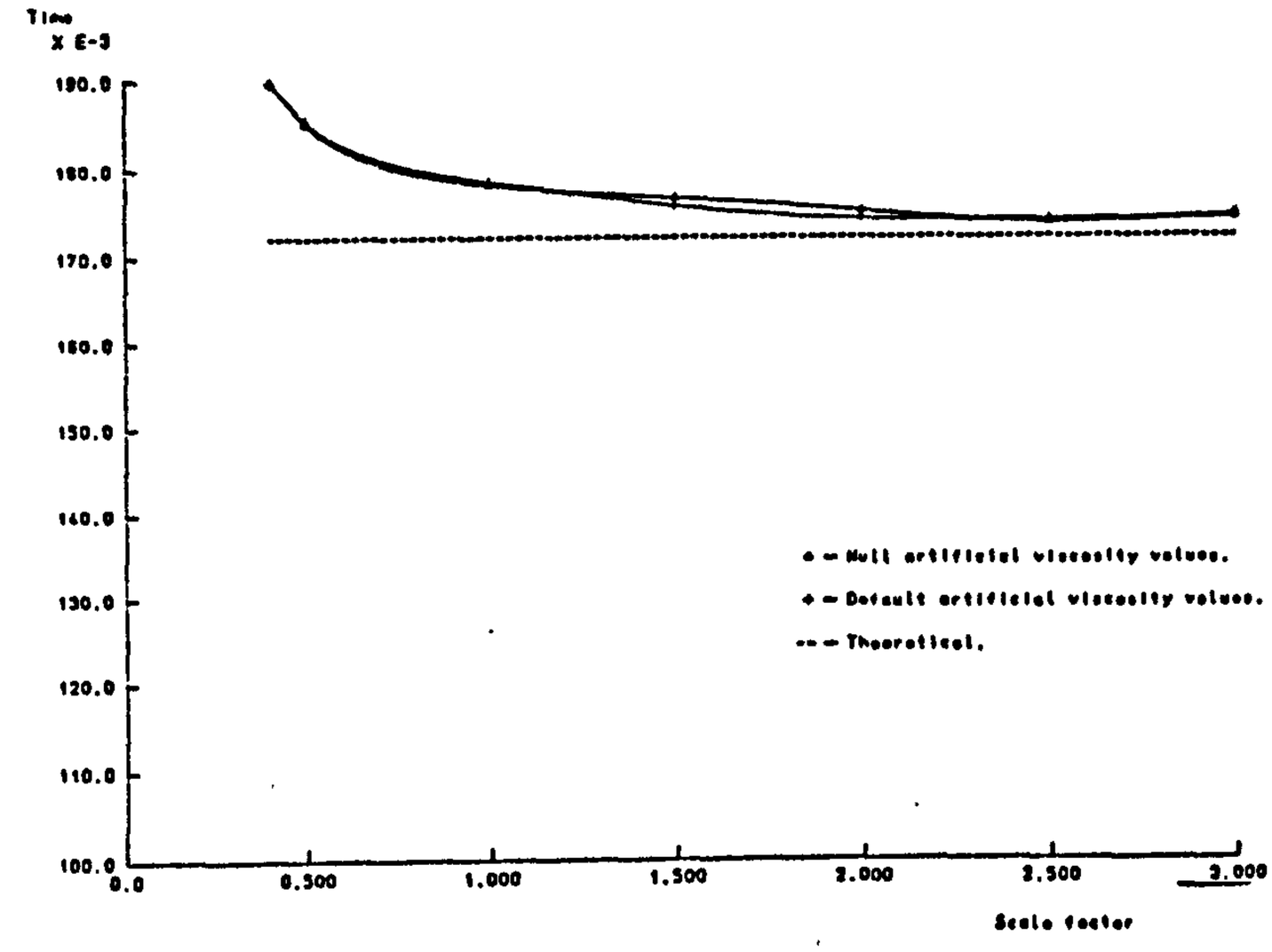

Figure 4.5

Contact duration time versus scale factor for the impact of an elastic bar against a rigid wall

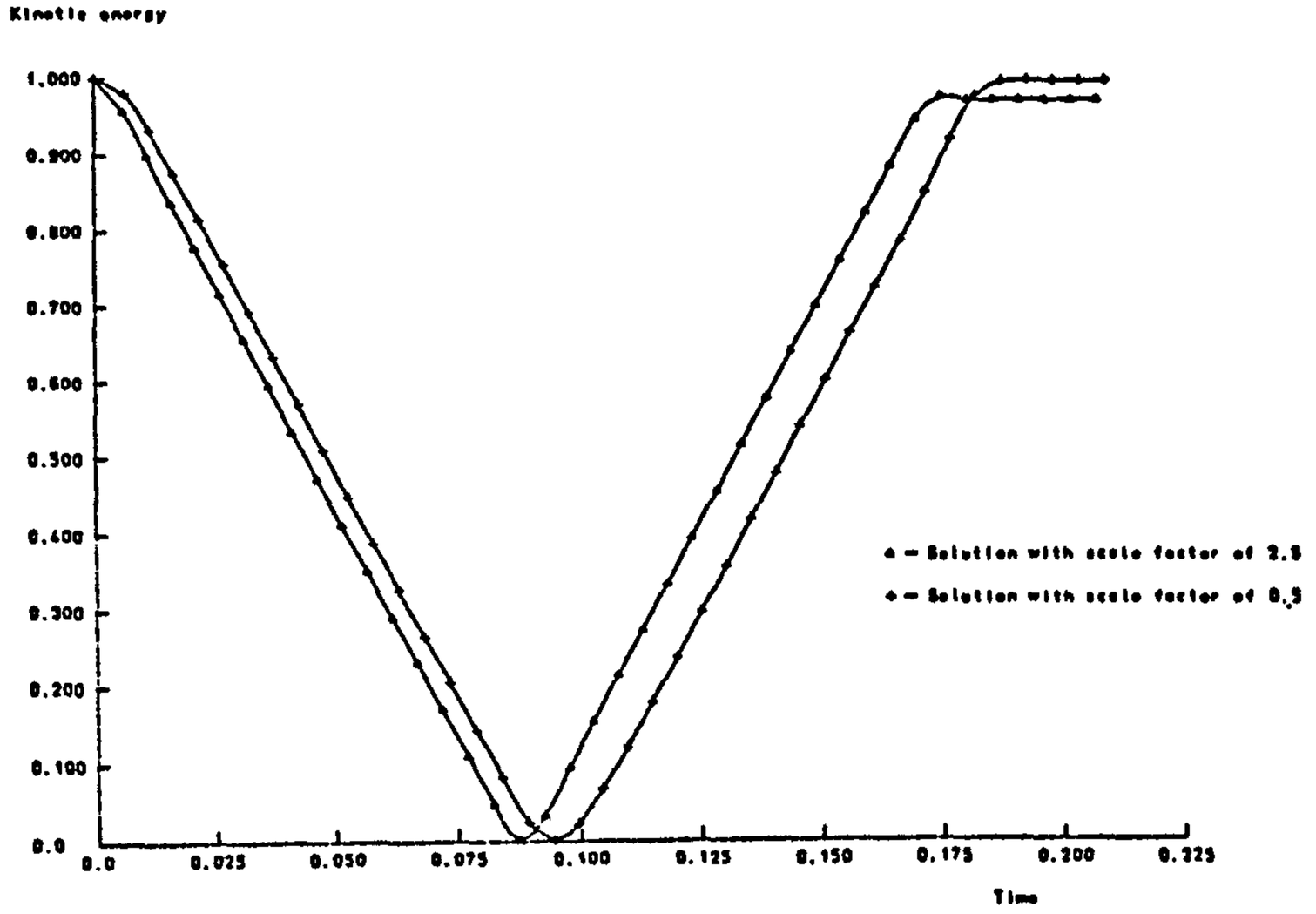

Figure 4.6

Variation of kinetic energy loss with time for the impact of an elastic bar against a rigid wall using default values of the artificial viscosity coefficients

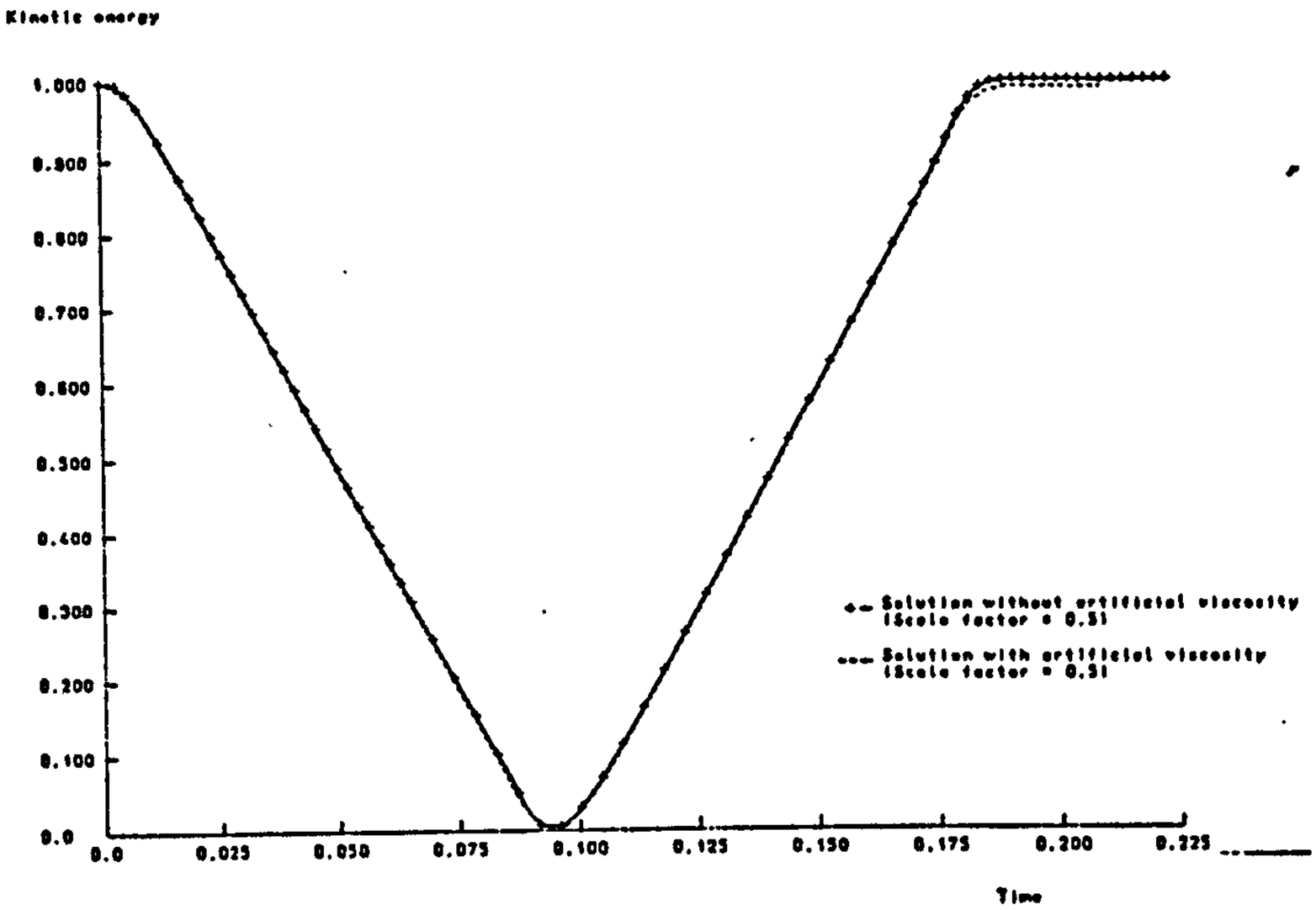

Figure 4.7

Variation of kinetic energy loss with time for the impact of an elastic bar against a rigid wall using null values of the artificial viscosity coefficients

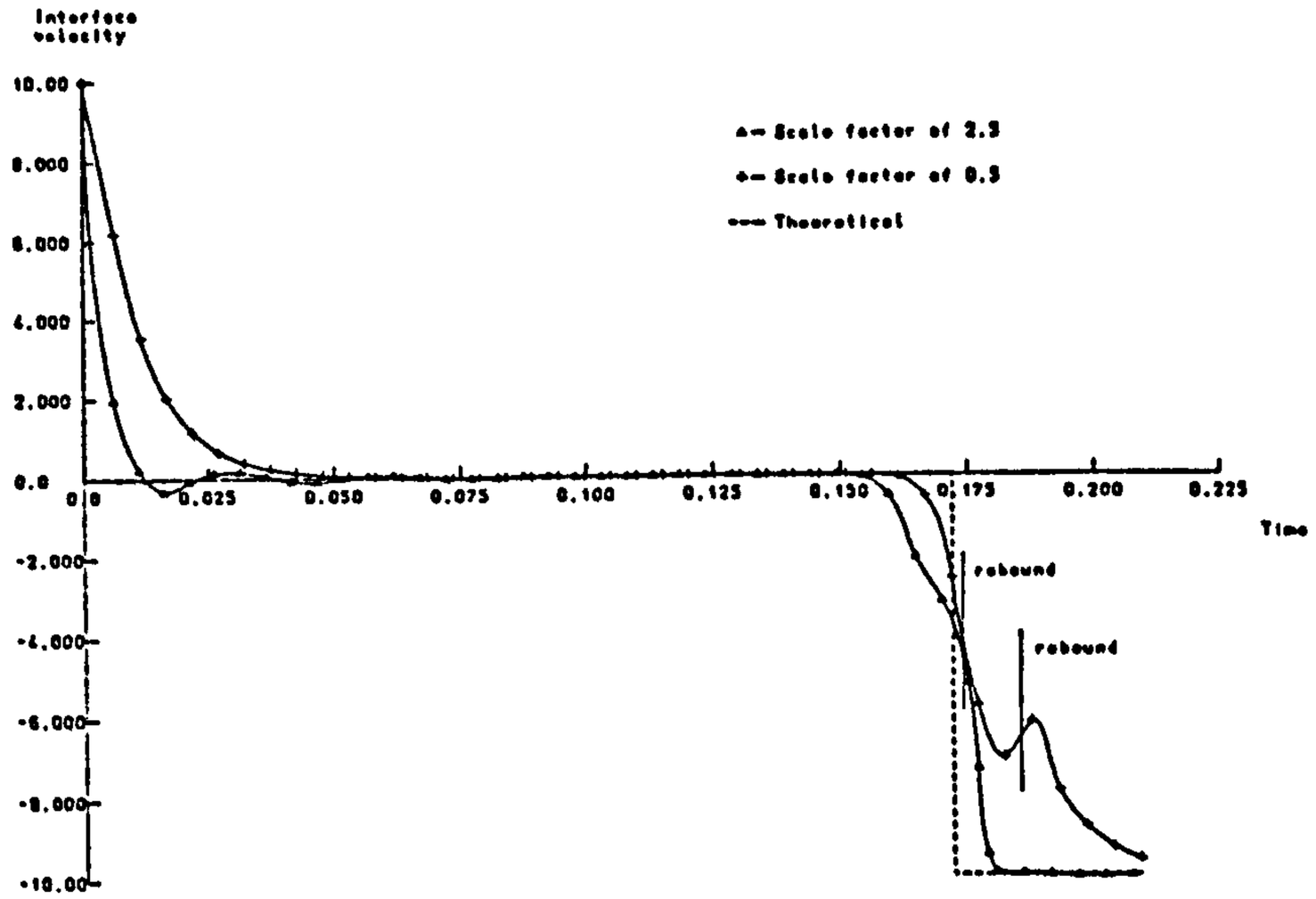

Figure 4.8

Variation of interface velocity with time for the impact of an elastic bar against a rigid wall using default values of the artificial viscosity coefficients

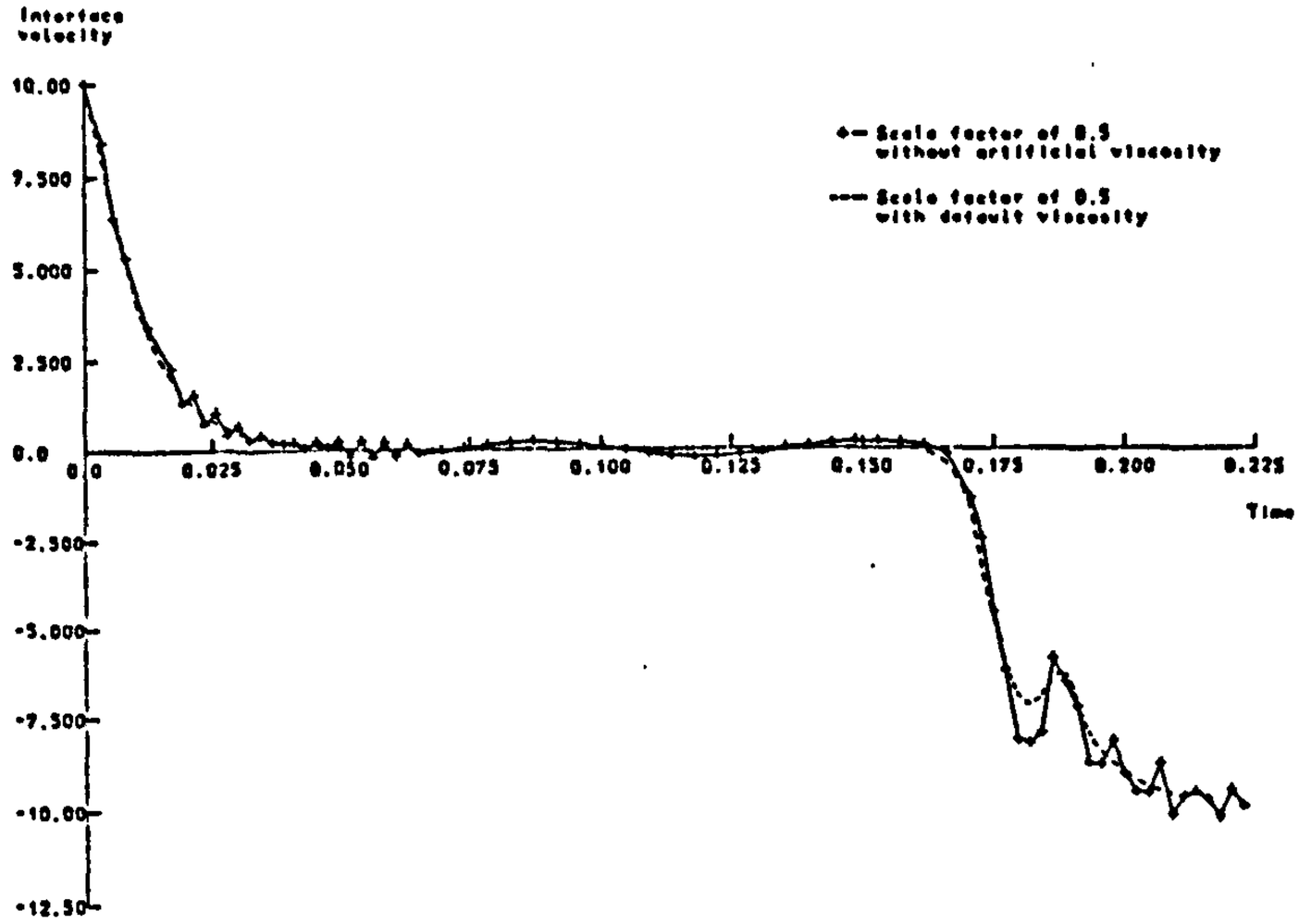

Figure 4.9
Variation of interface velocity with time for the impact of an elastic bar against a rigid wall using null values of the artificial viscosity coefficients

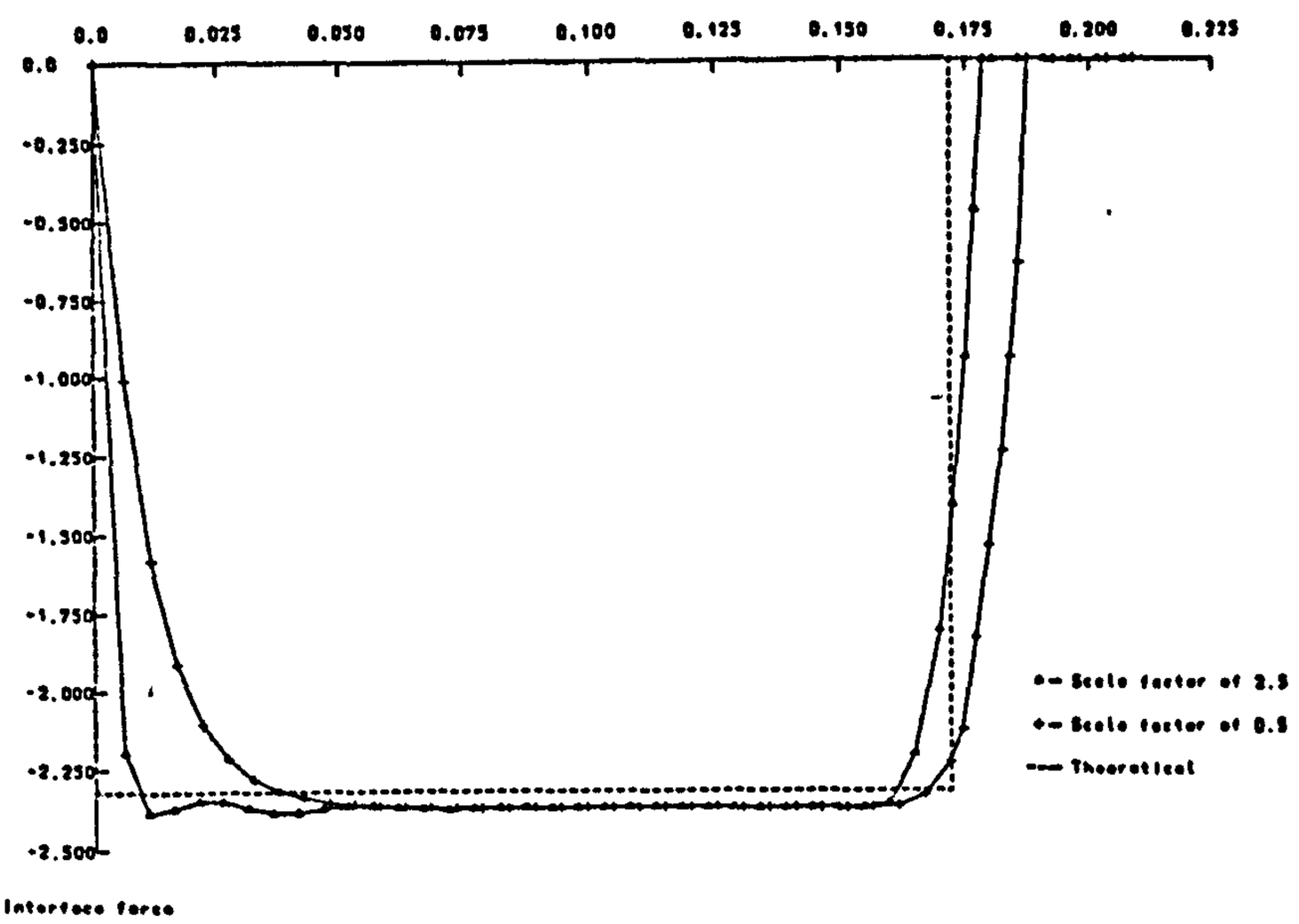

Figure 4.10
Variation of nodal interface force with time for the impact of an elastic bar against a rigid wall using default values of the artificial viscosity coefficients

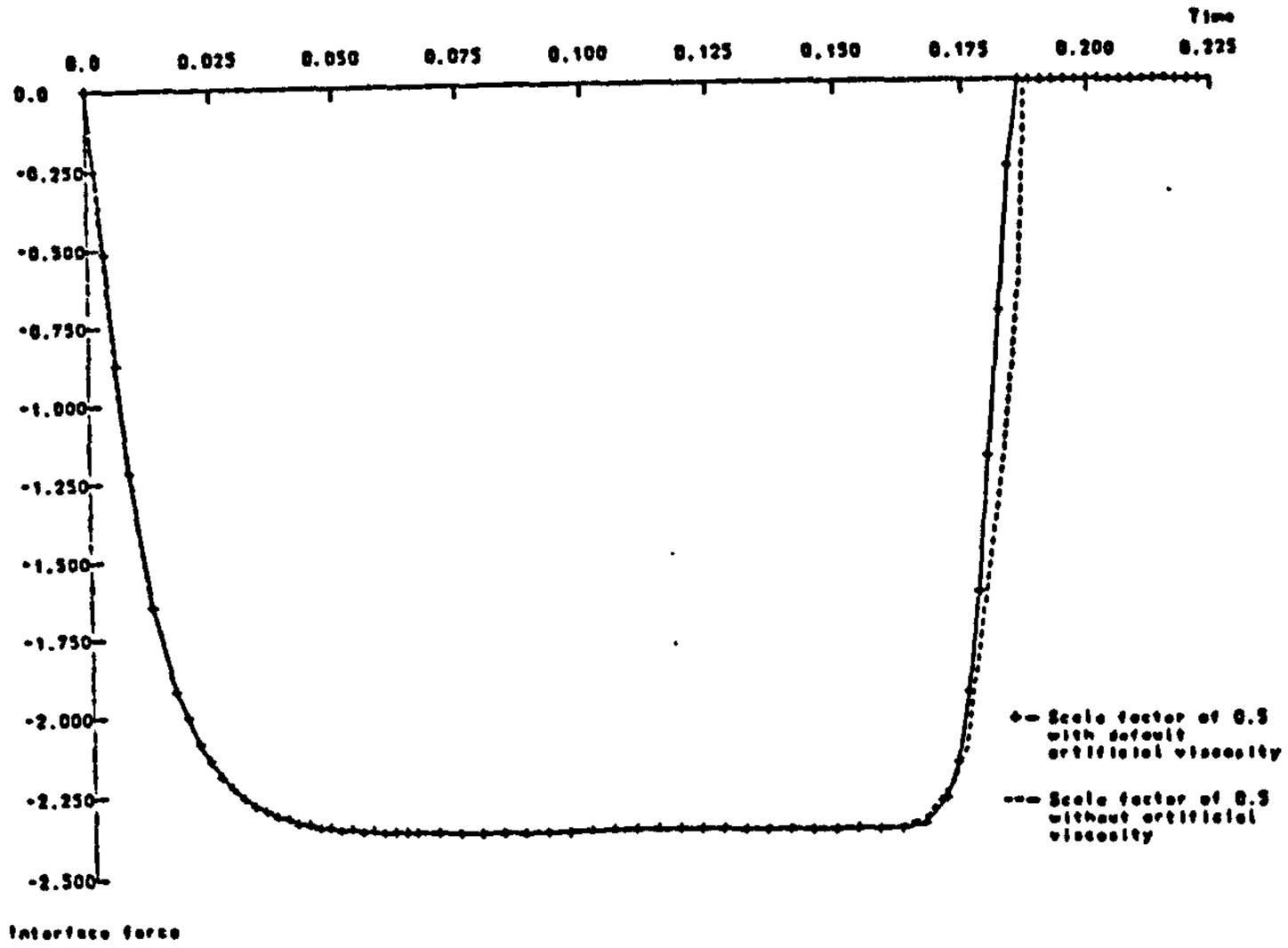

Figure 4.11

Variation of nodal interface force with time for the impact of an elastic bar against a rigid wall using null values of the artificial viscosity coefficients

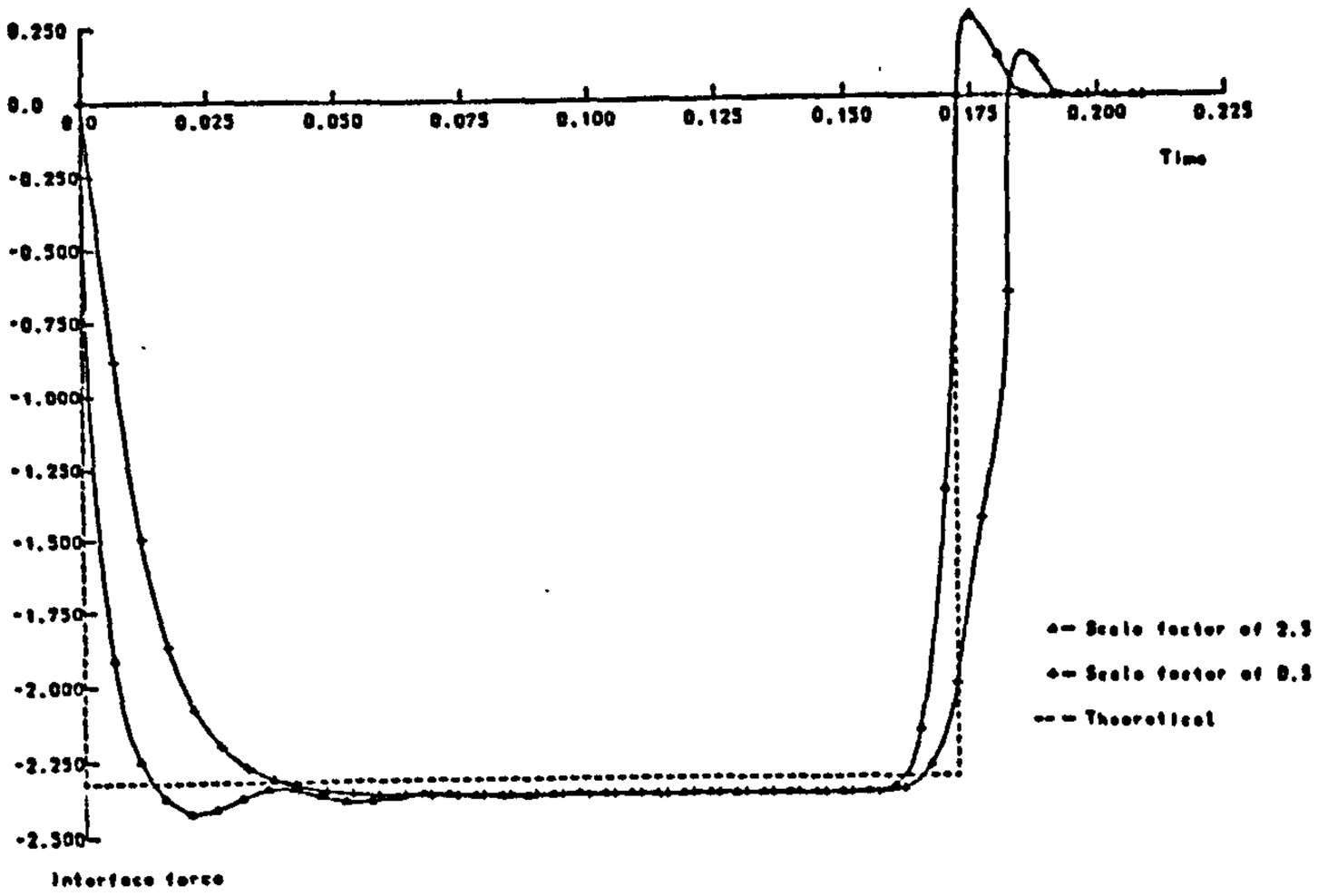

Figure 4.12

Variation of element derived interface force with time for the impact of an elastic bar against a rigid wall using default values of the artificial viscosity coefficients

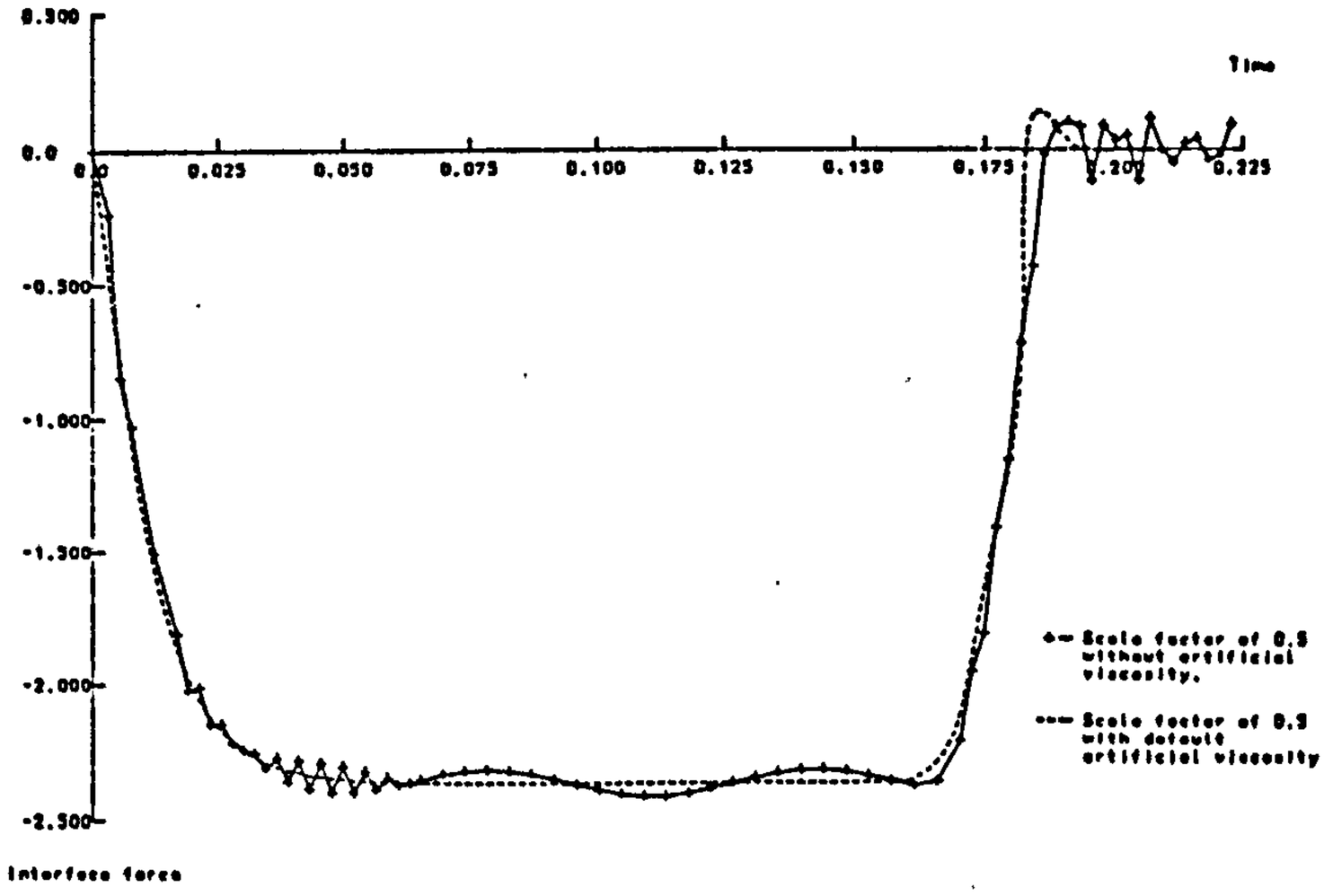

Figure 4.13

Variation of element derived interface force with time for the impact of an elastic bar against a rigid wall using null values of the artificial viscosity coefficients

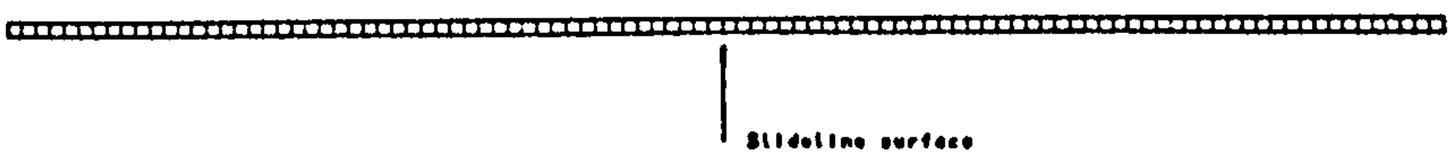

Figure 4.14

Finite element discretisation for the longtitudinal impact of two elastic bars

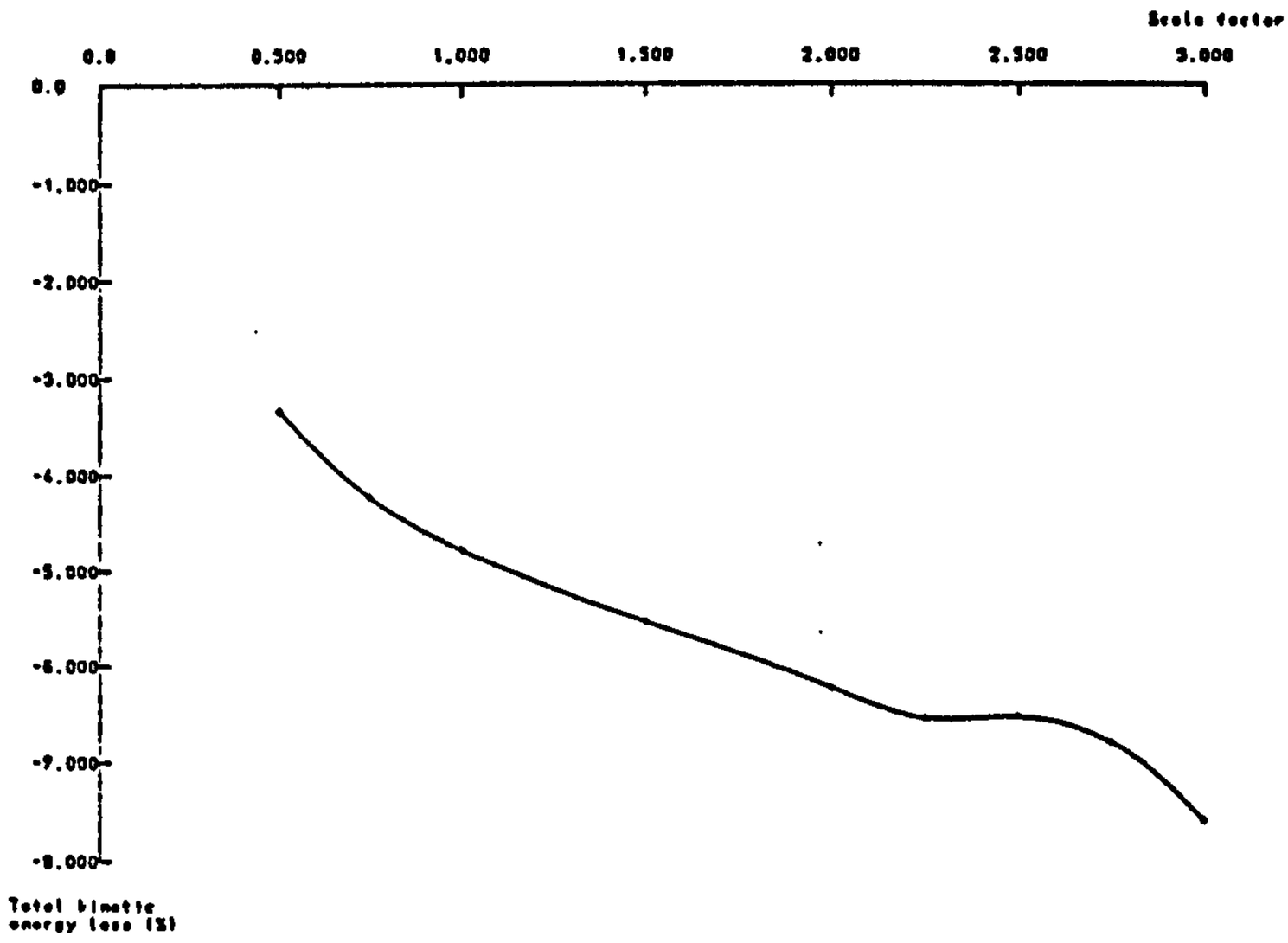

Figure 4.15

Variation of total kinetic energy loss with scale factor for the longtitudinal impact of two elastic bars

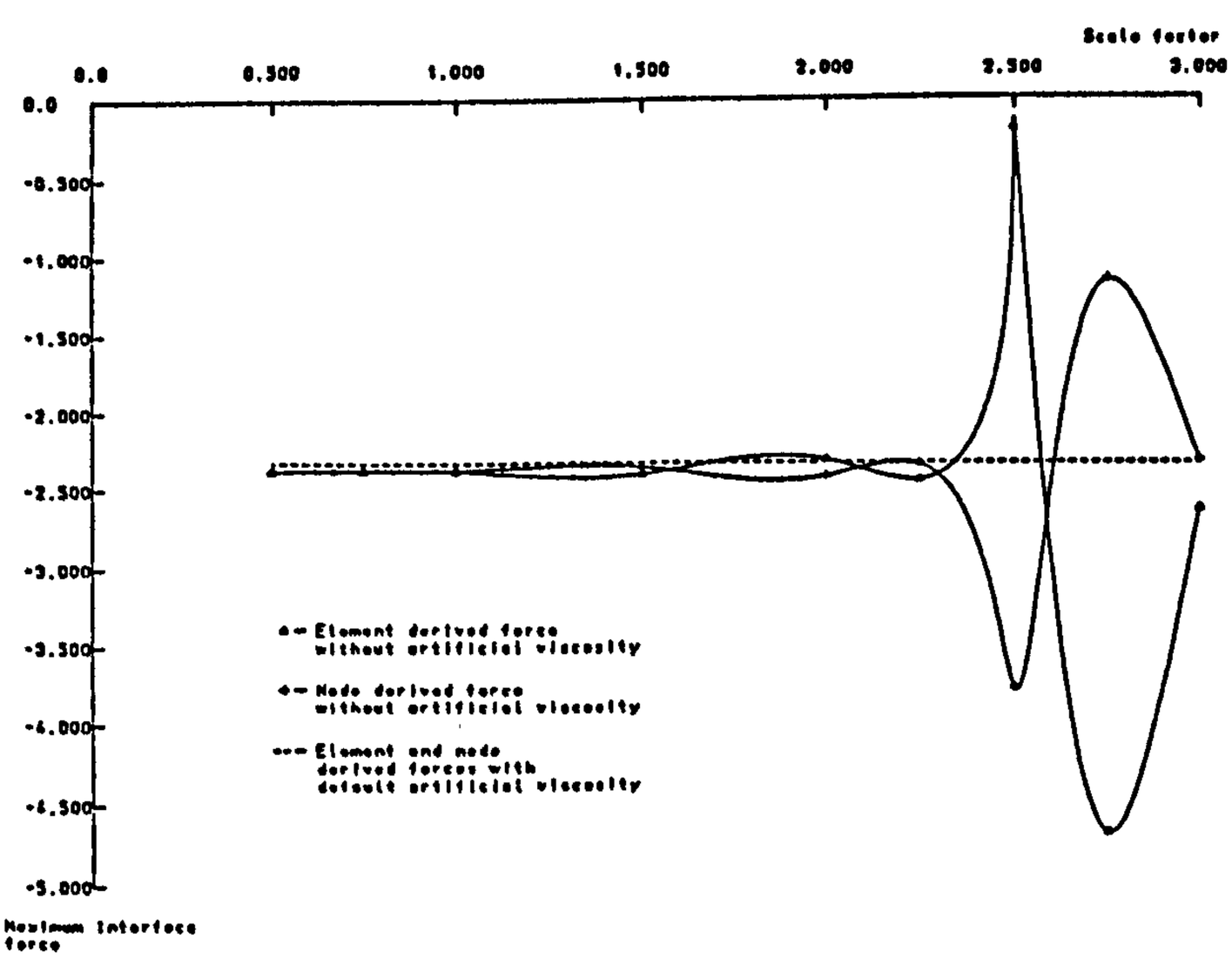

Figure 4.16

Variation of maximum developed interface force with scale factor for the longtitudinal impact of two elastic bars

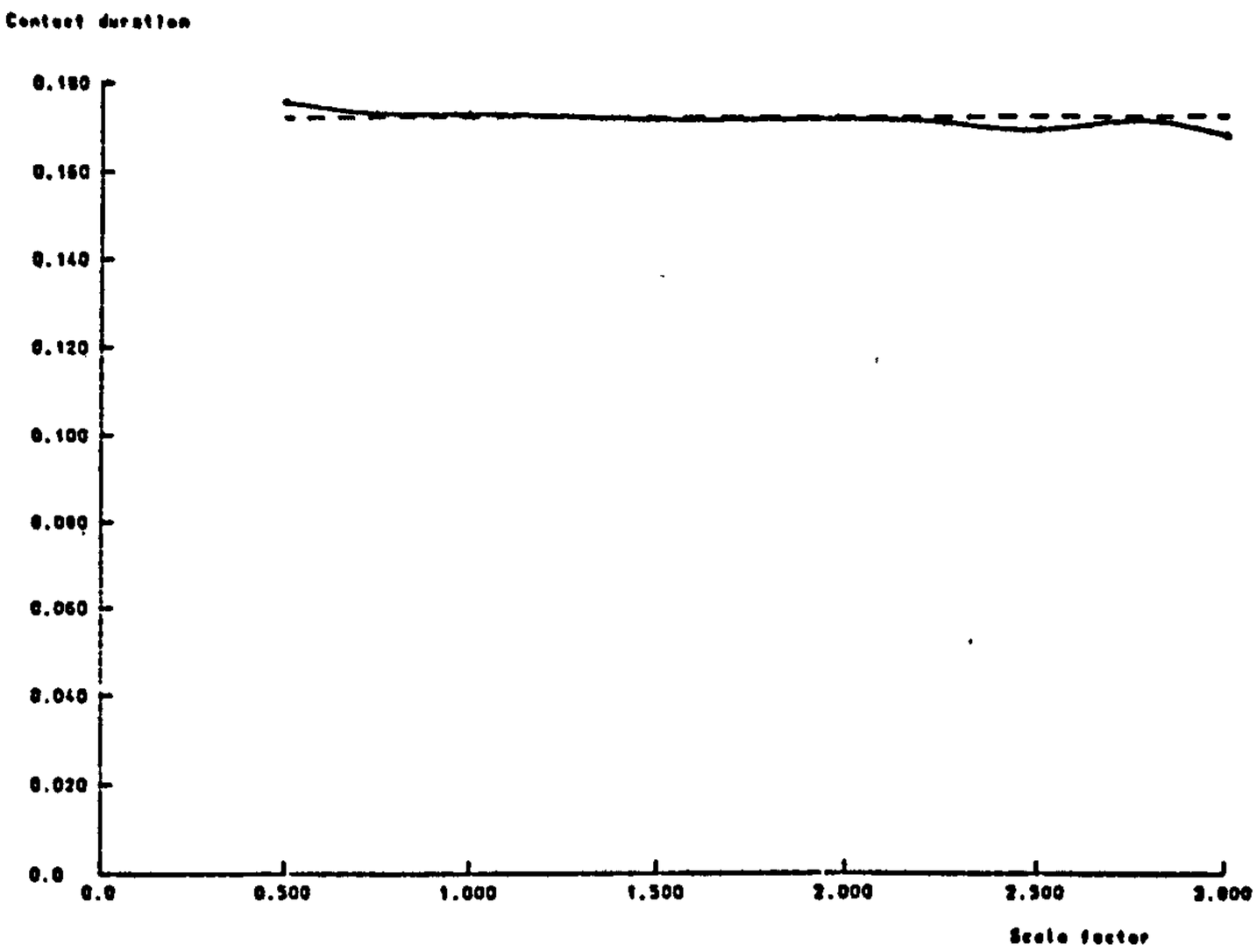

Figure 4.17

Variation of contact duration time with scale factor for the longtitudinal impact of two elastic bars

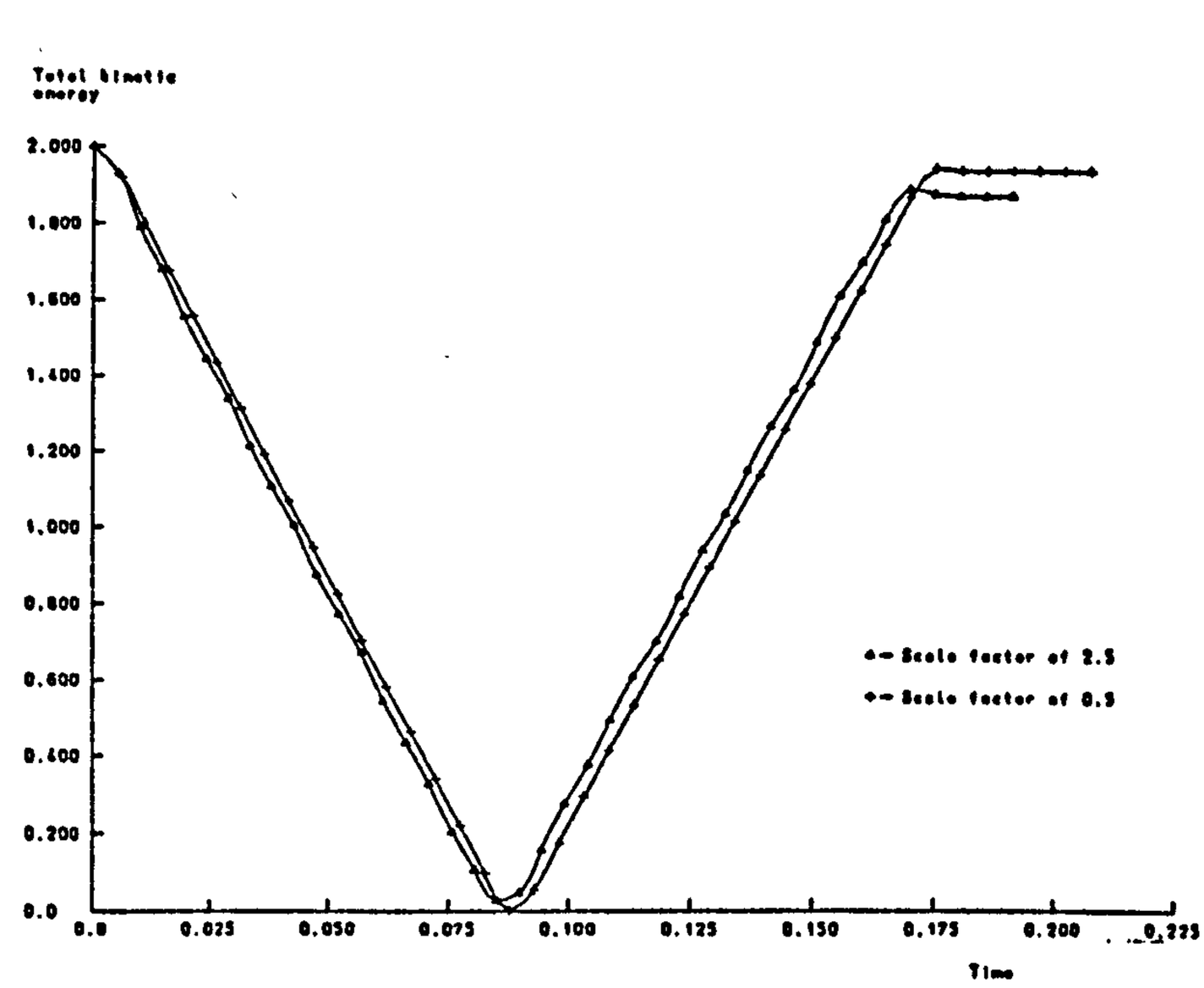

Figure 4.18

Variation of total kinetic energy loss with time for the longtitudinal impact of two elastic bars using differing values of scale factor

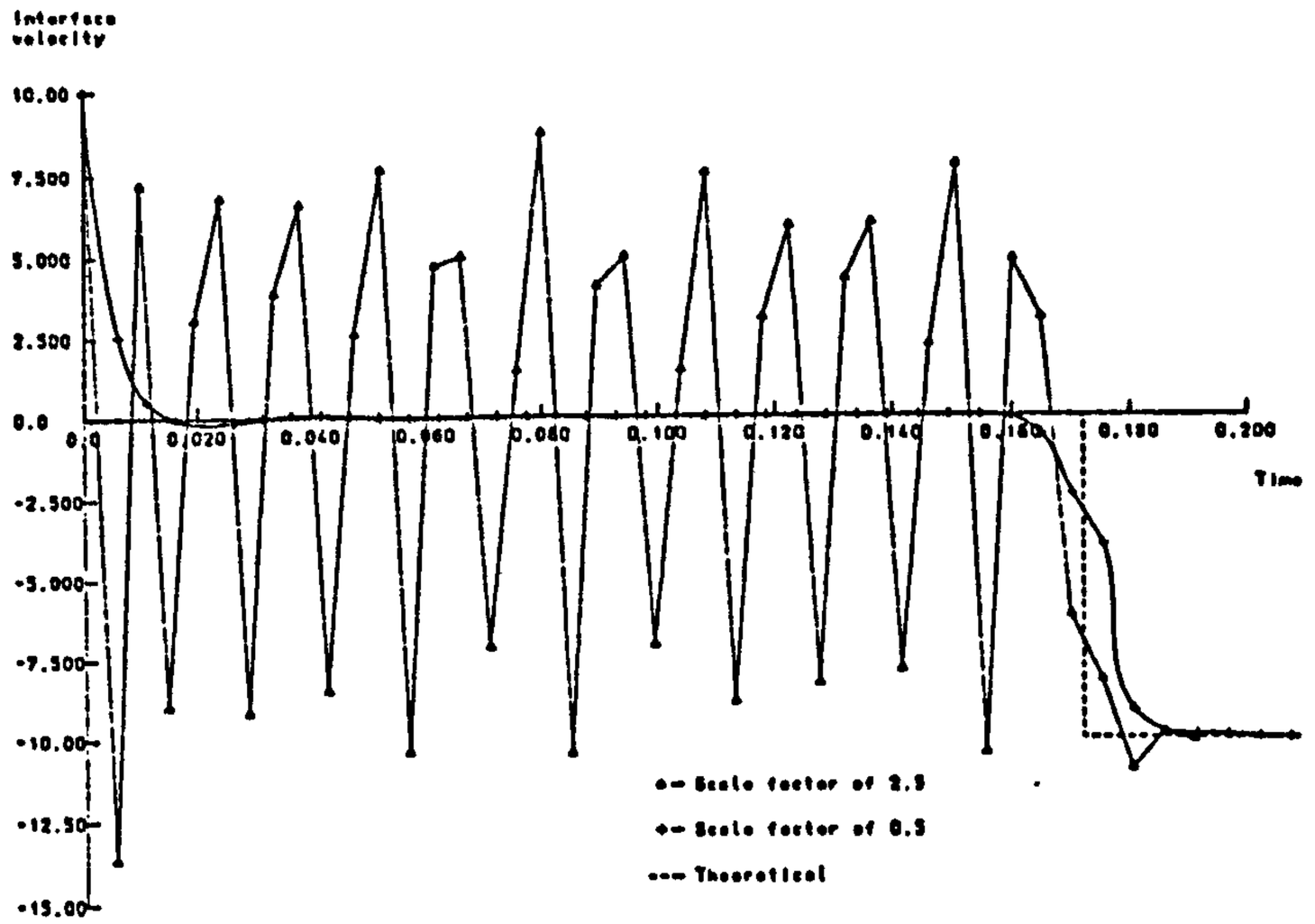

Figure 4.19

Variation of interface velocity with time for the impact of an elastic bar against a rigid wall using differing values of scale factor

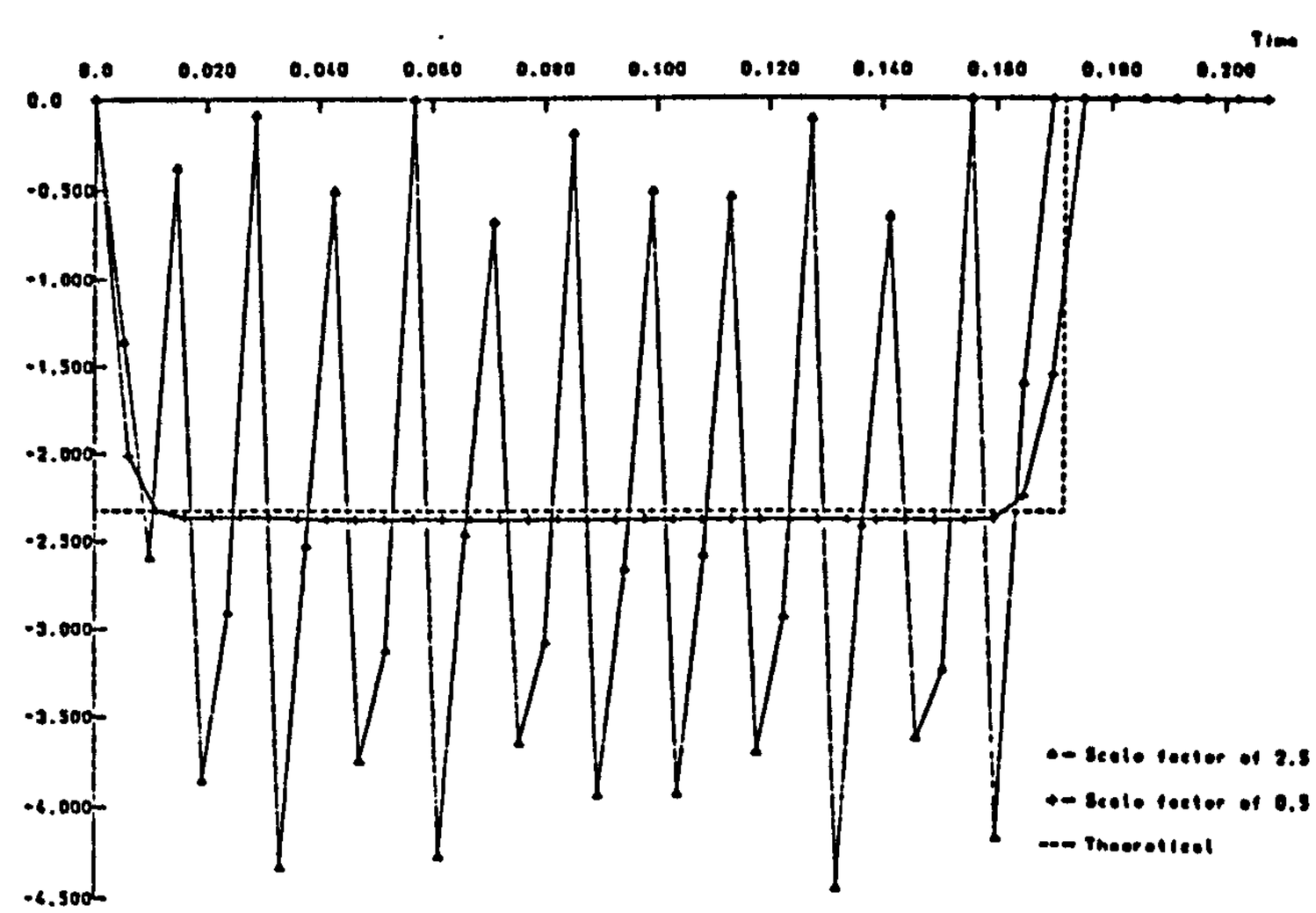

Figure 4.20

Variation of nodal interface force with time for the longtitudinal impact of two elastic bars using differing values of scale factor

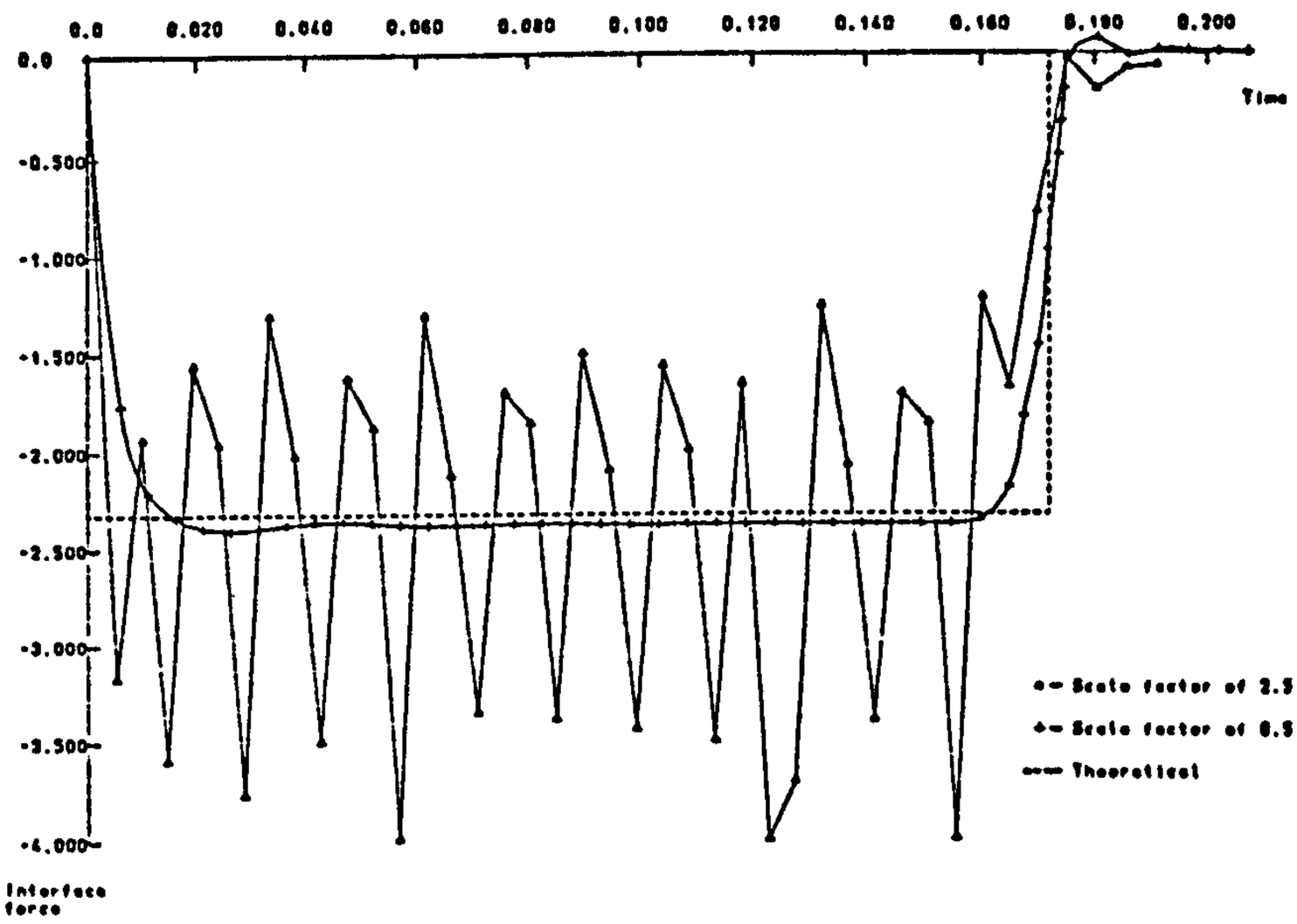

Figure 4.21
Variation of element derived interface force with time for the longtitudinal impact of two elastic bars using differing values of scale factor

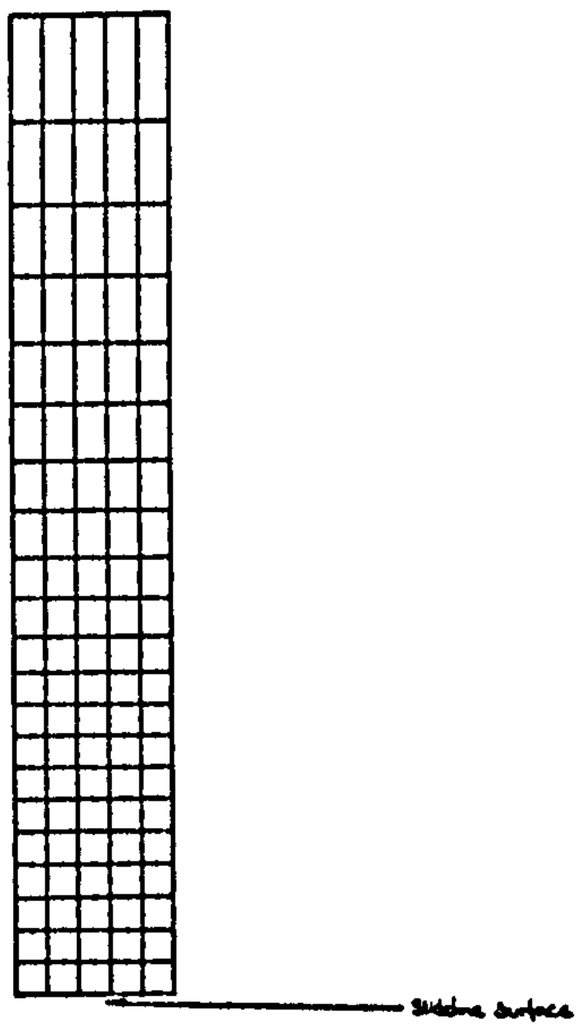

Figure 4.22
Finite element discretisation for the impact of an elastic-plastic bar against a rigid wall

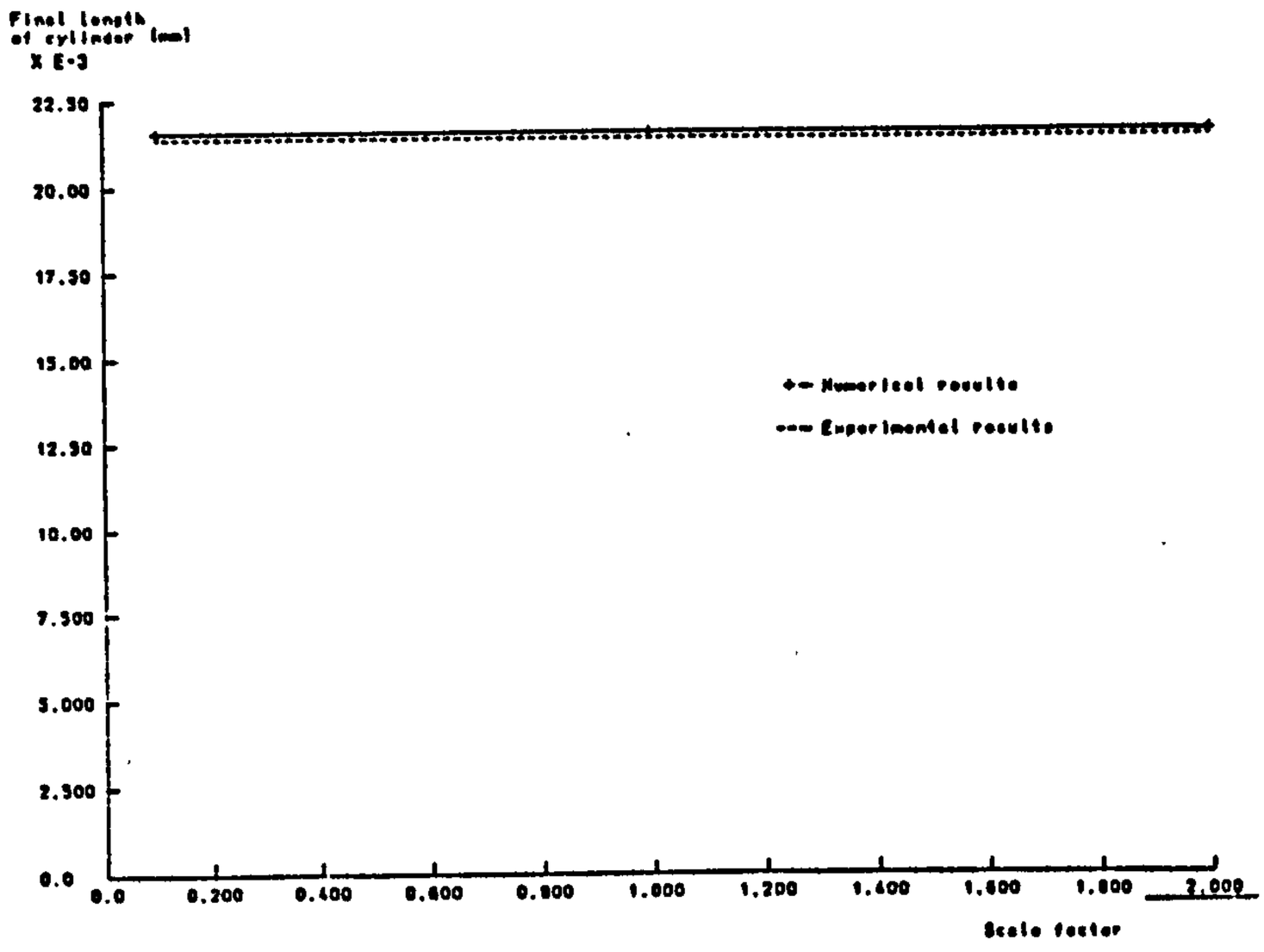

Figure 4.23

Variation of the final length of an elastic-plastic bar impacted against a rigid wall with scale factor

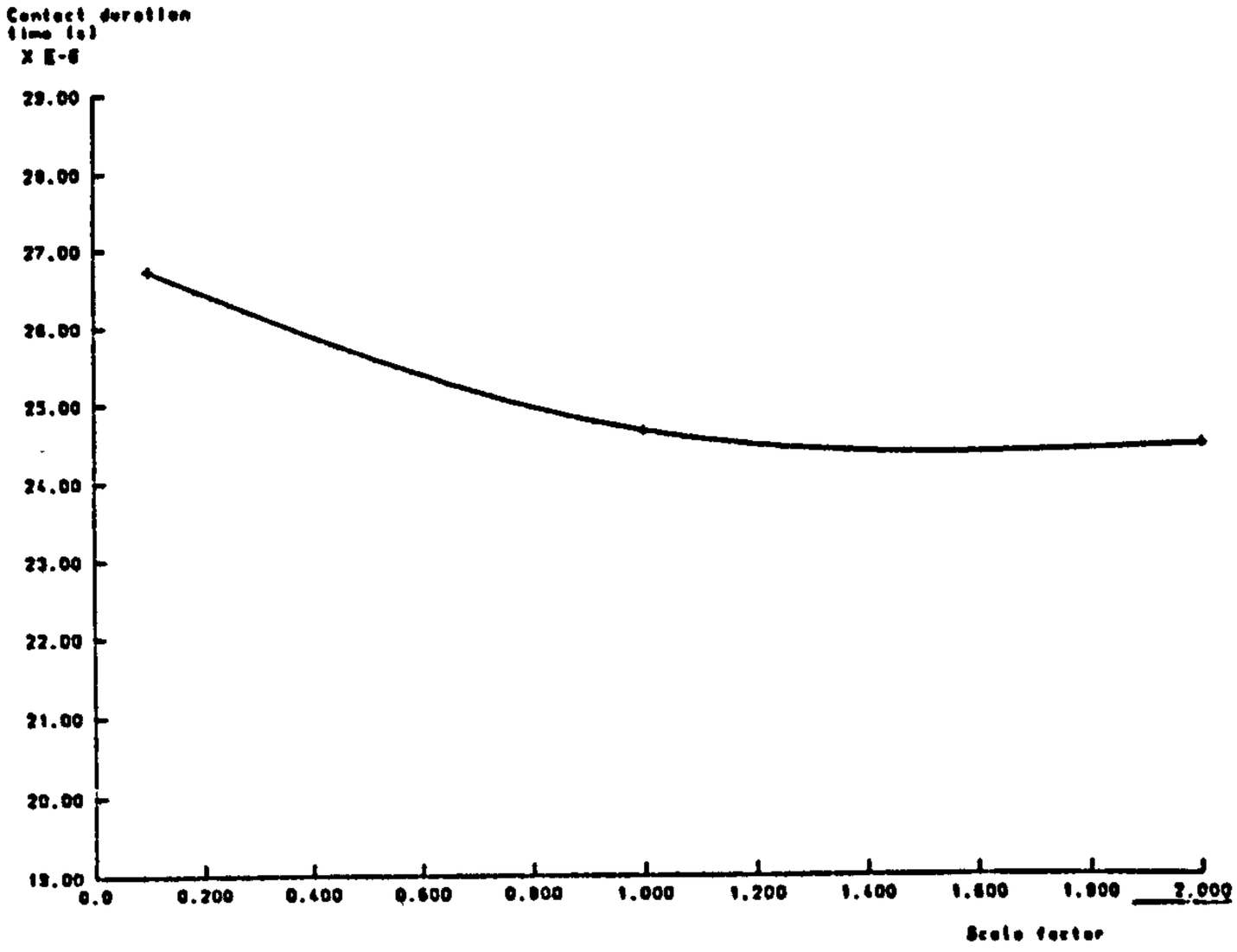

Figure 4.24

Variation of contact duration time with scale factor for the impact of an elastic-plastic bar against a rigid wall

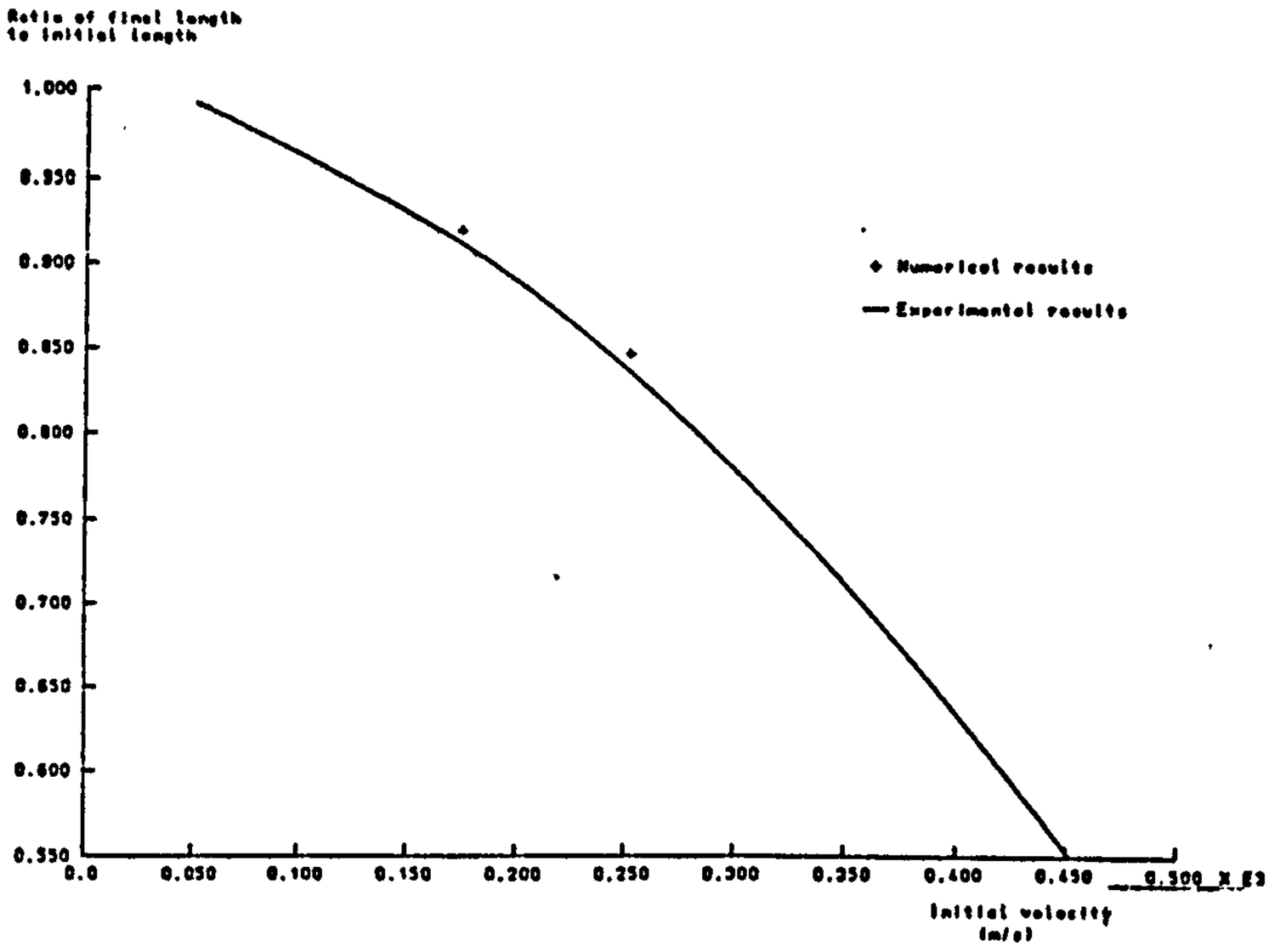

Figure 4.25

Experimental curve of final cylinder lengths versus impact velocity together with the results of present work for an elastic-plastic bar against a rigid wall

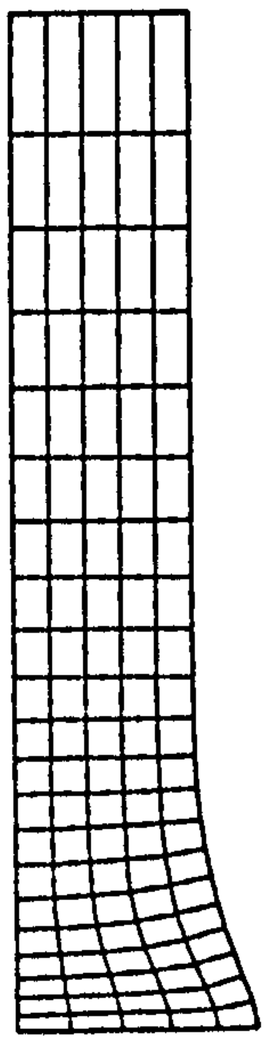

Figure 4.26

Final deformation pattern of an elastic-plastic bar against a rigid wall with an impact velocity of 175 ms^{-1}

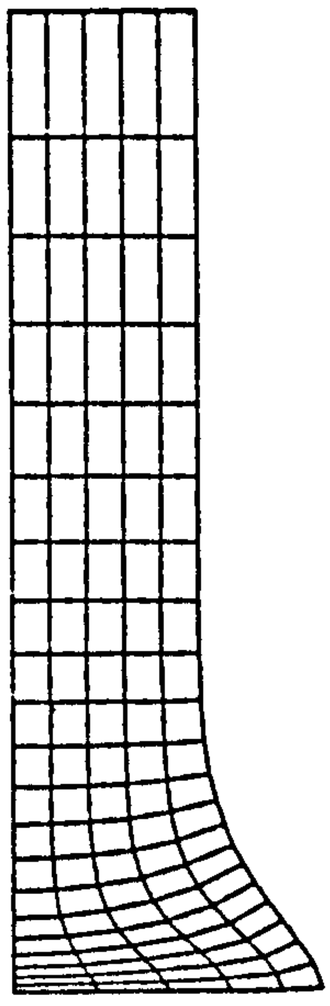

Figure 4.27

Final deformation pattern of an elastic-plastic bar against a rigid wall with an impact velocity of 252 ms^{-1}

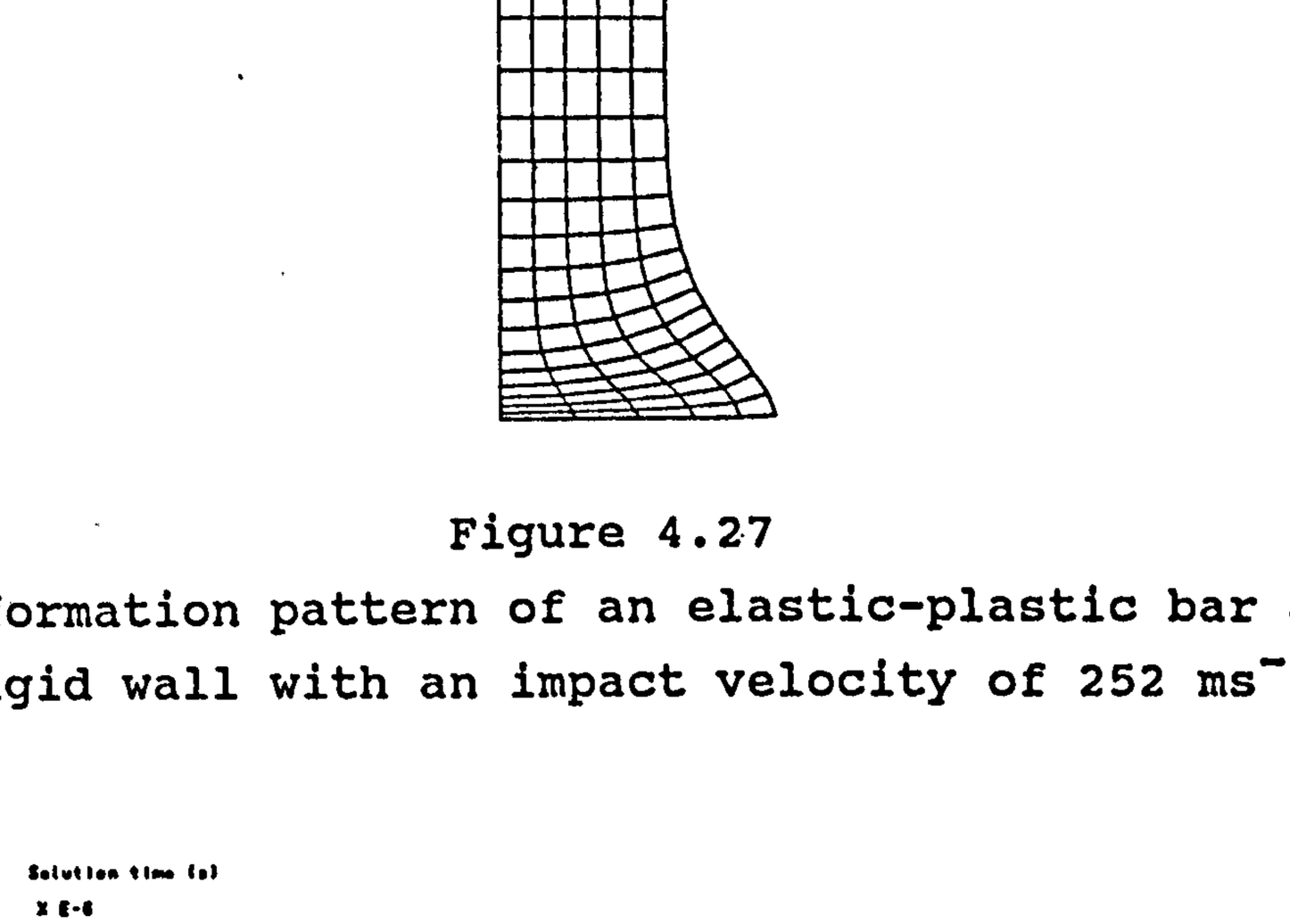

Figure 4.28

Variation of accumulated solution time with number of time steps for an elastic-plastic bar impact against a rigid wall

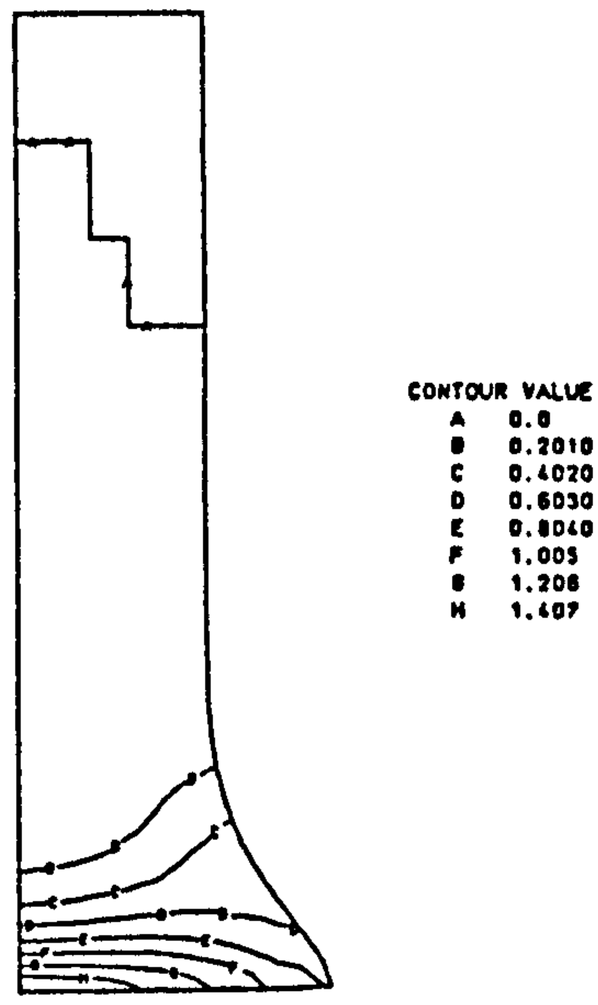

Figure 4.29
Terminal effective plastic strain contours of an elastic-plastic bar impact against a rigid wall for an initial velocity of 252ms^{-1}

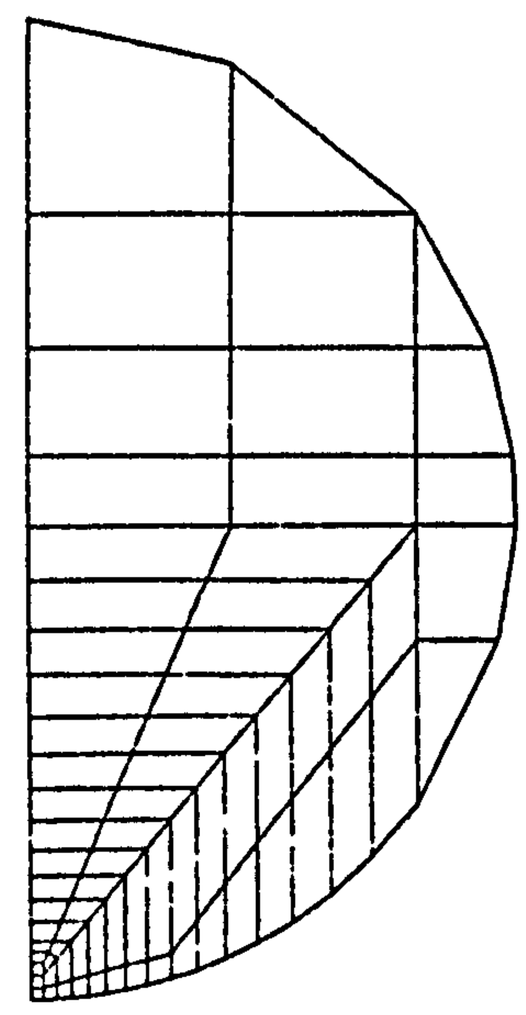

Figure 4.30
Finite element discretisation for the impact of an elastic sphere against a rigid wall

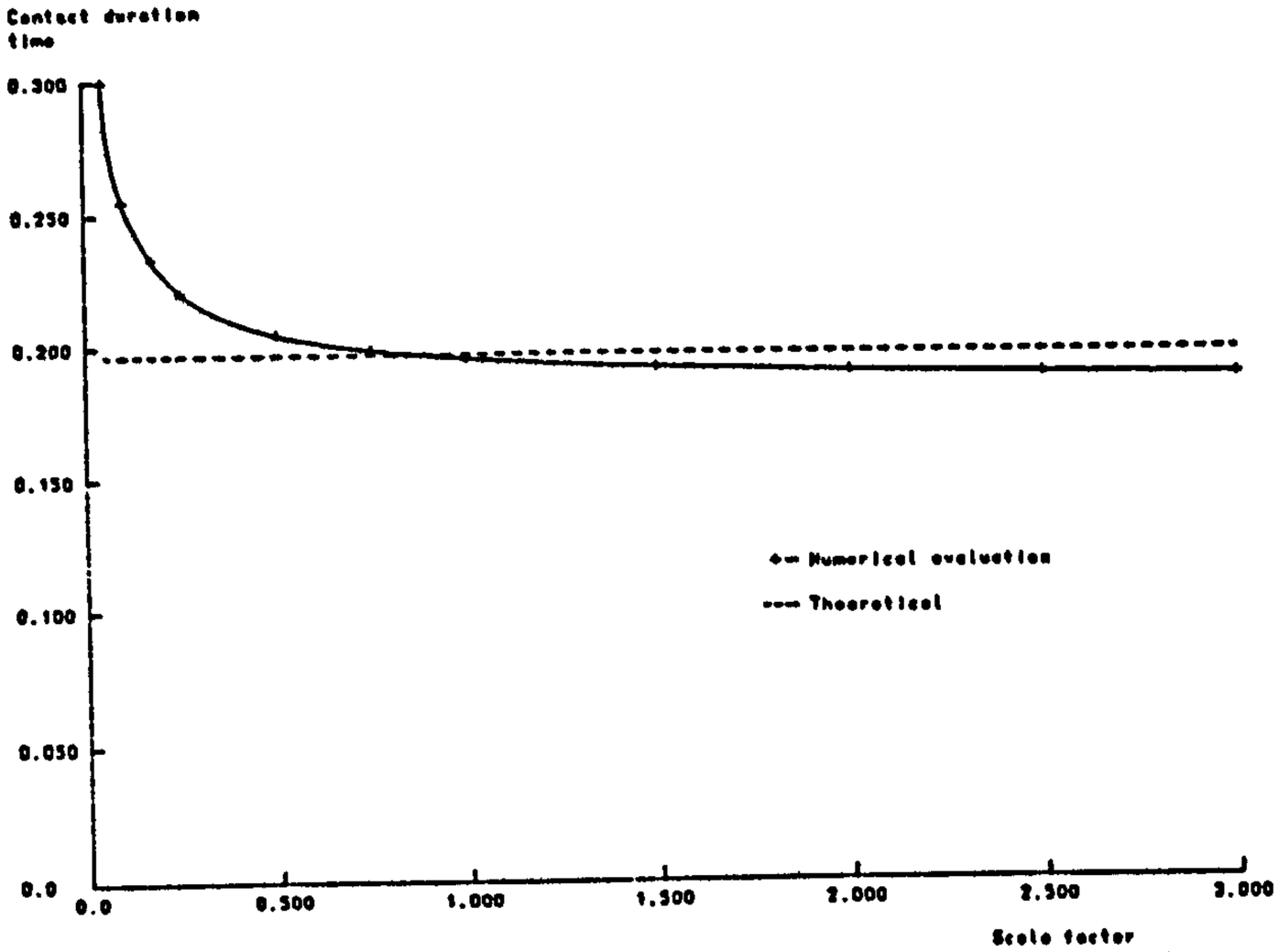

Figure 4.31

Variation of contact duration time with scale factor for the impact of an elastic sphere against a rigid wall

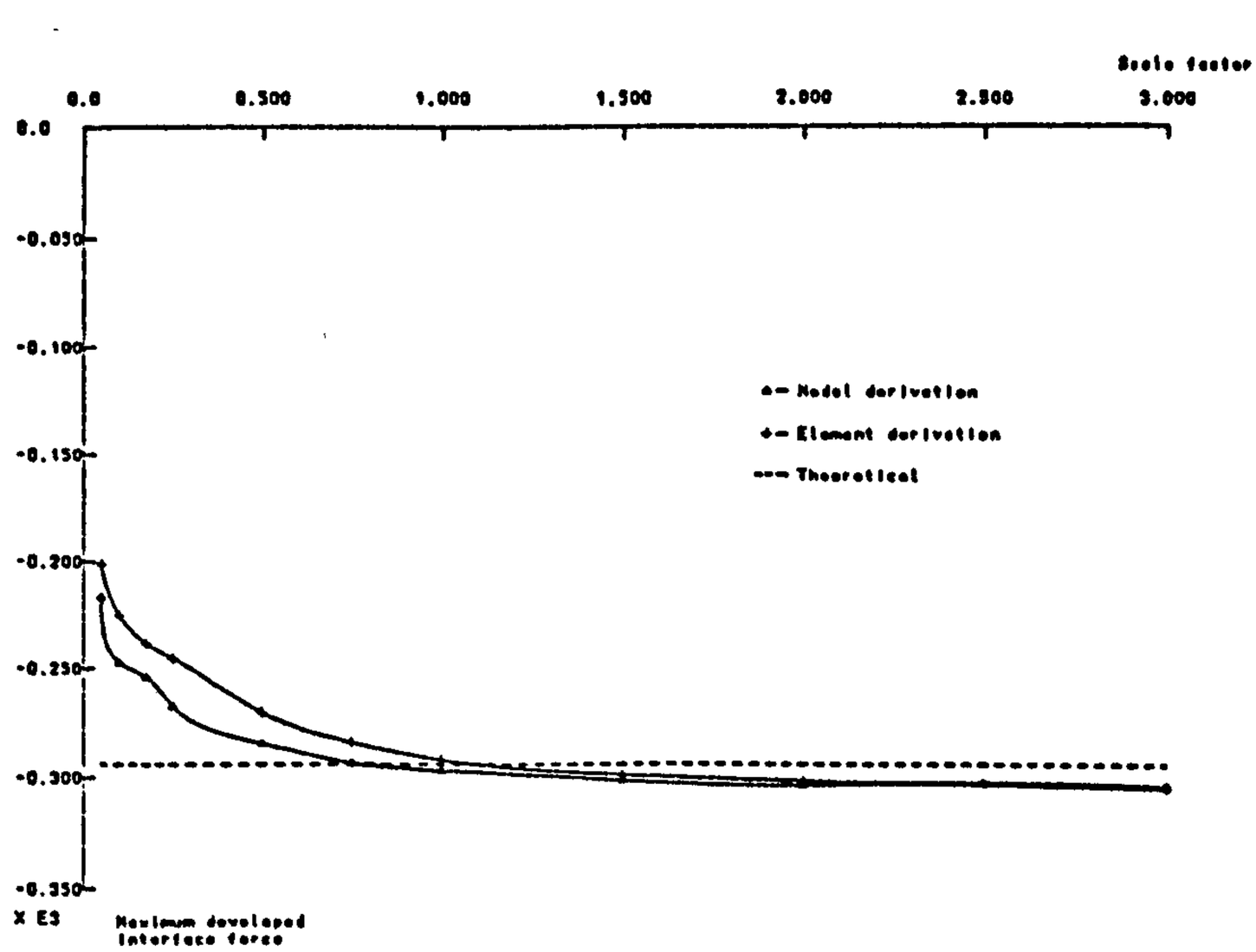

Figure 4.32

Variation of maximum developed interface force with scale factor for the impact of an elastic sphere against a rigid wall

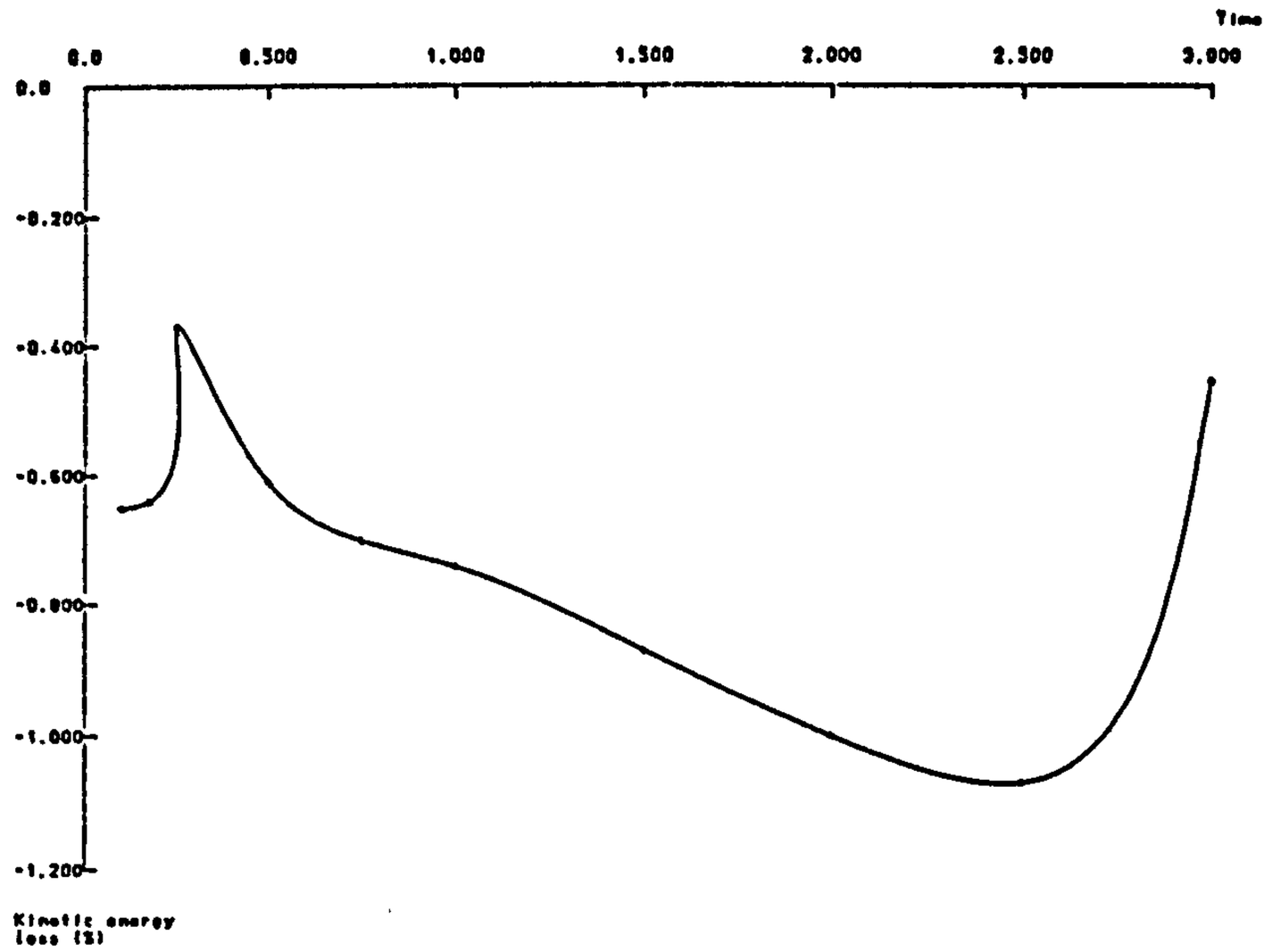

Figure 4.33

Variation of total kinetic energy loss with scale factor for an elastic sphere impact against a rigid wall

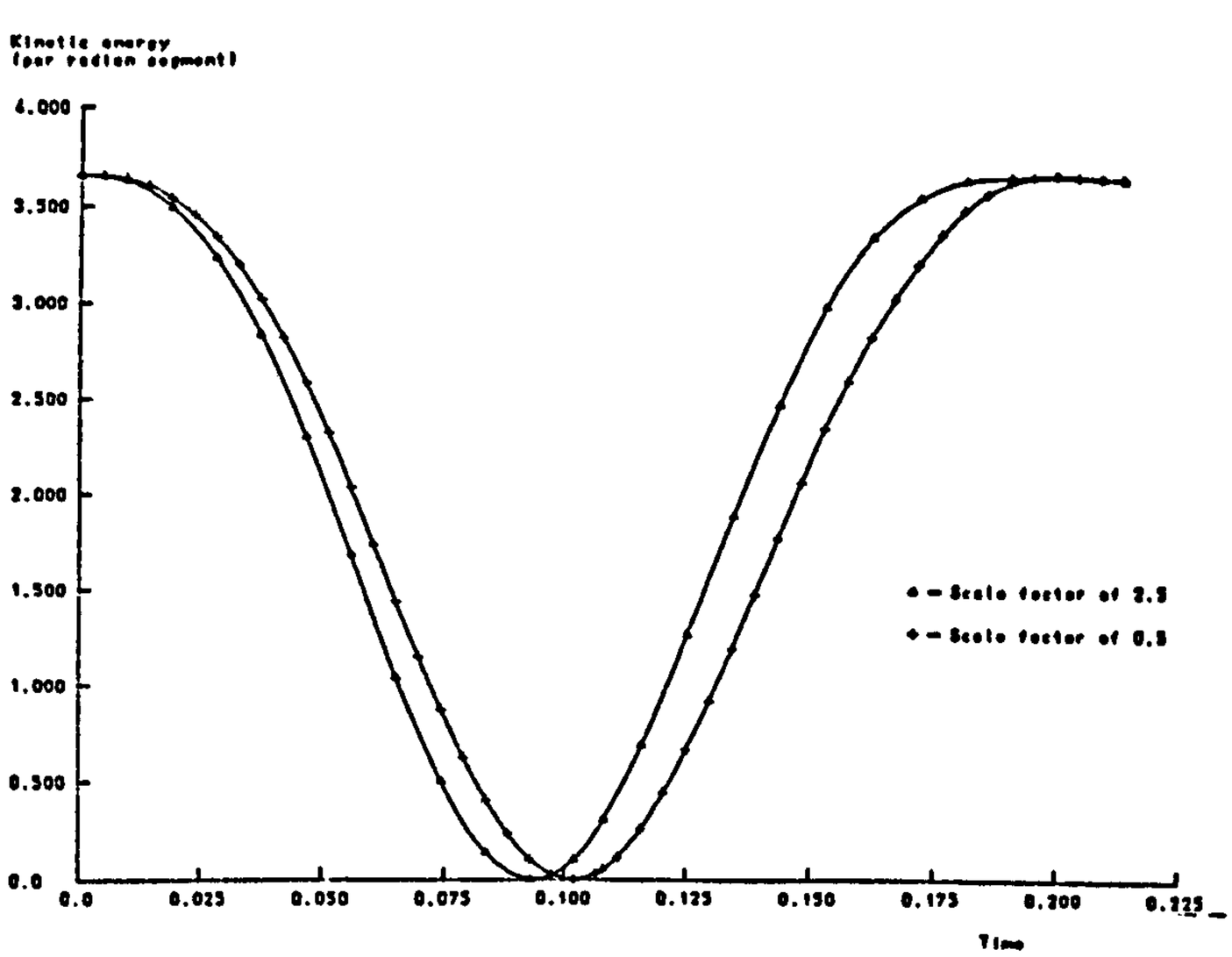

Figure 4.34

Variation of total kinetic energy loss with time for an elastic sphere impact against a rigid wall using differing values of scale factor

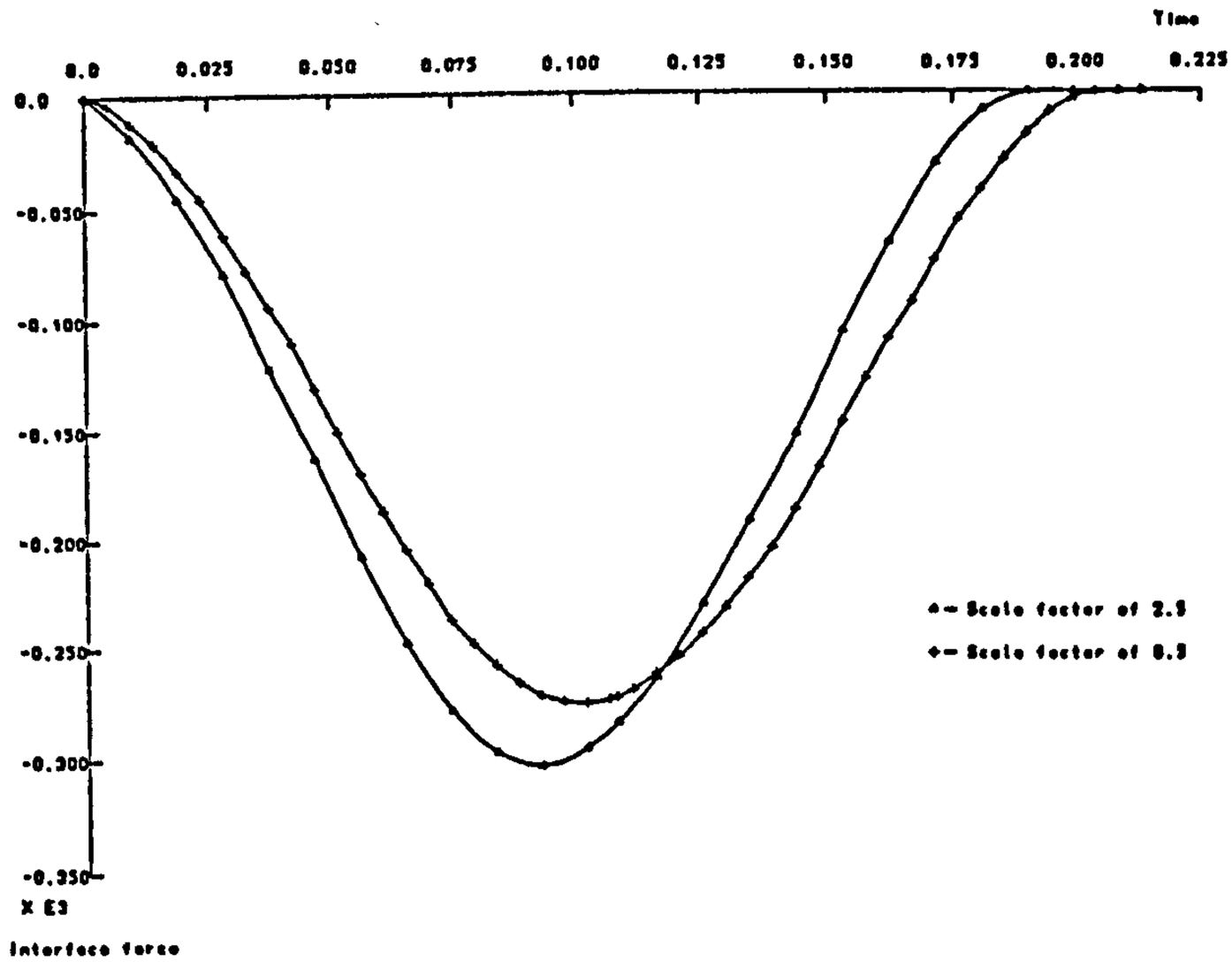

Figure 4.35
Variation of element derived interface force with time for an elastic sphere impact against a rigid wall using differing values of scale factor

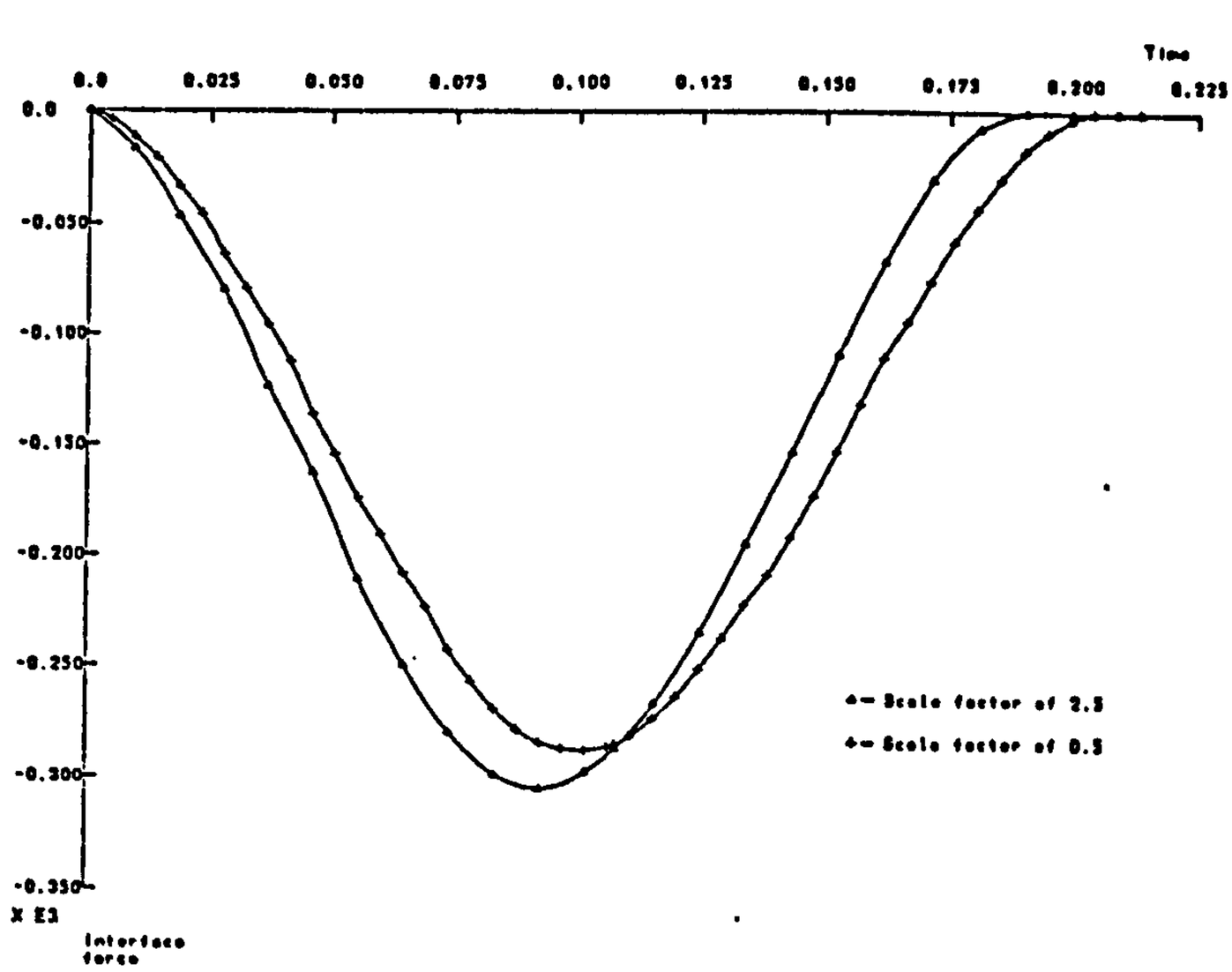

Figure 4.36
Variation of nodal interface force with time for the impact of an elastic sphere against a rigid wall using differing values of scale factor

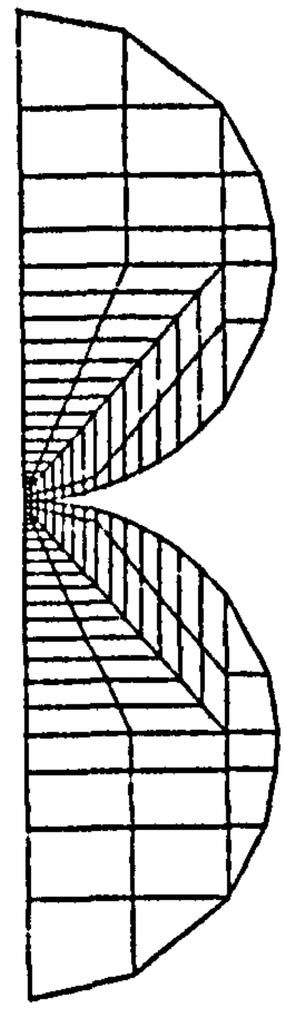

Figure 4.37

Finite element discretisation for the longtitudinal impact of two elastic spheres

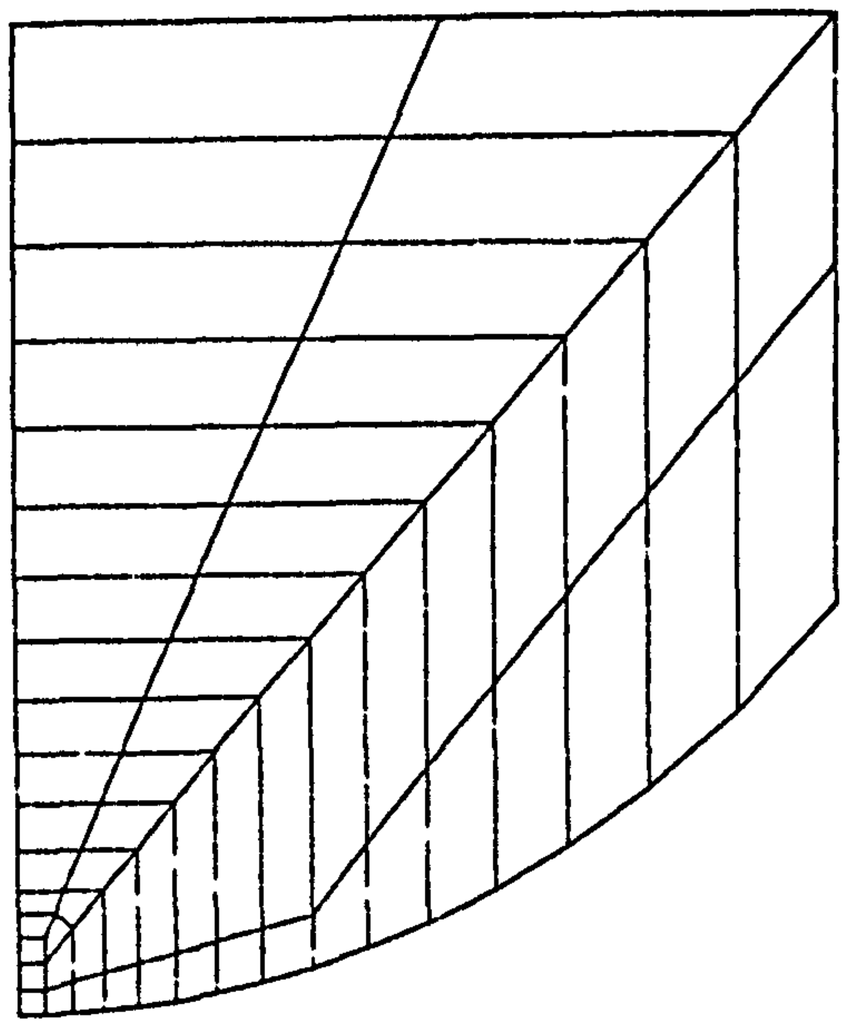

Figure 4.38

Close up of the mesh for the longtitudinal impact of two elastic spheres

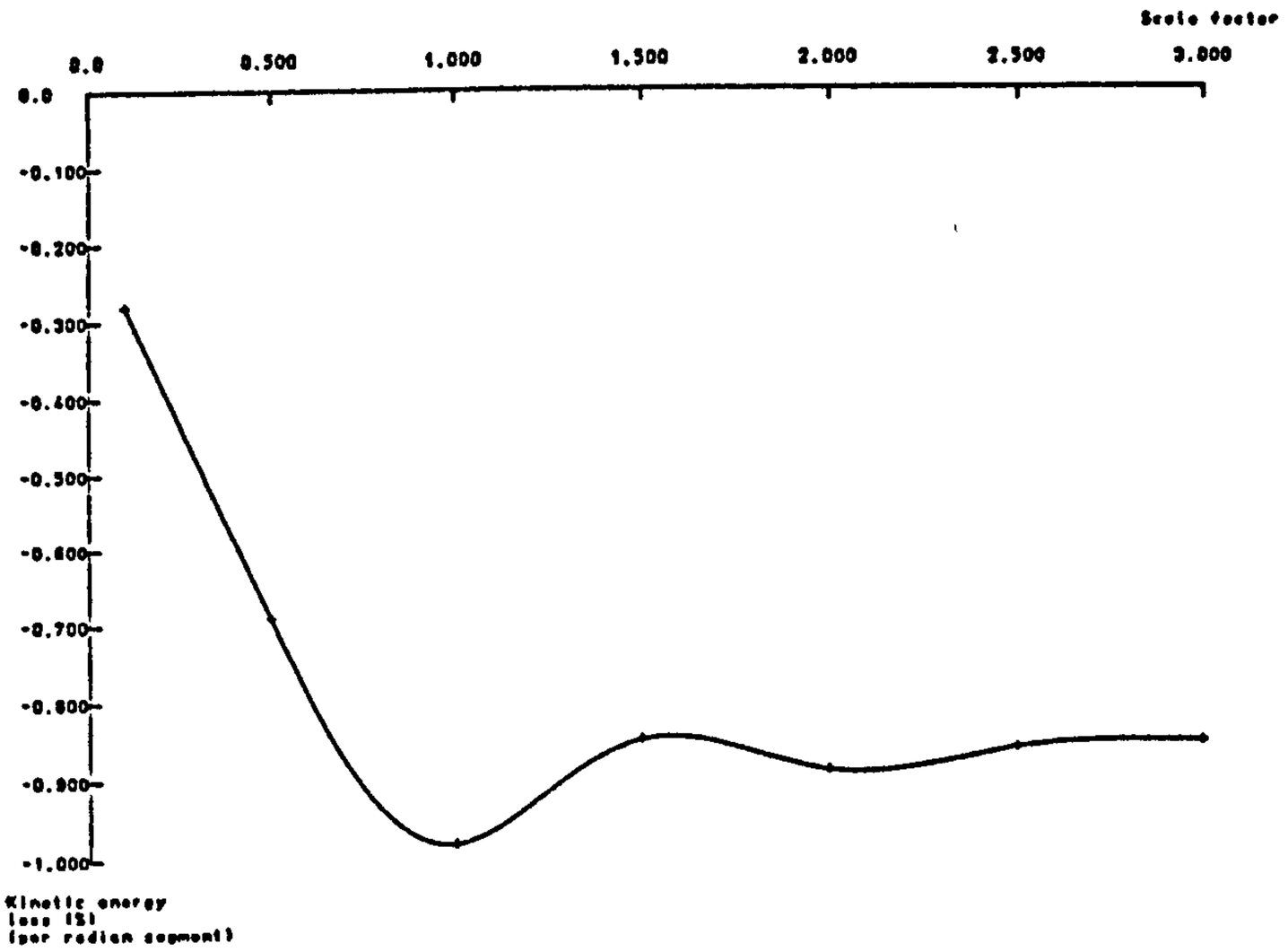

Figure 4.39

Variation of total kinetic energy loss with scale factor for the longtitudinal impact of two elastic spheres

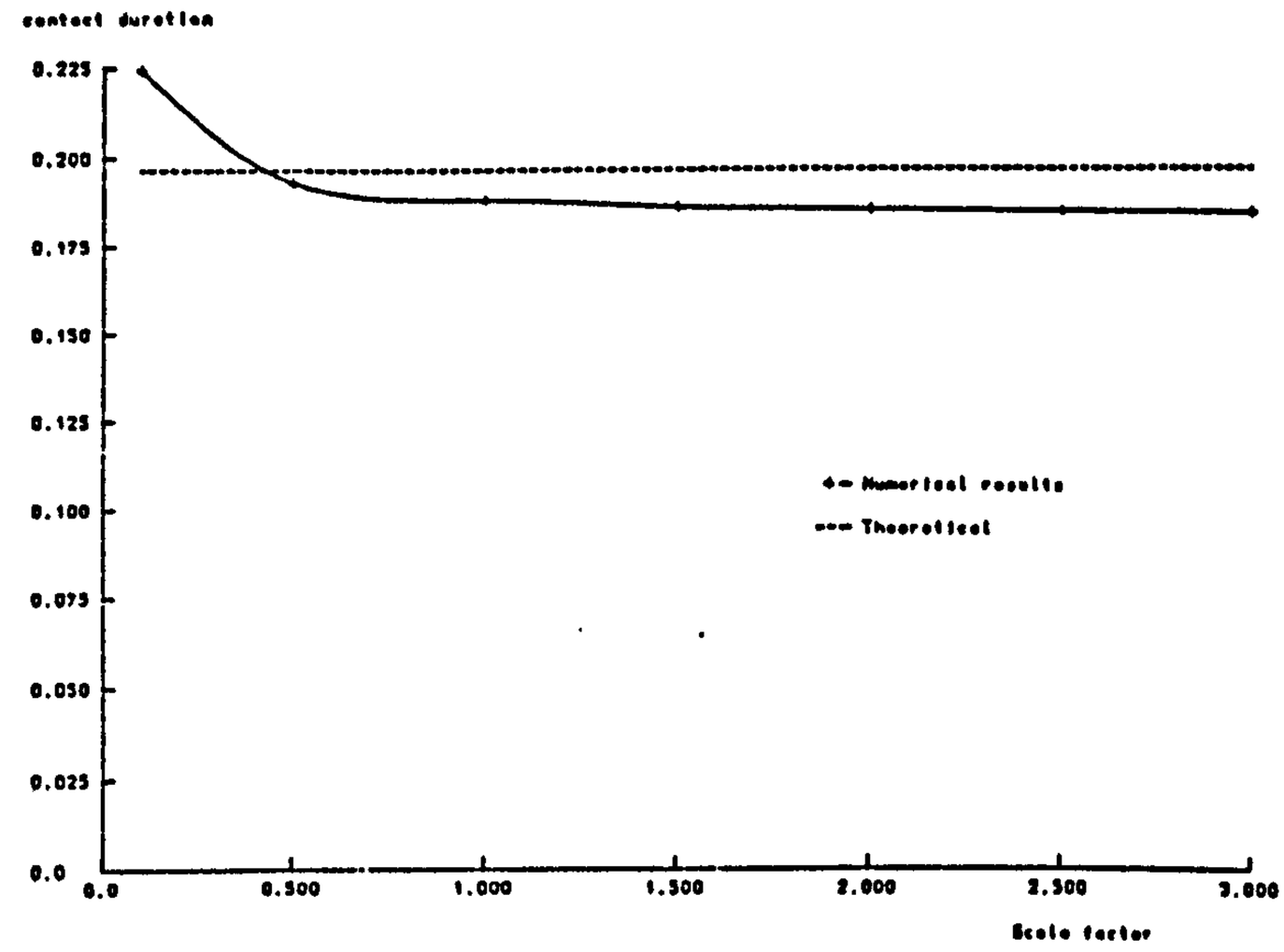

Figure 4.40

Variation of contact duration time with scale factor for the longtitudinal impact of two elastic spheres

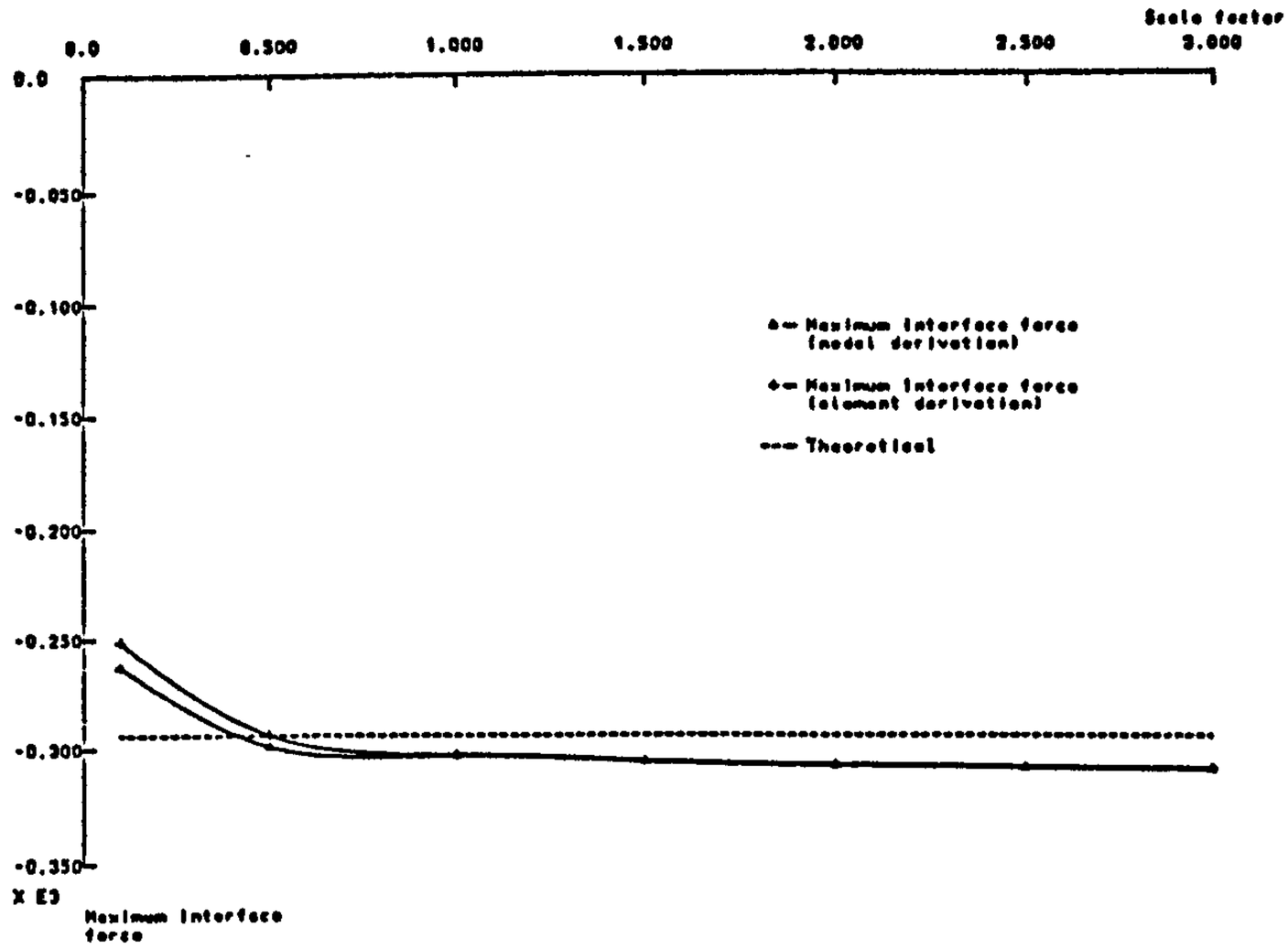

Figure 4.41
Variation of maximum developed interface force with scale factor for the longtitudinal impact of two elastic spheres

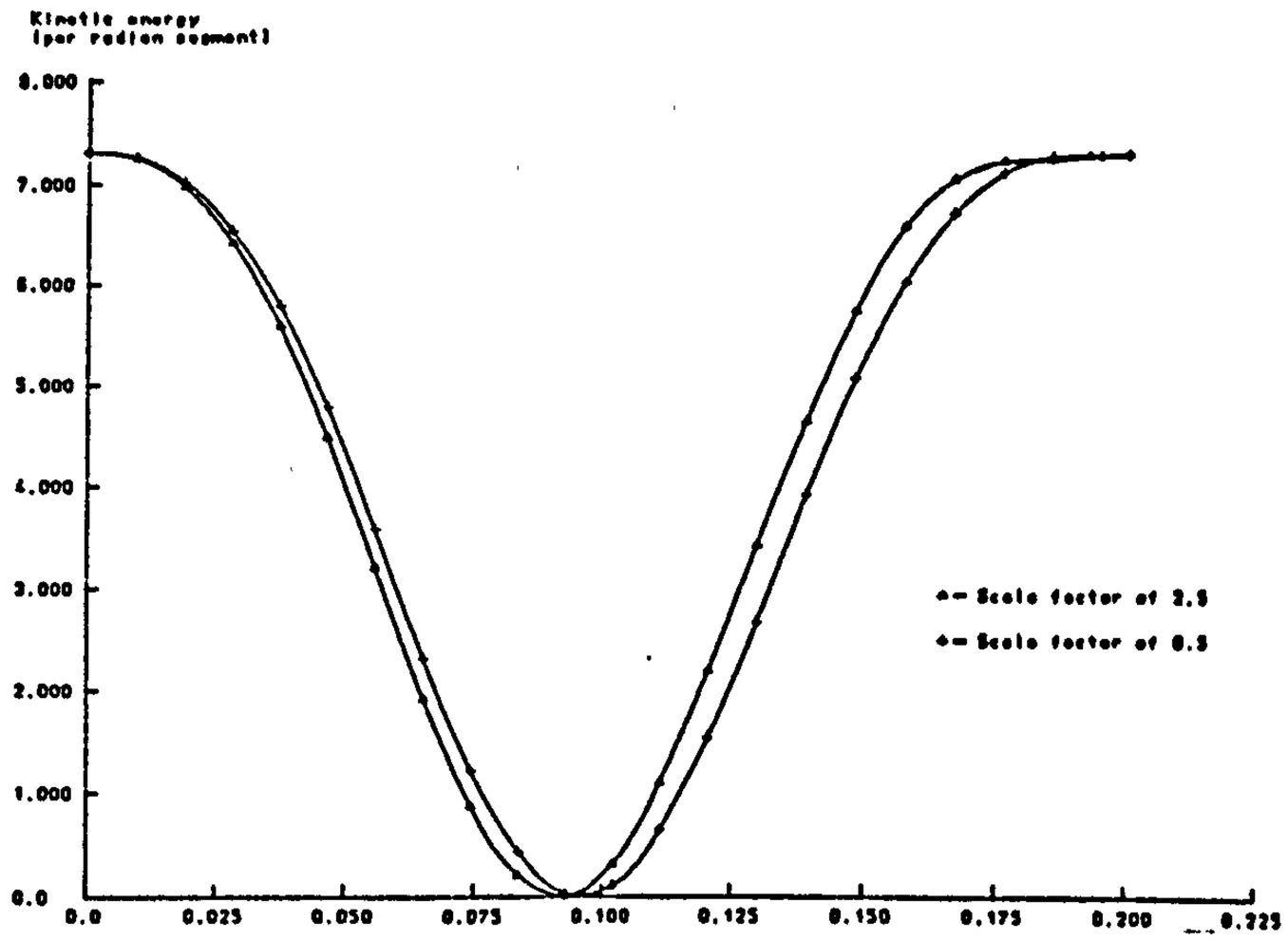

Figure 4.42
Variation of total kinetic energy loss with time for the longtitudinal impact of two elastic spheres using differing values of scale factor

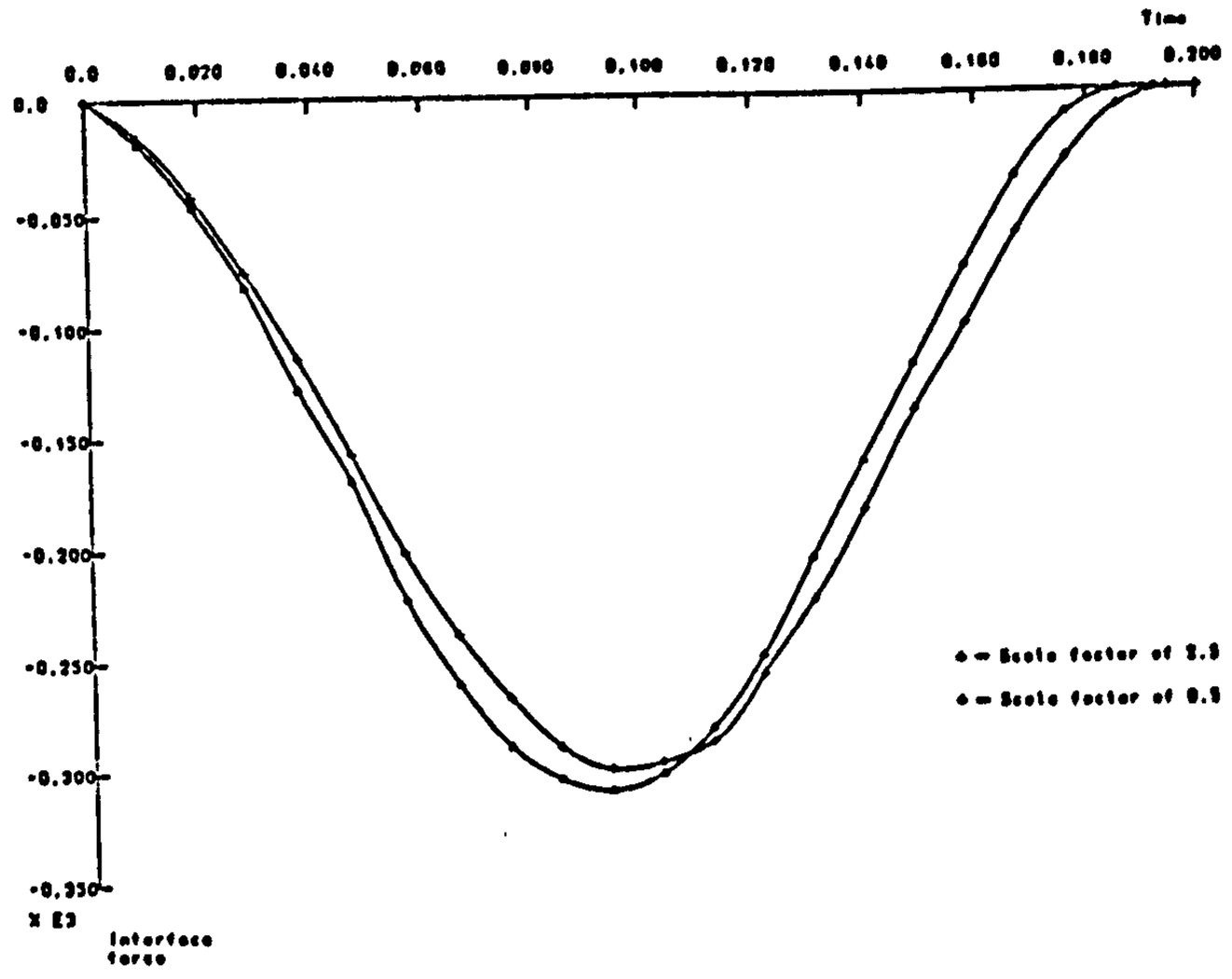

Figure 4.43

Variation of nodal interface force with time for the longtitudinal impact of two elastic spheres using differing values of scale factor

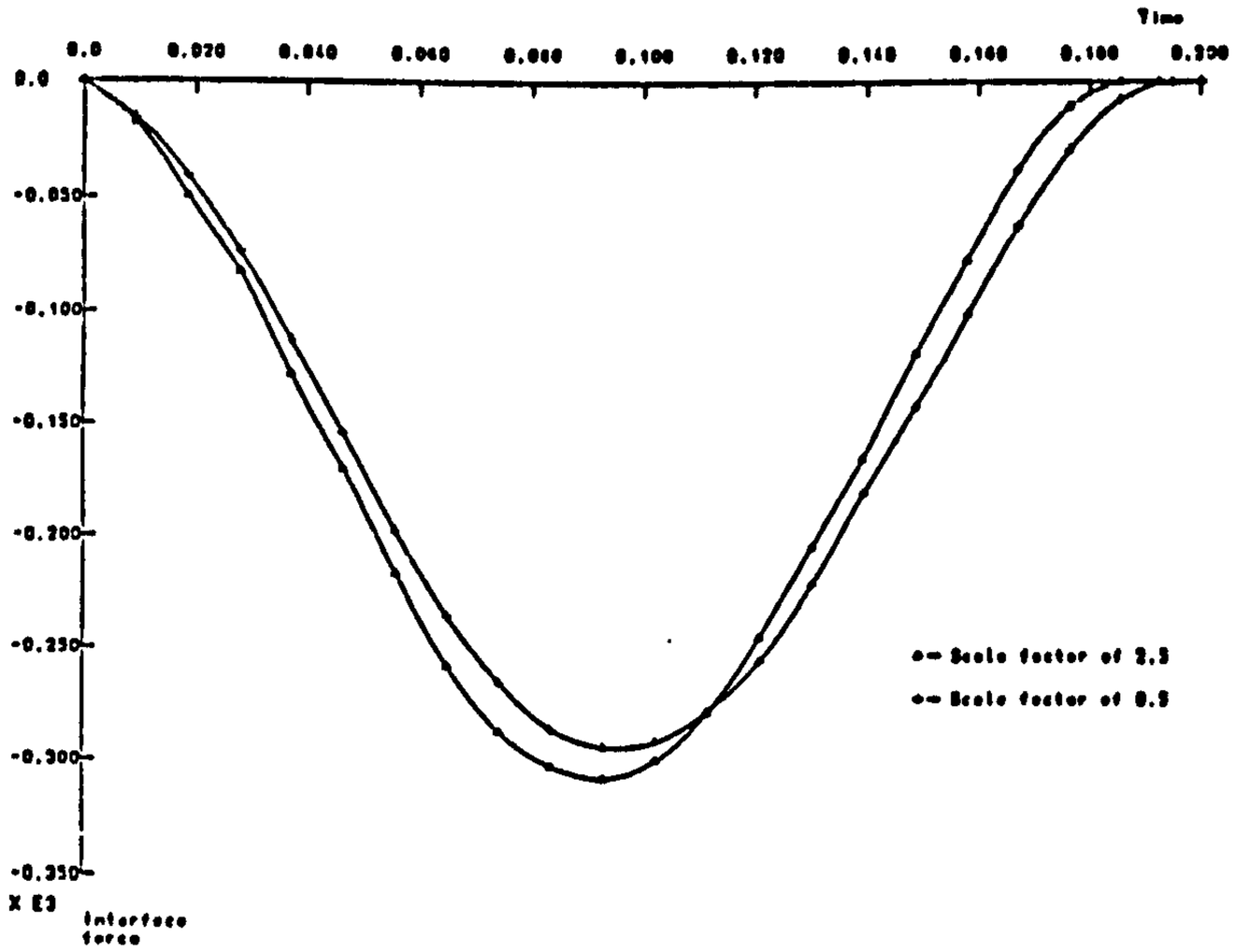

Figure 4.44

Variation of element derived interface force with time for the longtitudinal impact of two elastic spheres using differing values of scale factor

Figure 4.45
Finite element idealisation of an impulsively loaded beam fully fixed at its two extremities

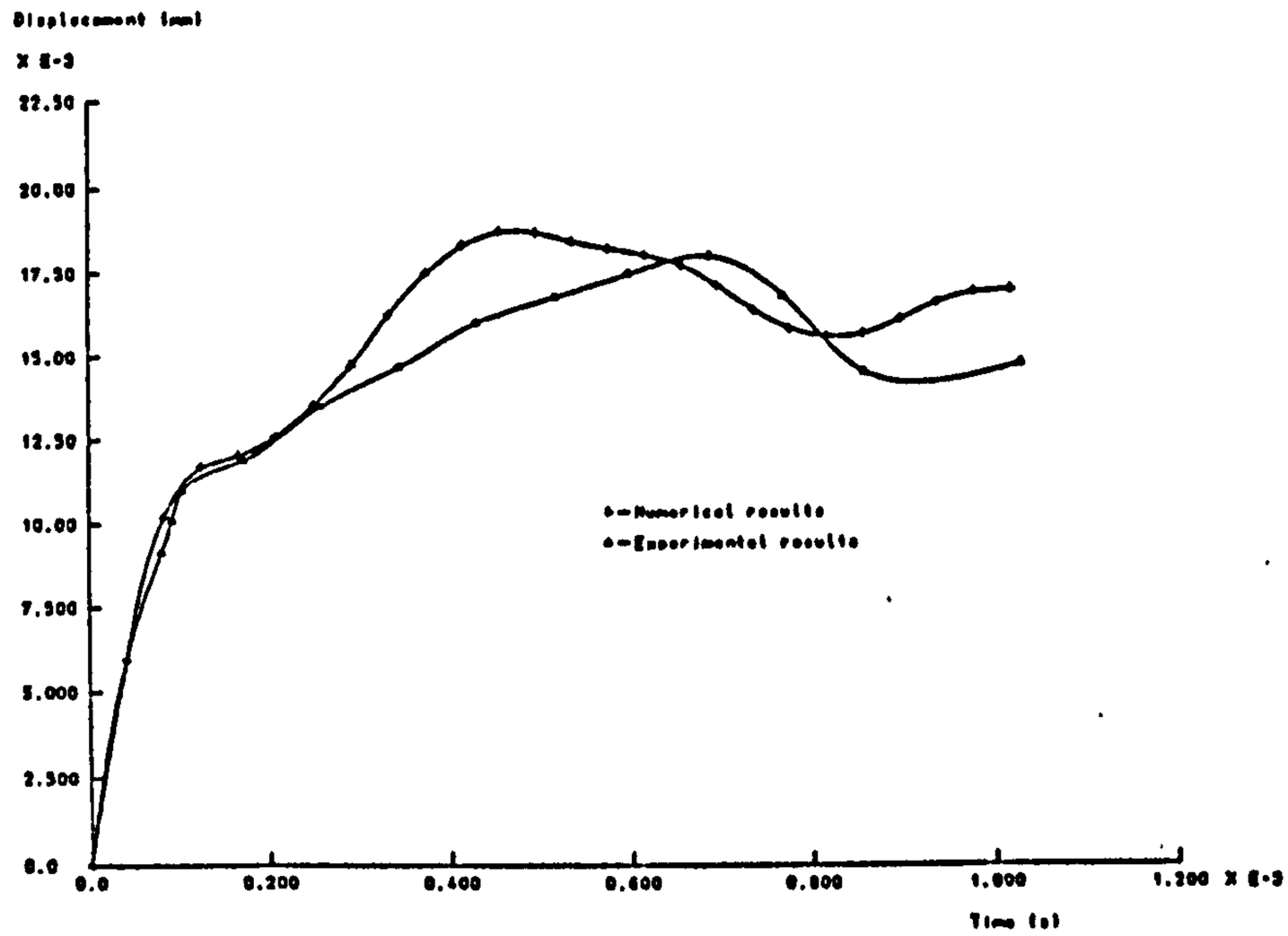

Figure 4.46
Variation of midspan displacement with time for an impulsively loaded beam

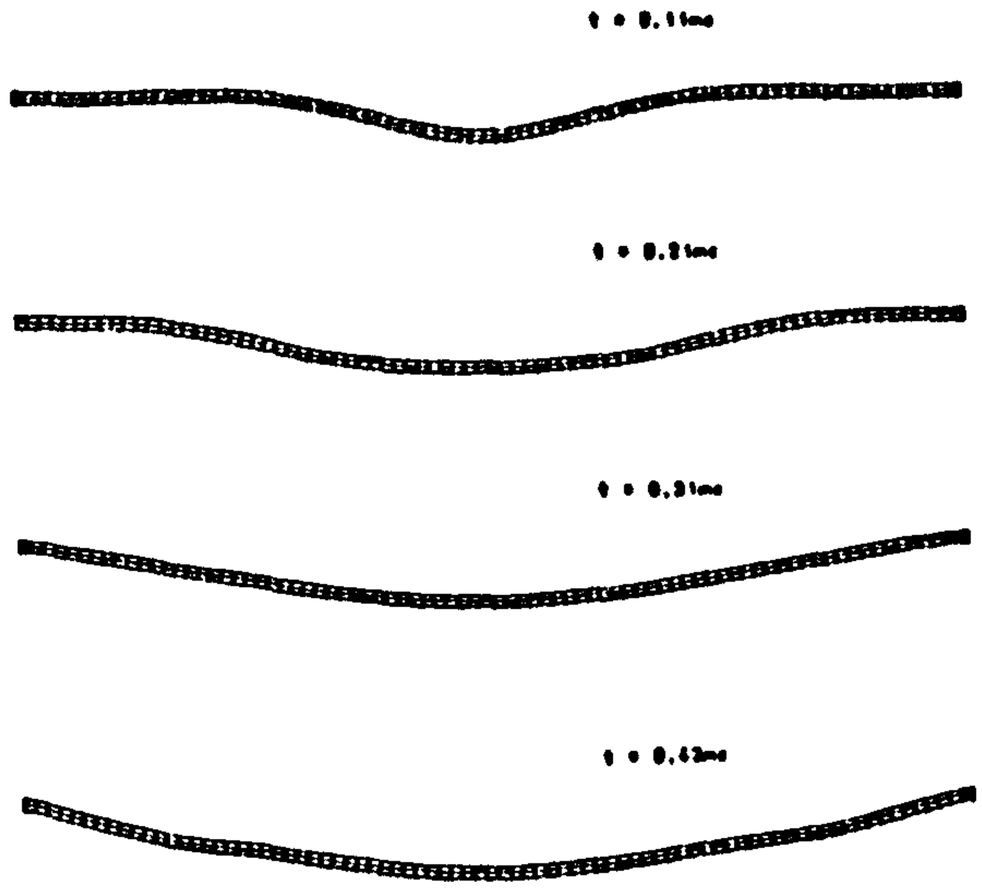

Figure 4.47
Deformation sequence for an impulsively loaded beam using the default values of the artificial viscosity coefficients

Figure 4.48
Finite element idealisation of a square plate being struck by a blunt cylindrical projectile

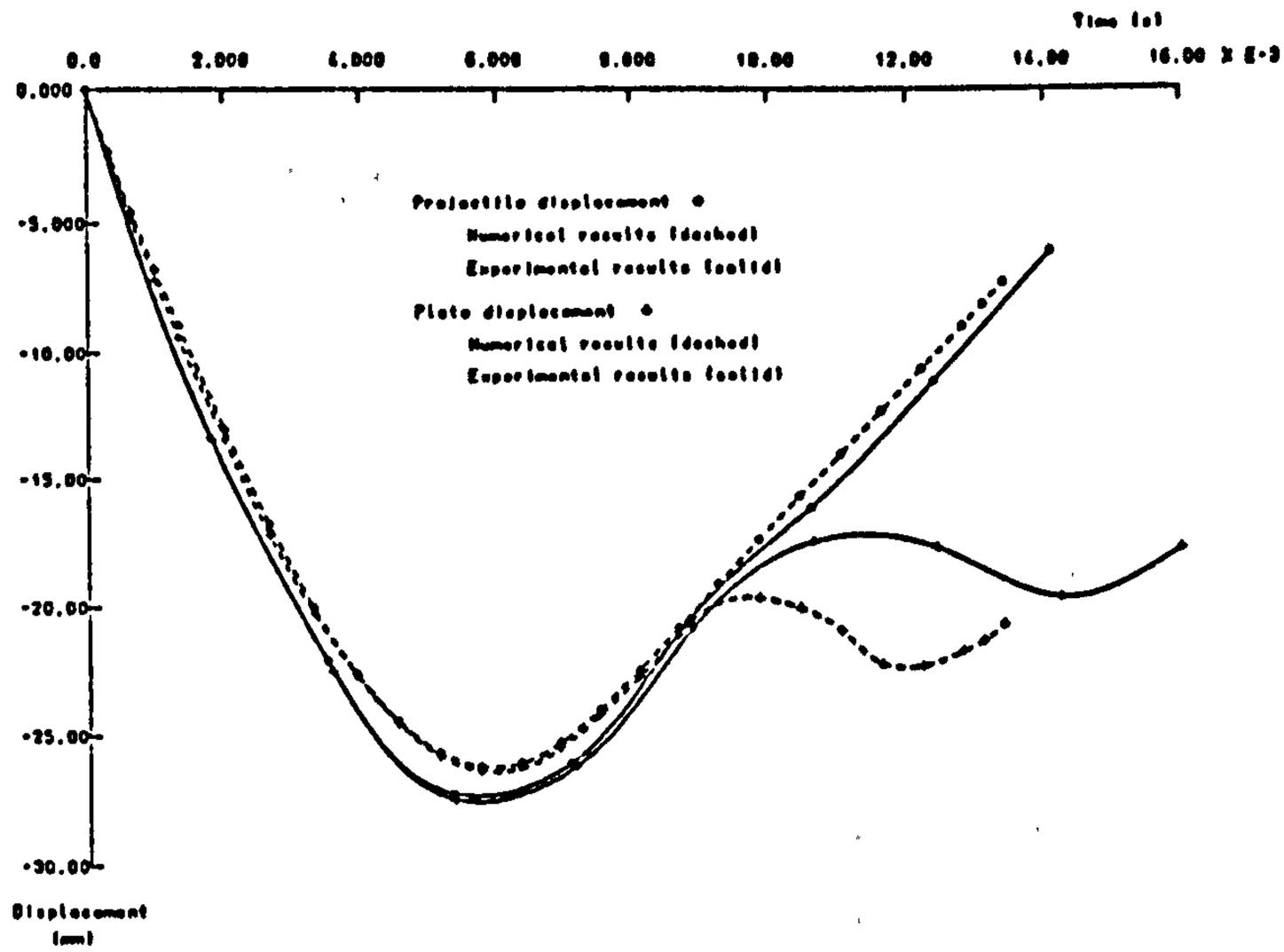

Figure 4.49

Variation of midspan displacement with time for a square plate together with that of the adjacent blunt cylindrical projectile

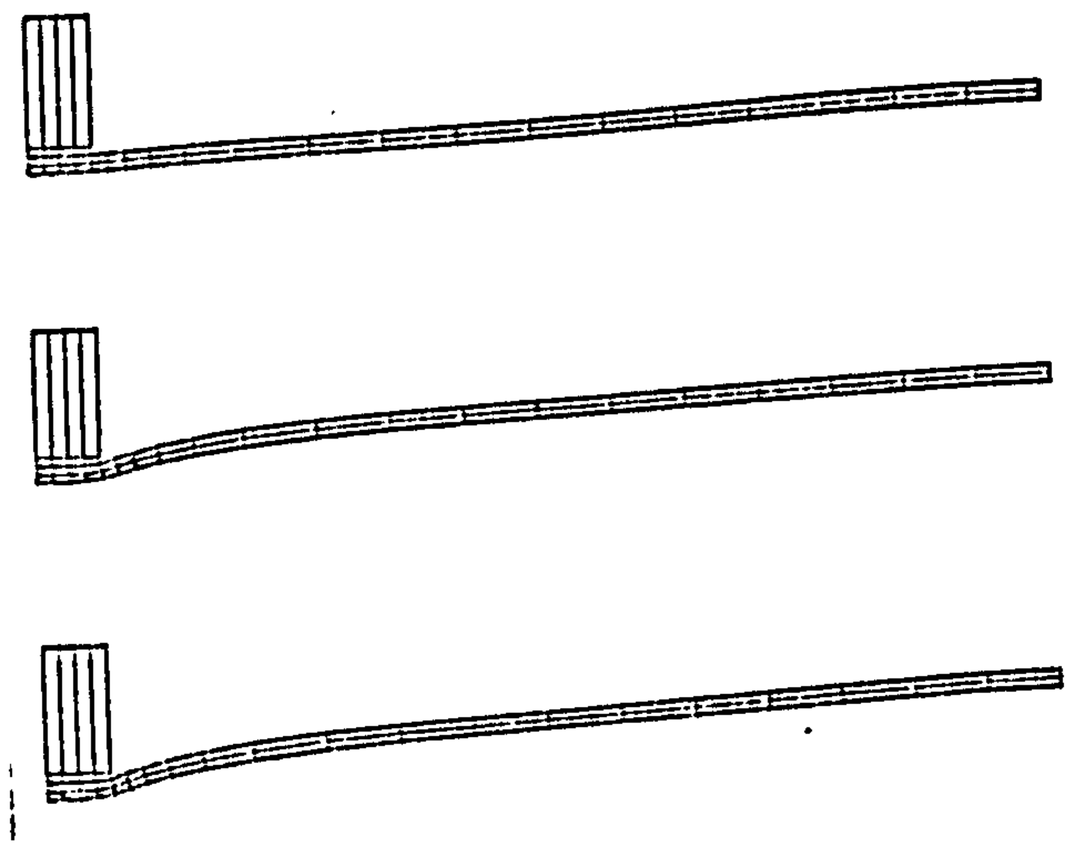

Figure 4.50

Deformation sequence for a square plate together with that of the adjacent blunt cylindrical projectile using the default values of the artificial viscosity coefficients

CHAPTER 5

THE FRACTURE SLIDELINE TECHNIQUE

5.1 INTRODUCTION

Numerous approaches have been suggested for propagating cracks through a finite element mesh. Their classification comprises of two principal groups; the smeared crack and the discrete crack approach.

In the smeared crack approach, elements through which a crack is to propagate have their stiffness matrices modified to simulate displacement discontinuity along the fracture interface. The application of this approach to physical problems involving large relative deformation of the fracture surfaces, however, represents a crude approximation.

A more appropriate approach in the presence of large fracture deformation fields is that of discrete cracking, which is able to simulate the physical behaviour more closely. Several alternative methods has been proposed to implement this approach which include a simple nodal release mechanism for crack extension along lines of symmetry, Siegele and Schmitt (1983) and 'double noding' and 'node grafting' methods to process off-axis crack propagation, Liaw et al (1984), Ingraffea (1977). These techniques have been implemented within implicit time integration schemes and combined with high order elements. Section 2.2.3 explains the limitations encountered with such a combination and, in particular, the prohibitive cost in high velocity impact calculations.

The 'double noding' method, or the ability of a code to allow a node to split upon satisfaction of a predetermined criteria, was the basis for the work performed by Ringers (1983). This recent work extended the 'double noding' method to facilitate the initiation and propagation of fracture surfaces in

an automated manner. The method was implemented within an explicit time integration scheme and utilised the velocity constraint slideline technique (see Section 3.3.2).

A number of deficiencies inherent in both the smeared and discrete crack methods have restricted their usefulness in the study of high velocity plugging failure modes, and may be summarised in the following;

(i) The very large relative sliding distances of the adjacent failure surfaces present during the shear band process dictates modelling by a discrete cracking process.

(ii) In the numerical simulation of ballistic impact the thickness of shear bands are of the order of microns, whilst a typical mesh designed for such use incorporates finite element dimensions measured in hundreds of microns. The simulation of fracture along element boundaries only, as required by the discrete crack approach is, therefore, a reasonable assumption in the presence of shear band regions two orders of magnitude smaller than the element dimensions.

(iii) The fine mesh discretisation which is characteristic of high velocity impact modelling enables the high stress concentrations in the vicinity of the fracture region to be adequately resolved with no special element requirements.

(iv) The limitations imposed on the maximum time step to ensure that the crack propagation occurs as soon as the solution predicts, renders the use of an implicit time integration scheme impractical.

(v) The limitations of the velocity constraint method used in Ringers' work have been described in Sections 1.4 and 3.3.6 and should be consulted for further reference.

For these reasons, the penalty-based slideline algorithm as discussed in Chapter three, which is itself a 'double noding' type method, will be used in this work to extend the capability of these discrete methods. The proposed method will henceforth be termed the "fracture slideline" method. There are several reasons, in addition to points (i) to (v) above, for using this algorithm, namely;

(i) The application of the penalty-based algorithm to fracture simulation in the high velocity impact regime has not previously been investigated in spite of its characteristic stability and robustness. A large amount of commercial interest is currently being shown in the application of numerical methods to plate impact problems and this extension would represent a significant contribution in facilitating the simulation of penetration and perforation.

(ii) With the exception of Ringers' work, the automatic generation of fracture surfaces during a solution is presently only possible in conjunction with a restart facility, whereby the solution is stopped, the required modifications included into the database dump, and the computations resumed. The manual intervention by the user is thus considerable, requiring a priori knowledge of the appropriate times at which such a dump is to be performed. The restart facility is most useful in the multiple impact between several bodies in succession such as the case of multi-layered shell structures impacted by a projectile, wherein the interval between impact of each successive surface is more readily located. The use of this method is obviously not possible for the study of plugging without incurring serious overheads in computational effort.

(iii) The penalty-based slideline technique provides the additional facility to model shear force effects along the plug/plate interface.

(iv) To the authors knowledge, no quantitative results exist in the application of any slideline method to the shear plugging failure mode.

The principal features of the proposed fracture slideline method are as follows. For each time step, a number of pre-determined fracture criteria are applied to every node to detect for the occurrence of failure. The node at which failure occurs is automatically replaced by two nodes. In this manner a segment definition node is generated which defines both the new contact segment and signifies the present limit of crack growth. This segment definition node is appended to the slideline database to redefine the fracture surface. Growth of the crack continues as this new slideline is extended until fracture of the distal face is detected. The fracture calculations are terminated subsequent to the processing of the distal fracture node.

The fracture slideline technique consists of three principal areas of development; the failure criteria, fracture slideline adjunction, and the database structure. Each will be discussed in turn.

The ensuing discussions will use a typical impact configuration consisting of a target plate of two layers of elements being impacted by a blunt cylinder. A partial view of the initial arrangement is shown in Figure 5.1.

5.2 FAILURE CRITERIA

The most serious limitation of high velocity impact codes is the uncertainty in the material response description with regards to failure. In dynamic failure a range of damage is possible, the damage growing as a function of time and applied stress. As damage grows, material stiffness decreases so that even incipient

damage levels can be important. Simple, empirical failure models of varying degrees of complexity exist and have been applied successfully in this regime. For the most part, though, failure criteria and models are of an ad-hoc nature, lacking the micromechanical basis to comprehensively treat problems involving brittle, ductile and shear failure.

There are a number of failure descriptions used in currently available codes, and are generally grouped within three categories; simple time independent criteria, time dependent criteria incorporating damage at a structural level and micromechanical fracture criteria.

Despite the fact that material failure is a time dependent process, most production calculations are performed with simple time independent criteria based on maxima or minima of field variables (such as maximum tensile stress or maximum shear strain). Computer simulations of ordnance impacts using an incremental elastic-plastic material model have yielded excellent results when used in conjunction with a simplistic description of material failure in this way. This approach is popular, not only because of the lack of any realistic alternatives but also the code efficiency resulting from the compact material characterisation. Moreover, recent discussions among material model developers have emphasised that the shear band phenomenon is essentially a plastic process and as such, path dependent. The use of an effectual plastic flow rule should, therefore, lead to these shear band instabilities without the inclusion of special material damage parameters (1983).

Time dependent initiation criteria represent the next level of sophistication and have been successfully applied to numerous fracture problems. One of the earliest is the Tuler and Butcher model, Kimsey (1983), in which failure is assumed upon the occurrence of a critical value of a damage parameter. The principal application of this model has been predominantly in spall failure.

A damage model for fracture has also been recently developed by Johnson (1982). It has the capability to take into account the effects of strain, strain rate, temperature and dimensionless pressure; variables which are readily available in impact codes of this type. The model is path dependent and requires only one history variable per element, thus making the scheme ideally suitable for the high velocity regime. It is being actively evaluated at present, Johnson et al (1983), and a series of extensive material tests have been undertaken for a number of commonly used materials to quantify the five material parameters required.

Micromechanical failure theories, however, are seen to be the ultimate solution to this problem in which the nucleation of fracture surfaces are considered at the atomic level and where crack growth proceeds by experimentally determined rate equations. These models are currently in the developmental stages and their use is limited to cases in which no macroscopic crack is present but where failure occurs through the nucleation, growth, and coalescence of millions of microscopic voids. Examples of such a situation include the ductile failure of a smooth bar in tension. Unfortunately, such an analysis currently requires too complicated a material representation for efficient use in this work, Goldsmith (1983).

It should be noted that since failure occurs by a variety of interrelated mechanisms it can be expected that different forms of criteria will be appropriate at different times in the solution process. It is postulated that the combination of a comprehensive micromechanical material model able to distinguish between the numerous failure modes, together with a solution procedure having the fracture slideline capability as described in this work would represent a significant advancement in the ability of numerical codes to analyse problems involving failure.

The failure criteria used in this work are based upon investigations performed by Ringers (1983) and which essentially represents a time independent model using the Von Mises

equivalent strain as the failure measure. Geometric criteria accompany this continuum model and express an effective 'natural' failure mode in the region of interest.

The criteria differs in this work from that of Ringers with respect to the equivalent strain measure. This measure is path independent and as a consequence may either increase or decrease and cannot properly be used to indicate material failure. It is thought that its use accounts for the incorrect initial fracture location on the frontal surface experienced in the investigatory test results obtained by Ringers. The effective plastic strain measure is used in this work, ensuring both path independence and promoting a more stable growth of the fracture surface through the material.

The dominant criterion is thus the effective plastic strain and is compared with the user defined failure threshold each time step to detect the occurrence of failure. For each element exceeding this threshold the magnitude of the element shear stress is also checked. This value is required to be greater than both the magnitude of the axial and radial deviatoric stresses respectively. The requirement of a critical relative value of shear stress is to further verify that a shear band formation is being treated and not another highly strained part of the body. This essentially represents a maximum shear stress criterion and is specifically included to treat shear plugging situations.

If these continuum based tests are satisfied further geometric tests are then required, the discussion of which may be subdivided into three groups. A description of the failure criteria, together with these geometric tests is summarised in Table 5.1

5.2.1 Nodal fracture initiation

The object of this test is to obtain, from the four nodes contained within the failed element, the most likely candidate contact node at which to commence cracking. The element node at which the greatest internal force is experienced is chosen to

signify the mesh location at which initiation of failure is to occur. The inclusion of additional forces into the element internal force vector to treat the interface conditions makes this a reasonable choice.

Experimental observations show that a shear band is initiated from the frontal surface. Therefore, a secondary test is performed on each candidate failed node to establish its association with the previously defined surface contact nodes. Only if the candidate failed node has been defined as a surface contact node will the criterion be satisfied.

5.2.2 Failure propagation

Fracture is seen to propagate towards the distal surface in a continuous manner during experimental testing and is simulated here by ensuring that the crack propagates from the last defined node on the current failure surface, that is, the segment definition node.

In high velocity impact which is dominated by the plugging mode of failure, the amount of shear in the crack region is significant and circumstances would often permit a crack to actually proceed in opposition to the actual motion of the problem (Figure 5.2). The further restriction of the propagating crack to proceed with no changes in direction greater than 90° prevents this occurrence.

5.2.3 Direction of fracture propagation

The direction of fracture is determined only for those nodes satisfying the nodal fracture propagation criteria, and is computed using the strain rate values of the failed element. If the magnitude of the radial strain rate is greater than the magnitude of the axial strain rate, fracture continues to the nearest axial node (Figure 5.3). Otherwise fracture is to the nearest radial node.

The direction of fracture may be determined from the nodal

forces, however, results obtained using nodal forces for this purpose have shown that the crack frequently propagates in a different direction to the thrust of the problem, Ringers (1983). The fluctuations in the nodal forces were seen to be the principal cause of this discrepancy. In comparison, however, the strain rate was found to provide a significantly more stable basis in determining the fracture propagation direction. This stability is undoubtedly due to dependence of strain rate on the kinematic parameters of the individual element rather than the averaged nature of the derived nodal internal forces.

The unrealistic failure modes in which the direction of a crack changes by greater than 90° requires the use of a history variable, that is a definition of the unit tangent vector to the previous local segment. A simple vector product between both the current and previous tangent vectors acts efficiently as a basis to eliminate any false fracture directions.

5.3 SLIDELINE ADJUNCTION

The dynamic addition of sliding surfaces may be further segregated into three sections for simplicity. The procedures for nodal crack initiation, nodal crack propagation and distal face fracture.

5.3.1 Nodal fracture initiation

Consider the schematic diagram of a finite element mesh in the region of the projectile periphery (Figure 5.1), showing a assumed initial configuration. Assume that element F has satisfied criteria [1a] and [1b], and that node k has satisfied criterion [1c]. The satisfaction of criterion [1d] is obviously satisfied directly.

With this arrangement, node k is defined as the location of initial fracture, and the method essentially creates a new node within the system. The terms used in the ensuing discussion are

taken from Ringers report.

Upon fracture detection, a 'new' node is created and assigned the next available node number. The original node (henceforth, 'split' node) retains its node number. The relevant nodal system arrays are first increased in size and then updated with this new information.

Figure 5.4 depicts the updated mesh formation after splitting has occurred, showing the split node and the new node. The 'next' node will be discussed in the following section. These three nodes are appended to the surface interaction table and the corresponding arrays, any subsequent slideline processing will then include this new surface. Figure 5.5 shows the modified definition of slideline surfaces at this same stage. The portion of surface two lying to the right of surface four, although defined initially, will be outside the range of the zonal contact detection test and is excluded from further discussions. It is not deleted from the calculations so that deformable projectiles may be considered.

The question of the definition of the new and split nodes is an important point in the success of the method, since an incorrect designation of these nodes confuses the slideline detection routines.

Figure 5.6 indicates this problem. The surface gap is exaggerated for clarity and the dotted line represents the frontal slideline surface of the target. At some stage in the solution, subsequent to fracture, the definition of the slideline will cause a non-physical boundary condition (n_j-n_k) to be imposed on node o resulting in an intolerably high degree of mesh deformation. Furthermore, no displacement restrictions in the axial direction will be experienced if the impact momentum is sufficient for node o to pass through this boundary since node v is not included in the initial surface 1 slideline definition.

The redefinition of the slideline is one alternative to this problem but requires additional computational effort and, indeed,

is not necessary if the definition of the new and split nodes is performed with care. Figure 5.7 shows the current method, in which the definition of the discontinuity n_k-n_l on the frontal surface ensures that node o will be correctly restrained in the axial direction at all times.

5.3.2 Failure propagation

Consider the plate impact situation at a later stage in which extension of the crack is now required (Figure 5.4). Assume that element C has satisfied criteria [2a] and [2b]. The concept of allowing the crack to proceed only from the next node is now obvious since growth from any other node would create a completely new fracture surface, a result only present in adiabatic plugging failures. Further, let criterion [2c] be satisfied in node g, with the direction of crack propagation assuming the same previous axial mode and thus satisfying criterion [2d].

The new and split nodes arising from the next node g are now defined as before, while the direction of fracture yields the axial node c as the next node. The necessary modifications to include the additional slideline surface variables in both the slideline database and the finite element system arrays are made and the computations resumed. The configuration is shown in Figure 5.8.

It is the observation that the fracture surface propagates at the rate of one element per detected element failure which further dictates both the temporal integration scheme and the degree of spatial discretisation utilised. The rate of growth of a fracture slideline is of paramount importance and would not be resolved adequately within an implicit context and, as such, an accurate indication of each nodal splitting time would not be available. Furthermore, accuracy will be enhanced with finer mesh descriptions.

5.3.3 Distal face fracture

Crack propagation may continue through the mesh to a point whereby a node lying on the distal surface defines the next node and a complete separation of the plug is imminent (Figure 5.8). Detection of such a node is accomplished easily with the use of the element connectivity table (Section 5.4). In this configuration the current crack direction cannot be defined and requires that criterion [2d] be ignored.

The occurrence of distal face cracking terminates the failure criteria tests and the solution proceeds normally with no further reference to the fracture slideline routines. The fracture surface developed to that point is, of course, retained in any subsequent processing.

5.3.4 Discussion of slideline adjunction

The methodology of fracture slidelines described thus far has been limited to the occurrence of only one failure surface during each solution. However, the method does not preclude the simultaneous growth of several such surfaces. This is rarely encountered in practice except for stress fields in which adiabatic shear failure is excited, and is a state beyond the scope of this work. A major contribution to this flexibility has been the development of a suitable database structure with specific reference to the slideline technique.

5.4 THE DATABASE STRUCTURE

The dynamic location of sliding surfaces in a finite element mesh will be discussed from the standpoint of the underlying storage and data manipulation facilities. The specific requirements for the fracture slideline database and the modifications required in the system arrays are separated for clarity.

5.4.1 Fracture slideline database structure

Discussion of this subject is extended from the basis given in Section 3.5.

Consider the plate impact situation of Figure 5.5, where the contact surfaces are denoted. At input, surfaces 1 and 2 are defined in terms of an orderly arrangement of the contact nodes (Section 3.4.1) and represent the interaction between the blunt face of the projectile and the frontal surface of the plate. Together, these surfaces constitute slideline 1. Slideline 2 represents the interaction between the projectile perimeter, surface 3, and the circumferential failure surface of the plate, surface 4, exposed during the formation and ejection of the plug. The nodes defining contact surface 3 are currently defined by the user during the input stage but may just as easily be accomplished in an automatic fashion. The contact nodes corresponding to surface 4 which complete this particular slideline are dictated by the solution process and consequently will not be known a priori. Finally, slideline 3 represents the interaction along the fracture surfaces generated during the solution and comprises of surfaces 4 and 5. Both surfaces are appended to the existing contact tables in a manner which will be discussed later in this Chapter.

A surface interaction table is used to define those surfaces permitted to interact. The procedure by which this table points to the required data has been previously discussed in Section 3.5.

Figure 5.10 depicts an initial slideline pattern, whose database arrangement is shown in Table 5.2. The array names have been defined previously and the nodal data i,j,... represents that data specifically related to node i,j,... as given in Table 3.4.

Upon satisfaction of the crack initiation criteria the finite element mesh is modified locally as shown in Figure 5.4, creating surfaces 4 and 5 and permitting both slidelines 2 and 3

to be defined. Table 5.3 describes the slideline database at the end of this stage together with the associated data for each newly defined contact node.

The initial creation of slidelines 2 and 3 leaves a common contact node which has been termed the segment definition node. The presence of this node (node g), serves to indicate that the fracture propagation criteria is required, and is itself the designated node from which the crack must propagate. Figure 5.8 shows the final result of an axial crack satisfying this criteria, while Table 5.4 represents the corresponding database modifications.

Incipient separation of the plug is the last operation to be discussed with respect to database augmentation. It is detected when the next node also represents a distal surface node. Only minor modifications of the fracture slidelines are necessary at this point since the definitions of a crack propagation direction and the subsequent contact segment node are not meaningful. Figure 5.11 indicates the final modified mesh in which node c is split and substituted with node x in the usual manner.

Note that the slideline database size need only be increased when a new slideline is defined and the number of contact nodes on any one surface exceeds the locations currently available. Generally, the number of database manipulations are dominated by the former.

5.4.2 The element connectivity table

The fundamental process by which the fracture slideline method is monitored has been given. One further development now remains, its motivation originating from the following numerical situations, viz;

(i) On detection of element failure, the adjacent element number is used to provide a correct definition of the master and slave elements. For instance, if the initial configuration of Figure 5.1 is considered and node k of

element F has been defined as satisfying the failure criteria, then an efficient method of obtaining the adjacent element number E is necessary.

(ii) The dynamic creation of slidelines requires that certain element arrays be updated, the element node number array being one particular example. Consider a radial fracture commencing from node g (Figure 5.9), from which it is clear that only element array F requires the substitution of node w for node g. The differing crack growth history depicted in Figure 5.8, however, requires that both elements C and F are modified in this respect. The element arrays requiring modification thus alter with the crack direction. The determination of these particular element numbers in an efficient manner is important.

(iii) A simple check to detect incipient plug separation should also be included so that further computations within the fracture slideline routines may be halted.

(iv) The criteria to restrain crack propagation to physically realistic directions requires a history variable to accurately describe the crack direction during the previous node splitting operation.

Together, these problems represent serious deficiencies with respect to the numerical efficiency, typically overcome by a global search through the mesh at each occurrence or, alternatively, a severely restricted spatial discretisation. This work demonstrates the effective use of an element connectivity array.

Consider the partial view of a typical finite element mesh as shown in Figure 5.1. Table 5.5 shows the corresponding element connectivity array, LCONEC, for element B.

The general table arrangement is shown in Table 5.5-(I) where, for each of the four element nodes i, there are three

element numbers defined, corresponding to those elements which share node i, in the radial, central and axial directions. Note that the node pointer is based upon the element node numbering sequence, in which the radial direction is that experienced when moving from the first defined node to the second. Evidently the nodes b-c define the radial direction for element B.

The procedure to obtain the current adjacent element number requires only the current failed node pointer of the failed element and the current crack growth direction. Each of these variables have been derived in previous calculations and are readily available without extra effort. By way of example consider Figure 5.8 and assume node c of element B has satisfied the crack propagation criteria with an axial mode of failure. In this instance the nodal pointer is 2 and the adjacent element is given as C.

The central node is included in the connectivity array to permit the direct determination of all elements containing the failed node. The current and previous crack direction variables are used to determine the orientation of the required elements with respect to the failed node for any crack.

It may be seen that both the axial and central nodes are set as null values for element nodes lying on the distal surface (nodal positions 1 and 2). The distal surface node check now becomes a simple examination of the adjacent axial element number for each failed node, prior to node splitting.

The negative sign before certain element numbers, together with the local element axis system assumed here, indicates the disposition of the crack with respect to the adjacent element. A negative prefix to an element number indicates that the adjacent element is in the negative local direction with respect to the current failed element. The association of the new and split nodes is thereby facilitated and non-physical boundary conditions avoided (see Section 5.3.1).

The use of the element connectivity array has been found to

be a most efficient method for storing the necessary mesh topological data. In terms of the degree of flexibility, it is a rudimentary method by virtue of the sole usage of the four node quadrilateral element, although the concept may obviously be extended to higher order elements.

Each element array is compiled on an element level at the commencement of each fracture slideline problem and contains 12 locations. The benefits obtained in terms of speed outweigh the small proportion of memory which is consumed.

5.4.3 System array modification

The requirement for the dynamic expansion of the global nodal arrays is detected by monitoring each occurrence of node splitting. For all cases, except incipient cracking on the distal face, this represents the only time during the solution that a new node is created.

The new node is assigned the same global coordinates, velocities, and restraint properties as the split node and hence will experience no contact boundary conditions during the time step in which it is created. However, the internal force and mass assigned to the global equations comprising the new and split nodes are based upon the number of elements which now share each node. The relaxation of the interface stiffness will occur automatically during the next time step. It should be noted that the new node retains the values of the mass and internal force of its underlying element.

The equation number and element topology arrays are also adjusted to substitute the next available values for the particular new node.

5.5 CONCLUSIONS

A new fracture slideline method to propagate a fracture through a finite element mesh has been proposed and the principal

facets of the method discussed. The new method utilises the penalty-based slideline technique and represents a discrete crack approach. A number of additional benefits have been achieved over the currently available methods discussed in Section 5.1, and are as follows;

(i) The use of effective plastic strain as the principal failure criteria yields a more stable and accurate representation of damage than the equivalent strain used in Ringers' (1983) work.

(ii) The problem of confusing surface orientation resulting from the very large deformations typical of fracture propagation analyses has been overcome in Ringers' work by the use of interposing surfaces. These surfaces are utilised as a comparison against which a series of numerically expensive tests are performed. These additional computations are not required in the present work by virtue of the zonal contact detection test (as described Section 3.4.3) which ensures that any ambiguities in the detection of contact are virtually eliminated.

(iii) The proposed slideline database accommodates the generation of any number of fracture slidelines during the solution of a problem.

(iv) The implementation of a global element connectivity table has enabled the high level of monitoring necessary in fracture slideline calculations to be achieved with insignificant numerical overheads and, moreover, has met the objectives as described in Section 5.4.2 (i)-(iv).

5.6 REFERENCES

__ (1983). 'General Discussion', Proceedings of the Workshop on the Theoretical Foundation for Large Scale Computations of Nonlinear Material Behaviour, Evanston, pp 177-181, Nemat-Nasser (Editor), Martinus Nijhoff Publishers.

Goldsmith, W. (1983). 'Prepared Discussion', Proceedings of the Workshop on the Theoretical Foundation for Large Scale Computations of Nonlinear Material Behaviour, Evanston, pp 181-186, Nemat-Nasser (Editor), Martinus Nijhoff Publishers.

Ingraffea, A.R. (1977). 'Nodal Grafting for Crack Propagation Studies', Int. J. Num. Meth. Engg., Volume 11, pp 1185-1197.

Johnson, G.R. (1982). 'Status of the EPIC Codes, Material Characterisation and New Computing Concepts', Proceedings of the Army Research Office Workshop on Computational Aspects of Penetration Mechanics, Chandra and Flaherty (Editors), Springer-Verlag, New York.

Johnson. G.R. and Hoegfeldt, J.M. and Lindholm, U.S. and Nagy, A. (1983). 'Response of various metals to large torsional strains over a large range of strain rates - Part I : Ductile metals', Trans. ASME., J. Engg. Mat. Tech., Volume 105

Kimsey, K.D. (1983). 'Calculation of Penetration', Proceedings of the Workshop on the Theoretical Foundation for Large Scale Computations of Nonlinear Material Behaviour, Evanston, pp 165-181, Nemat-Nasser (Editor), Martinus Nijhoff Publishers.

Liaw, B.M. and Kobayashi, A.S. and Emery, A.F. (1984). 'Double Noding Technique for Mixed Mode Crack Propagation Studies', Int. J. Num. Meth. Engg., Volume 20, pp 967-977.

Ringers, B.E. (1983). 'New Sliding Surface Techniques enable the Simulation of Target Plugging Failure', Ballistic Research Laboratory, Aberdeen Proving Ground, Maryland, Report ARBRL-TR-02541.

Siegele, D. and Schmitt, W. (1983). 'Determination and Simulation of Stable Crack Growth in Adina', Comp. Struct., Volume 17, Number 5-6, pp 697-703.

TABLE 5.1

Shear Plugging Failure Criteria

Criterion 1 : Nodal Fracture Initiation

[a] The effective plastic strain of the associated element is greater than a specified value

[b] The magnitude of the shear stress of the associated element is greater than the magnitude of its radial and axial deviator stresses

[c] The node experiences the highest internal force of the element

[d] The node is a contact node

Criterion 2 : Nodal Fracture Propagation

[a] The effective plastic strain of the associated element is greater than a specified value

[b] The magnitude of the shear stress of the associated element is greater than the magnitude of its radial and axial deviator stresses

[c] The node corresponds to the segment definition node

[d] The direction of crack propagation does not change by more than 90°

Criterion 3 : Direction of Fracture Propagation

[a] Axial fracture occurs when the magnitude of the radial strain rate is greater than the magnitude of the axial strain rate

[b] Radial fracture occurs when the magnitude of the axial strain rate is greater than the magnitude of the radial strain rate

TABLE 5.2

Slideline Database for Initial Plate Impact Arrangement

I. Surface Interaction Table

	SURFACE POINTER	ADJACENT SURFACE POINTER
ISURFD	1	2

II. Real Nodal Contact Data

	SURFACE 1				SURFACE 2		
ECONTD	i	j	k	l	o	n	m

TABLE 5.3

Slideline database subsequent to initial cracking

I. Surface interaction table

	SURFACE POINTER	ADJACENT SURFACE POINTER
ISURFD	1	2
	3	4
	5	4

II. Real nodal contact data

	SURFACE 1				SURFACE 2		
ECONTD	i	j	k	l	o	n	m
	u	r	o	–	g	v	–
	k	g	–	–	g	v	–

TABLE 5.4

Slideline Database During Crack Propagation

I. Surface interaction table

	SURFACE POINTER	ADJACENT SURFACE POINTER
ISURFD	1	2
	3	4
	5	4

II. Real nodal contact data

	SURFACE 1				SURFACE 2		
ECONTD	i	j	k	l	o	n	m
	u	r	o	–	c	w	v
	k	g	c	–	c	w	v

TABLE 5.5

Typical Element Connectivity table

I. General table arrangement

	NODAL POINTER	ADJACENT ELEMENT NUMBER		
LCONEC	i	RADIAL	CENTRAL	AXIAL

II. Table arrangement for element B

	NODAL POINTER	ADJACENT ELEMENT NUMBER		
LCONEC	1	-A	–	–
	2	C	D	–
	3	C	F	E
	4	-A	D	E

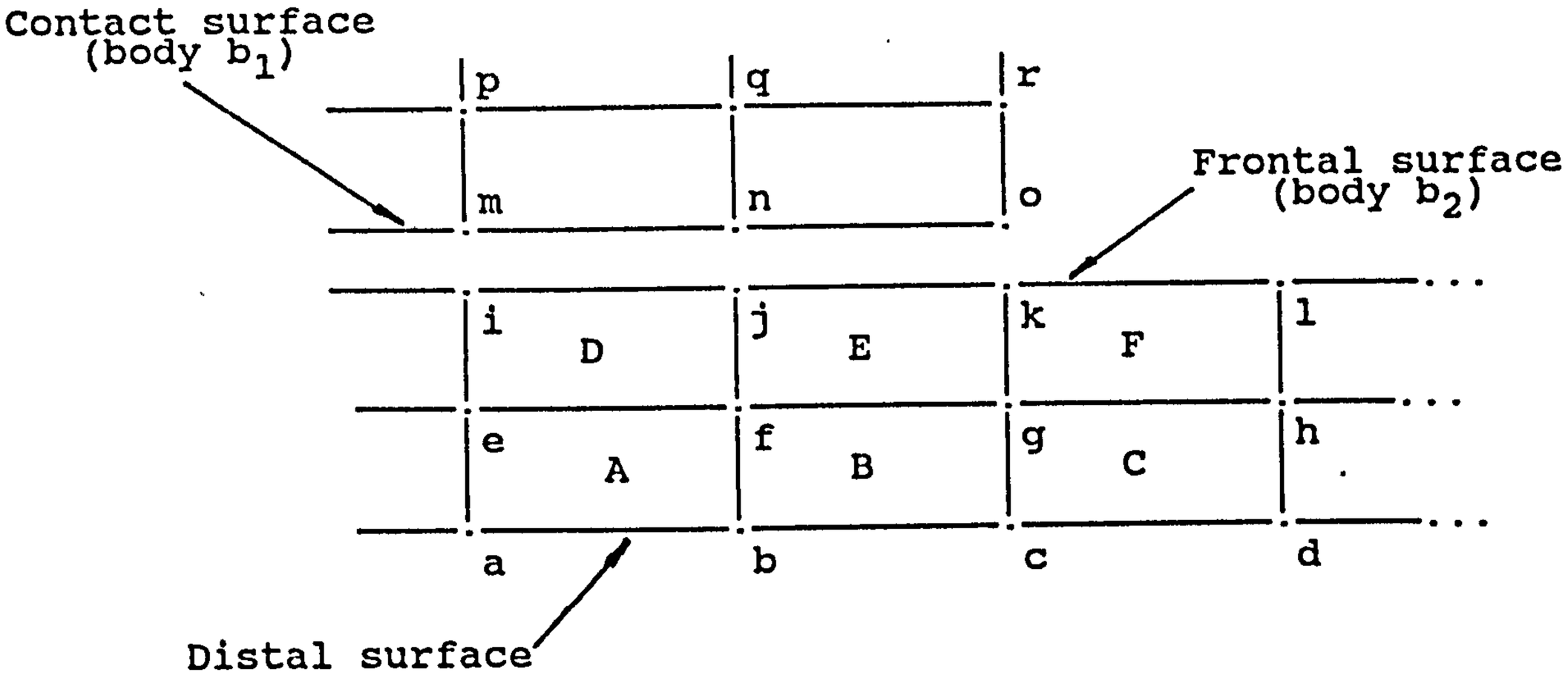

Figure 5.1

Partial view of a typical finite element discretisation for an assumed plate impact configuration

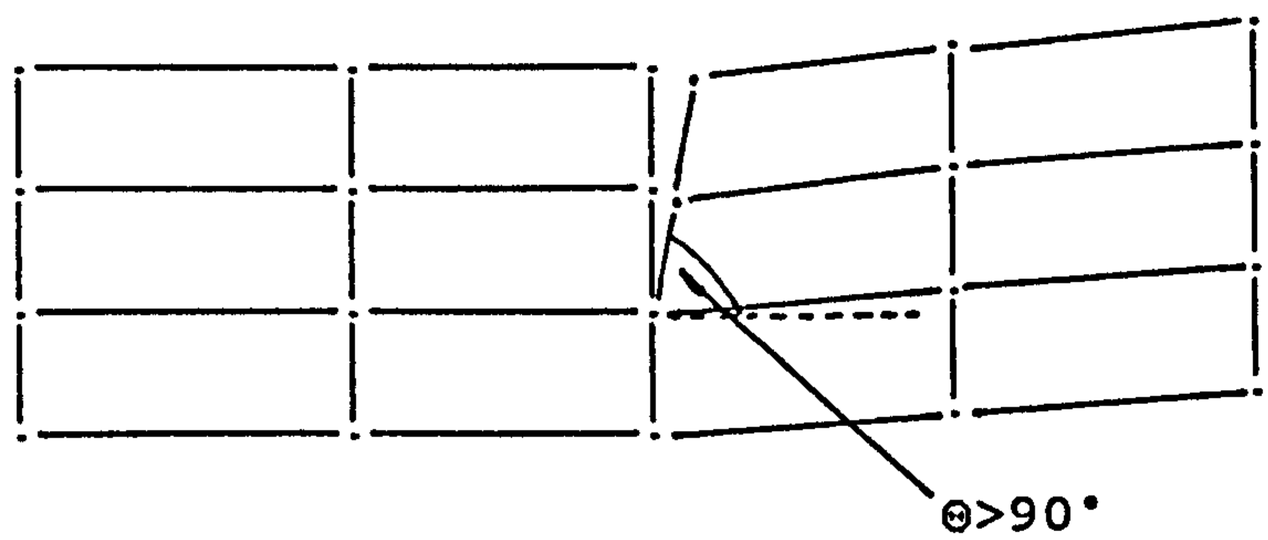

Figure 5.2

Crack propagation restriction

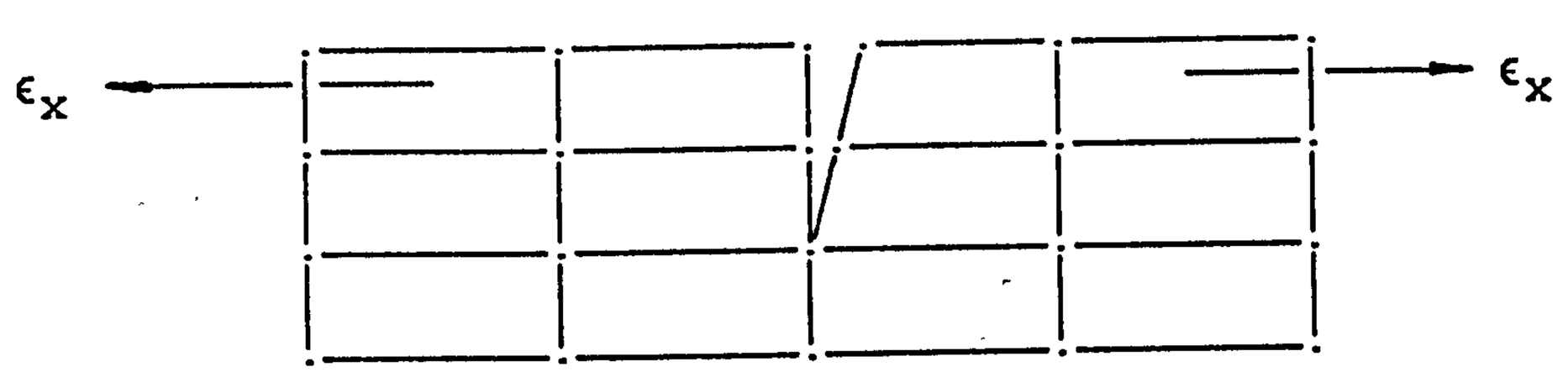

Figure 5.3

Axial fracture mode in the presence of radial strain

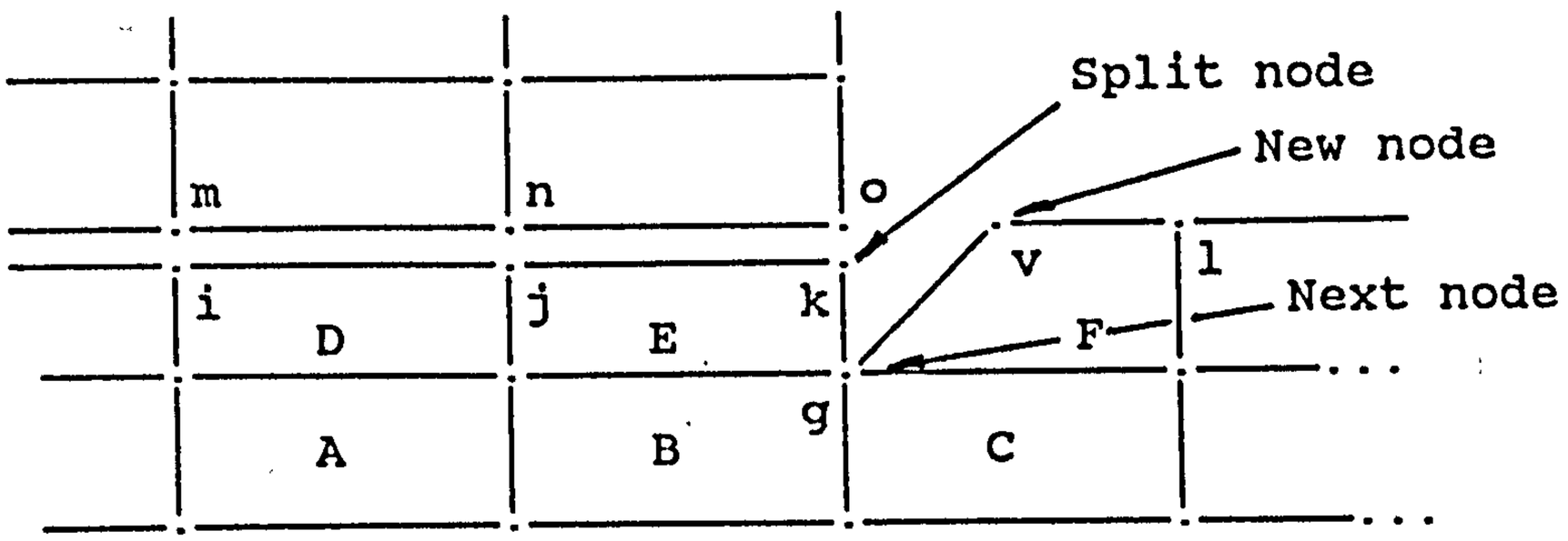

Figure 5.4

Updated finite element mesh subsequent to initial fracture

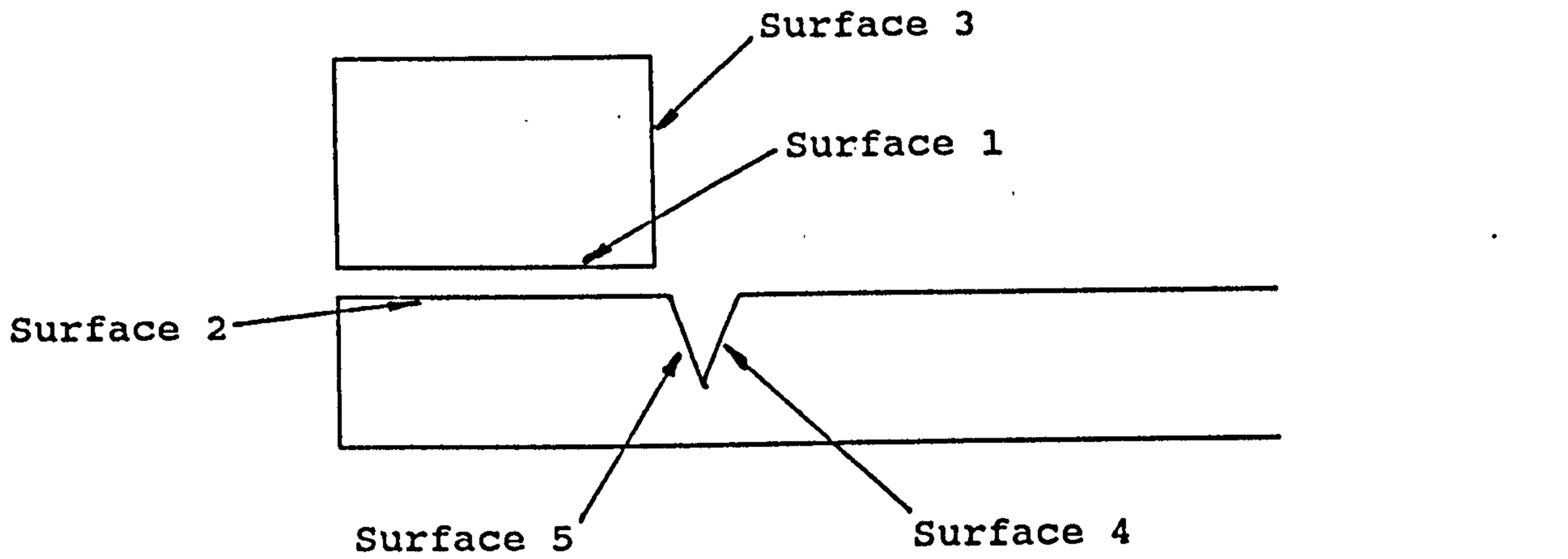

Figure 5.5

Definition of slideline surfaces after initial fracture

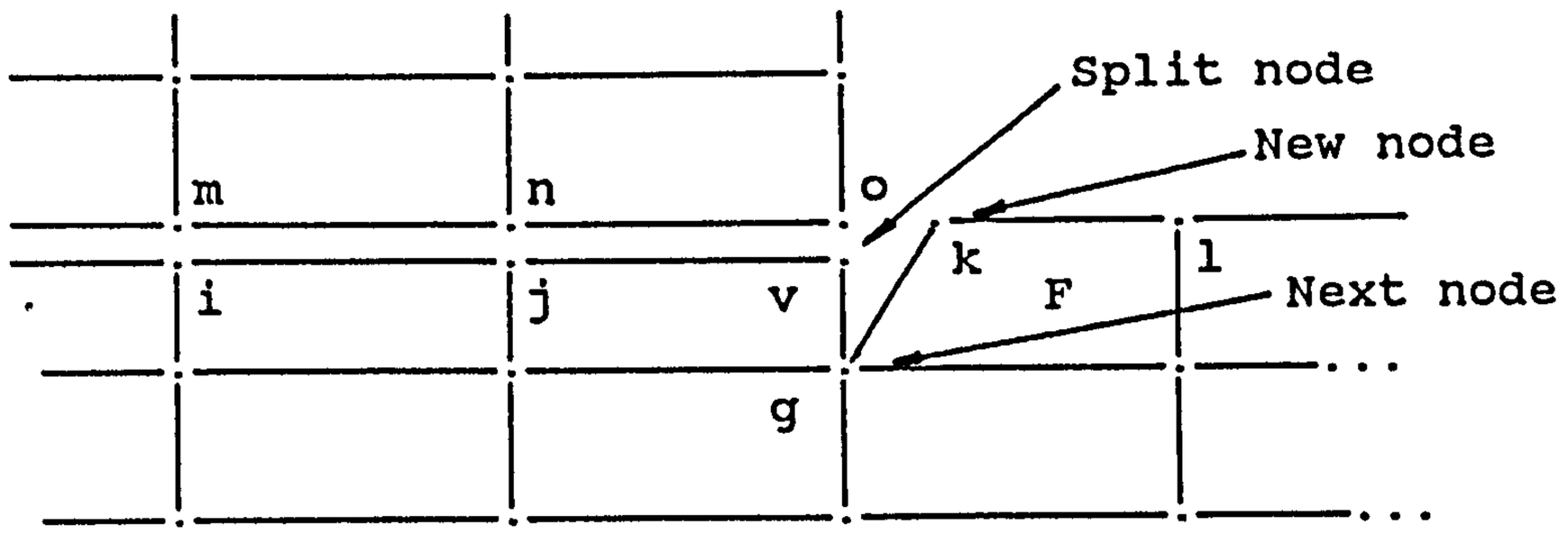

Figure 5.6

Incorrect designation of new nodes

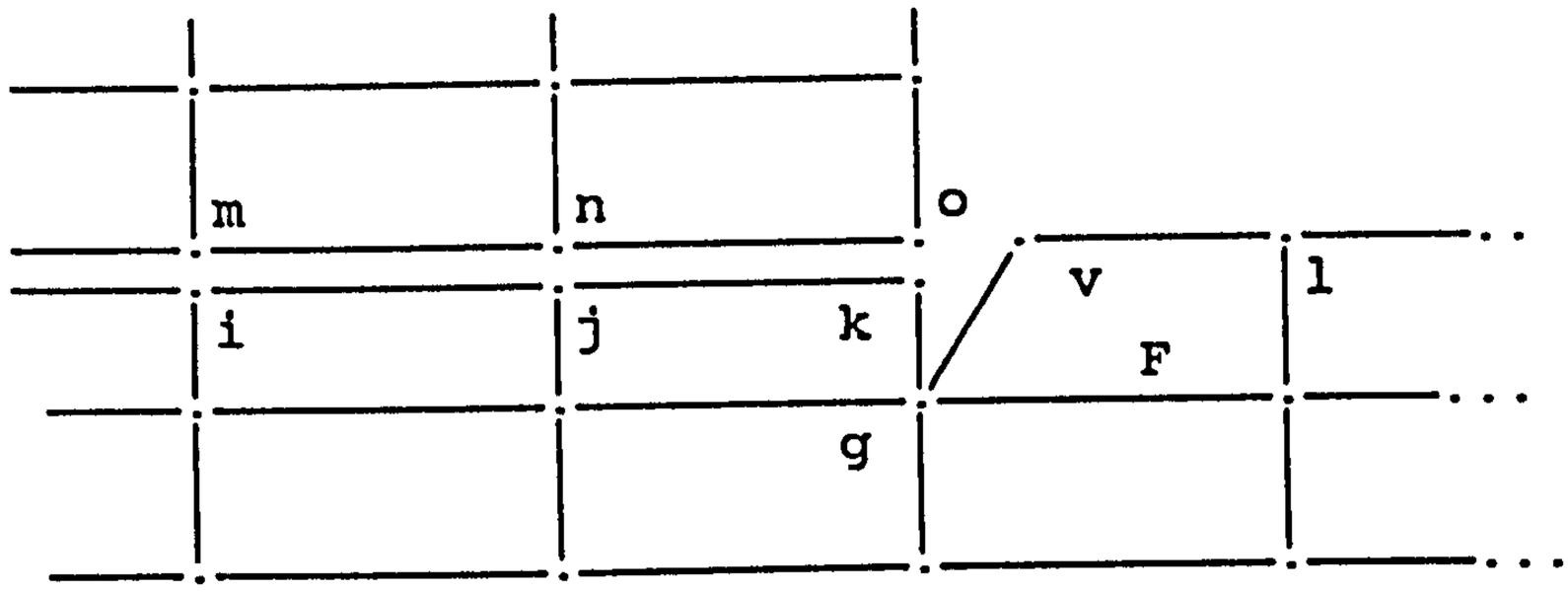

Figure 5.7
Correct designation of new nodes

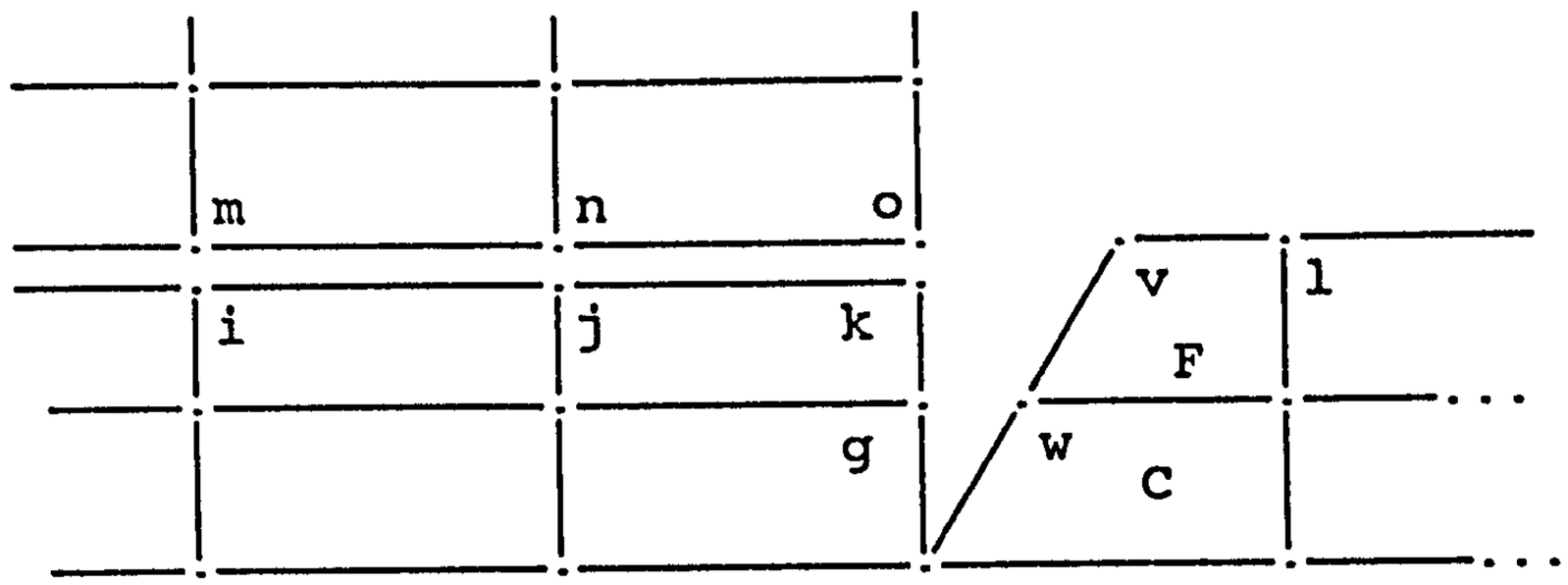

Figure 5.8
Finite element mesh prior to distal face fracture

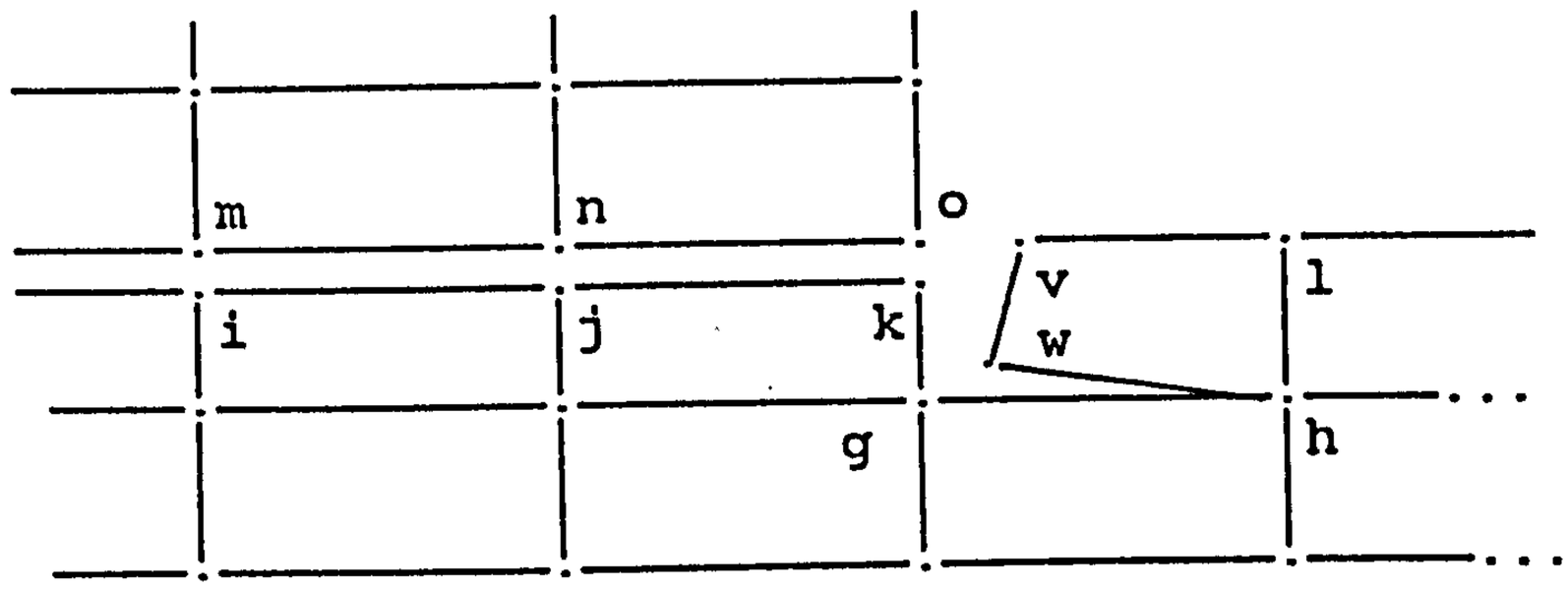

Figure 5.9
Radial fracture propagation

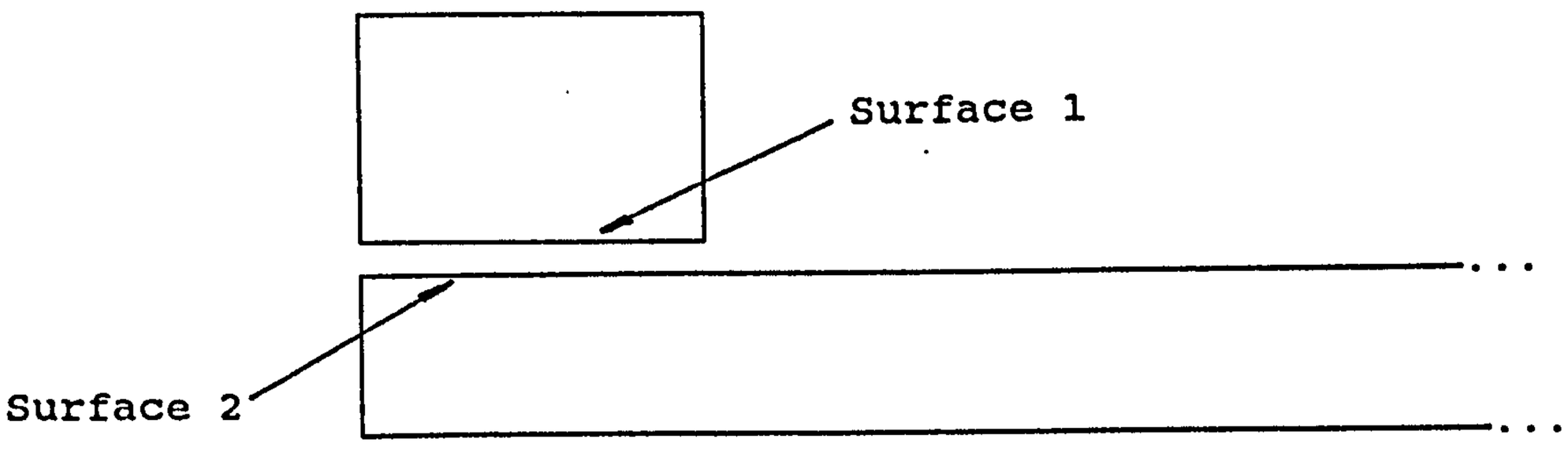

Figure 5.10
Definition of initial slideline surfaces

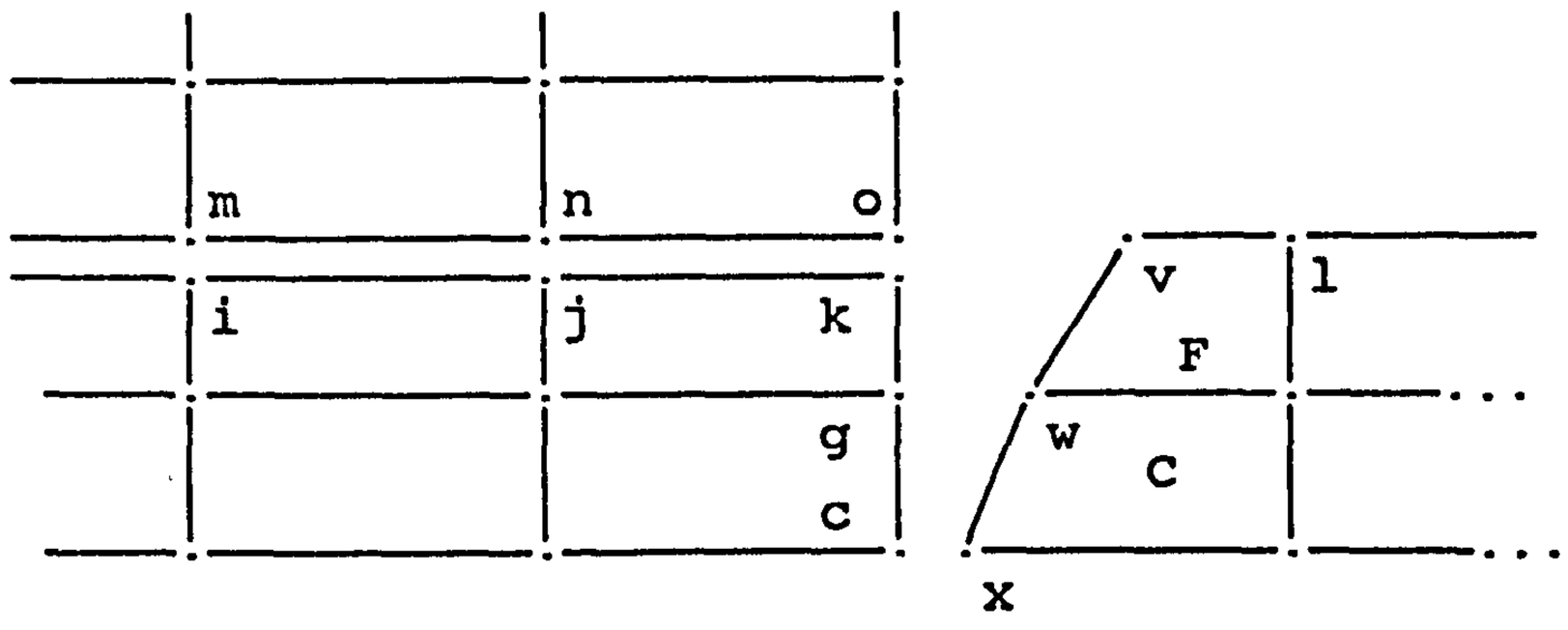

Figure 5.11

Finite element mesh subsequent to distal face fracture

CHAPTER 6

VALIDATION OF THE FRACTURE SLIDELINE TECHNIQUE

6.1 INTRODUCTION

The objective of this chapter is to demonstrate the effectiveness of the proposed fracture slideline technique. Numerical results will be obtained for a total of eight plate impact problems and comparisons made against their corresponding experimental results.

Although a considerable amount of experimental data has no doubt been collated internationally in Government institutions, information concerning plate perforation is still extremely sparse, particularly for the combination of blunt projectiles and circular plates of moderate thickness. A number of experimental results have been investigated in this work to determine their suitability for numerical comparison purposes.

Corran et al (1983) presented a series of results at sub-ordnance velocities for a variety of projectile nose shapes impacting against thin plates (≈1-2 mm), to demonstrate the dominant response mechanism encountered in differing perforation processes. Little information was presented, however, concerning plate deformation modes relating specifically to the plugging process, particularly transient response information. Experimental investigations involving thin plates have been carried out to obtain detailed sets of results using conical or spherical impact faces. Calder (1971), Goldsmith et al (1965), Levy and Goldsmith (1984), Goldsmith and Finnegan (1971), whilst a further series of results for oblique impact has also been presented, Awerbuch and Bodner (1977), Rickerby and Macmillan (1980) and Backman et al (1977).

Goldsmith (1985) has also published results relating to the perforation of thin plates by various shaped projectiles which

included, albeit in a passing manner, a limited number of terminal plugging results. A number of other recent papers have treated plugging in a similar manner, Goldsmith and Finnegan (1986) and Wingrove (1972). Liss and Goldsmith (1984), however, have recently produced a very comprehensive set of results for circular aluminium plates struck by hard, flat ended, steel projectiles, whilst a more dated, but nevertheless equally relevant, paper also gives substantial experimental data for both steel and aluminium plates of square face sections, Awerbuch and Bodner (1974). It is unfortunate that the test arrangement for restraining the plates included restraints along only two of the four edges to aid high speed filming of the events, making the process fully three dimensional.

The results of Liss and Goldsmith (1984) will predominantly be used in validating the fracture slideline technique. A series of solutions have been obtained using four differing impact velocities for each of the two chosen plate thicknesses. The effects of variations in parameters such as the effective plastic strain and scale factor will be brought out in these tests.

6.2 PROJECTILE IMPACT ON A THIN ALUMINIUM PLATE

This section investigates the plugging phenomena experienced during the impact between a blunt-faced, hard steel, cylindrical projectile and a circular 2024-0 aluminium plate. The relevant initial problem data is given in Table 6.1 for the four experimental tests considered in this section, whilst Figure 6.1 depicts the finite element model to be used for this configuration. In each case the diameter of the projectile is 12.5 mm, the plate clamp diameter is 119.4 mm, and the plate thickness is 3.2 mm. The mesh consists of 141 elements with a three-element depth through the thickness.

The use of a reduced length of projectile combined with an increased mass density to maintain the total mass has been mentioned previously in Section 4.8.1, and will again be utilised

to model the projectile in this and the following sections. Note that the hardened steel material and its small vibrational response in comparison with that of the plate permit this assumption.

Initial tests using the default value for the hourglass control coefficient revealed a significant amount of hourglassing within the contact region, particularly along the elements constituting the plug/plate interface. An increase in the magnitude of this control factor from 0.1 to 0.3 virtually eliminated the effect. The default values for the artificial viscosity coefficients were used once again.

The material properties for both projectile and plate were obtained from the cited paper and are given in Table 6.2.

6.2.1 Results and discussion

A description of the measurements involved in the experimental post impact results of Table 6.3 are given in Figure 6.2 and represent dimensional accuracy of ±0.1 mm.

Table 6.4 presents the corresponding results from the numerical tests performed.

In each of the tests, the final velocities of both the projectile and plug provided the basis for the choice of effective plastic strain failure magnitude. A list of effective plastic strain criteria is given in Table 6.5.

A preliminary test of the material characterisation was performed for which perforation was not experienced (test (a)), to compare the overall deformation field.

The final deformed thickness of the plate along the central axis was computed as 3.0 mm in comparison with the 3.0 mm obtained by experiment. The response in terms of the final deflection is not so accurate, however, with a computed value now of 10.7 mm and an experimental value of 14.0 mm. A number of factors contributed to this overly 'stiff' response, the

principal reason, however, was seen to be associated with the rather coarse mesh both through the thickness and in the region of the plate supports imposed by the computational restraints. Figure 6.3 depicts the deflected shape of the plate and projectile at the moment of maximum deflection, which clearly demonstrates the large bending effects present. The reduced accuracy of the constant strain element in a bending environment has previously been discussed, particularly the increase in sensitivity of the final displaced solution with the hourglass coefficient as the non-rectangular bending effects are increased across an element. Once again, the ideal of utilising many, practically equi-sided quadrilaterals with at least five elements to model the thickness has met with compromise in the face of restricted computer resources. The error associated with this particular comparison is of the order of 17% which was found to increase with impact velocity (see Table 6.6).

The remaining three test cases each include perforation at some point during the solution process. With respect to the final velocity magnitudes, it is clear that a correct momentum transfer between both solids has been adequately achieved. The maximum deviation occurs for test (b) but continues to represent a solution to within 10% of the experimental values. The plug thickness and base diameter magnitudes are also computed adequately for each of the tests. The plate results, however, are not as closely matched and it is thought that these values are particularly sensitive to the degree of refinement of the discretisation and also the material characterisation employed. These latter results would tend to indicate that a higher degree of plastic flow occurred numerically than actually did in the experiment.

Table 6.6 summarises the errors experienced in the numerical calculations from this test suite with respect to their respective experimentally determined values.

The Von Mises plastic strain criteria required to align the numerical results with those of the experiment may be seen to

vary for each test case, particularly for test (b). This is a consequence of the inadequacies of this discretisation to model the bending effects, since it is known that there is a sharp increase in plate deflection in the region of the ballistic limit. The results at higher velocity, however, are very much closer and indicate the ability of the algorithm to be used at such post-ballistic velocities.

To demonstrate the sensitivity of the final solution to a variation in this failure criteria three different values were used in test (c) and, to this end, the variation of several field parameters is shown in Figures 6.4 to 6.6. Convergence to the experimental values of the parameters with decreasing plastic strain criterion is indicated by the curves for all except the plug velocity and the two plate diameters, although the latter do converge within the range considered. From this set of solutions, therefore, it may be concluded that a reasonable degree of insensitivity is experienced such that a solution is readily permissible within a range of failure criteria.

The final deflection is overestimated here, as indeed is the exit hole diameter of the plate. The former would seem to indicate further the presence of a greater amount of plastic flow in the numerical solution than was actually experienced in the experimental tests, and is borne out further in the lack of radial elastic recovery at the distal plate surface, together with the underestimated magnitude of the final plug thickness. This is probably also the reason for the underestimate in the entry hole diameter in that elastic recovery on the frontal surface would tend to increase the hole diameter.

The usefulness of the fracture slideline technique may perhaps be seen best in the context of the transient response of the plug/plate system. The following discussions will use test (c) as a basis for an investigation of the plugging process within the time frame commencing with initial contact and terminating at the moment of distal surface fracture. Table 6.7 depicts the nodal fracture times for this particular system and

will be referred to later.

The variation of kinetic energy with time up to plug ejection shown in Figure 6.7, from which a number of observations may be made. Three distinct phases are represented; an initial rapid decrease of the kinetic energy associated with the compression of the plug is followed by a period of lower decrement rate which is typically associated with the formation of the shear plug from the material. The latter is terminated when the initial elastic wave reaches the plate boundary. Thirdly, a further decrease in slope is experienced in the proximity of the first crack occurrence which is maintained to the full separation of the plug from the plate. This final period actually represents the 'steady state' conditions present as the crack propagates through the material and the plug is ejected.

The expected decrease in the system stiffness is also implied by the decrease in the slope of the force history curve. The dominant fracture in this respect being for crack initiation whilst subsequent fractures have increasingly less effect. The computed force-time curve of Figure 6.8 shows the large initial force arising from the aforementioned compression of the plug material, which is followed by a sharp decrease as the shear plug is formed in the plate material. The ensuing increase in force is in agreement with experimental observations, occurring due to the need for a large force to rapidly accelerate the plate material in the vicinity of the fracture region, which is confirmed if the plate deformation sequence of Figures 6.9 to 6.12 are inspected, in which it will be seen that relatively little plate deformation occurs until after the first crack has been created. At this point the highly localised effects have had sufficient time to extend beyond the boundary of the projectile diameter and consequently larger displacements are seen as greater sections of the plate begin to absorb energy from the projectile.

The experimental observation that the majority of shear strain is experienced outside of the plug region, along the fracture surface of the plate, is also observed in these

deformation diagrams. Moreover, the tendency toward a slight amount of hourglassing in the column of elements to the right of the fracture surface is a further confirmation. A consequence of this is observed in the final shape of the plate fracture surface, which does not exhibit the typically smooth nature expected from test firings. The degree of mesh refinement is dominant in the elimination of this factor from the numerical solution and will be discussed further with respect to the intermediate plate thickness.

The element failure sequence for this problem is shown in Figure 6.13 to indicate the flexibility of the method to account for the changes in the drive of the solution. For instance, the geometric considerations in this problem used to propagate the fracture surface within the plate confirm experimental observation that the terminal plate diameter is convergent in shape.

An estimate of the fracture propagation speed may be obtained based upon the depth of crack propagation at the moment of fracture as 132, 77 and 155 ms^{-1} respectively. These are not unreasonable, albeit at a lower magnitude, when compared to the theoretical value of 554 ms^{-1} (obtained from $[E_p/w]^{1/2}$). Table 6.7 shows that the fracture process commenced at 8.10 μs and terminated at 28.95 μs, indicating correlation with the experimentally observed behaviour of the initial compression stage occurring over a very short time frame.

Figure 6.14 to 6.17 shows the progression of fracture with time through the plate together with the propagation of the Von Mises plastic strain contours. It is clear that this measure is a good qualititative gauge of failure in the obvious concentration of this field variable in the vicinity of the crack. With respect to the strain field experienced by this particular configuration, there are strong indications that experimental observations are once again confirmed. The radially constant field within the plug is followed by a rapidly changing field in the region of the crack, subsequent to which, there is evidence of asymmetric

bending strain superimposed on the tensile membrane strain. At points increasingly distant from the axis of symmetry this is indicated by the increasing slope on the zeroth plastic strain contour. The radial stress contours of Figure 6.18 to 6.21 also indicate the presence of bending, the effect of which again increases along the plate away from the axis. Estimates obtained from the contour values give the proportion of stress of an asymmetric nature to that of the membrane stretching between 1/3 and 1/2 and justify the previous assumption that the problem is actually in between these two states.

The effects of elastic recovery are seen in the contour changes occurring between Figures 6.20 and 6.21 in which the stresses due to membrane action are sharply reduced, although the actual stress field remains largely the same. The final plot in the sequence is largely free from bending in the region of fracture. This transition zone is dominated by the effects of shear due to the previous plug/plate interaction.

6.3 PROJECTILE IMPACT ON AN INTERMEDIATE ALUMINIUM PLATE

This section investigates further the plugging phenomena experienced during the impact between a blunt-faced, hard steel, cylindrical projectile and a circular 2024-0 aluminium plate. The relevant initial problem data is given in Table 6.8 for the four experimental tests considered in this section, whilst Figure 6.22 depicts the finite element model to be used. In each case the diameter of the projectile is 12.5 mm, the plate clamp diameter is 114.8 mm and the plate thickness is 6.4 mm. The mesh consists of 222 elements with a six-element depth through the thickness.

The material properties for both projectile and plate were obtained from the cited paper and are given in Table 6.2.

6.3.1 Results and discussion

Table 6.9 shows the experimental post impact results, whilst

Table 6.10 represents the corresponding results from the numerical tests performed. A list of effective plastic strain criteria is given in Table 6.11.

A preliminary test of the material characterisation was performed once again, for which perforation was not experienced, (test a) to compare the overall deformation field. The final deformed thickness of the plate along the central axis was computed as 5.7 mm, the terminal deflection as 10.3 mm, and the target entry hole diameter as 12.4 mm. These initial results represent an accuracy to within 2% of the experimental values and would indicate that the material parameters used, together with the mesh discretisation are sufficient to model the dynamic effects in operation for a non-failure application.

Initial tests revealed the use of a single value of scale factor for each of the three interfaces to be impracticable since the pressure experienced along slideline two (see section 5.4.1) is typically an order of magnitude greater than that for slideline three. The value required for slideline one is also slightly reduced from that of slideline three. The numerical problem manifests itself in the form of a significant amount of surface overlap which eventually results in an unreasonable degree of mesh deformation. Figure 6.23 depicts a typical response with the use of a single value in this way.

The numerical solution currently expects a unique value of scale factor to be defined for each surface which, for the experienced analyst, represents a greater degree of control over the solution. This is particularly true when considering frictional conditions along the slideline interface where the normal force is directly related to the shear force generated. The method is actually based on the results of the previous section in which the effect of a varying scale factor on the solution was found to be limited, particularly as the plate thickness is increased. The values used for the two plate thicknesses considered herein are given in Table 6.12, in which the slideline numbers once again refer to the surface pairs

defined in Chapter Five.

The results for the intermediate thickness plate are generally closer in agreement to the experimental values than those obtained for the thin plate. This is a consequence of the greater mesh density through the thickness of the intermediate plate. The projectile and plug final velocities have been used as the datum point for initial failure criterion initialisation and are similar in their percentage error. It is clear that the plug thickness and the maximum deflection results are significantly closer to the experimentally determined values.

The accuracy in the maximum deflection is a consequence of both the reduced sensitivity to the hourglass coefficient and the increase in the number of integration points through the thickness, permitting a higher resolution of the bending strain field. The accuracy obtained in the plug thickness is similarly expected, again because of the 'softer' solutions resulting from the rather coarse use of this element in the previous example. Table 6.13 summarises the percentage errors experienced in the intermediate thickness plate test suite. Note however that the mesh was refined principally in the axial direction rather than radially. This has resulted in the radial field variables such as plug base diameter and plate hole diameters having the same order of error as the previous example, indicating the potential improvement in results to be gained in this manner.

In a similar fashion to the previous section, a single test case from this suite will be used to investigate certain transient aspects of the solution procedure, for this purpose, test (b) will be utilised. In anticipation of future use, Table 6.14 gives the time at which each nodal fracture takes place for this configuration.

Figure 6.24 represents the variation of kinetic energy loss of the system with time up to the moment of distal face fracture. Although the three phases discussed previously are to be seen once again, the curve is substantially smoother in nature since the effect of the initial elastic wave is virtually eliminated by

the increase in the number of support nodes at the clamped edge, enabling a smoother reflection as the initial elastic wave encounters this boundary. The interface force curve of Figure 6.25 depicts a similar response to that of the previous example also (see Figure 6.8), in which an initial peak is followed by a brief trough from which a secondary, rather broader maximum proceeds, subsequently tailing off to zero. The cause of the initial transient peak has already been seen to arise as a result of the compression of the plug material beneath the projectile face, and is further demonstrated in Figure 6.26 in which the significant difference in the plug centreline velocities when measured at both the base and tip are clearly shown. This difference, and particularly the higher frontal velocity than that of the distal surface within the first 3 μs, demonstrates the large compressive accelerations present within the plug. At subsequent times this difference becomes much reduced.

The plate velocity time history is given in Figure 6.27, the data for which is obtained from the nodes immediately adjacent to the projectile edge and which eventually form part of the fracture surface of the plate. The diagram is similar in form to that of Figure 6.26 in the initial contact phase in the sense of the immediate disparity between the frontal and distal surface velocities, again indicating a substantial amount of compressive acceleration, albeit at a decreased level.

The rather jagged nature of the force and velocity time curves is due principally to the degree of mesh refinement used in this solution. An increase in the number of elements through the thickness would have the effect of decreasing this effect since the time between nodal releases would be reduced. It is to be noted that the force generally experiences a local decrease in the presence of a nodal fracture while the corresponding velocities experience an increase. The notation (1) to (6) correspond to the nodal fracture times. The nodal velocity differential across the projectile (Figure 6.28) is negligible in this test and indicates the observed experimental observation

that little deformation is seen in this region, implying an almost wholly rigid body translation.

The cause of the secondary peak is not as clear from the velocity time histories but may be seen in the deformation plots of the previous example (Figures 6.9 to 6.12), in which it was noted that very little bending occurred outside of the plug region until the first nodal fracture. The fracture actually has little effect here, rather it is the propagation of the elastic wave front through the material which is predominant. Taking the longtitudinal wave speed as a basis ($\sqrt{[e/w]} \approx 5200\ ms^{-1}$) it may be seen that the initial peak occurs while the wave is still travelling within the plug region. As soon as the main compressive stage is terminated, the first fracture occurs and the wave is now traversing through the plate away from the centreline. At this stage a dynamic balance is achieved between the increasing bending effects due to the propagating wave and the decreasing driving force as the plug passes through the plate material. The secondary peak is thus a result of the resistance of the plate to the plug through bending action and which appears in the solution only after a certain amount of elapsed time.

The increase in the magnitude of the effective plastic strain over the values obtained in the thin plate test cases is demonstrated in the deformation plots of Figures 6.29 to 6.31, together with the typical locally propagating plastic field. Note that the full radius of the plate is not shown in order to exhibit the fracture zone more clearly. It is also of interest that the deflection of the distal surface is correctly shown to be a direct result of the propagation of the plastic strain field, the distal surface of the plug eventually having practically radially constant lines of plastic strain through the thickness whose magnitude decrease towards the frontal surface. The maximum plastic strain is again experienced, however, along the fracture surface.

The radial stress field is also given in Figures 6.32 to 6.34. The effects of an increase in the number of elements

through the thickness is clearly evident in the accurate positioning of the neutral axis of the plate. Once again, the stress field is seen to be radially constant in the region of the newly formed plug, although varying through the thickness. After a brief transitory region the typical bending stress field is indicated together with a small amount of membrane action. As time progresses, the transitory zone may be seen to increase along the length of the plate.

The average fracture propagation velocity, based upon the initial length of the elements in the axial direction, has been calculated as 127 ms^{-1}. This estimation, however, is dependent to a large degree on the spatial discretisation of the structure and it was found that the six individual components comprising this averaged value varied quite considerably between 50 and 202 ms^{-1}, implying the need of further refinement for this particular parameter. The magnitudes are similar to those obtained for the plate and once again represent an adequate estimation when compared with the theoretical plastic wave speed.

The elements which satisfied the failure criteria are once again given in Figure 6.35 for the sake of completeness, and demonstrate a similar response to that of the previous example.

6.4 CONCLUSIONS

The application of the fracture slideline method to the simulation of plugging failure in the manner described is ideally utilised in conjunction with experimental test data as described in Chapter One. In this way any inadequacies in the numerical simulation may be minimised through an initial comparison with a known datum so that numerical predictions may be more confidently obtained.

The overall results are clearly consistent between calculations, a higher impact velocity producing perforation together with the resultant unrestrained projectile and plug motion, whereas the lower velocity resulted in projectile contact

only. A lower level of effective plastic strain criterion enables complete perforation with the formation of a plug while high levels resulted in considerable penetration but no perforation.

With respect to the more detailed experimentally observed behaviour, the model correlates well qualitatively with respect to all of the chosen field parameters. Moreover, quantitative estimates are also computed which have been shown very close to the experimental observations, such as final plate displacement, plug thickness, projectile and plug final velocities and the plate entry hole diameters. The plate exit diameters experienced the least accuracy yet remained within 24% of the experimental values. The principal limiting factor in these calculations was seen to be the restriction on computer resources which constrained the mesh to contain less than 250 elements. The elimination of this restriction by, for example, porting this code to one of the many supercomputers now available, would enable significantly more accurate simulation of this type of problem.

The results given in this section demonstrate that the effective plastic strain failure criterion remains essentially constant over a large range of impact velocities for a given plate thickness. The stability of this failure parameter appears to be reduced in the vicinity of the ballistic limit as exhibited in the thin plate tests.

The use of a unique value of scale factor for each slideline has been shown to be both robust and flexible. Moreover, when used within the guidelines given in Table 6.12, the results produced are very good. In all the test cases there was no need of manual intervention during the solution, either to modify the slidelines to take into account changing surface interaction or to rezone the mesh in regions of unsatisfactorily high deformation.

6.5 REFERENCES

Awerbuch, J. and Bodner, S.R. (1974). 'Experimental Investigation of Normal Perforation of Projectiles in Metallic Plates', Int. J. Solids Structures, Volume 10, pp 685-699.

Awerbuch, J. and Bodner, S.R. (1977). 'An Investigation of Oblique Perforation of Metallic Plates by Projectiles', Exp. Mech., Volume 17, pp 147-153.

Calder, C.A. and Goldsmith, W. (1971). 'Plastic Deformation and Perforation of Thin Plates Resulting from Projectile Impact', Int. J. Solids structures, Volume 7, pp 863-881.

Corran, R.S.J. and Shadbolt, P.J. and Ruiz, C. (1983). 'Impact Loading of Plates - An Experimental Investigation', Int. J. Impact Engng., Volume 1, Number 1, pp 3-22.

Goldsmith, W. (1985). 'Initiation of Perforation in Thin Plates by Projectiles', Metal Forming and Impact Mechanics, Pergamon Press, Reid (Editor).

Goldsmith, W. and Liu, T.W. and Chulay, S. (1965). 'Plate Impact and Perforation by Projectiles', Exp. Mech., Volume 5, pp 385-404.

Goldsmith, W. and Finnegan, S.A. (1971). 'Penetration and Perforation Processes in Metal Targets at and above Ballistic Velocities', Int. J. Mech. Sci., Volume 13, pp 843-866.

Goldsmith, W. and Finnegan, S.A. (1986). 'Normal and Oblique Impact of Cylindro-conical and Cylindrical Projectiles on Metallic Plates', Int. J. Impact Engng., Volume 4, Number 2, pp 83-105.

Levy, N. and Goldsmith, W. (1984). 'Normal Impact and Perforation of Thin Plates by Hemispherically-tipped Projectiles- II. Experimental Results', Int. J. Impact Engng., Volume 2, Number 4, pp 299-324.

Liss, J. and Goldsmith, W. (1984). 'Plate Perforation Phenomena due to Normal Impact by Blunt Projectiles', Int. J. Impact Engng., Volume 2, Number 1, pp 37-64.

Rickerby, D.G. and Macmillan, N.H. (1980). 'On the Oblique Impact of a Rigid Sphere against a Rigid-Plastic Solid', Int J. Mech. Sci., Volume 22, pp 491-494.

Wingrove, A.L. (1972). 'The Forces for Projectile Penetration of Aluminium', J. Phys. D: Appl. Phys., Volume 5, pp 1294-1303.

TABLE 6.1

Geometric data summary of thin plate experiments

Test case number	Projectile	
	Impact Velocity (m/s)	Mass (g)
a.	92.9	39.7
b.	132.2	39.8
c.	172.5	39.7
d.	187.2	40.0

TABLE 6.2

Summary of material properties

Property	Projectile	Target
E	211 Gpa	69 Gpa
μ	0.30	0.33
w	50548 Kgm^{-3}	2770 Kgm^{-3}
E_t	690 Mpa	850 Mpa
σ_o	2290 Mpa	167 Mpa

TABLE 6.3

Experimental results from the thin plate impact tests

	Projectile	Plug			Target	
	Final Velocity	Final Velocity	Thickness	Base Diam.	Max. Defl.	Hole Diameter Entry(Exit)
	(m/s)	(m/s)	(mm)	(mm)	(mm)	(mm)
a.	0.0	–	3.0	–	14.0	12.1 (–)
b.	102.8	109.8	2.8	12.5	10.9	12.5 (12.5)
c.	156.9	172.8	3.0	12.5	6.1	12.5 (13.0)
d.	175.6	188.3	3.1	12.3	1.7	12.3 (12.9)

TABLE 6.4

Numerical results from the thin plate impact tests

	Projectile	Plug			Target	
	Final Velocity	Final Velocity	Thickness	Base Diam.	Max. Defl.	Hole Diameter Entry(Exit)
	(m/s)	(m/s)	(mm)	(mm)	(mm)	(mm)
a.	0.0	–	3.0	–	11.7	–
b.	93.0	103.0	2.8	12.7	11.4	12.6 (14.4)
c.	151.0	174.0	2.7	12.6	7.4	12.8 (15.8)
d.	169.0	186.0	2.7	12.7	7.0	13.0 (16.1)

TABLE 6.5

Effective plastic strain criteria for the thin plate impact tests

Test case	Effective plastic strain criteria
a.	—
b.	0.34
c.	0.38
d.	0.37

TABLE 6.6

Comparative (percentage) errors from the thin plate impact tests

	Projectile	Plug			Target	
	Final Velocity	Final Velocity	Thickness	Base Diam.	Max. Defl.	Hole Diameter Entry (Exit)
a.	0	-	-1.7	0	-16.8	-
b.	-9.5	-6.2	0	+2.0	+5.0	+0.8 (+15.2)
c.	-3.8	+0.7	-10.0	+1.0	+21.3	+2.4 (+21.5)
d.	-3.3	-1.2	-12.9	+3.3	+311.8	+5.7 (+24.8)

TABLE 6.7

Time for each nodal fracture

Node Number	Time of fracture μs
126	8.10
67	22.03
39	28.90
11	28.95

TABLE 6.8

Geometric data summary of intermediate plate experiments

Test case number	Projectile	
	Impact Velocity (m/s)	Mass (g)
a.	132.6	39.8
b.	149.0	39.7
c.	155.6	39.8
d.	175.1	40.0

TABLE 6.9

Experimental results from the intermediate plate impact tests

	Projectile	Plug			Target	
	Final Velocity	Final Velocity	Thickness	Base Diam.	Max. Defl.	Hole Diameter Entry(Exit)
	(m/s)	(m/s)	(mm)	(mm)	(mm)	(mm)
a.	0.0	–	5.7	–	10.1	12.2 (–)
b.	95.4	103.3	5.8	12.2	6.3	12.2 (12.2)
c.	105.0	111.5	5.9	12.3	6.0	12.2 (12.2)
d.	135.9	151.6	5.9	12.5	4.8	12.0 (12.5)

TABLE 6.10

Numerical results from the intermediate plate impact tests

	Projectile	Plug			Target	
	Final Velocity	Final Velocity	Thickness	Base Diam.	Max. Defl.	Hole Diameter Entry(Exit)
	(m/s)	(m/s)	(mm)	(mm)	(mm)	(mm)
a.	0.0	–	5.7	–	10.3	12.4 (–)
b.	87.5	102.5	5.8	13.1	6.7	12.9 (15.0)
c.	104.4	122.7	5.8	13.2	6.2	12.9 (14.9)
d.	131.4	159.2	5.9	13.4	5.0	12.8 (14.7)

TABLE 6.11

Effective plastic strain criteria for the intermediate plate impact tests

Test case	Effective plastic strain criteria
a.	—
b.	0.42
c.	0.42
d.	0.42

TABLE 6.12

Typical scale factors used in plugging simulation

Slideline Number	Typical scale factor magnitude
1.	0.1 - 2.0
2.	0.2 - 0.3
3.	0.05 - 0.07

TABLE 6.13

Comparative (percentage) errors from the intermediate plate impact tests

	Projectile	Plug			Target	
	Final Velocity	Final Velocity	Thickness	Base Diam.	Max. Defl.	Hole Diameter Entry (Exit)
a.	0	-	0	-	+2.0	+1.6 (-)
b.	-8.3	-0.8	0	+7.4	+6.0	+5.7 (+23.0)
c.	-0.6	+10.0	-1.7	+7.3	+4.2	+5.7 (+22.1)
d.	-3.3	+5.0	0	+7.2	+4.2	+6.7 (+17.6)

TABLE 6.14

Time for each nodal fracture

Node Number	Time of fracture μs
179	8.02
151	15.26
123	36.67
95	48.30
67	55.82
39	61.11
11	61.16

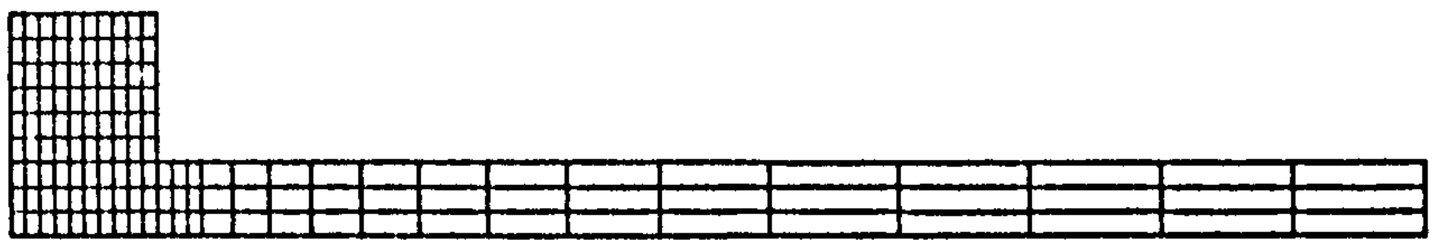

Figure 6.1
Finite element mesh for the thin plate impact test

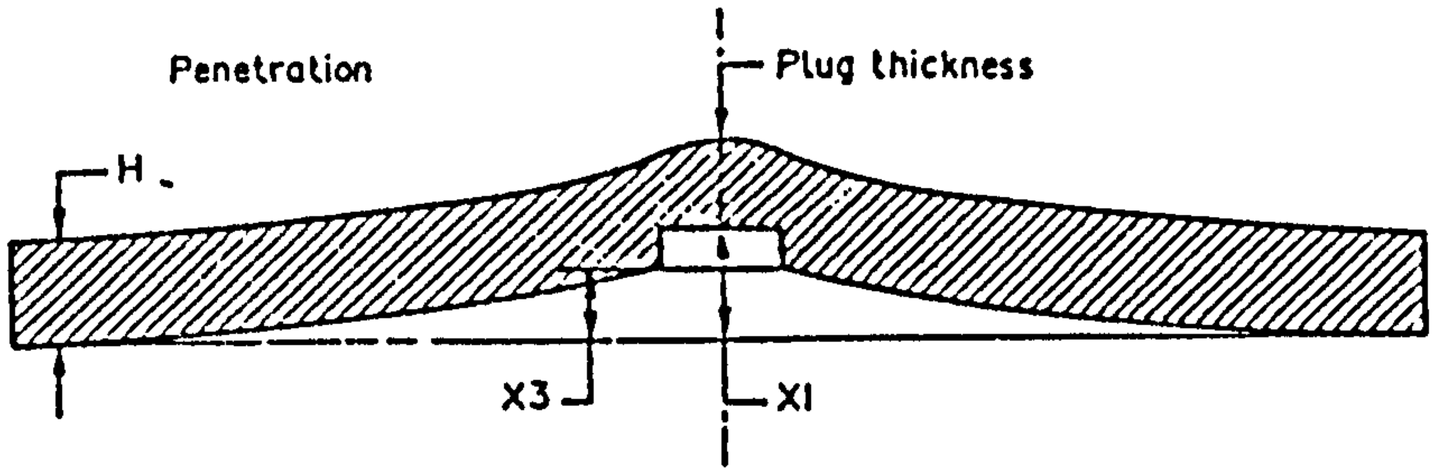

Figure 6.2
Description of the experimental measurements involved in the plugging tests

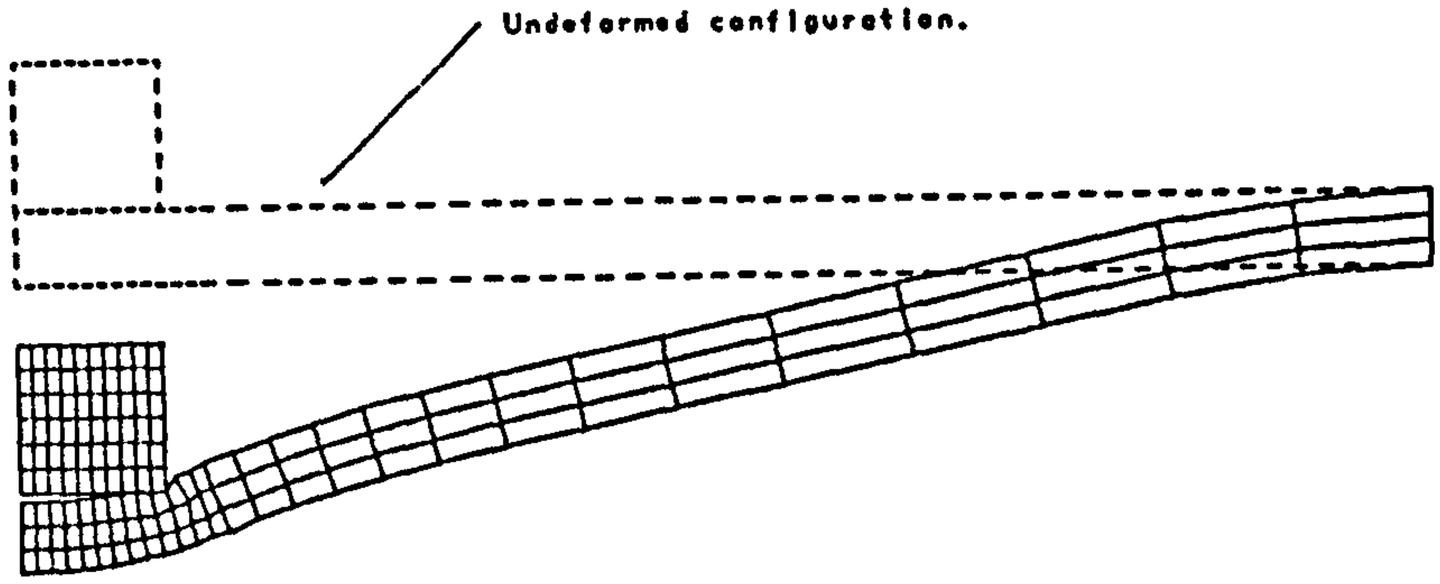

Figure 6.3
Deflected shape of the transient thin plate test at the moment of maximum deflection

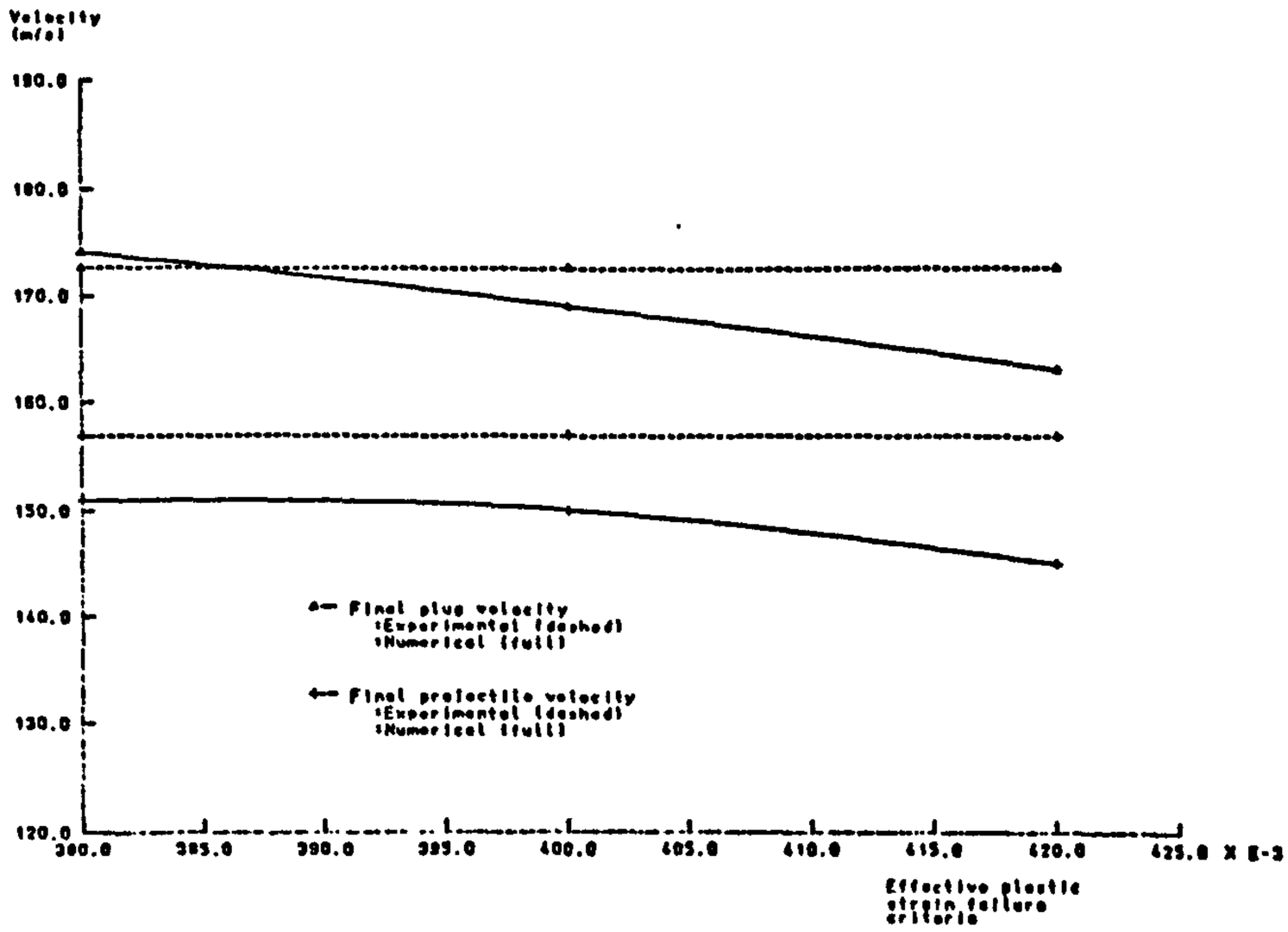

Figure 6.4
Variation of plug and projectile final velocities with effective plastic strain failure criterion

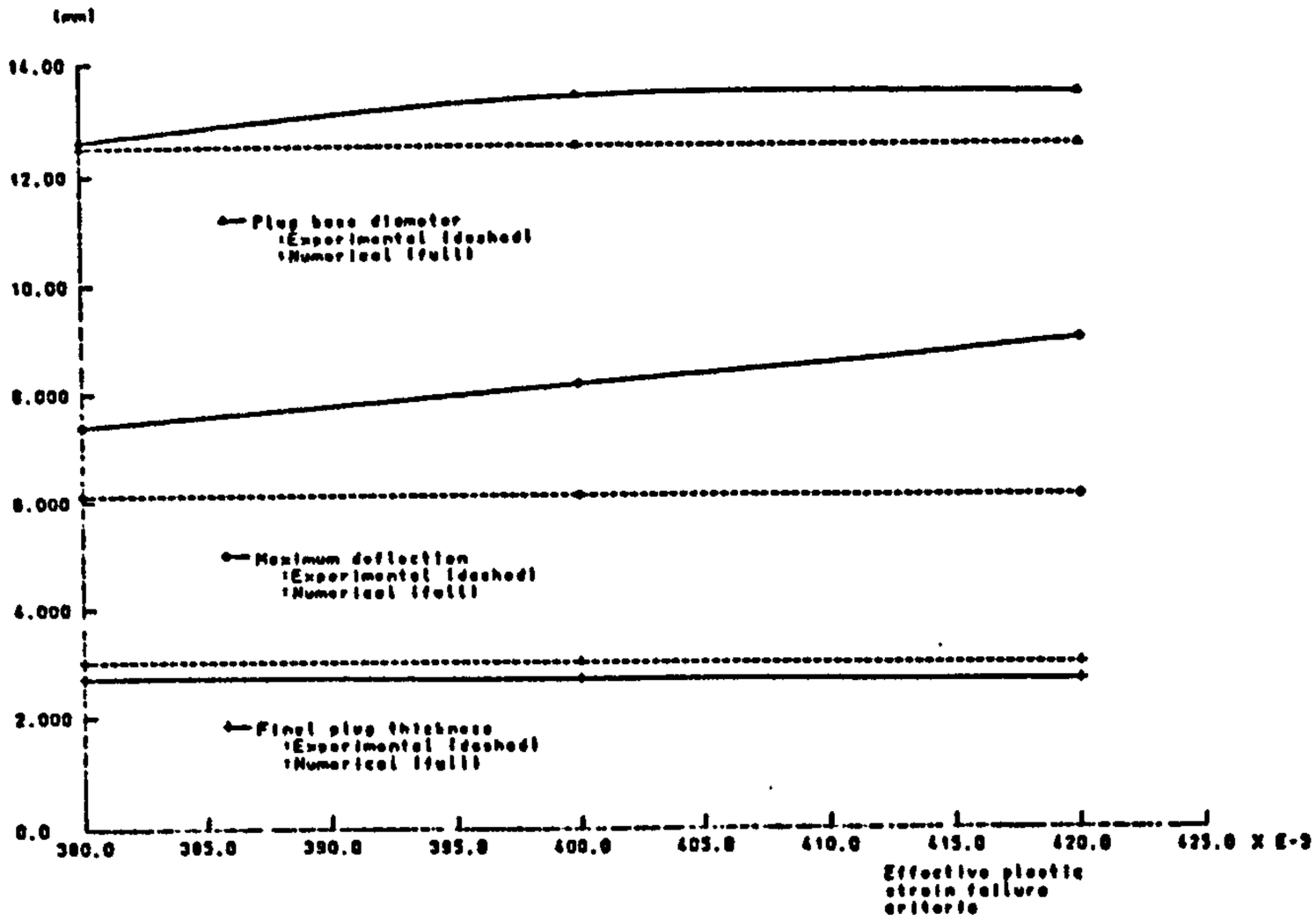

Figure 6.5

Variation of various dimensional parameters with effective plastic strain failure criterion

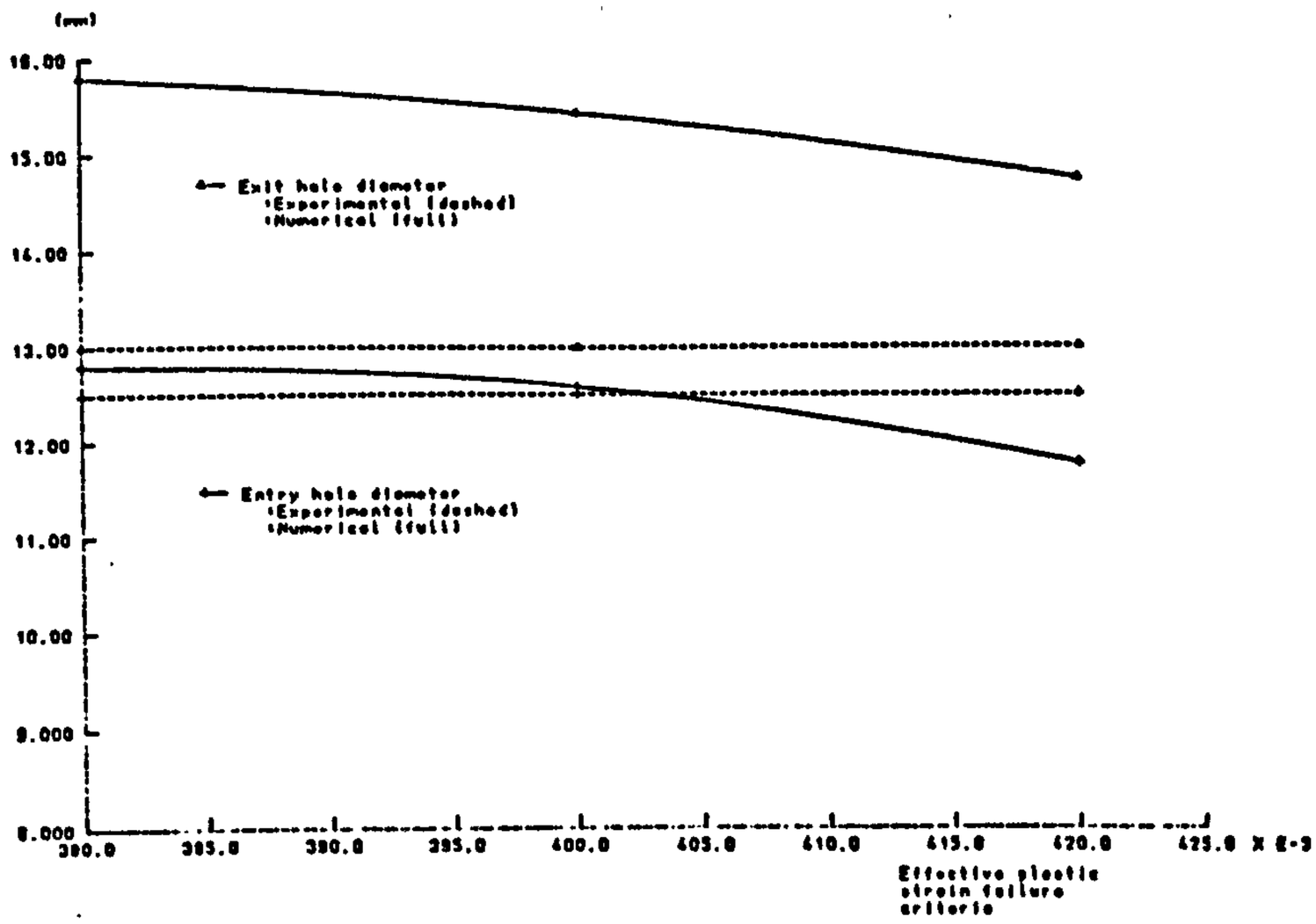

Figure 6.6

Variation of plate hole diameters with effective plastic strain failure criterion

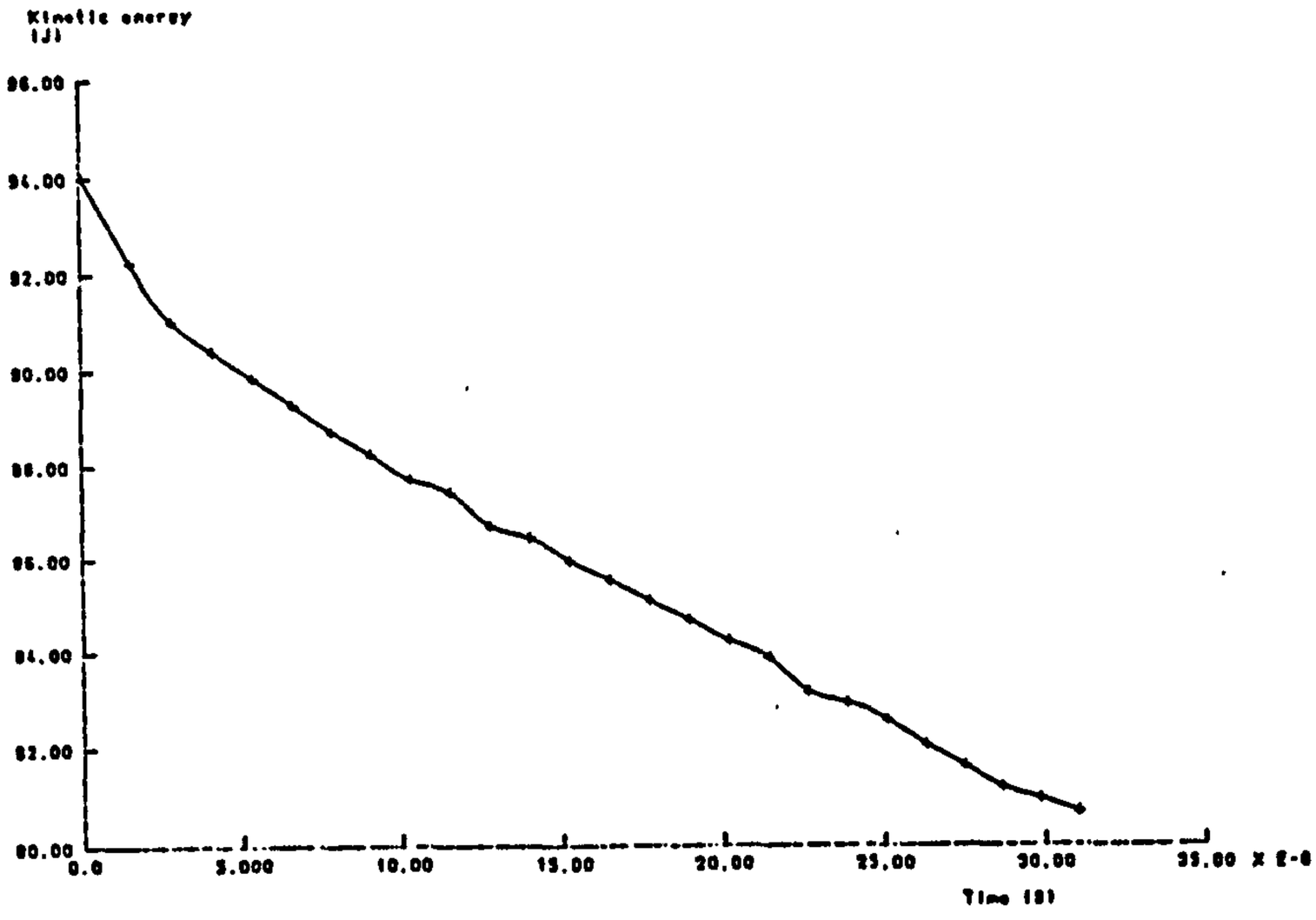

Figure 6.7
Variation of kinetic energy with time for the transient thin plate test

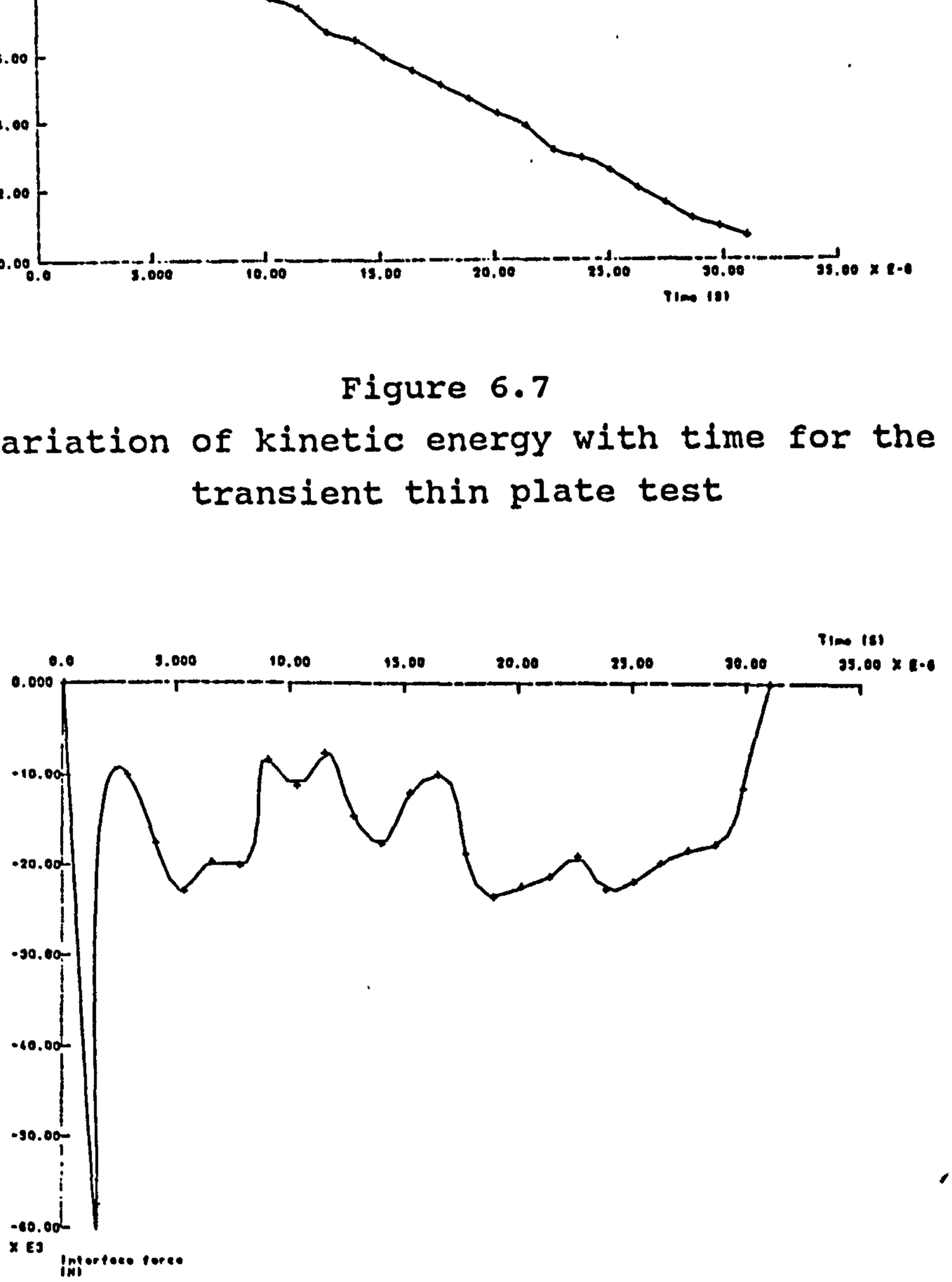

Figure 6.8
Variation of interface force with time for the transient thin plate test

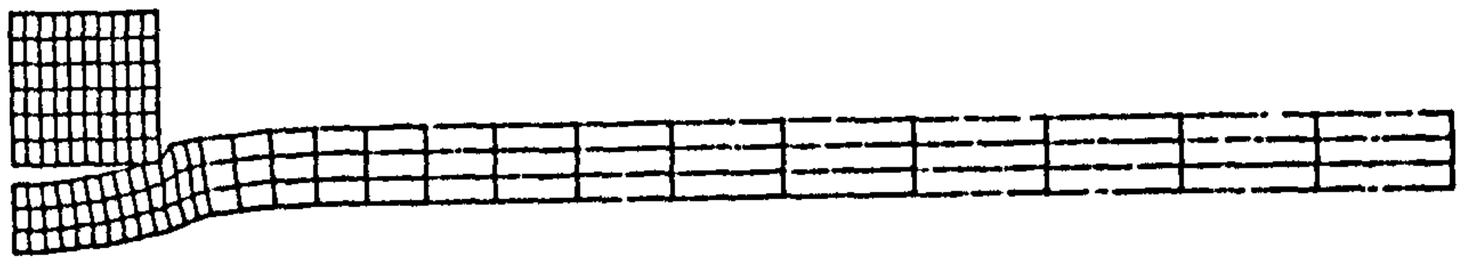

Figure 6.9
Deformation configuration of the transient thin plate test at t=8.5μs

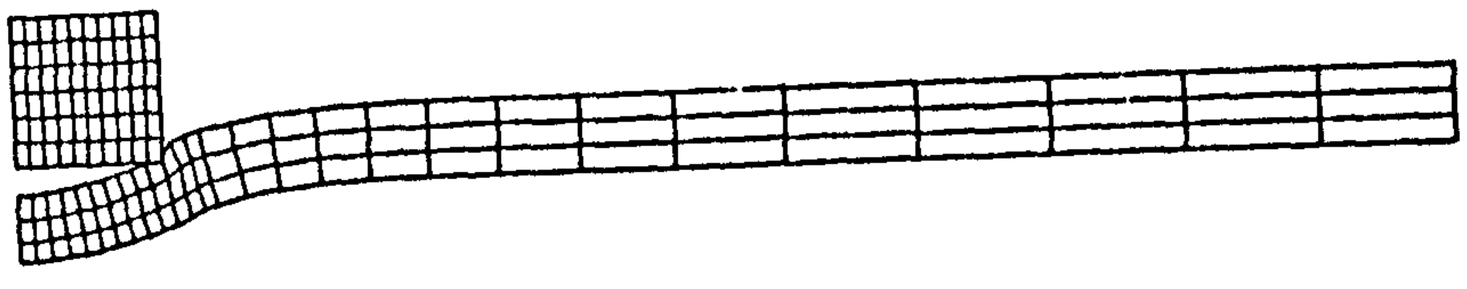

Figure 6.10
Deformation configuration of the transient thin plate test at t=12.7μs

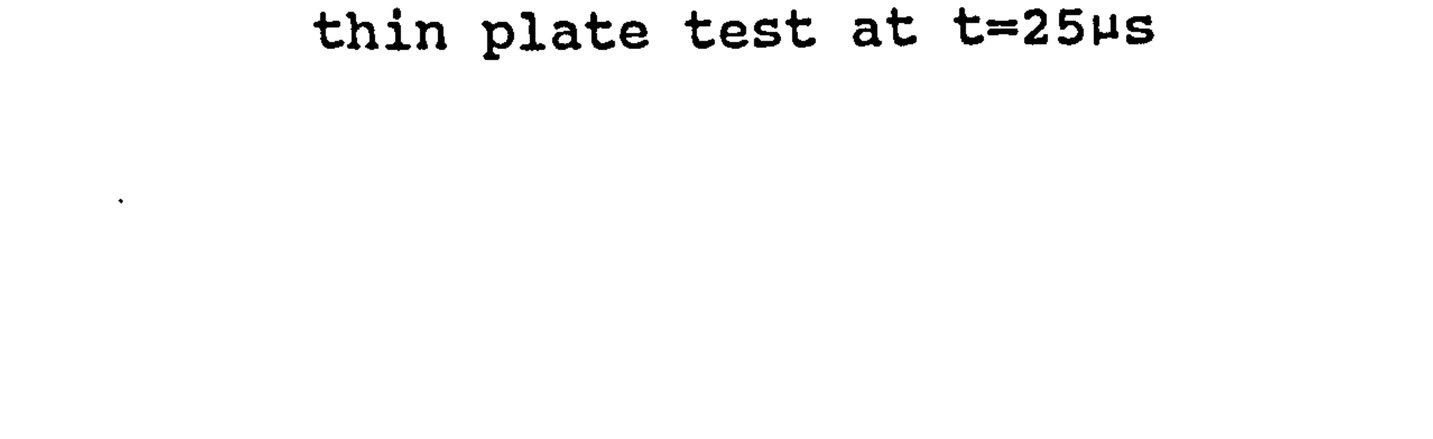

Figure 6.11
Deformation configuration of the transient thin plate test at t=25μs

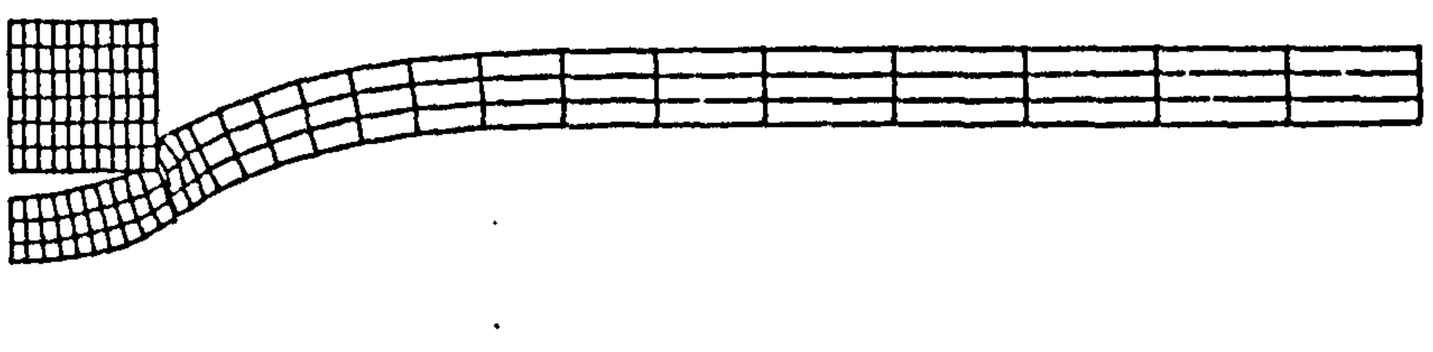

Figure 6.12
Deformation configuration of the transient thin plate test at t=31μs

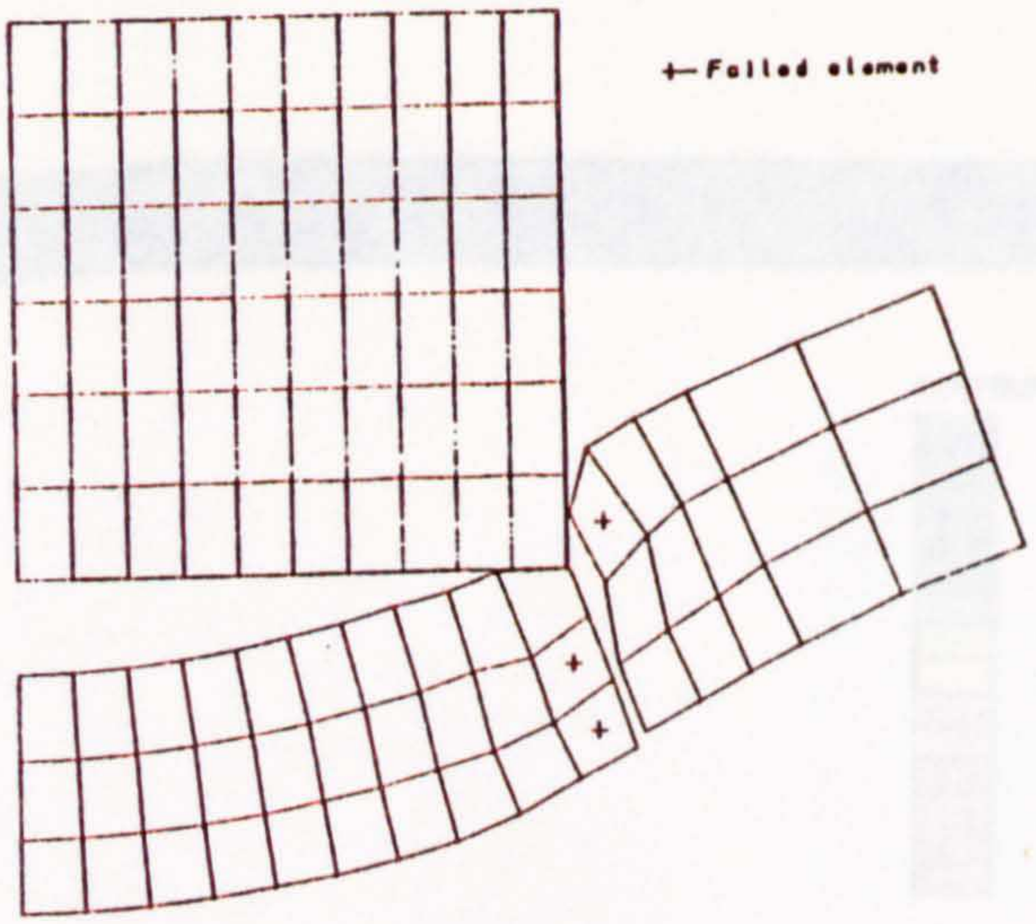

Figure 6.13
Thin plate test element failure sequence

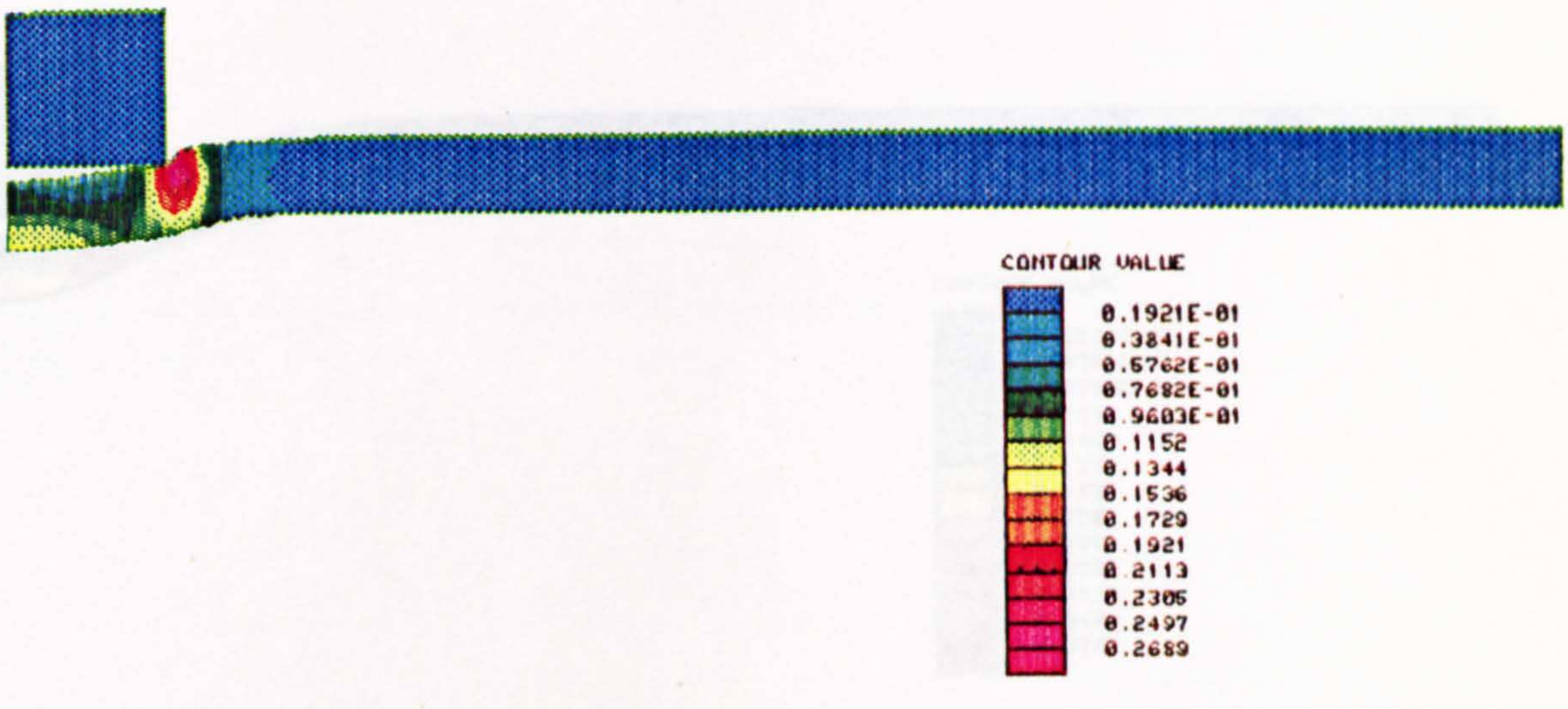

Figure 6.14
Von Mises plastic strain contours for the transient thin plate test at t=8.5μs

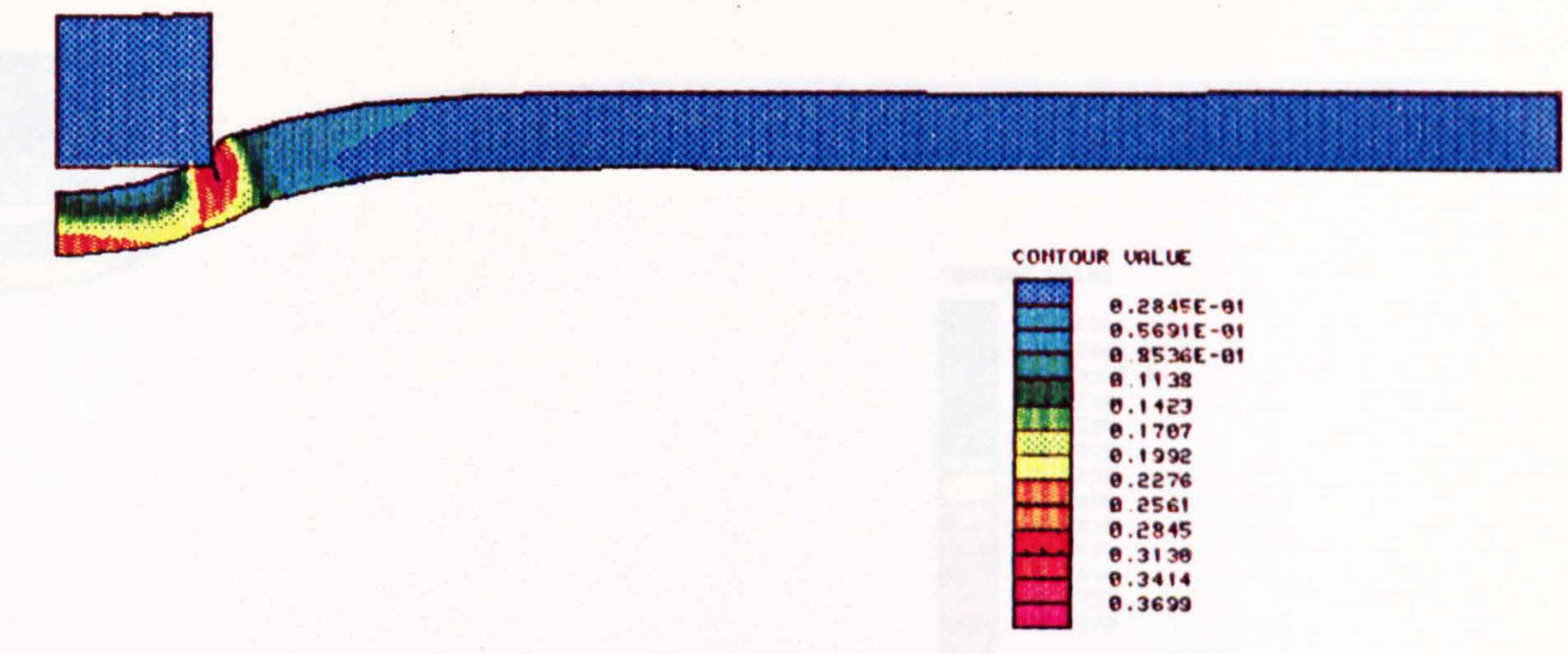

Figure 6.15
Von Mises plastic strain contours for the transient thin plate test at t=12.7μs

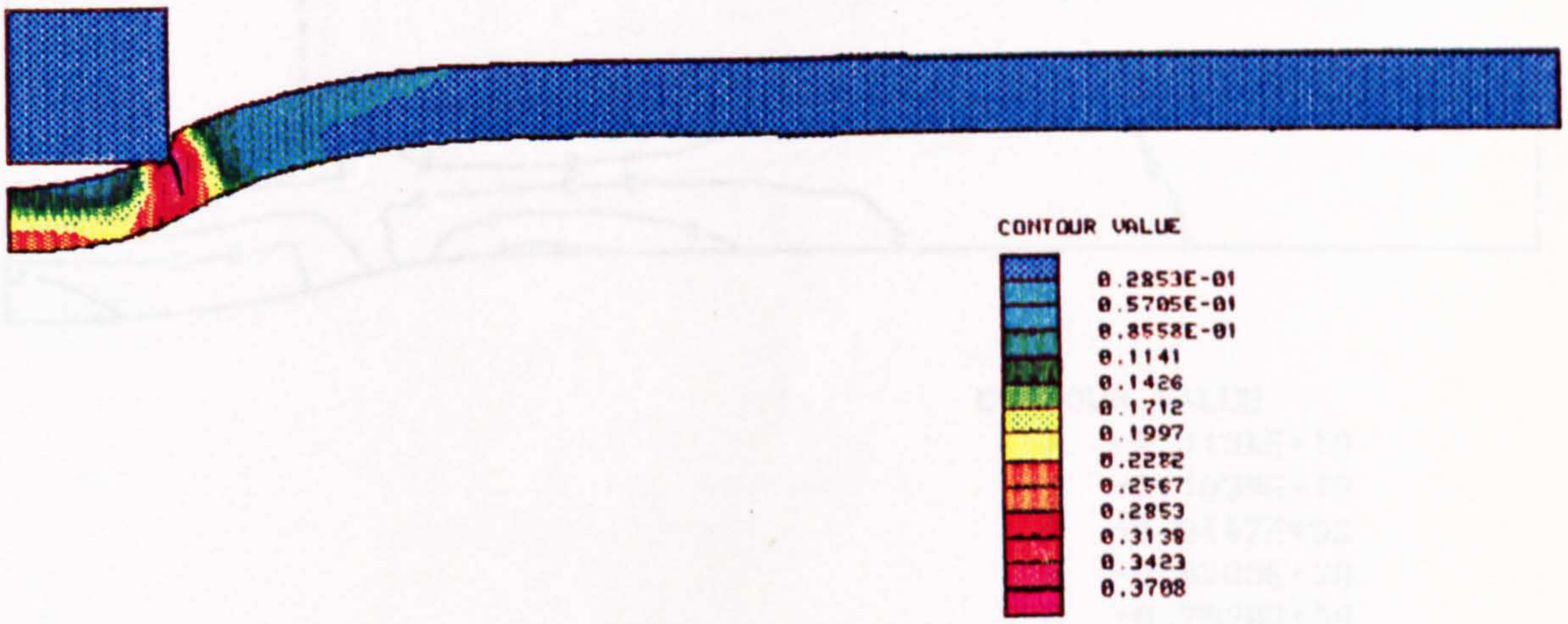

Figure 6.16
Von Mises plastic strain contours for the transient thin plate test at t=25μs

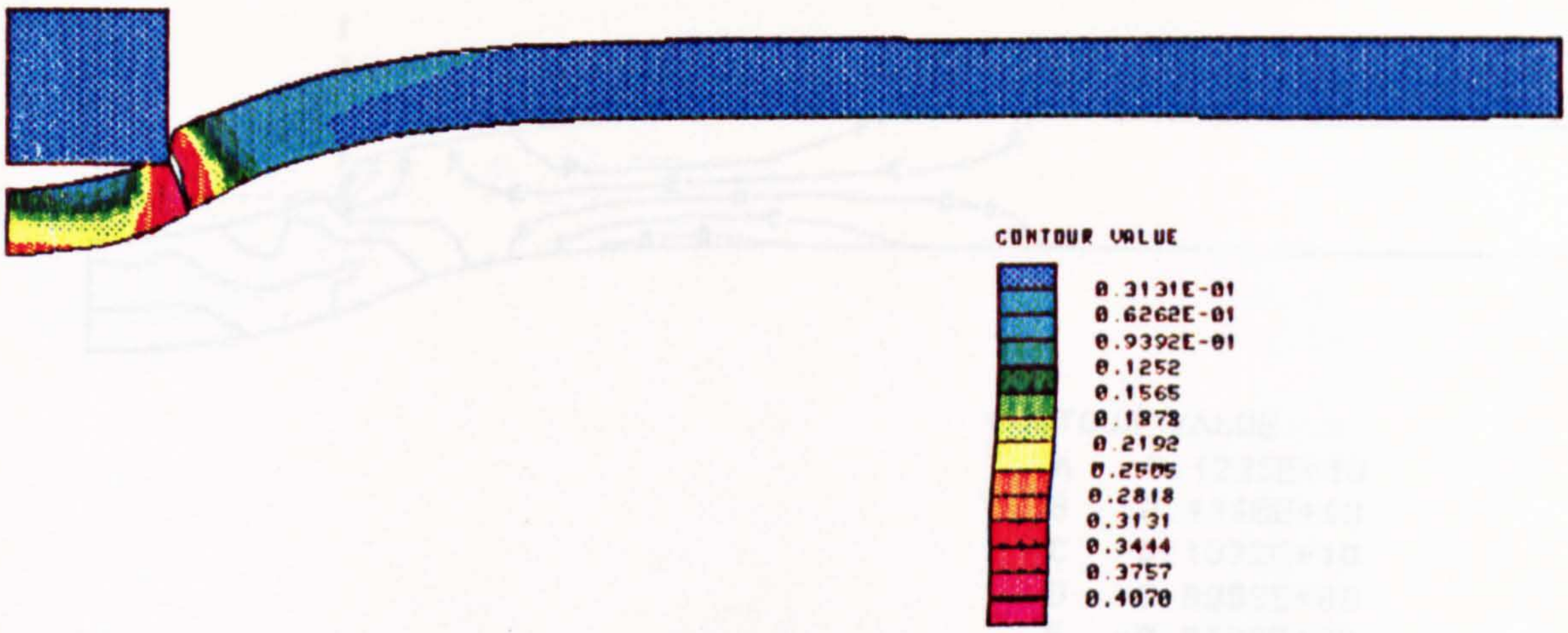

Figure 6.17
Von Mises plastic strain contours for the transient thin plate test at t=31μs

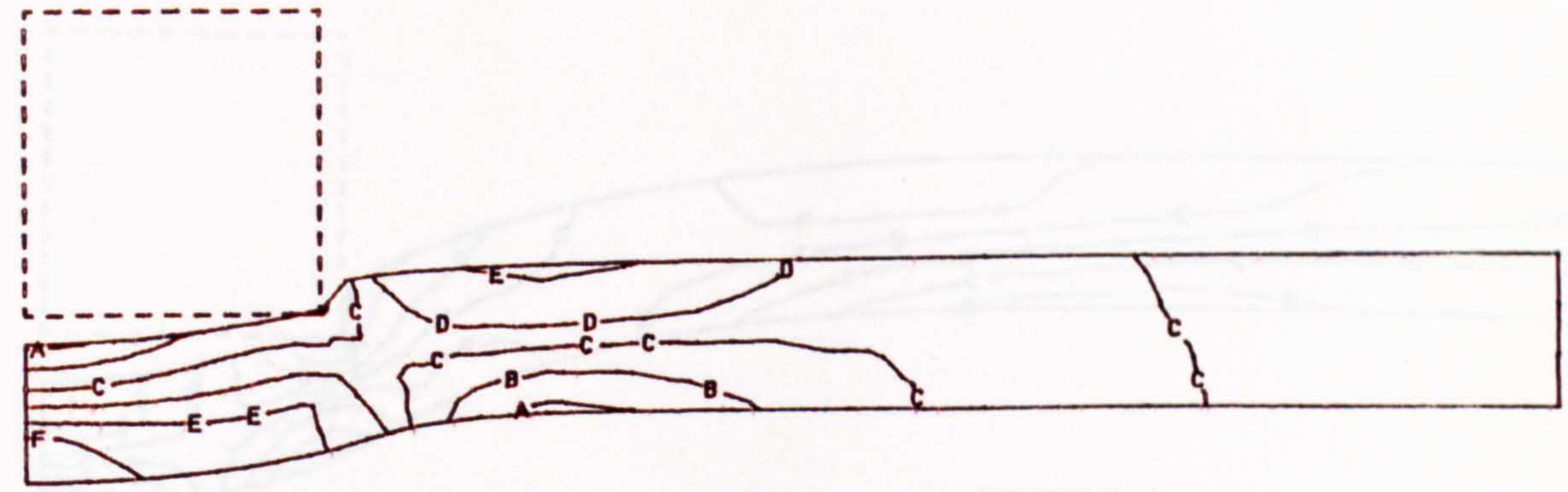

Figure 6.18
Radial stress contours for the transient thin plate test at t=8.5μs

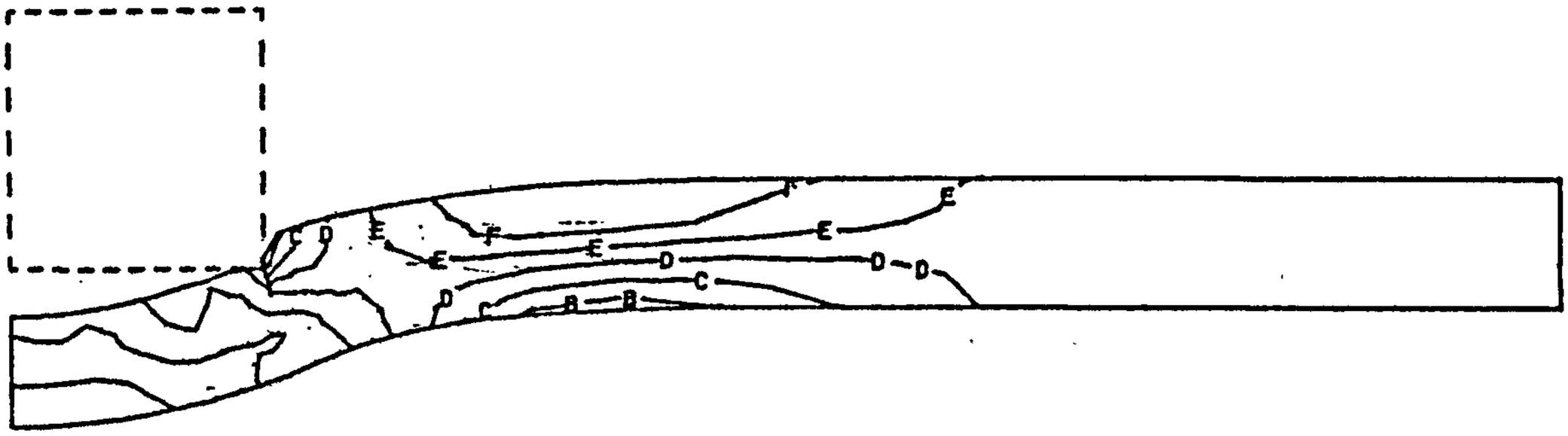

Figure 6.19
Radial stress contours for the transient thin plate test at t=12.7μs

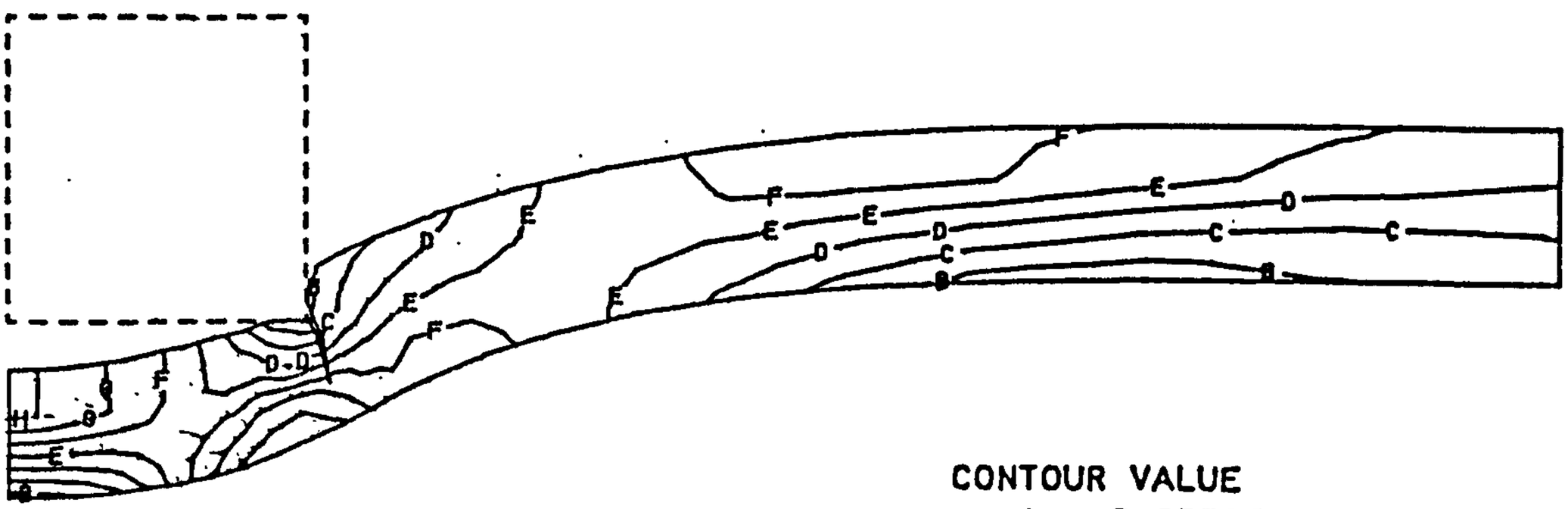

Figure 6.20
Radial stress contours for the transient thin plate test at t=25μs

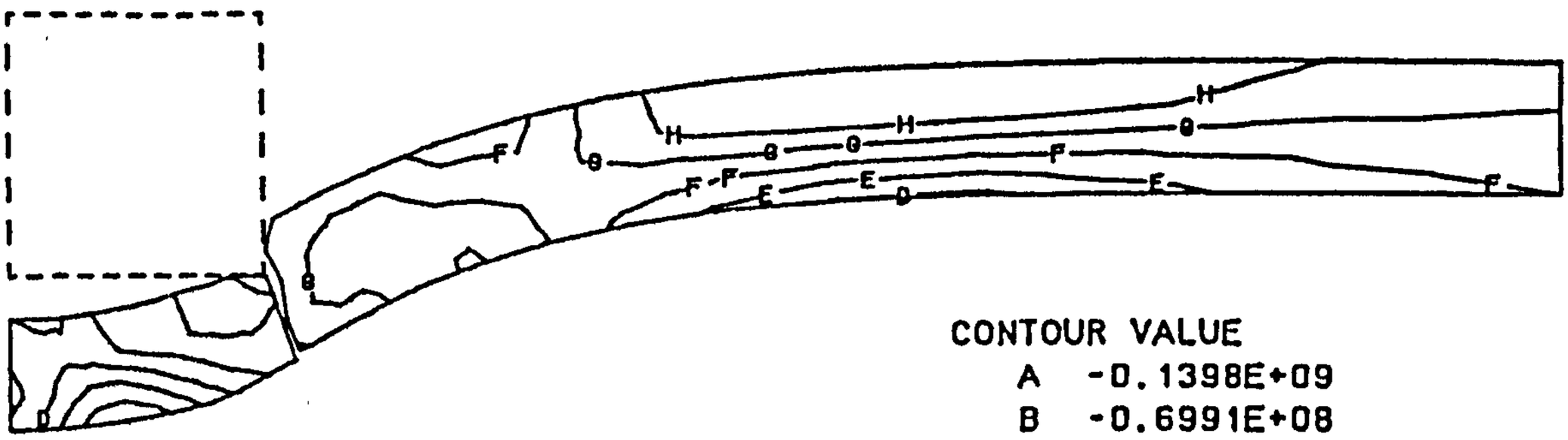

Figure 6.21
Radial stress contours for the transient thin plate test at t=31μs

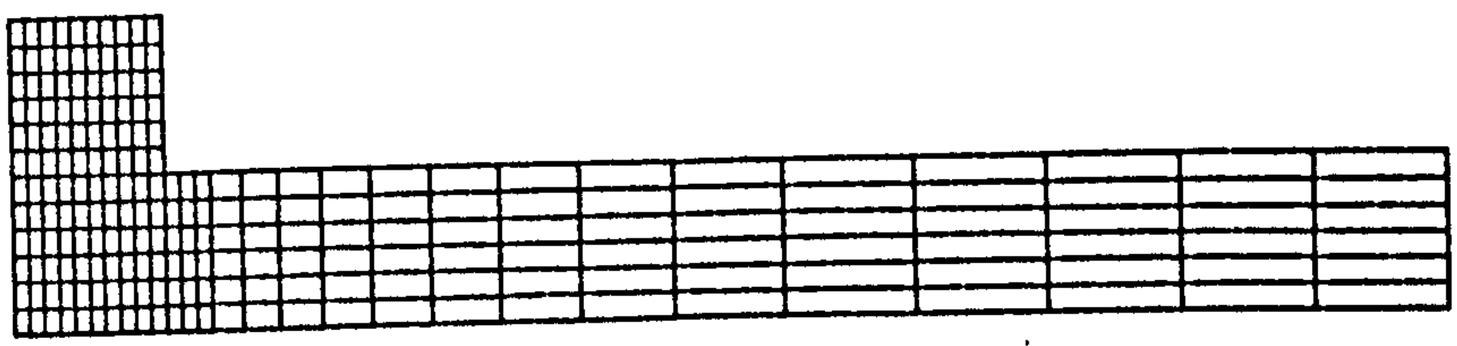

Figure 6.22
Finite element mesh for the intermediate plate impact test

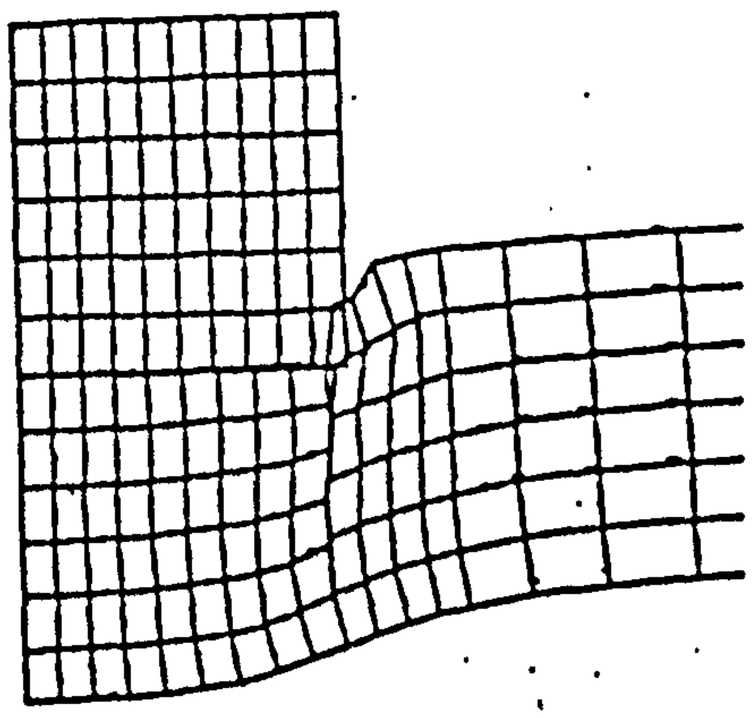

Figure 6.23
Deformation of the transient intermediate thickness plate test with a singly defined scale factor

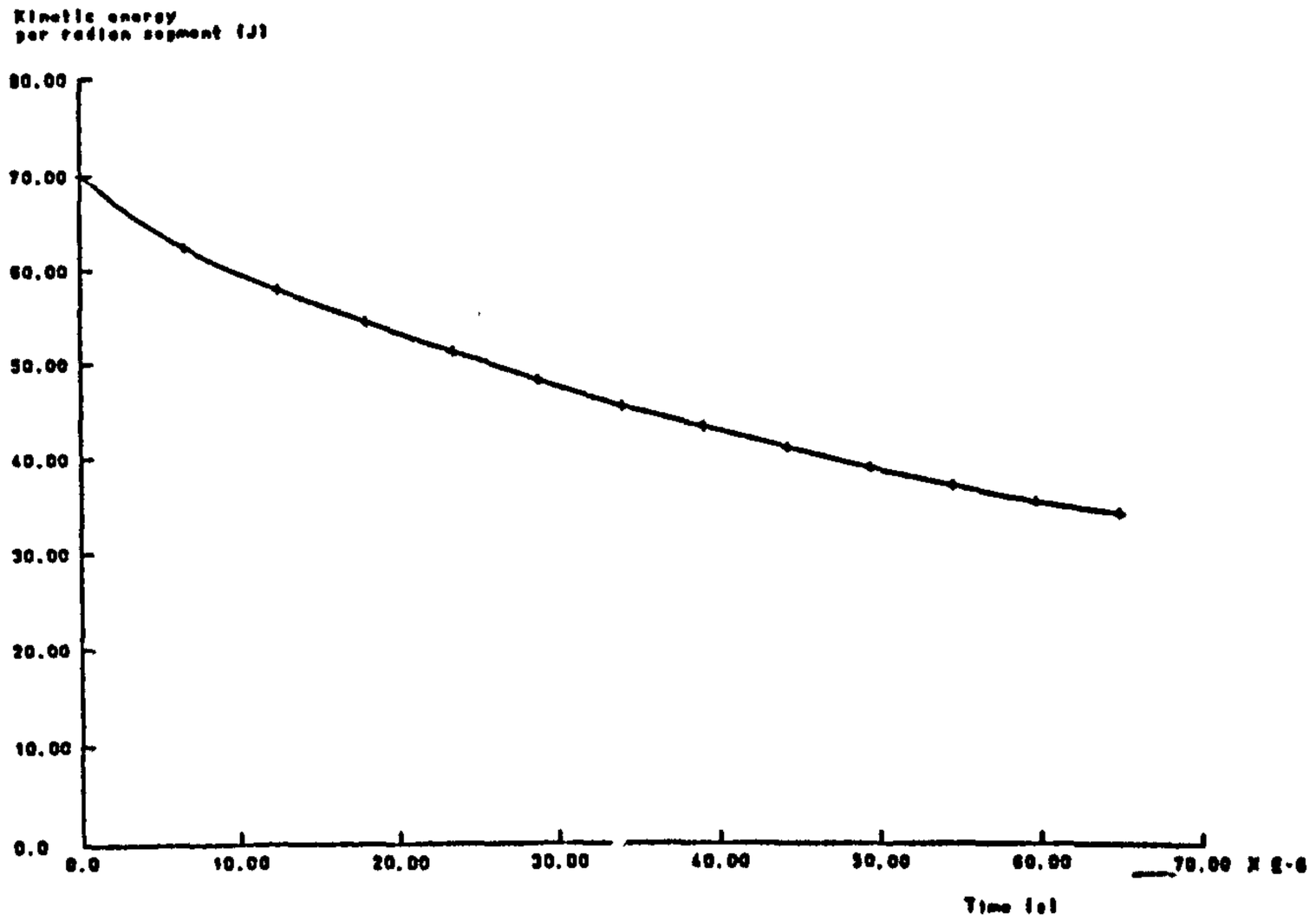

Figure 6.24
Variation of kinetic energy with time for the transient intermediate thickness plate test

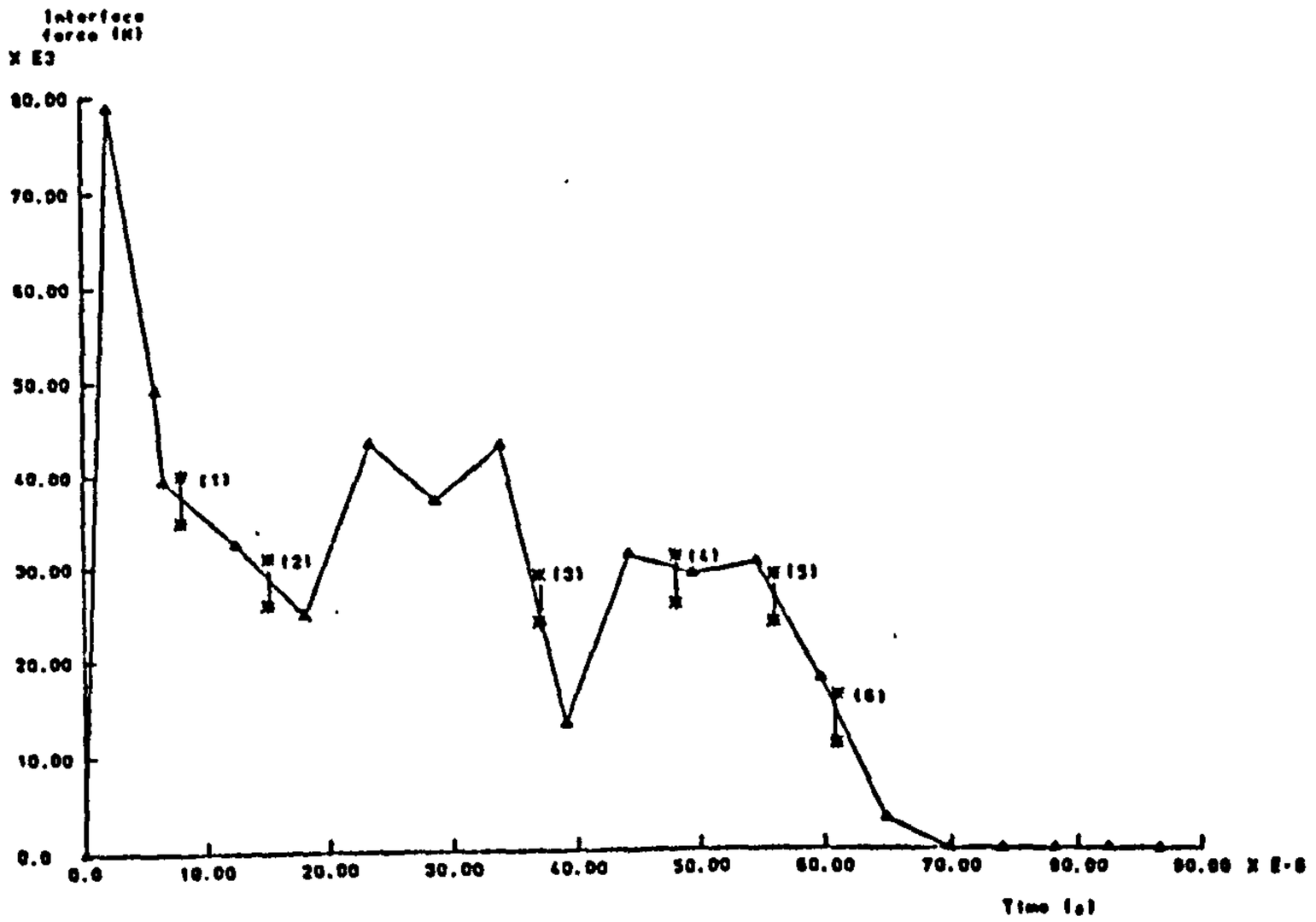

Figure 6.25

Variation of interface force with time for the transient intermediate thickness plate test

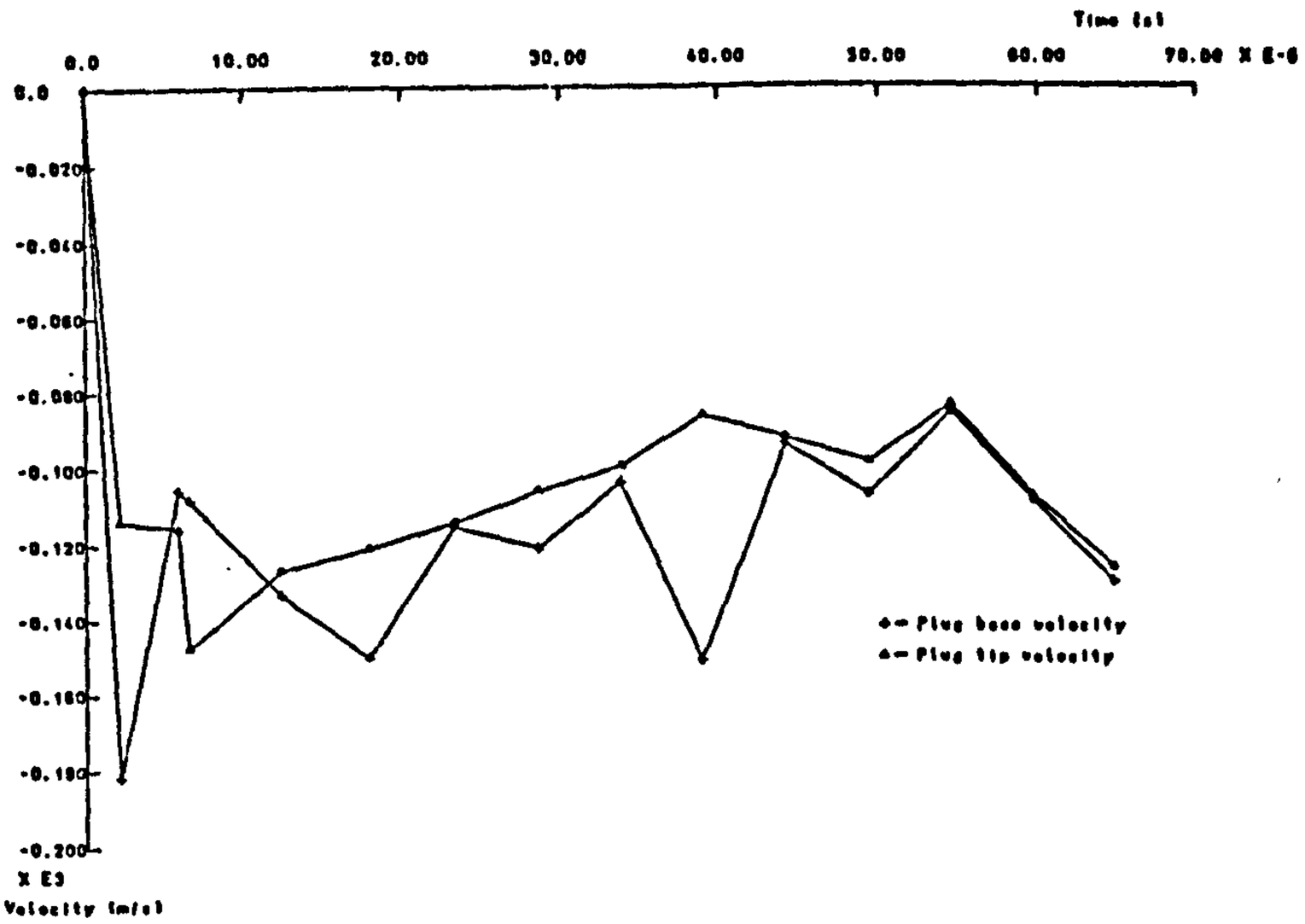

Figure 6.26

Variation of plug centreline velocities with time for the transient intermediate thickness plate test

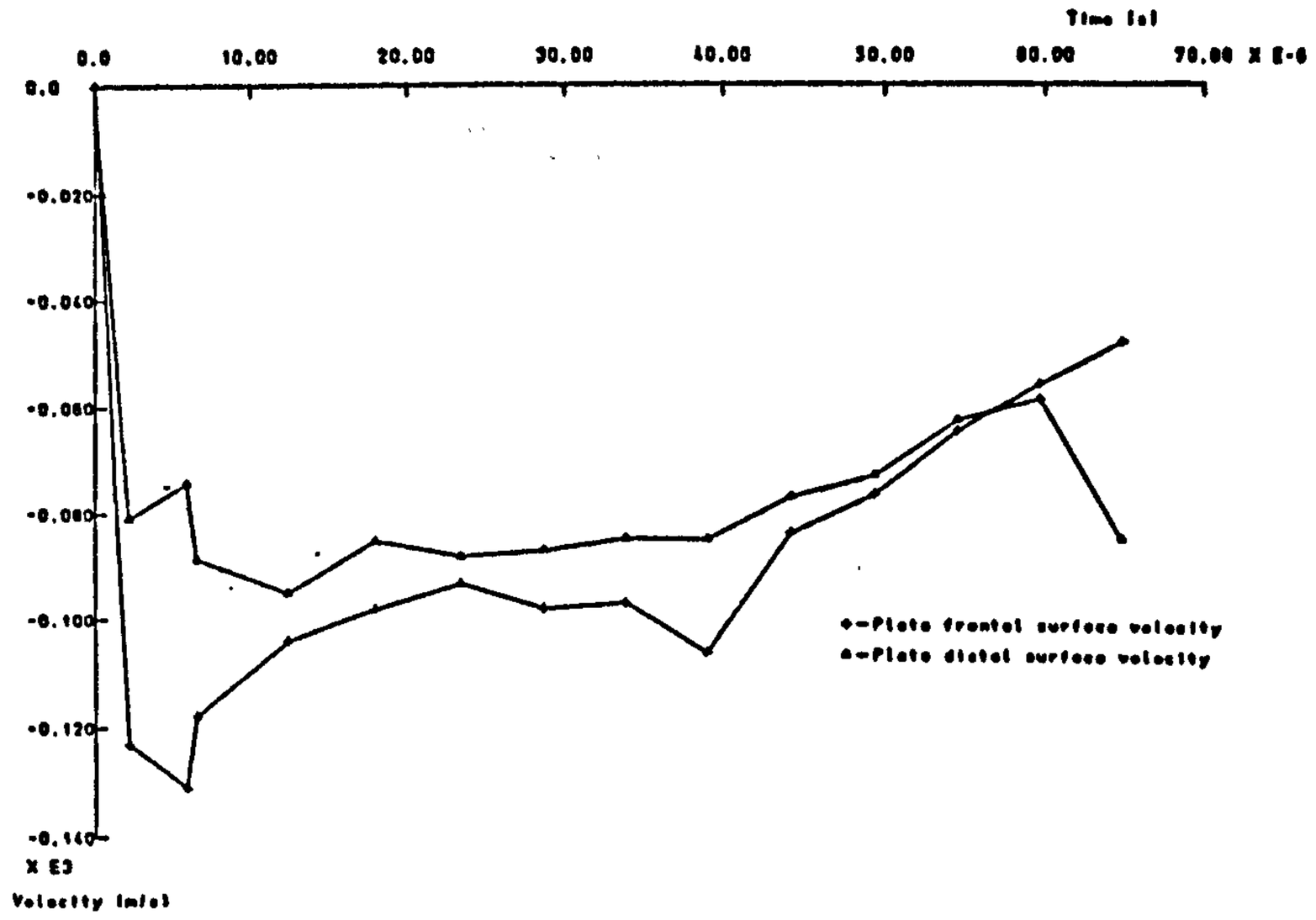

Figure 6.27

Variation of plate velocities with time for the transient intermediate thickness plate test

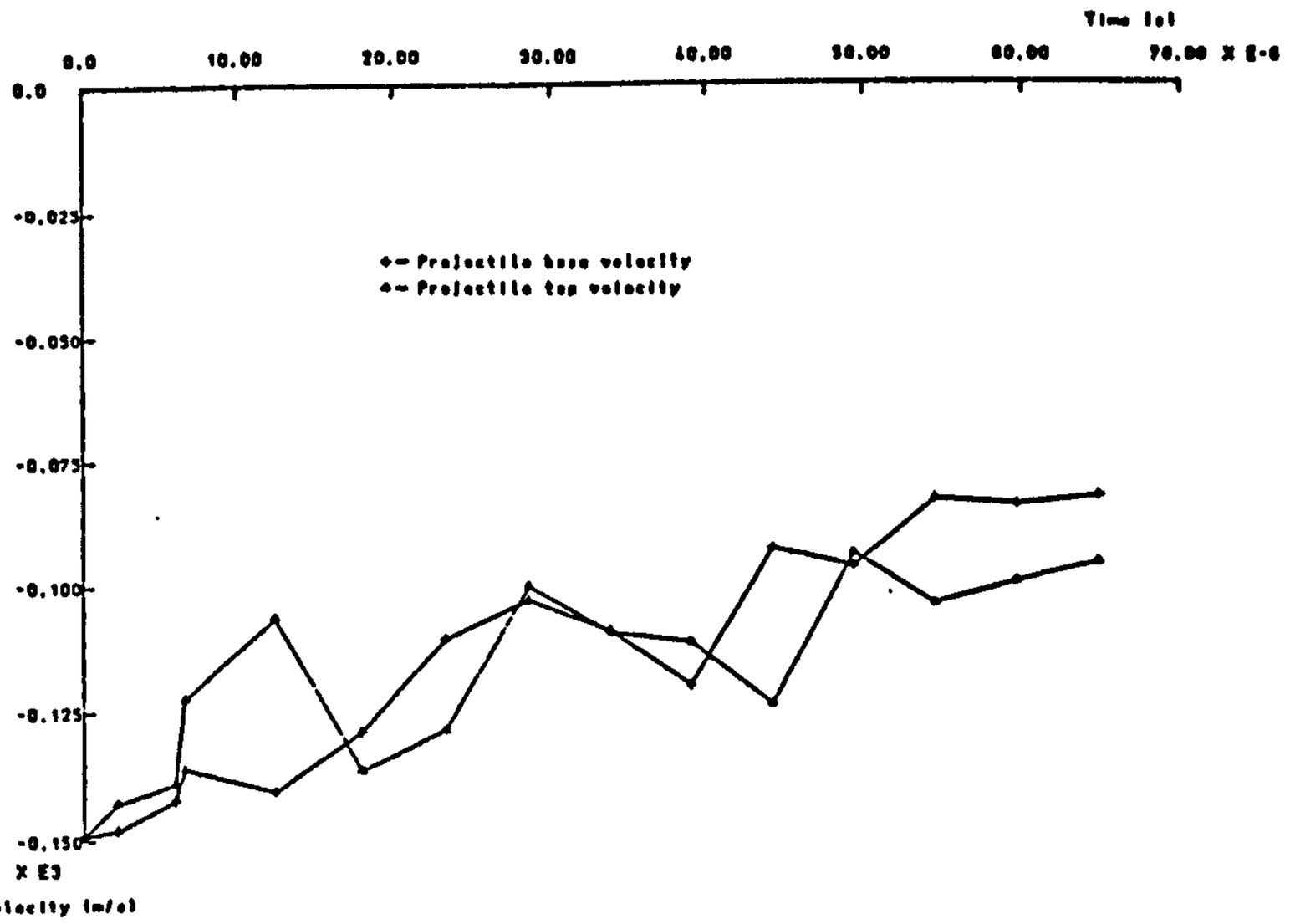

Figure 6.28

Variation of projectile velocities with time for the transient intermediate thickness plate test

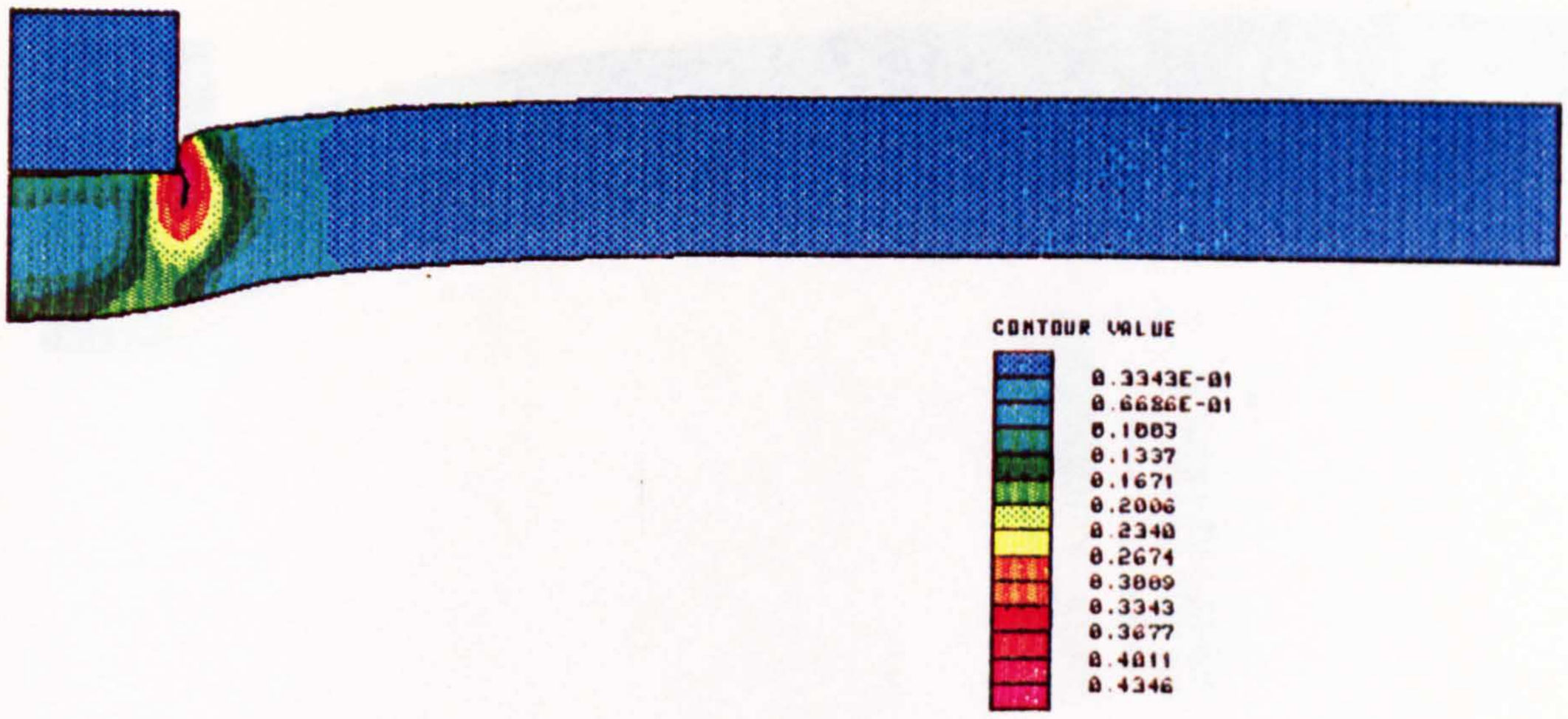

Figure 6.29

Von Mises plastic strain contours for the transient intermediate thickness plate at t=23μs

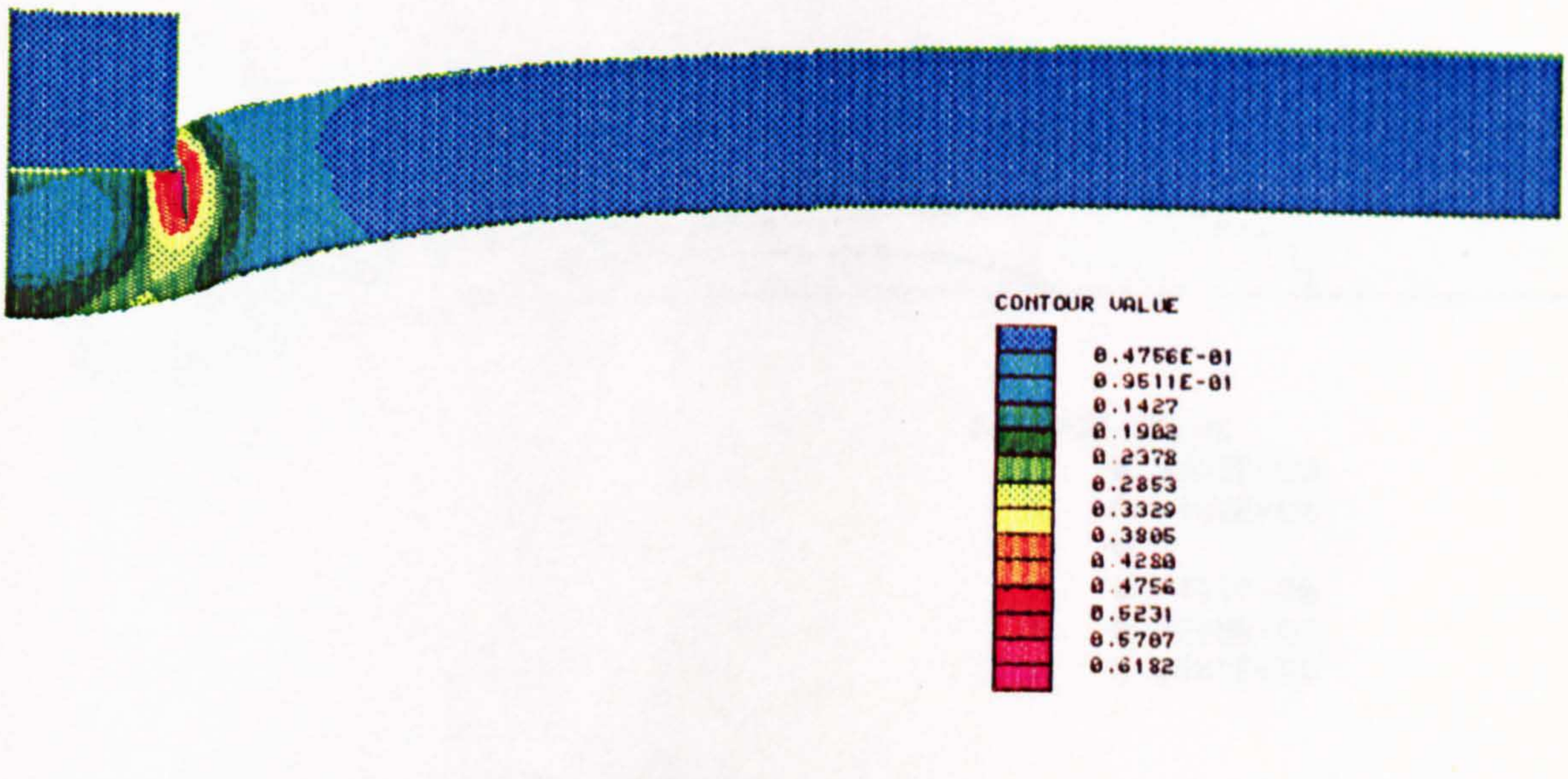

Figure 6.30

Von Mises plastic strain contours for the transient intermediate thickness plate at t=44μs

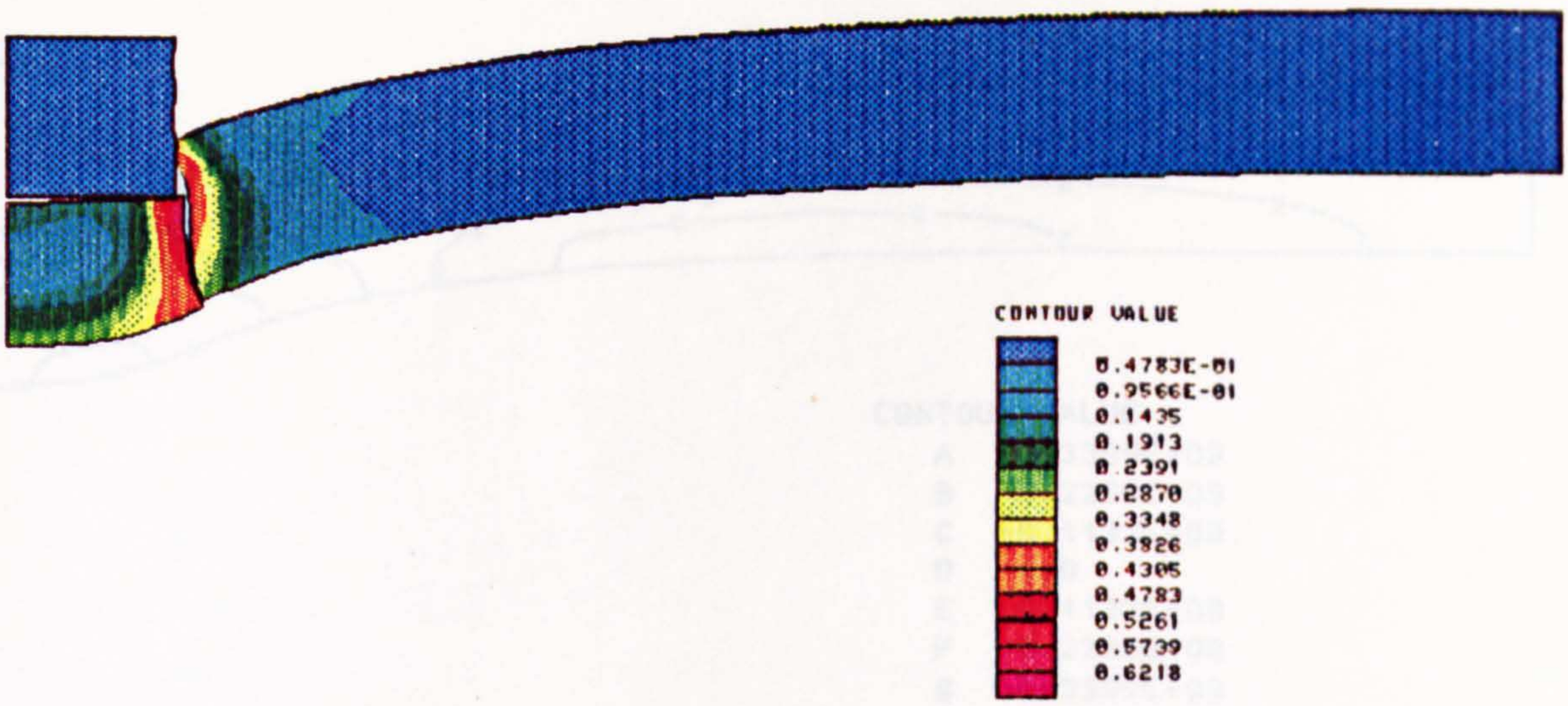

Figure 6.31

Von Mises plastic strain contours for the transient intermediate thickness plate at t=65μs

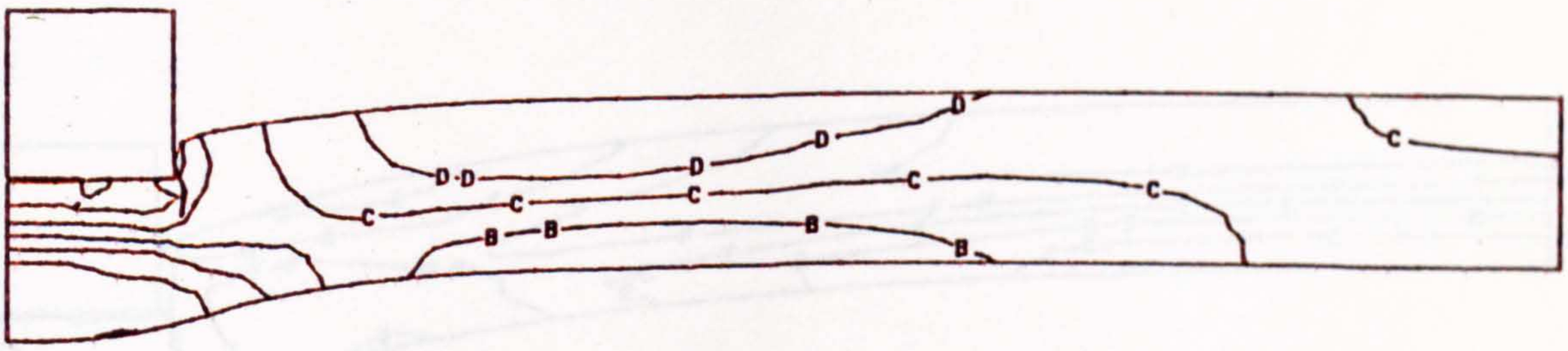

Figure 6.32

Radial stress contours for the transient intermediate thickness plate at t=23μs

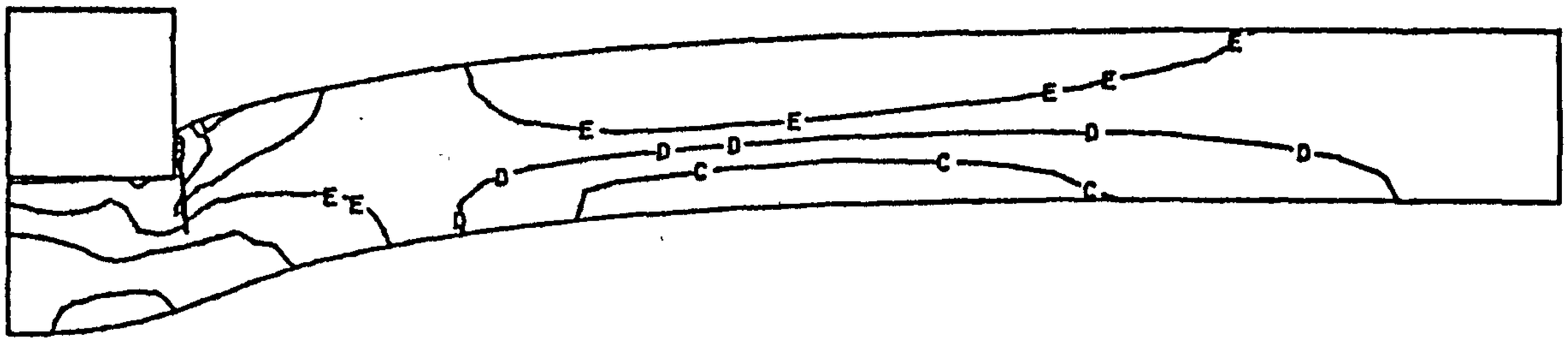

Figure 6.33

Radial stress contours for the transient intermediate thickness plate at t=44μs

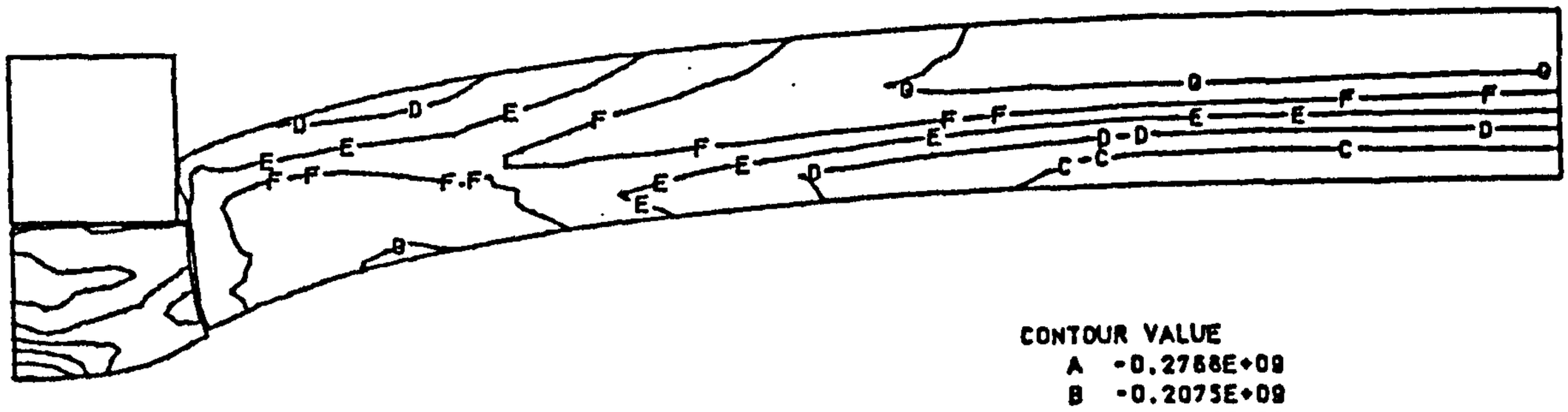

Figure 6.34

Radial stress contours for the transient intermediate thickness plate at t=65μs

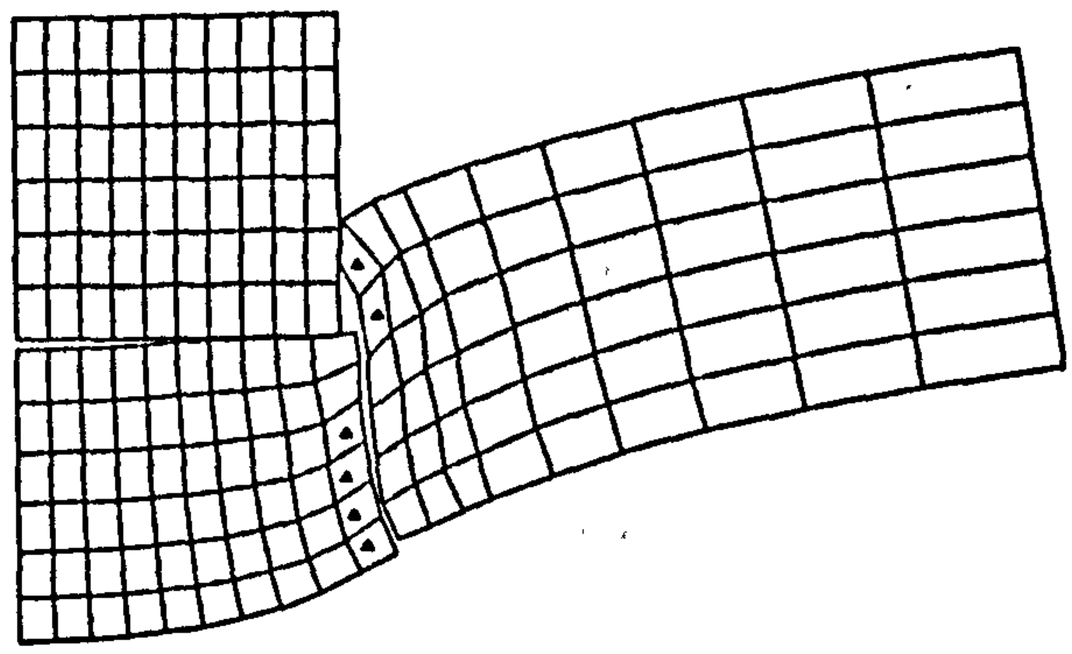

Figure 6.35
Intermediate thickness plate test element
failure sequence

CHAPTER 7

GENERAL CONCLUSIONS

The primary intent of this thesis has been to develop a numerical method of solution, whereby an Engineer may be better equipped to predict the initiation and growth of metallic fracture in the presence of plugging modes of failure. The product of this research has been an improved fracture slideline technique based on the penalty function slideline method. This improved technique has been embedded within a two dimensional, materially and geometrically nonlinear, explicit dynamics, finite element computer program. In the process of this work a number of contributions have been made, namely;

(a) The penalty function slideline technique utilised as a basis for the numerical simulation of shear band failure has been enhanced to include;

(i) A reduced amount of computer time spent in the mandatory slave search by acknowledgement of the small displacement increments present within each time step.

(ii) The use of a zonal contact detection check to eliminate the majority of the potential contact nodes prior to the more exacting contact detection processing.

(iii) Development of a simple datastructure specifically designed for use in slideline problems, particularly those involving the generation and addition of slidelines as the solution progresses. The capacity is indefinite and is limited only by the confines of the host computer.

(b) The development of a fracture slideline method based upon the penalty function slideline technique. This

proposed scheme has a number of benefits with respect to the methods utilised currently and includes;

(i) The ability to operate effectively without any reduction in the critical time step magnitude to maintain stability.

(ii) The elimination of the excitation of any interface hourglassing through the utilisation of a double pass procedure.

(iii) The greater flexibility in dealing with tangential interface motion, particularly along the plug-plate interface.

(c) The implementation of the proposed fracture slideline technique within an improved nonlinear explicit dynamics finite element code which includes;

(i) The use of a more consistent failure criteria in the form of the Von Mises effective plastic strain measure. The use of this field variable has been shown to produce an improved initial fracture location.

(ii) The use of quadrilateral elements to eliminate the unrealistically stiff response experienced with triangular elements in the presence of significant plastic flow.

(iii) The utilisation of the central difference method to integrate temporally in preference to the negatively damped Newmark-Beta scheme.

(d) Demonstration of the effectiveness of the proposed fracture slideline method to model crack initiation and propagation in plugging modes of failure. The close correlation between the quantitative comparisons with experimental results presented in Chapter Six indicate

that this has been accomplished, particularly for increasingly transient applications.

(e) Identification of the principal sources of computational inefficiency during the solution of high velocity impact problems. The inefficiencies occur as a result of disk transfer overheads and unnecessary calculations within the element post processing loop, each of which is discussed in Chapter Two.

(f) The variation of the numerical results with the interface scale factor, the effective plastic strain failure criteria and the bulk viscosity coefficients have been investigated and discussed. The results of this investigation should lead to a more efficient and correct usage of these type of impact codes in the future.

The proposed Finite Element solution scheme has been applied to several impact problems, both with and without the presence of perforation, from which several conclusions may been made concerning the effectiveness of the method;

(a) A criticism of the penalty-based slideline method is with regard to the determination of an interface scale factor prior to the analysis. Several guidelines have been suggested in Chapter Four to assist in the task based upon the comparative studies performed, however the range of scale factor which permits an adequate degree of accuracy has been shown to be large and is not seen as a limiting factor. It is concluded, therefore, that the slight variation in the results due to differing scale factors is not a severe penalty to pay for the substantial computational efficiency gained.

(b) Problems that are not governed by the effects of wave propagation, and for which only displacement fields are of interest, may be simulated with a coarse mesh without detriment to the results. The computational effort required for such problems is, thus, not restrictive on most contemporary computers provided a sufficient amount of high speed memory is available.

(c) The choice of the effective plastic strain material failure parameter, albeit not ideal, is a reasonable approximation within the limits of the current state of knowledge.

(d) The recommendation of the NMAB committee quoted in Chapter One is regarded as a reasonable approach to high velocity impact problems involving perforation. The numerical comparisons performed have indicated that the extrapolation of known results to prototype designs may be performed with confidence provided a reference set of results is available with which to validate the dynamic material characterisation.

A number of areas of concern have been highlighted in this work which have been rather restricting and will require further attention. These are as follows;

(a) The material models currently utilised in high velocity perforation dynamics problems are rather rudimentary in their ability to model failure phenomena. Furthermore, the material constants available for many of even the most commonly used materials have not been defined at either the strain rates or temperatures involved in impact loading. The further development of fracture slideline solution schemes will be limited until material models are developed which are capable of simulating such physical characteristics and, moreover, fulfil the requirements of numerical efficiency.

(b) The present method used to stabilise the hourglassing patterns generated in the four node element is not yet optimal, requiring a greater element density to accurately model bending deformation fields than should actually be necessary. The benefits accrued with its use are, however, immense and the quest for an efficient and reliable stabilisation technique must continue.

(c) Transient measurements from impact tests are not easily available outside of Government research centres and a few commercial establishments, furthermore, the results obtained tend to yield only post perforation measurements. Consequently, there is need for openly published results from impact experiments which concentrate on transient phenomena such as deflection, strain, depth of penetration and force histories. These measurements and many others, albeit very difficult to obtain, would be invaluable in the validation of numerical impact codes. A further result of the dissemination of such information would be the ensuing discussions on the interpretation of the physical behaviour implied by such experiments.

(d) The proposed fracture slideline method still requires additional work to determine the effects of variations in the effective stiffness of the interface regions during the solution process. It is thought, at present, that the effects are limited but for problems in which there are large amounts of unloading, the hysteretic losses may become significant.

(e) The mechanism of nodal release derived within this report does not take into account any intermediate damage effects. Further work is required to quantify

the effects of instantaneous release of nodes in a structure.

(f) The modelling of plugging failure in the high velocity regime would be enhanced by including mass loss due to phase changes at the projectile surface in the calculations. Techniques are currently being developed to include eroding slidelines, which have already given good results for the ultra-high velocity regime and would be of use to account for these second order temperature effects.